Visual Stratigraphy of the EastGRIP Ice Core
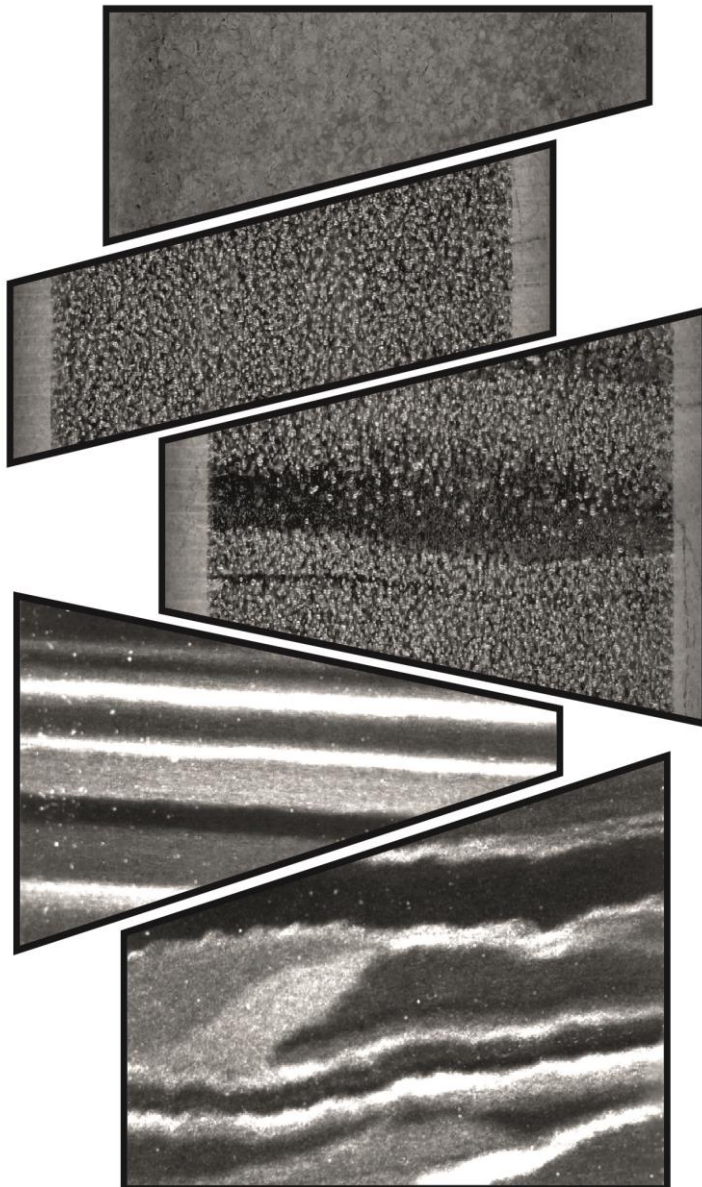
Of the Lost Ice Core Orientation, Deformation Structures,
Extreme Warm Events, and Trapped Ancient Air

PhD Thesis

Julien Westhoff

Supervisors:

Prof Dorthe Dahl-Jensen

Prof Ilka Weikusat

October 31st, 2021

This thesis has been submitted to the
PhD School of the Faculty of Science,
University of Copenhagen.

To my father
Herbert Westhoff
13.11.1956 - 15.06.2019

Abstract (English)

The polar regions are the ideal place to observe the effects of climate change. Ice sheets accumulate annual layers of snow, and later ice, over millennia and thereby create a valuable climate archive. To date, most ice cores have been drilled to unravel the secrets of the past climate, i.e. to reconstruct atmospheric conditions and temperatures.

With the ongoing EastGRIP ice core drilling, the main focus is to increase our understanding of the flow of ice. We can then make better predictions of how much, and especially how fast, the Greenland ice sheet will contribute to sea level rise. To learn about ice flow, the core is drilled through the fast moving Northeast Greenland ice stream (NEGIS).

The main focus of my work lays on understanding ice flow on the centimeter scale. To investigate small-scale features in the ice cores, I use high resolution line scan images, which cover the entire 2120 m of the ice core drilled so far.

To date, all images-data were analyzed without knowledge about the orientation of the sample. For an accurate description and analysis of deformation structures in ice, knowledge of the orientation of the sample is crucial. Thus, I have developed a method to reconstruct the orientation of physical properties image samples.

I use this newly won knowledge to analyze and interpret small-scale deformation structures found in the line scan images. I find sudden changes in the tilt of layers and interpret these as duplex structures, where stacks of layers imbricate between shear zones. Understanding the small-scale structures will help advance our knowledge on ice flow and how ice internally deforms. Furthermore, it can help unfold disturbed and folded stratigraphy in the bottom sections of ice cores, and thus extend climate archives even further into the past.

I also analyze the line scan images to investigate prominent, millimeter-thick melt layers in the ice stratigraphy. These melt layers are caused by melting on the surface of the ice sheet and tell us about extreme warm events. I provide a reconstruction of these melt events on the Greenland ice sheet over the past 10,000 years.

As snow falls, and is buried over the years, the air between the single grains is trapped and enclosed into the ice matrix. Ancient air is preserved and enables us to reconstruct atmospheric conditions of the past. The depth at which the air is sealed into the matrix, the lock-in depth, is crucial to determine the age of the air. By analyzing reflections caused by rounded air-ice interfaces, I have developed an optical method to find the lock-in depth.

My findings presented in this thesis can be considered a large boost in ice coring knowledge. Not only have I further extended the application range of the line scan device, I have also solved the problem of determining ice core orientation, which had persisted for decades. I have applied the newly won knowledge to interpret deformation structures. Furthermore, I have created a valuable melt layer archive and found a low cost solution to determine the lock-in depth of air into the ice matrix.

vi

Resumé (Danish)

Polarområderne er det ideelle sted at observere effekterne af klimaændringerne. Indlandsisen akkumulerer årlige lag af sne, og senere is, over årtusinder og skaber derved et værdifuldt klimaarkiv. Hidtil er de fleste iskerner blevet boret for at afdække hemmelighederne bag fortidens klima, dvs. for at rekonstruere atmosfæriske forhold og temperaturer.

Med det igangværende iskerneborings projekt, EastGRIP, er hovedfokus at øge forståelsen af isens flydning. Vi kan dermed lave bedre forudsigelser af, hvor meget, og ikke mindst hvor hurtigt, at Grønlands Indlandsis vil bidrage til stigningen af havniveaue. For at få viden om isens flydning bores iskernen igennem den hurtigt bevægende isstrøm i det nordøstlige Grønland (NEGIS).

Hovedvægten i mit arbejde lægger på at forstå isstrømningen på centimeterniveau. For at undersøge elementer på småskala i iskernerne, bruger jeg højtopløselige linescan billeder, som dækker hele 2120 m af den EastGRIP iskerne, der er boret indtil videre.

Hidtil blev alt billeddata analyseret uden kendskab til prøvens orientering. For en præcis beskrivelse og analyse af deformationsstrukturer i isen, er det afgørende at kende prøvens orientering. Jeg har således udviklet en metode til at rekonstruere orienteringen fra isens fysiske egenskaber fra billedprøverne.

Jeg bruger denne nyvundne viden til at analysere og fortolke små deformationsstrukturer, som findes i linescan billederne. Jeg finder pludselige ændringer i lagenes hældning og fortolker disse som dupleks-strukturer, hvor stakke af lag fletter sig ind mellem forskydningszoner. Forståelsen af de små strukturer vil bidrage til at fremme vores viden om isens flydning, og hvordan isen deformeres internt. Desuden kan det være med til korrigere for den forstyrrede og foldet stratigrafi i de nederste dele af iskerner, og dermed forlænge klimaarkiverne endnu længere ind i fortiden.

Jeg analyserer også linescan billederne for at undersøge fremtrædende millimetertykke smeltelag i iskerne stratigrafien. Disse smeltelag er forårsaget af afsmeltning på iskappens overflade og fortæller os om ekstremt varme begivenheder. Jeg rekonstruere disse smeltebegivenheder på den grønlandske indlandsis de seneste 10.000 år.

Når sneen falder, og bliver begravet i årenes løb, bliver luften mellem de enkelte snefnug fanget og indkapslet i iskernen. Den antikke luft bevares og gør det muligt for os at rekonstruere fortidens atmosfæriske forhold. Den dybde, hvor luften er forseglet i isen, lock-in-dybden, er afgørende for at bestemme luftens alder. Jeg har udviklet en optisk metode til at finde lock-in-dybden ved at analysere refleksioner forårsaget af afrundede grænseflader mellem luften og isen.

Mine resultater, der præsenteres i denne afhandling, kan betragtes som et stort bidrag i viden om isboringer. Jeg har ikke blot påvist, at linescan apparatet er nyttigt, jeg har også løst problemet med at bestemme iskerneorienteringen, som har været et udestående problem i årtier. Jeg har også anvendt denne nyvundne viden til at analysere deformationsstrukturer. Derudover har jeg skabt et værdifuldt smeltelagsarkiv, og fundet en billig løsning til at bestemme luftens lock-in dybde i issøjlen.

Zusammenfassung (German)

Die Polarregionen sind der ideale Ort, um die Auswirkungen des Klimawandels zu beobachten. Eisschilde sammeln über Jahrtausende hinweg jährliche Schneeschichten, welche später zu Eis werden, an und bilden so ein wertvolles Klimaarchiv. Bislang wurden die meisten Eiskerne gebohrt, um die Geheimnisse des vergangenen Klimas zu lüften, d. h. um die atmosphärischen Bedingungen und Temperaturen zu rekonstruieren.

Bei der laufenden EastGRIP-Eiskernbohrung geht es vor allem darum, unser Verständnis der Eisströme zu verbessern. So können wir besser vorhersagen, wie viel und vor allem wie schnell der grönländische Eisschild zum Anstieg des Meeresspiegels beitragen wird. Um etwas über das Fließen von Eis zu erfahren, wird der Kern durch den sich schnell bewegenden nordostgrönländischen Eisstrom (NEGIS) gebohrt.

Der Schwerpunkt meiner Arbeit liegt auf dem Verständnis des Eisflusses auf der Zentimeterskala. Um kleinräumige Strukturen in den Eiskernen zu untersuchen, verwende ich hochauflösende Linescanbilder, die die gesamten 2120 m des bisher gebohrten Eiskerns abdecken.

Bislang wurden alle Bilder ohne Kenntnis der Orientierung der Probe analysiert. Für eine genaue Beschreibung und Analyse von Deformationsstrukturen im Eis ist die Kenntnis der Orientierung der Probe allerdings entscheidend. Daher habe ich eine Methode entwickelt, um die Orientierung von Bildproben zu rekonstruieren.

Dieses neu gewonnene Wissen nutze ich, um kleinräumige Deformationsstrukturen, die in den Linescanbildern zu finden sind, zu analysieren und zu interpretieren. Ich finde plötzliche Änderungen in der Schichtneigung und interpretiere diese als Duplexstrukturen, bei denen Schichtenstapel gekippt zwischen Scherzonen eingelagert sind. Das Verständnis der kleinräumigen Strukturen wird dazu beitragen, unser Wissen über den Eisfluss und die internen Verformungen des Eises zu erweitern. Außerdem kann es dazu beitragen, die gestörte und gefaltete Stratigraphie in den unteren Abschnitten von Eiskernen zu entschlüsseln und so die Klimaarchive noch weiter in die Vergangenheit auszudehnen.

Ich analysiere die Linescanbilder auch, um auffällige, millimeterdicke Schmelzschichten in der Eisstratigraphie zu untersuchen. Diese Schmelzschichten werden durch Schmelzereignisse an der Oberfläche des Eisschildes verursacht und geben Aufschluss über extreme Wärmeereignisse. In dieser Arbeit stelle ich eine Rekonstruktion dieser Schmelzereignisse auf dem grönländischen Eisschild in den letzten 10.000 Jahren vor.

Wenn Schnee fällt und im Laufe der Jahre begraben wird, wird Luft zwischen den einzelnen Körnern gefangen und in der Eismatrix eingeschlossen. Die alte Luft bleibt eingeschlossen erhalten und ermöglicht es uns, die atmosphärischen Bedingungen der Vergangenheit zu rekonstruieren. Die Tiefe, in der die Luft in der Matrix eingeschlossen ist, die Lock-in-Tiefe, ist entscheidend für die Bestimmung des Alters der Luft. Durch die Analyse von Reflexionen, die von abgerundeten Luft-Eis-Grenzflächen verursacht werden, habe ich eine optische Methode zur Bestimmung der Lock-in-Tiefe entwickelt.

Meine in dieser Arbeit vorgestellten Ergebnisse können als ein großer Wissenszuwachs im Bereich der Eiskernbohrung angesehen werden. Ich habe nicht nur die Nützlichkeit des Linescangeräts demonstriert, sondern auch das jahrzehntelang bestehende Problem der Bestimmung der Eiskernorientierung gelöst. Ich habe das neu gewonne Wissen angewandt um Deformationsstrukturen zu analysieren. Zudem habe ich ein wertvolles Schmelzarchiv der letzten 10,000 Jahre geschaffen und eine kostengünstige Lösung zur Bestimmung der Lock-in-Tiefe der Luft in die Eismatrix gefunden.

Acknowledgments

A big thank you goes to my main supervisor Dorthe for making all this possible. Thank you for giving me the chance to have my first day of the PhD on the Greenland ice sheet and thank you for all the opportunities throughout my three years of the PhD. I very much appreciated the energy with which you solved problems for me, especially when they were really important. Thank you also for the understanding words and acts during difficult times in the past three years.

Another big thanks goes to my supervisor from Germany, Ilka. Also thanks to you I was offered the unique chance to go to the field. Thank you also for giving me a free hand in what to do with the line scan images and for giving me full responsibility over the device and data.

Thank you to Anders, whom I would consider my bonus supervisor, for all the time we spent discussing melt layers, grayscale images, and stories about the vikings in your office.

Thank you to the Villum Foundation for supporting Dorthe's ice flow project, and thus also making my position possible.

A big thank you to the group at CIC/PICE: To Christine and the ice flow modeling group, for all the exciting meetings every week where I learned a lot. Thank you to Helle, for giving me the chance to help organize the summer school ICAT. A big thanks to Paul for the regular climbing sessions and all the good times. And thanks to everyone else with whom I had great chats about ice cores and Greenland over a cup of coffee.

A big thank you to all my junior colleagues at CIC/PICE: Iben, Nicholas, David, Tamara, Giulia, Jia-Mei, Jesper, Diana, Michael, the other Michael, Mikkel, and all the other PhD, master and bachelor students, for the good times in the office, for the retreat to Sweden, and after-work activities.

A big thank you also goes to Nico and Steven for all the great collaborations and good times we had over the years. Thank you also to Daniela, Johanna, Johannes, and Sepp from AWI for the great collaborations.

Thank you also to Paul from Tübingen, for all the inspiring ideas and suggestions about folds and other structures.

Thank you to everyone else I meet over the past three years, at CIC, at various conferences, meetings, or summer schools, and who I should have mentioned here...

Thank you to my mom and brother for always supporting me in everything I did. In the memory of my father, I would like to especially thank him for making me interested in nature and science and for paving the way that lead me to where I am today. Without your advice, all this would not have been possible.

Thank you to Lisa, for all the support over the past three years (and more). Thank you for moving to Denmark with me and joining me on all the kite surf adventures around the country. And of course, thank you for all the first revisions of my manuscripts.

Abbreviations

AFA	Automated Fabric Analyzer
AWI	Alfred Wegener Institute Helmholtz Centre for Polar and Marine Research
BCD	Bubble Close-off Depth
DEP	Di-electric Profiling
DRT	Deformation, Rheology, and Tectonics (conference)
EastGRIP	East Greenland Ice Core Project
ECM	Electric Conductivity Measurement
EDML	EPICA Dronning Maud Land
EGU	European Geoscience Union
EPICA	European Project for Ice Coring in Antarctica
ICAT	Ice Core Analysis Techniques PhD School
LASM	Large Area Scanning Microscope
GICC05	Greenland Ice Core Chronology 2005
GRIP	Greenland Ice Core Project
GISP2	Greenland Ice Sheet Project 2
μCT	micro Computer Tomography
NEEM	North Greenland Eemian Ice Drilling
NEGIS	Northeast Greenland Ice Stream
NorthGRIP	North Greenland Ice Core Project
RECAP	Renland Ice Cap
SPICEcore	South Pole Ice Core
WAIS	West Antarctic Ice Sheet

Contents

List of Figures

Preface - Objective, Thesis Structure, and Time-line

Objective of PhD   The aim of my PhD was to get a deeper insight into the flow of ice and ice deformation, i.e. ice rheology, by analyzing the EastGRIP ice core mainly using line scanner data. The project is part of, and contributes to, the Ice Flow Project, lead by Dorthe Dahl-Jensen and funded by the Villum Foundation (grant nr. 16572). This thesis presents my research as a synopsis of my first-authored manuscripts. My research helps deepen our understanding of ice rheology, of melt events on the ice sheet, and of the formation of air bubbles in polar ice.

Thesis structure   The introduction of this thesis (chapter 1) aims to cover the basics of my scientific publications in an accessible and comprehensive style.

Since all my publications are based on the analysis of visual stratigraphy images acquired with the line scanner, the device and its various applications are explained in chapter 2.

chapter 3 provides an overview of my manuscripts, including my contribution, a short state-of-the-art section, and a brief summary. It also contains an overview of co-author publications, conference participation, scientific work before my PhD, and dissemination during my PhD.

Chapters 4, 5, 6, and 7 contain my research manuscripts, the making of which is explained in the next paragraph. chapter 8 puts my work into perspective and provides figures and ideas, that could become future manuscripts. The appendix contains overviews of the line scan images.

Time-line of PhD-work   In this thesis I present my work from August 2018 to October 2021. In mid 2018, I began analyzing folded ice stratigraphy, i.e. deformation structures, in the EastGRIP ice core (chapter 5). I presented this work at various conferences (EGU, in Austria and DRT, in Germany) and meetings (Onsen meeting, in Japan). After some months of research on folds in ice cores, it became obvious that a detailed description of folds is difficult without knowing the orientation of the ice core. Thus, I developed a method to reconstruct ice core orientation. The manuscript (chapter 4) was published in October 2020 in the *Annals of Glaciology*.

While I was working on reconstructing the ice core orientation, the EastGRIP drilling was semi-halted in 2019, and fully paused in 2020 and 2021. The bottom, and possibly folded and rheologically interesting part of the ice core, would not be drilled and analyzed during my PhD period, so my work on folds was put on hold.

I began climate-related research on melt layers in the Holocene section of the EastGRIP core in late 2019 and through 2020 (chapter 6). The manuscript also contains a short discussion on rheology in the upper parts of an ice sheet. I submitted this manuscript about melt layers to the EGU journal *Climate of the Past* in July 2021. To date, it is through the

first round of reviews and I am partly done with the revision of the manuscript.

Simultaneously to the melt layers, I investigated the processes of firn to ice metamorphosis and the bubble lock-in, using the line scanner images. The manuscript to this work is in its final stages and almost ready for submission (chapter 7).

Although the acquisition of the full EastGRIP line scan data-set lays outside the timeframe of my PhD, I continued the analysis on folds and deformation structures in ice cores (chapter 5) on the side. Deformation structures in an ice core's stratigraphy become visible with passive strain markers, such as cloudy bands. With the first cloudy bands (going from top to bottom of the ice core), deformation structures are visible and furthermore, some types of the deformation structures have not been seen in any other previously drilled deep ice core.

Chapter 1

Of Greenland, Ice Cores, and the Past Climate

1.1 The Past Climate from Ice Cores
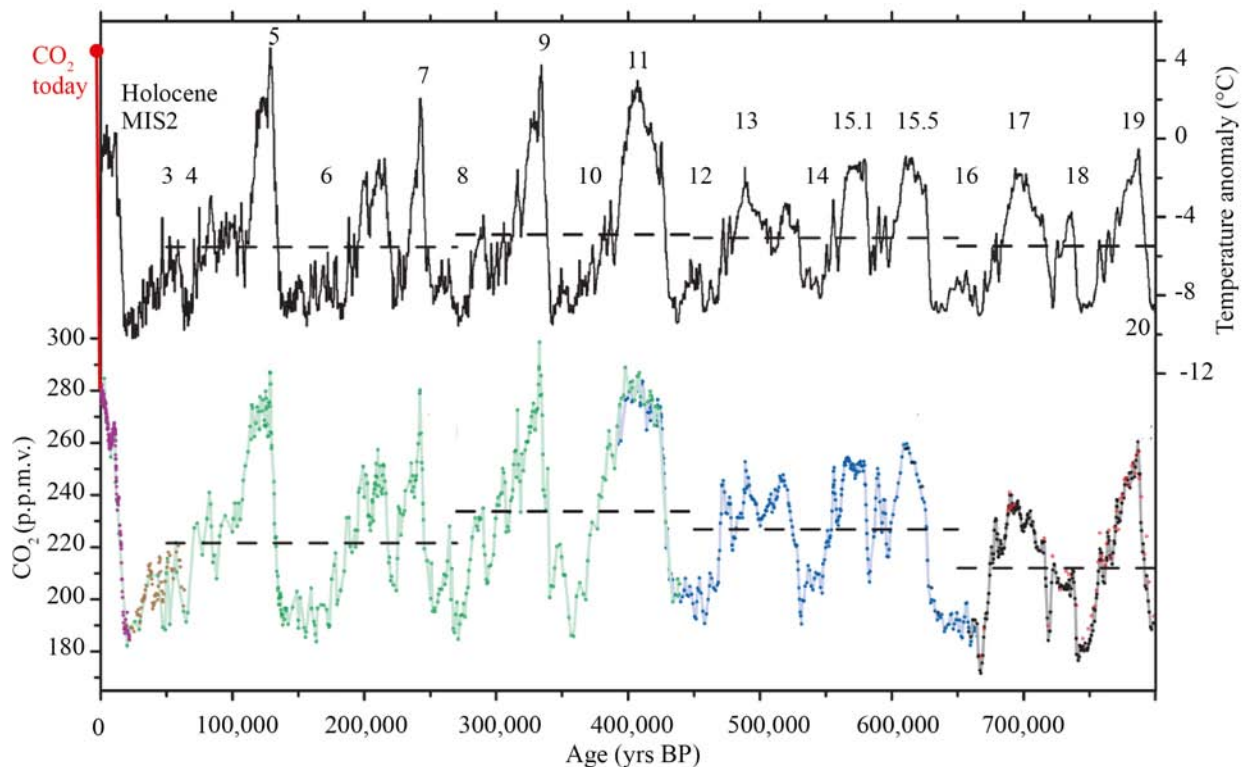
Figure 1.1: EPICA Dome C temperature anomaly and compilation of CO_2 records over the past 800,000 yrs, including the the CO_2 value from the year 2021. Modified from Lüthi et al. (2008).

Over the centuries, millenia, and eons, the global climate has constantly been changing. The polar regions are the ideal place to observe climatic changes, as they offer a valuable climate archive. Year by year, and over the millenia, ice sheets accumulate layers of snow and ice, and thereby preserve information of the past climate.

Stable water isotopes from snow are analyzed to derive a proxy for the temperature at the time of deposition (Dansgaard et al., 1969). As snow falls, and is buried over the years, the air between the single grains is trapped and enclosed into the ice matrix. Like this, the atmospheric CO_2 composition of ancient air is preserved in the ice (fig. 1.1).

Drilling though the ice sheets and analyzing the ice cores can retrieve valuable information. Reconstructions from the Antarctic Dome C ice core provide an overview of a proxy for temperature (δD) over the past 800,000 years (EPICA community members, 2004; Lüthi et al., 2008). The compilation of CO_2 measurements shows a strong correlation to the temperature reconstruction (fig. 1.1). While both temperature and CO_2 somewhat oscillate on a 100,000 year cycle, the CO_2 values measured today greatly exceed the scale on the left side of fig. 1.1. Understanding the past climate variations is important to predict the future and understand the climatic changes we see today (IPCC report, 2021).

However, the polar ice sheets are not a rigid body. They are constantly in motion, partly by sliding and partly by deformation. Understanding the internal deformation of ice, on the large (kilometers) and small scale (centimeters), is essential to predict the ice discharge contributing to sea level rise and to untangle disturbed climate records (e.g. NEEMCommunityMembers, 2013).

1.2   From Snow and Firn to Ice

Before one can analyze the ice in an ice sheet, it is important to understand the process of how snow becomes ice. Snow falls across the ice sheet in a more or less evenly distributed manner. Wind redistributes the deposited snow and creates a rather flat surface, with surface features such as sastrugi or small-scale variations in topography (Zuhr et al., 2021). At the EastGRIP site, every year one meter of snow is added to the surface, submerging structures on the surface. This accumulation corresponds to approximately 10 cm of ice equivalent per year. Assuming a steady state ice sheet, the surface is lowered by the same amount which is accumulated. This lowering is accommodated by internal deformation, i.e. thinning of the ice, and basal melting.

Fresh fallen snow has a density (d) of 50 to 100 $kg\ m^{-3}$ and over time, densification driven by overlaying snow layers leads to grain boundary sliding, which rearranges the grains and results in further compaction ($d = 200\ to\ 300\ kg\ m^{-3}$, Cuffey and Paterson, 2010). Further settling and physical compaction increases the density to 550 $kg\ m^{-3}$. Snow is now compacted to firn, where grains cannot be packed tighter. At this stage, air pathways remain throughout the firn column and a constant exchange with the atmosphere is possible. Sintering further increases the density to 830 $kg\ m^{-3}$ by crystallization and the deformation of ice crystals. Now firn has turned into ice and air pathways gradually close off. As closed-off bubbles form, a gas exchange with the atmosphere is no longer possible and a paleo atmospheric composition is preserved. Due to compaction of the air bubbles, the density further increases to a typical value of 917 $kg\ m^{-3}$ for pure glacial ice.

1.3   About the Rheology of Ice

Ice is a composite of the elements Hydrogen and Oxygen and can appear in twelve solid states on earth. In the most common and stable appearance of ice (I_h), it forms a hexagonal crystal structure (Petrenko and Whitworth, 1999). From now on, the term "ice" represents ice I_h. Single crystals and their composition in the ice, i.e. fabric, contain a lot of information on ice rheology. Ice has one c-axis and perpendicular to it, three a-axes, pointing towards the corners of the hexagonal crystal structure (fig. 1.2). The c-axis, which can be displayed using polarized light, is used to describe the orientation of each grain.

As snow falls and is compacted to firn, the grains have a random orientation. Over time, with increasing overburden and deformation in the ice, these grains rearrange. This rearrangement can be accommodated by the creep of ice, where ice can be considered a
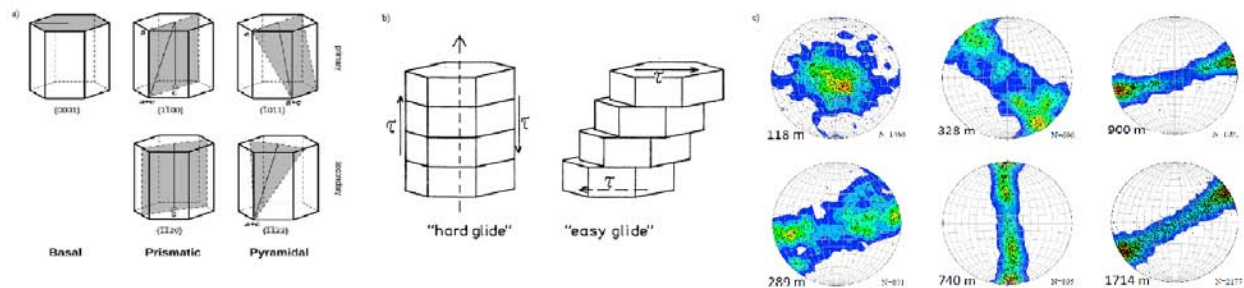
Figure 1.2: a) Possible glide planes in ice (based on Hondoh, 2000, displayed in Faria et al., 2014), b) easy glide along the basal planes and hard glide along other planes (Thorsteinsson, 1996), and c) fabric of the EastGRIP ice core (Stoll, 2019, Master Thesis).

viscous fluid, with a viscosity of $10^4 Pas$ at $-10°C$ (Cuffey and Paterson, 2010). The plastic flow of an ice sheet, and creep of ice, are driven by the weight of the ice sheet. Each grain has a high mechanical anisotropy, resulting in crystals with a favorable orientation to deform first. Ice deforms 60-100 times easier via basal gliding, i.e. the plane perpendicular to the c-axis, than along other planes (fig. 1.2a,b, e.g. Duval et al., 1983, Schulson and Duval, 2009, or Faria et al., 2014). Thus, some fabrics are more responsive to deformation than others.

As ice flows, the fabric of ice changes under deformation and recrystallization. There are two main processes which influence the fabric of ice cores: 1) the c-axis will rotate towards the direction of maximum finite shortening as described by e.g. Alley (1992) or Qi et al. (2019) or 2) new grains form due to recrystallization and have a different orientation than the surrounding or host grains (Llorens et al., 2017). This information can be used to describe the deformation history as done by e.g. Kamb (1972), Thorsteinsson et al. (1997), Wang et al. (2002), Montagnat et al. (2014), or Weikusat et al. (2017).

1.4 The Greenland Ice Sheet

1.4.1 Ice Sheet Dynamics

On the large scale, we have access to observations from space, e.g. satellite data and thus can determine the surface velocity of an ice sheet (fig. 1.3a, same as fig. 4.1). Based on the MEaSUREs velocity dataset from Joughin et al. (2010), we can identify a central area that consists of domes and ice divides (white line in fig. 1.3a), with a surface velocity close to zero. From these domes and ice divides the ice flows to the margins, while surface velocity increases (see logarithmic color-scale in fig. 1.3a). The central parts of the ice sheet are more than three kilometers thick, and the highest point is at summit station, 3216 m above sea level.

Haefeli (1961), and later Dansgaard et al. (1969), identify gravity to be the main driving force for large-scale ice flow (fig. 1.3d). The flow is driven by snow and ice accumulation in the central areas of the ice sheet (accumulation zone) and by melting around the margins of the ice sheet (ablation zone) or by channeling into a glacier and then calving-off as an iceberg (Cuffey and Paterson, 2010). The idealized ice sheet from Dansgaard et al. (1969) was developed based on the descriptions of flow from Nye (1951) and Glen (1952). To compare the dimensions of the ideal ice sheet to the real one, I present a 200-fold vertically exaggerated profile of the Greenland ice sheet (fig. 1.3b) and a 10-fold exaggerated profile (fig. 1.3c).
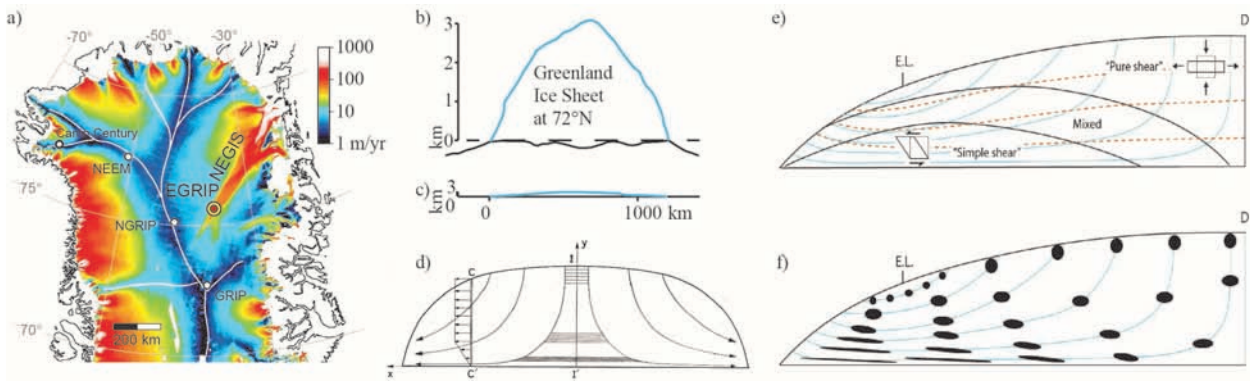
Figure 1.3: a) Map of Greenland, including drill sites and ice sheet surface velocities (Westhoff et al., 2020, on the basis of Joughin et al., 2010). b) Greenland ice sheet, vertically exaggerated by a factor of 200 and c) Greenland ice sheet, vertically exaggerated by a factor of 10, to display the vertical exaggeration of d,e,f. d) Sketch of ice flow in an ice sheet (Dansgaard and Johnsen, 1969, on the basis of Haefeli, 1961), and e) deformation regimes in an ice sheet, with particle pathways (blue), and iso-time line (orange), and f) schematic illustration of cumulative strain of selected particles, (e,f) on the basis of Hooke and Hudleston (1978).

During ice flow from the accumulation zone to the ice sheet margins, the ice crosses different deformation regimes. Hooke and Hudleston (1978) show a profile with a pure shear regime (vertical thinning, horizontal stretching) in the upper and central part of the ice sheet, a mixed regime, and a regime where simple shear dominates (fig. 1.3e). The deformation of a circular particle is also sketched for illustration of the deformation regimes (fig. 1.3f). Figure 1.3e,f also indicate the equilibrium line (E.L.), separating the accumulation and ablation zone.

Most ice core drillings so far have aimed to find the flattest and most un-disturbed stratigraphy, to get a perfect sequence of layers as far back in time as possible, for appropriate climate reconstructions. Thus, sites have been chosen close to ice divides (white line in fig. 1.4) where upstream effects are low (e.g. Gerber et al., 2021). Additionally, sites with cold ice at the base limits basal motion and reduced basal melting. Cold ice is therefore preferred over sites with temperate or wet basal ice, where basal sliding, or motion, is easier accommodated and basal melt rates are expected to be higher.

1.4.2   Folded Stratigraphy and Ice Streams

Climate reconstructions have been the main focus for most ice core drilling campaigns so far. But for this, we need undisturbed layers, which can only be found in the upper two thirds of an ice core (Faria et al., 2010, Jansen et al., 2016). So it is of high significance to understand the deformation that the flow of ice causes to layers. With more knowledge on the effect of ice flow, we can learn to unfold folded stratigraphic layers. Ultimately, we can then retrieve a continuous sequence of layers even further back in time, and are not limited to layers being preserved in stratigraphic order.

The broad interest in folded stratigraphy was sparked, when the NEEM community members (2013) managed to reconstruct the folded stratigraphy of the bottom parts of the NEEM ice core. They analyzed the profile of the oxygen isotopes ($\delta^{18}O$), which showed a repetitive signal. Thus, they came up with a sequence of folding events that could have lead to this folded stratigraphy. A similar method had been used to unfold the bottom sections of the GRIP core. Suwa et al. (2006) compare the measured atmospheric methane and $\delta^{18}O$ from GRIP to Antarctic ice core records and managed to reconstruct the folded stratigraphy for the GRIP record.
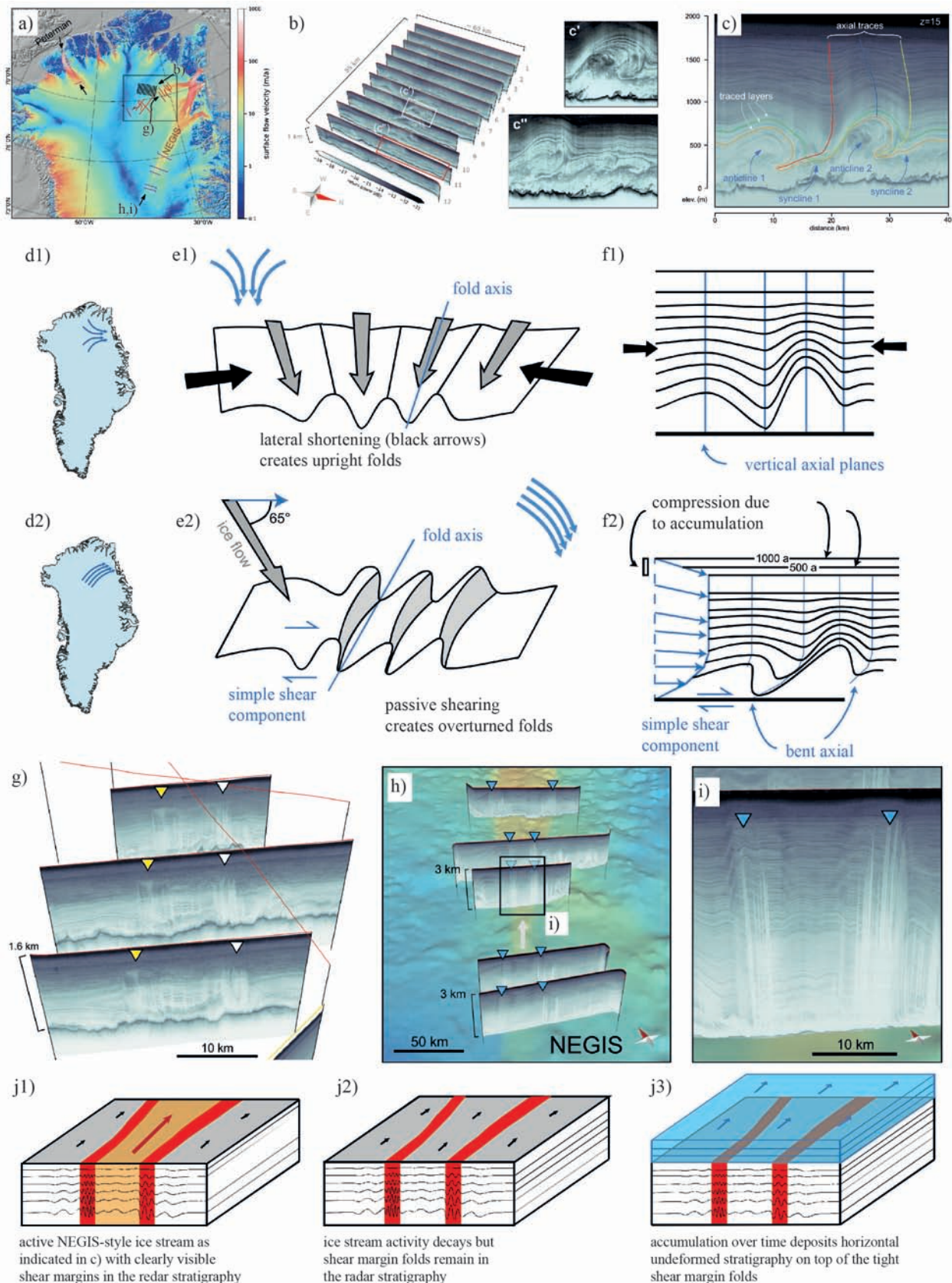
Figure 1.4: Compilation of figures from Franke et al. (in prep.). a) to f) covers the dynamics folding events, and g) to j) the mechanics of ice streams. a) Overview of selected radar profile lines. b) The radargrams contain folds North of NEGIS, interpreted as overturned cylindrical folds due to a shift in ice flow regime. A closeup of the folds is shown in c', c", and c) highlighting the axial traces, traced layers, and the synclines and anticlines. d,e,f) illustrate the change in ice flow direction. Upper row (of d,e,f) is in a paleo compressional flow regime, and bottom row introduces a simple shear component due to a shift in ice flow. g) Radargrams containing paleo (g) and active NEGIS (h,i) shear margins. The shear margins in g) indicate a paleo ice stream, and its evolution is sketched in j).

To make the stratigraphy of a large ice sheet visible, the sets of images derived from radar measurements, so called radargramms (e.g. Schroeder et al., 2020), are a very powerful method. These radargramms can be obtained by radars mounted on aircrafts or on surface track vehicles. Hereby, electromagnetic signals are transmitted into the ice and their reflected echo is recorded. Later, the reflected signal is displayed in vertical profiles and with processing the internal stratigraphy becomes visible.

Bons et al. (2016) present a study from the Peterman ice stream, in the central North of the Greenland ice sheet (fig. 1.4a). Ice streams are areas inside the ice sheet with a significantly higher surface velocity. The authors describe the folds visible in the radargrams and propose that these are sheath folds, where the fold hinges lay perpendicular to flow direction (not in fig. 1.4). The layers then overturn in ice flow direction. The authors argue, that channeling of the ice into an outlet valley, i.e. into a compressional regime, can additionally create upright folds on the large scale (fig. 1.4e1) and on the small (more details in chapter 4 and 5).

To further understand ice streams, Franke et al. (in prep.) investigate radargrams from a region in the far Northeastern part of Greenland (black box in fig. 1.4a). The team around Franke, which I am part of, find overturned upright folds (fig. 1.4b,c). We argue that these folds used to be upright folds in a paleo ice flow regime. Due to a shift in flow regime these upright folds have then been overturned. (fig. 1.4d,e,f).

We also investigate radargrams just upstream of a small ice stream north of NEGIS (fig. 1.4a,g). We find features in the radargrams (fig. 1.4g) that appear very similar to the shear margins of NEGIS (fig. 1.4h,i) and argue, that these are shear margins of a paleo ice stream. To understand the sequence of events, Franke et al. (in prep.) sketch the theory: first an active NEGIS-type ice stream flows, folds the layers, and creates shear margins (fig. 1.4j1). It then ceases to flow, but the features remain (fig. 1.4j2). Finally the general ice flow direction changes and new layers do not contain information of this former ice stream (fig. 1.4j3).

The most outstanding ice stream in Greenland today is NEGIS, in the Northeastern part of the ice sheet (fig. 1.3a and 1.4a,h,i). NEGIS reaches 600 km inland, from the coast almost to the ice divide and has a surface velocity, a magnitude higher than the surrounding ice (55 and 5 m/yr, respectively, Hvidberg et al., 2020). The idea, that an extremely high geothermal heat flux ($970 mW/m^2$), or a hot spot, drives NEGIS has been brought up by Fahnestock et al. (2001) and later been used for many modeling studies. The comment from Bons et al. (2021), a paper I contributed to, elaborate on why such a high geothermal heat flux is unrealistic not just for below the Greenland ice sheet, but also on Earth. Thus, other so far unknown processes must be driving NEGIS.

The aim of the currently ongoing EastGRIP ice core drilling project is to drill through NEGIS and to enhance our understanding about ice streams and the flow of ice. Before the EastGRIP project today, research on the Greenland ice sheet has been going on for over a century.

1.5 The Beginning of Ice Coring Sciences

Figure 1.5: The most iconic picture of Willi Dansgaard analyzing an ice core. The image may spark discussions on sample contamination. (Picture from Dansgaard, 2005)

First Overwintering in Greenland In 1912, J.P. Koch and Alfred Wegener were the first Europeans to overwinter on the Greenland ice sheet. They drilled through 25 m of ice for temperature measurements throughout the winter. The following summer (1913), they crossed Greenland at its broadest point and proved the theory of an ice-free area in central Greenland wrong. This confirmed earlier observations and assumptions from Nansen and Quervain.

From 1929 to 1930, Wegener set out to have an overwintering team at station Eismitte. He never returned from there, but his mission was a success. Among other things, him and his team developed an elegant method for measuring snow accumulation by driving a stick into the snow pack, a method still used today (e.g. Zuhr et al., 2021). They estimated the ice thickness to be around 2500 m by the means of recording the echo from surface dynamite explosions on the bedrock. They also found the shape of Greenland's bedrock to resemble a bowl, where the ice flows out from the center to the sides.

Willi Dansgaard Two decades later, the Danish scientist Willi Dansgaard (fig. 1.5) found the relationship of heavier and lighter water isotopes (H_2O^{18} and H_2O^{16}, respectively) to be dependent on the height, and thus on the temperature, in which water vapor and rain form (Dansgaard, 1953). The relationship of the two isotopes is expressed using the notation $\delta^{18}O$ and can be used as a proxy for past temperature. Regardless of the numerous complications, which come along with the findings of Dansgaard, and which are investigated today, Dansgaard's temperature reconstructions work. His discovery of temperature dependent isotope fractionation lays the basis for later scientific ice core drilling and analysis.

Dansgaard used the oxygen isotope relationship to study the past climate. First on icebergs off the coast of Greenland with his colleague Per Scholander (Scholander et al., 1962). Then on 10 to 20 m long firn cores along the Expedition Glaciologique International au Groenlande (EGIG) from 1959 to 1967. Here the first continuous isotope climate record was created on an ice core.

The First Deep Ice Core The Camp Century deep ice core from 1966 was the first of its kind: reaching from the surface of the ice sheet to bedrock, with a length of 1390 meters (Dansgaard, 2005). The discoveries from this ice core mark the beginning of deep ice coring sciences. Dansgaard and his colleagues were able to reconstruct the past climate over the last 100,000 years (Dansgaard et al., 1969) and from the age-to-depth relation in the ice core Dansgaard and Johnsen created the ice-flow model still used today (Dansgaard and Johnsen, 1969). With the ice flow model, they were able to describe the flow and thinning of ice and the layers inside the ice sheet (fig. 1.3).

Deep Ice Core Drillings in Greenland After a very successful drilling campaign at Camp Century, the value of an ice core had been noticed. The next deep drilling drilling in Greenland was in the southern part of the ice sheet in the 1970's. For logistical reasons a site close to the American Distant Early Warning (DEW) line was chosen: DYE-3.

The next adventure awaited at the GRIP and GISP2 sites in the end of the 1980's and early 1990's. GRIP, the European-lead project and GISP2, the American-lead project were only separated by 27 km. A comparison of the two cores showed how much they differ, despite the short proximity between the sites (Grootes et al., 1993). The Glacial section measured about half the length of the core, and advances in ice core analysis techniques brought a huge gain in understanding the Glacial Climate from these two cores. Yet the bottom sections of the last Interglacial Period were disturbed due to ice flow over bed rock undulations. A compilation of 47 publications from the two Greenland summit cores is published in the special issue of the Journal of Geophysical Research in 1998.

The NorthGRIP drilling in the mid 1990's to early 2000's lead to a high resolution record of the Last Glacial Period and into the Eemian (Rasmussen et al., 2006). It lead to an established timescale for ice cores and also brought in the Golden Spike from the Chronological Chart, giving the Middle Holocene the name Northgrippian (Cohen et al., 2016).

After the Eemian had been drilled, but found stratigraphically disturbed, the next project, the North Greenland Eemian Ice Drilling (NEEM) aimed to find undisturbed ice from the last Interglacial Period. The drilling was completed in 2012, and, among others, a large success was the unfolding of the folded layers in the bottom section of the ice core (NEEMCommunityMembers, 2013).

Now the flow and deformation of ice had sparked scientific interest and the current ongoing project is to drill through the Northeast Greenland Ice Stream (NEGIS) at the EastGRIP site.

1.6 Ice Core Drilling and Processing

Figure 1.6: a) EastGRIP camp with 'the dome', b) entrance to the drill trench, c) core storage, and d) measurement device for DEP. Height of Playmobil figure is approximately 7.5 cm.

The pictures used in this section (fig. 1.6, 1.7, and 1.8) will lay the basis to a funding proposal we (Julien Westhoff, Iben Koldtoft, and Marie Kirk) plan to submit to LEGO. We plan to write a children's book using little LEGO people, who will tell what is happening in and around the EastGRIP drilling camp. It should contain information for the Greenlandic people, and illustrate why and how we drill ice cores and what we do with them. The idea is to create a children's book, in a pixi-book comic-style, but filled with sufficient information to also give adults insight into our ice core work. The book will have a first version in Danish and Greenlandic language and we hope to acquire funding for the book printing process. The images here are from a picture campaign I ran in 2018 with PlayMobil figures, which will be repeated with LEGO during the next field season and processing campaign.

The EastGRIP camp is situated around a three-story high sphere, with cocking, eating, working, and sleeping facilitates called 'the dome' (fig. 1.6a). The heart of the EastGRIP drill camp are the trenches below the surface (fig. 1.6b). Here the actual drilling, ice core processing, storage, and packing take place. The trenches ensure a relatively constant temperature and shelter from the elements. While shelter from storms is an obvious one, shelter is also needed from "heat". During the summer on the ice sheet, it can get warm enough to make the snow "slushy" and ice core handling would not be possible on the surface. Additionally, some measurements require the ice core to be kept cool, which ensures that trapped air bubbles in the ice core expand less explosively, reducing further fractures of the core (Neff, 2014).

The drill used at EastGRIP is constructed with the proven design of the Hans Tausen Drill (Johnsen et al., 2007). The core diameter is three inch (approximately 10 cm). For
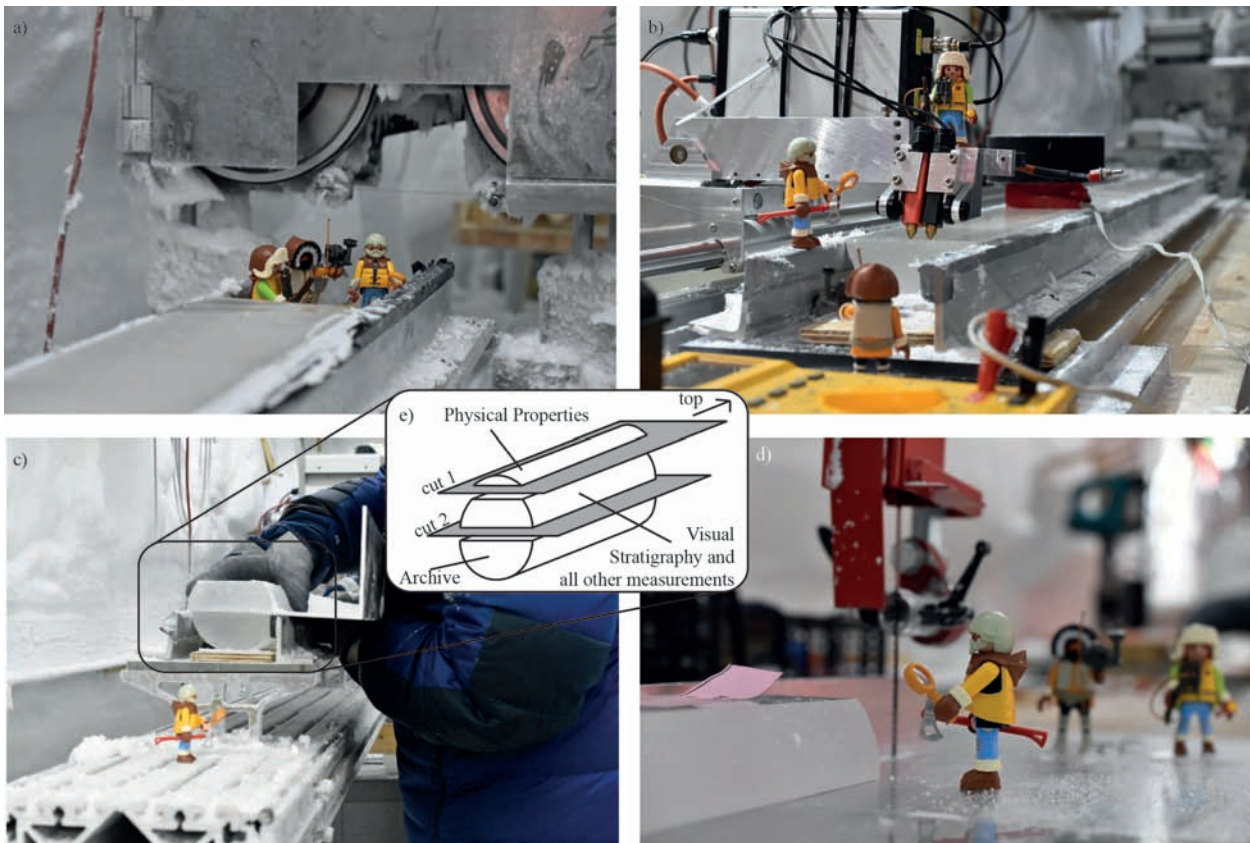
Figure 1.7: Ice core processing: a) the "swiss saw" for horizontal cuts, b) measurement device for electronic conductivity, c) the cut ice core, uppermost piece already removed, and d) vertical saw for further ice cutting and distribution, with the line scan sample next to it. e) sketch of ice core cutting, from Westhoff et al. (2020)

scale: the height of a Playmobil figure is approximately 7.5 cm. After core recovery and logging, the ice cores are stored at approximately -30°C until scientific processing begins (fig. 1.6c). To ensure the best core quality, ice from the brittle zone (Neff, 2014) was stored over one winter. This has proven to work very well and core quality was greatly increased compared to previous deep drillings (Westhoff et al., 2021). The number of core breaks in one sample can affect measurement quality and the accuracy of counting melt layers. In chapter 6, I provide an overview of core breaks throughout the upper 1100 m of the EastGRIP core.

After drilling and storage, the ice core is analyzed in the science trench. The first non-destructive measurement, di-electric profiling (DEP), is to obtain the di-electric properties of an ice core. This is done on the full core (fig. 1.6d), prior to any cutting. This analysis reveals volcanic signals (Mojtabavi et al., 2020). The results from the measurements can also be used to create an artificial radar image, as the ice core property behind radar reflections and DEP is fairly similar (Mojtabavi et al., in prep. and Gerber et al., in prep.).

As a second ice core processing step, the core is cut along its long axis using a horizontal band saw (fig. 1.7a). The final cuts (as seen in fig. 1.7c,e) then separate the Physical Properties piece (top), from the visual stratigraphy sample, which is also the piece for various other measurements (middle), to the archive piece (bottom).

Before the archive piece is packed for transport, the non-destructive electronic conductivity measurements (ECM) are performed on it's surface. The electric conductivity is measured between two electrodes (red and black in fig. 1.7b) and the ECM shows a distinct summer and winter signal (seasonal variations in concentrations of $[NH_+^4]$ and $[Ca^{2+}]$) and can also be used to detect the acidity spikes of volcanoes (Rasmussen et al., 2006). The ECM signal

Figure 1.8: Ice core processing: a) polishing the surface for line scan measurements, b) a thick section in the LASM, c) attaching the thick section to a glass plate, and d) a thin section under crossed polarized light, making the crystal orientations visible.

has also been used to investigate deformation features on the WAIS divide ice core (Fudge et al., 2016). Fudge et al. (2016) use multiple parallel ECM traces covering the width of the ice core to make the internal layers visible. They then analyze width and inclination of layers and derive deformation features.

The line scan sample is 3.6 cm thick (fig. 1.7d) and is the middle piece in fig. 1.7e. Before the measurement, the surface is polished using a microtome knife (fig. 1.8a). The line scanner is a non-destructive application, making internal features of the ice visible (see chapter 2).

For the measurements of crystal-scale physical properties, (upper section in fig. 1.7e) every 30th bag is selected and cut in six sections of approximate nine centimeters. It is then attached to glass plates with drops of water. First, the thick section is analyzed using the Large Area Scanning Microscope (LASM, fig. 1.8b). The upper surface is polished using a stationary microtome knife and then left to sublimate. This process makes grain boundaries, grain sub boundaries, and bubbles clearly visible (e.g. Faria et al., 2014; Weikusat et al., 2009). Then, the thick section is flipped and attached to another glass plate (fig. 1.8c). The upper part is removed to produce a 0.5 mm thin section. Under cross polarized light, the orientation of the crystals becomes visible (fig. 1.8d). The fabric of the thin sections is analyzed in an automated manner using the G50 fabric analyzer. The methods described above and displayed in fig. 1.8 lay the basis for understanding crystal-scale rheology, i.e. small-scale ice flow.

My work does not aim to cover deformation processes on the crystal-scale (e.g. Stoll, 2019), yet this background knowledge (chapter 1.3) is crucial for understanding the flow of ice. I will analyze the results of deformation on the macroscale, i.e. what is visible by eye and in the line scan images. In chapter 2, I cover what has previously been done on deformation structures on the macroscale, and the basics of the line scanner.

Bibliography - Of Greenland, Ice Cores, and the Past Climate

Alley, R. B. (1992). "Flow-law hypotheses for ice-sheet modeling". In: *Journal of Glaciology* 38.129, pp. 245–256. DOI: 10.3189/s0022143000003658.

Bons, P. D., De Riese, T., Franke, S., Llorens, M. G., Sachau, T., Stoll, N., Weikusat, I., Westhoff, J., and Zhang, Y. (2021). "Comment on "exceptionally high heat flux needed to sustain the Northeast Greenland Ice Stream" by Smith-Johnsen et al. (2020)". In: *Cryosphere* 15.5, pp. 2251–2254. DOI: 10.5194/tc-15-2251-2021.

Bons, P. D., Jansen, D., Mundel, F., Bauer, C. C., Binder, T., Eisen, O., Jessell, M. W., Llorens, M. G., Steinbach, F., Steinhage, D., and Weikusat, I. (2016). "Converging flow and anisotropy cause large-scale folding in Greenland's ice sheet". In: *Nature Communications* 7, pp. 1–6. DOI: 10.1038/ncomms11427.

Cohen, K. M., Finney, S. C., Gibbard, P. L., and Fan, J. .-. (2016). "International Chronostratigraphic Chart". In: *The ICS International Chronostratigraphic Chart* 36.3, pp. 199–204.

Cuffey, K. M. and Paterson, W. S. B. (2010). *The Physics of Glaciers*, p. 722.

Dansgaard, W. ., Johnsen, S. . J. ., Møller, J. ., and Langway, C. J. (1969). "One Thousand Centuries of Climatic Record from Camp Century on the Greenland Ice Sheet". In: *Science* 166.3903, pp. 377–381.

Dansgaard, W. (2005). *Frozen Annals*. 1st ed. Copenhagen: Narayana Press, Odder, Denmark, p. 124.

Dansgaard, W. (1953). "The Abundance of 18O in Atmospheric Water and Water Vapour". In: *Tellus*, pp. 461–469.

Dansgaard, W. and Johnsen, S. J. (1969). "A Flow model and a time scale for the ice core from camp century , Greenland". In: *Journal of Glaciology* 8.53, pp. 215–223.

Duval, P., Ashby, M. F., and Anderman, I. (1983). "Rate-controlling processes in the creep of polycrystalline ice". In: *Journal of Physical Chemistry* 87.21, pp. 4066–4074. DOI: 10.1021/j100244a014.

EPICACommunityMembers (2004). "Eight glacial cycles from an Antarctic ice core EPICA community members*". In: *Nature* 429.6992, pp. 623–628.

Fahnestock, M., Abdalati, W., Joughin, I., Brozena, J., and Gogineni, P. (2001). "High geothermal heat flow, basal melt, and the origin of rapid ice flow in central Greenland". In: *Science* 294.5550, pp. 2338–2342. DOI: 10.1029/2001JD900194.

Faria, S. H., Freitag, J., and Kipfstuhl, S. (2010). "Polar ice structure and the integrity of ice-core paleoclimate records". In: *Quaternary Science Reviews* 29.1-2, pp. 338–351. DOI: 10.1016/j.quascirev.2009.10.016.

Faria, S. H., Weikusat, I., and Azuma, N. (2014). "The microstructure of polar ice. Part II: State of the art". In: *Journal of Structural Geology* 61, pp. 21–49. DOI: 10.1016/j.jsg.2013.11.003.

Fudge, T. J., Taylor, K. C., Waddington, E. D., Fitzpatrick, J. J., and Conway, H. (2016). "Electrical stratigraphy of the WAIS Divide ice core: Identification of centimeter-scale irregular layering". In: *Journal of Geophysical Research: Earth Surface RESEARCH* 121, pp. 1218–1229. DOI: 10.1002/2013JF002871.Received.

Gerber, T. A., Hvidberg, C. S., Rasmussen, S. O., Franke, S., Sinnl, G., Grinsted, A., Jansen, D., and Dahl-jensen, D. (2021). "Upstream flow effects revealed in the EastGRIP ice core using a Monte Carlo inversion of a two-dimensional ice-flow model". In: *The Cryosphere* February.

Glen, J. W. (1952). "Experiments on the deformation of ice". In: *Journal of Glaciology* 2.12, pp. 111–114. DOI: `10.3189/S0022143000034067`.

Grootes, P. M., Stuiver, M., White, J. W. C., Johnsen, S., and Jouzel, J. (1993). "Comparsion of oxygen isotope records from the GISP2 and GRIP Greenland ice cores". In: *Nature* 366.33, pp. 552–554.

Haefeli, R. (1961). "Contribution to the Movement and the form of Ice Sheets in the Arctic and Antarctic". In: *Journal of Glaciology* 3.30, pp. 1133–1151. DOI: `10.3189/s0022143000017548`.

Hondoh, T. (2000). "Nature and behavior of dislocations in ice". In: *Physics of Ice Core Records*, pp. 3–24.

Hooke, R. L. and Hudleston, P. J. (1978). "Origin of foliation in glaciers". In: *Journal of Glaciology* 20.83.

Hvidberg, C. S., Grinsted, A., Dahl-Jensen, D., Khan, S. A., Kusk, A., Andersen, J. K., Neckel, N., Solgaard, A., Karlsson, N. B., Kjar, H. A., and Vallelonga, P. (2020). "Surface velocity of the Northeast Greenland Ice Stream (NEGIS): Assessment of interior velocities derived from satellite data by GPS". In: *Cryosphere* 14.10, pp. 3487–3502. DOI: `10.5194/tc-14-3487-2020`.

Jansen, D., Llorens, M. G., Westhoff, J., Steinbach, F., Kipfstuhl, S., Bons, P. D., Griera, A., and Weikusat, I. (2016). "Small-scale disturbances in the stratigraphy of the NEEM ice core: Observations and numerical model simulations". In: *Cryosphere* 10.1, pp. 359–370. DOI: `10.5194/tc-10-359-2016`.

Johnsen, S. J., Hansen, S. B., Sheldon, S. G., Dahl-Jensen, D., Steffensen, J. P., Augustin, L. J., Journé, P., Alemany, O., Rufli, H., Schwander, J., Azuma, N., Motoyama, H., Popp, T., Talalay, P. G., Thorsteinsson, T., Wilhelms, F., and Zagorodnov, V. (2007). "The Hans Tausen drill: Design, performance, further developments and some lessons learned". In: *Annals of Glaciology* 47, pp. 89–98. DOI: `10.3189/172756407786857686`.

Joughin, I., Smith, B. E., Howat, I. M., Scambos, T., and Moon, T. (2010). "Greenland flow variability from ice-sheet-wide velocity mapping". In: *Journal of Glaciology* 56.197, pp. 415–430. DOI: `10.3189/002214310792447734`.

Kamb, B. (1972). "Experimental recrystallization of ice under stress". In: *Washington DC American Geophysical Union Geophysical Monograph Series* 16, pp. 211–241.

Llorens, M. G., Griera, A., Steinbach, F., Bons, P. D., Gomez-Rivas, E., Jansen, D., Roessiger, J., Lebensohn, R. A., and Weikusat, I. (2017). "Dynamic recrystallization during deformation of polycrystalline ice: Insights from numerical simulations". In: *Philosophical Transactions of the Royal Society A: Mathematical, Physical and Engineering Sciences* 375.2086. DOI: `10.1098/rsta.2015.0346`.

Lüthi, D., Le Floch, M., Bereiter, B., Blunier, T., Barnola, J. M., Siegenthaler, U., Raynaud, D., Jouzel, J., Fischer, H., Kawamura, K., and Stocker, T. F. (2008). "High-resolution carbon dioxide concentration record 650,000-800,000 years before present". In: *Nature* 453.7193, pp. 379–382. DOI: `10.1038/nature06949`.

Masson-Delmotte, V., Zhai, P., Pirani, A., Connors, S., Péan, C., Berger, S., Caud, N., Chen, Y., Goldfarb, L., Gomis, M., Huang, M., Leitzell, K., Lonnoy, E., Matthews, J., Maycock, T., Waterfield, T., Yelekci, O., Yu, R., and Zhou, B. (2021). "IPCC, 2021: Climate Change 2021: The Physical Science Basis. Contribution of Working Group I to the Sixth Assessment Report of the Intergovernmental Panel on Climate Change". In.

Mojtabavi, S., Wilhelms, F., Cook, E., Davies, S., Sinnl, G., Skov Jensen, M., Dahl-Jensen, D., Svensson, A., Vinther, B., Kipfstuhl, S., Jones, G., Karlsson, N., Faria, S. H., Gkinis, V., Kjær, H., Erhardt, T., Berben, S., Nisancioglu, K., Koldtoft, I., and Rasmussen, S. O. (2020). "A first chronology for the East GReenland Ice-core Project (EGRIP) over the

Holocene and last glacial termination". In: *Climate of the Past Discussions* 16.December, pp. 2359–2380. DOI: 10.5194/cp-16-2359-2020.

Montagnat, M., Azuma, N., Dahl-Jensen, D., Eichler, J., Fujita, S., Gillet-Chaulet, F., Kipfstuhl, S., Samyn, D., Svensson, A., and Weikusat, I. (2014). "Fabric along the NEEM ice core, Greenland, and its comparison with GRIP and NGRIP ice cores". In: *Cryosphere* 8.4, pp. 1129–1138. DOI: 10.5194/tc-8-1129-2014.

NEEMCommunityMembers (2013). "Eemian interglacial reconstructed from a Greenland folded ice core". In: *Nature* 493.7433, pp. 489–494. DOI: 10.1038/nature11789.

Neff, P. D. (2014). "A review of the brittle ice zone in polar ice cores". In: *Annals of Glaciology* 55.68, pp. 72–82. DOI: 10.3189/2014AoG68A023.

Nye, J. F. (1951). "The flow of glaciers and ice-sheets as a problem in plasticity". In: *Proceedings of the Royal Society of London. Series A. Mathematical and Physical Sciences* 207.1091, pp. 554–572. DOI: 10.1098/rspa.1951.0140.

Petrenko, V. F. and Whitworth, R. W. (1999). *Physics of ice.* OUP Oxford.

Qi, C., Prior, D. J., Craw, L., Fan, S., Llorens, M.-G., Griera, A., Negrini, M., Bons, P. D., and Goldsby, D. L. (2019). "Crystallographic preferred orientations of ice deformed in direct-shear experiments at low temperatures." In: *Cryosphere* 13.1. DOI: 10.5194/tc-13-351-2019.

Rasmussen, S. O., Andersen, K. K., Svensson, A. M., Steffensen, J. P., Vinther, B. M., Clausen, H. B., Siggaard-Andersen, M. L., Johnsen, S. J., Larsen, L. B., Dahl-Jensen, D., Bigler, M., Röthlisberger, R., Fischer, H., Goto-Azuma, K., Hansson, M. E., and Ruth, U. (2006). "A new Greenland ice core chronology for the last glacial termination". In: *Journal of Geophysical Research Atmospheres* 111.6, pp. 1–16. DOI: 10.1029/2005JD006079.

Scholander, P. F., Dansgaard, W., Nutt, D. C., DeVries, H., Coachman, L. K., and Hemmingsen, E. (1962). *Radio-carbon age and oxygen-18 content of Greenland icebergs.*

Schroeder, D. M., Bingham, R. G., Blankenship, D. D., Christianson, K., Eisen, O., Flowers, G. E., Karlsson, N. B., Koutnik, M. R., Paden, J. D., and Siegert, M. J. (2020). "Five decades of radioglaciology". In: *Annals of Glaciology* 61.81, pp. 1–13. DOI: 10.1017/aog.2020.11.

Schulson, E. M. and Duval, P. (2009). *Creep and fracture of ice.* Vol. 9780521806, pp. 1–401. DOI: 10.1017/CBO9780511581397.

Stoll, N. (2019). "A first glimpse into the EGRIP ice core: An analysis of the influence of deformation and recrystallisation on fabric and microstructures of the Northeast Greenland Ice Stream". PhD thesis. University Bremen, p. 81.

Suwa, M., Fischer, J. C. von, Bender, M. L., Landais, A., and Brook, E. J. (2006). "Chronology reconstruction for the disturbed bottom section of the GISP2 and the GRIP ice cores: Implications for Termination II in Greenland". In: *Journal of Geophysical Research Atmospheres* 111.2, pp. 1–12. DOI: 10.1029/2005JD006032.

Thorsteinsson, T. (1996). "Textures and fabrics in the GRIP ice core, in relation to climate history and ice deformation Thorsteinn Thorsteinsson". PhD thesis, pp. 1–146.

Thorsteinsson, T., Kipfstuhl, J., and Miller, H. (1997). "Textures and fabrics in the GRIP ice core". In: *Journal of Geophysical Research* 102.C12, pp. 26583–26599. DOI: 10.1029/97JC00161.

Wang, Y., Thorsteinsson, T., Kipfstuhl, J., Miller, H., Dahl-Jensen, D., and Shoji, H. (2002). "A vertical girdle fabric in the NorthGRIP deep ice core, North Greenland". In: *Annals of Glaciology* 35, pp. 515–520. DOI: 10.3189/172756402781817301.

Weikusat, I., Jansen, D., Binder, T., Eichler, J., Faria, S. H., Wilhelms, F., Kipfstuhl, S., Sheldon, S., Miller, H., Dahl-Jensen, D., and Kleiner, T. (2017). "Physical analysis of an Antarctic ice core-towards an integration of micro-and macrodynamics of polar ice".

In: *Philosophical Transactions of the Royal Society A: Mathematical, Physical and Engineering Sciences* 375.2086. DOI: `10.1098/rsta.2015.0347`.

Weikusat, I., Kipfstuhl, S., Faria, S. H., Azuma, N., and Miyamoto, A. (2009). "Subgrain boundaries and related microstructural features in EDML (Antarctica) deep ice core". In: *Journal of Glaciology* 55.191, pp. 461–472. DOI: `10.3189/002214309788816614`.

Westhoff, J., Sinnl, G., Svensson, A., Freitag, J., Kjær, H. A., Vallelonga, P., Vinther, B., Kipfstuhl, S., Dahl-jensen, D., and Weikusat, I. (2021). "Melt in the Greenland EastGRIP ice core reveals Holocene warming events". In: *Climate of the Past Discu* July, pp. 1–36. DOI: `10.5194/cp-2021-89`.

Westhoff, J., Stoll, N., Franke, S., Weikusat, I., Bons, P., Kerch, J., Jansen, D., Kipfstuhl, S., and Dahl-Jensen, D. (2020). "A Stratigraphy Based Method for Reconstructing Ice Core Orientation". In: *Annals of Glaciology* 62.85-86, pp. 191–202. DOI: `10.1017/aog.2020.76`.

Zuhr, A., Münch, T., Steen-Larsen, H. C., Hörhold, M., and Laepple, T. (2021). "Local scale depositional processes of surface snow on the Greenland ice sheet". In: *The Cryosphere Discussions* February, pp. 1–33. DOI: `10.5194/tc-2021-36`.

Chapter 2

The Line Scanner

2.1   Visual Inspection of Ice Cores

Visual inspection of an ice core is the process of laying the ice core over a light source in a dark room/box and taking notes of features inside the core. This has been the standard mean of identifying and preserving information on features since the beginning of ice core drilling. It is still done by all groups around the world because it is an all-around 3D-analysis, and interesting features, e.g. melt layers, wind crusts, volcanic tephra layers, cloudy bands, and others, can be seen immediately.

Visual inspection has been the method to, e.g. produce a 2200 year melt layer record from the DYE3 ice core (Herron et al., 1981), or a full Holocene melt layer record from the GISP2 ice core Alley and Anandakrishnan (1995). Many more melt layer records were produced from ice cores and an overview can be found in chapter 6.1.1.

Another application of visual inspection was presented on the GRIP and GISP2 ice cores (Thorsteinsson, 1996 and Alley et al., 1997, respectively). They used the visual inspection to describe folds in the ice cores and compare these with the crystal orientation. It is the first description of z-folds in ice cores and the possible influence of folding on the stratigraphy.

While probably all ice cores are analyzed visually, few publications are based on this method. Fitzpatrick et al. (2014) use the visual inspection as an add-on to the physical properties description of the WAIS divide ice core. Fegyveresi et al. (2019) analyze the SPICEcore by means of visual inspection and create an initial chronology by counting summer firn and ice layers. With another team, Fegyveresi et al. (2018) present an overview of wind crusts and provide an estimate for density, also based on visual inspection.

Visual inspection makes many features in the ice core visible, yet preservation of the information is only possible by means of taking notes or pictures. The line scanner provides the opportunity to preserve the entire stratigraphy of the scanned bag in a very high resolution and also gives the opportunity for later analysis.

2.2   History of the Line Scanner

The line scanner for ice cores, which scans a polished ice core slab, is a device developed by Schäfter and Kirchhoff GmbH on behalf of the Alfred Wegener Institute, Helmholtz Center for Polar and Marine Sciences (AWI) in Bremerhaven, Germany. The line scanner makes the stratigraphy, i.e. layers and other features visible, and preserves these in images for further analysis. For Greenland ice core operations, the line scanner is commonly set up as part of the processing line in the field camp. The two main applications of the line scanner (before 2020) were counting annual layers and identifying disturbed stratigraphy (see below).

The first publication using data from the AWI line scanner was on the NorthGRIP ice core by Svensson et al. (2005) . The authors present line scan images and describe folding in the ice core. They also show that the brightness intensity of the images can be used to reconstruct a profile over the entire Glacial Period, which has a very strong correlation with the dust concentrations measured in the ice core.

Annual layer counting is a wide spread application of line scan data (Andersen et al., 2006; Svensson et al., 2006; Svensson et al., 2008). This works well in the Glacial Period, with an alternating sequence of dust-rich and dust-poor layers. McGwire et al. (2008) use an American version of the line scanner and with its data, they detect annual layers with a depth-varying low-pass filter and by fitting. They argue that their approach only has an error of 1% to the geochemically obtained annual layer counting. Winstrup et al. (2012) also use the German line scan data and algorithms from the statistical framework of hidden Markov models. With this method, they manage to reproduce the results from the manual annual layer counting.

Jansen et al. (2016) use the line scanner to present a detailed analysis of folding in the NEEM ice core. The basis for their investigation are line scan images, which I analyzed as a contribution to the paper, and they also include images of the crystal fabric and numerical modeling studies. The authors introduce the term 'tilted lattice bands' for lineal alignments of rotated grains, which coincide with fold hinges found in the line scan images.

When analyzing microstructures and physical properties of ice cores, the line scan images are usually used as an add-on to elaborate further on other features as they offer a great overview and are visually appealing. The advantage of line scan images over, e.g. LASM images, are that they also show a bigger section, as they are continuous throughout the ice core. The value of these line scan images has been noticed by Sergio Faria and his team and they wrote an entire book on the EDML line scan images (Faria et al., 2018). They describe the line scanner in detail and also discuss its value in connection to microstructures in polar ice. After a detailed introduction on the rheology of polar ice, they present the entire set of line scan images for the EDML ice core. Their book is partly based on Faria et al. (2010), where they use line scan and LASM data to evaluate the integrity of paleo climate records.

Following in the footsteps of Faria et al. (2010; 2018), Morcillo et al. (2020) use the line scanner to create a bubble distribution and size profile for the EDML ice core up to the bubble clathrate transition. With this method they extend the EDML bubble record of Ueltzhöffer et al. (2010). Morcillo et al. (2020) also describe the brightness intensity values to compare to dust concentrations, which works well below the bubble clathrate transition.

In the same year, my co-authors and I used the line scan images to reconstruct the ice core orientation (Westhoff et al., 2020, chapter 4). Up to that point, the analysis and discussions of physical properties and rheology of ice had been done without exact information about the spatial orientation of an ice core.

Taranczewski et al. (2019, not peer reviewed) use the line scan images to reconstruct a melt layer profile over the past 10,000 years based on data from the RECAP deep ice core, and two shallow ice cores in close proximity. They also compare the line scan data with the computer tomography (CT) data. They show that the CT has higher resolution and thus finds more melt layers, but the line scan data covers more ice core meters. In chapter 6.6.8 I provide a detailed discussion on the RECAP melt layer record and compare it to GISP2 (Alley and Anandakrishnan, 1995) and EastGRIP (Westhoff et al., 2021).
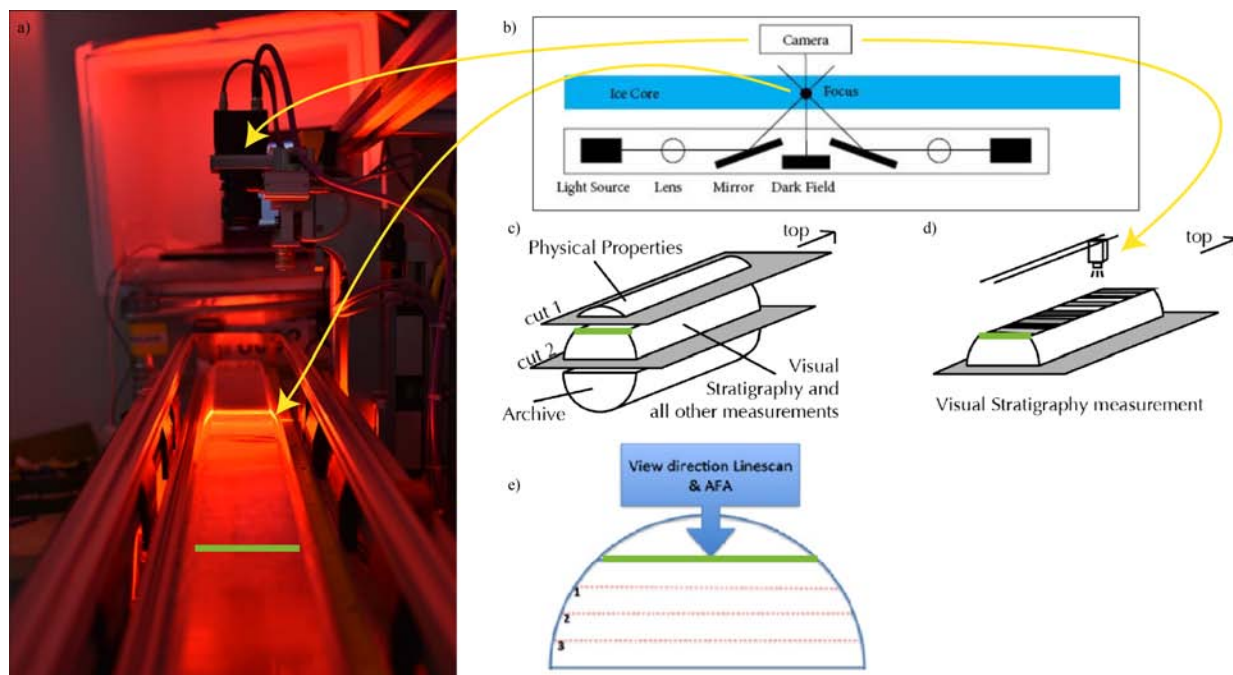
Figure 2.1: Green line marks the ice core slab's surface and yellow arrows corresponding parts across the figure. a) The line scanner device set up at EastGRIP. b) A schematic of the line scanner, modifyed from Svensson et al. (2005), c) Cutting the ice core into different samples, d) and a sketch of the surface which is analyzed (from Westhoff et al., 2020). e) Viewing direction of the line scanner and automated fabric analyzer (AFA), including different focus depth (from Jansen et al., 2016).

2.3   The Device Itself

The line scanner which we use at EastGRIP, was developed by Schäfter+Kirchhoff GmbH, in cooperation with AWI (Westhoff et al., 2020). It is the second generation device and has previously been used for sections of the NEEM ice core (see tab. 8.1). From EastGRIP, line scan images have been taken continuously from 13.75 m to 2120.80 m depth. The first being the beginning of the processing depth and the latter the last core drilled and analyzed in the 2019 field season.

The line scanner is used to make the stratigraphy, and other features inside the ice core, visible. For preparation, an ice core slab is polished on both sides using a microtome knife (fig. 1.8a). The slab is then illuminated at an angle from below and scanned from above with a camera. In sections with 'clean' ice, where nothing disturbs the light's path through the ice, a dark field below is imaged. Features that reflect or scatter the light, such as core breaks, bubbles, or dust layers, appear white. More details can be found in chapter 4.2.2, chapter 5.2.1, chapter 6.2.2, and chapter 7.2.1.

2.4   Line Scan Images and Data Processing

2.4.1   Acquisition of Images and Camera Settings

During a field season, the line scanner is, in general, operated by different personnel. During the current EastGRIP ice core drilling there have been three processing seasons in the field: 2017, 2018, and 2019. Each season had around three different operators, making consistency throughout the runs necessary. In fig. 2.2, I provide an overview of the line scan settings
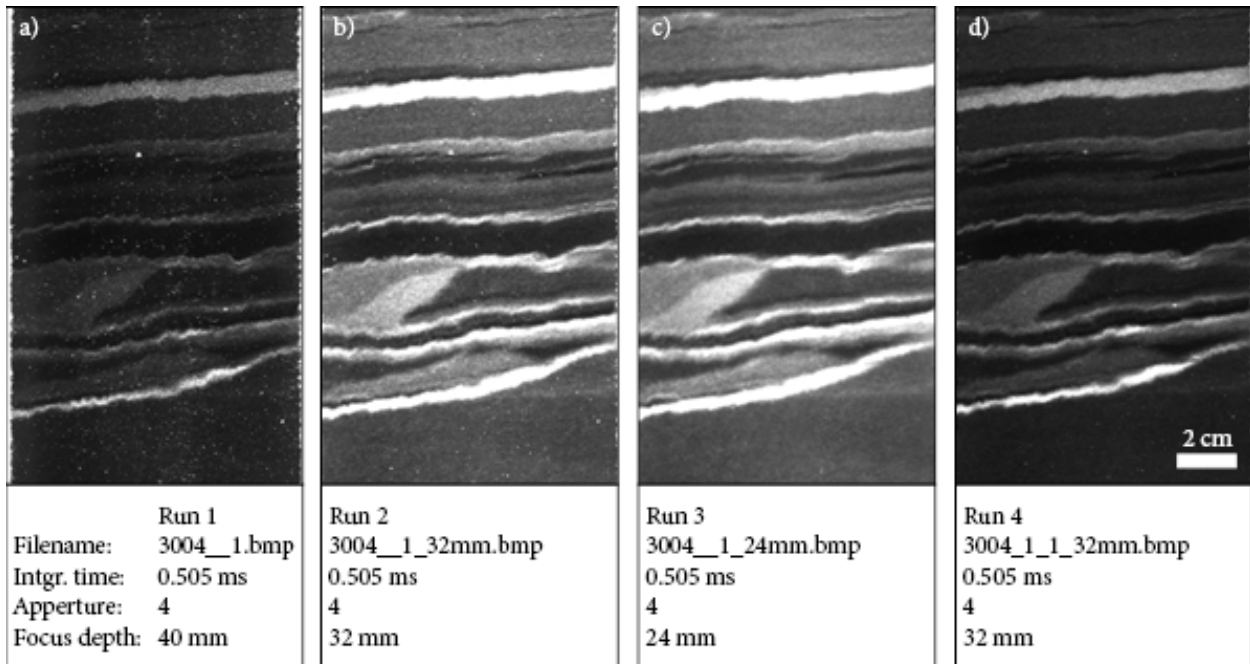
Figure 2.2: A 15x10 cm-section from bag 3004 (1651.85 m) displaying the effect of different camera settings. The folds visible is discussed in chapter 5.

used during the 2018 and 2019 field season processing. I strongly suggest to continue using these settings for the bottom sections of the EastGRIP ice core, to ensure comparable visual appearances of the images. A one page overview can be found in section A.1.

The settings that vary between different runs are (see fig. 2.2):
- integration time, i.e. exposure time for each image,
- the aperture, i.e. depth of field (or how much is in focus), and
- the focus depth, i.e. focus distance measured from a reference below the bottom of ice core slab.

The different camera settings are visualized in fig. 2.2. This is a very distinct deformation structure from a depth of 1651.85 m (bag 3004), which is discussed in detail in chapter 5.

Figure 2.2a,b,c have the same integration time (0.505 ms), but different focus depths (40, 32, and 24 mm, respectively), and fig. 2.2b,d have the same focus depth (32 mm) but different integration times (0.505 and 0.201 ms, respectively). The aperture ($f = 4$) is the same for all images.

The integration time for fig. 2.2a,b,c (0.505 ms) is chosen to create an image, where details are easily visible to the human eye. In very bright cloudy bands, these settings do saturate and are thus not the best choice. Yet, they are kept for consistency. The integration time for fig. 2.2d (0.201 ms) does not immediately make all details visible. It is therefore more useful for grayscale analysis, as only very few pixels saturate and changes are visible.

The aperture has been set to four ($f = 4$), for all scans (fig. 2.2). $f = 4$ has proven to generate the best depth of field.

The three different focus depths, 24, 32, and 40 mm, represent which layer of the ice core slab is in focus, relative to a reference just below the ice core slab (fig. 2.1e). Figure 2.2a (40 mm) scans just below the surface of the ice core slab, and preserves the most ice-core-slab-surface features, such as scratches from processing, or "popped" air bubbles close to the surface. While these features can be annoying for automated layer detection (e.g. Winstrup et al., 2012), or similar approaches, the focus just below the surface preserves the most structural features. This is visualized as fig. 2.2a appears the sharpest. Focusing 8 mm deeper below the surface (from 40 mm to 32 mm, fig. 2.2b) the edges of stratigraphic

features appear less sharp. This effect increases even further when focusing the camera another 8 mm deeper, as more ice lays between the focused layer and the camera (fig. 2.2c, 24 mm). Although integration time is not changed, fig. 2.2a appears darker than fig. 2.2b,c.

The darker image (fig. 2.2d) might be harder to analyze by the human eye, yet it preserves more details inside the fine structures of cloudy bands. The cloudy band running at an up-slope angle accross the bottom of the image, appears to have a uniform color in fig. 2.2b,c, but fig. 2.2a,d can resolve the fine changes of brightness throughout the cloudy band. This can be very very useful for a detailed analysis of particle concentrations throughout a cloudy band.

2.4.2 Stitching of Images

The following section explains the underlying processes used to stitch the line scan images. I use MATLAB, but am preparing the scripts in Python for the next processing season. The code is not included in this thesis.

The standard length of an ice core sample is 55 cm, also referred to as one bag. For the DEP measurement, the ECM, and the line scanner the sample length is 165 cm, i.e. three bags. The line scanner can only scan 110 cm in one run, thus two scans are necessary with later stitching of the images. The overlap of these images is approximately eight centimeters and in theory, the stitch point should always be at the same position. Yet in practice, the ice core shifts when moving the tray from scan one to two. To generate a seamless image of the entire sample, the challenge is to find the exact point of overlap between the two scans.
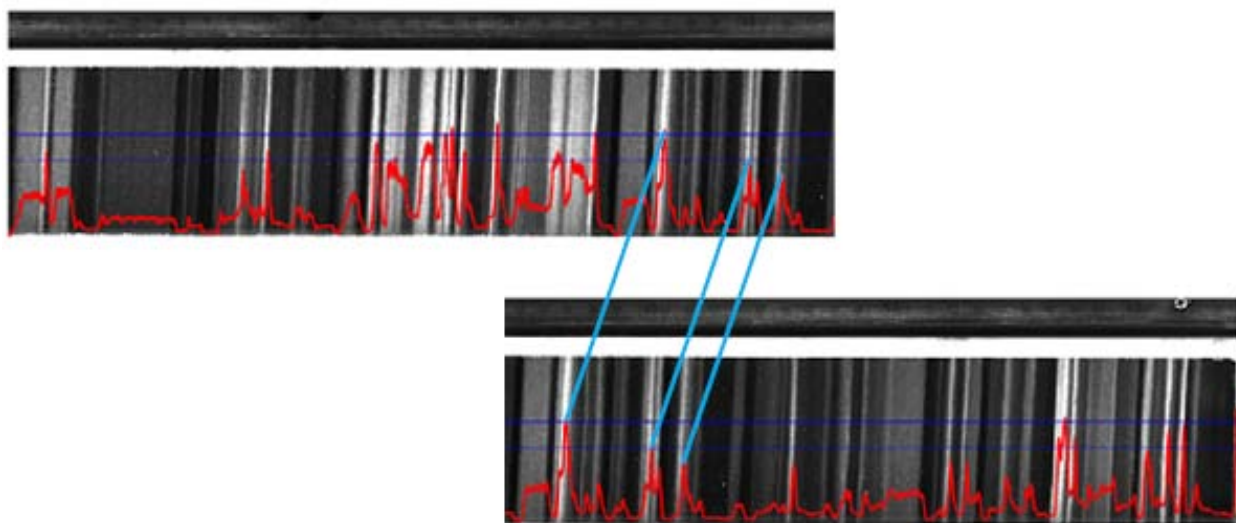
Figure 2.3: Example of finding peaks in the grayscale (red line). These peaks are used to align and stitch two line scans images. This stitching of two separate scans creates the full 165 cm ice core image.

For the Glacial section, I run a grayscale analysis over the two core sections (red in fig. 2.3). In an automated manner for all images, I use a MATLAB script and run the *find peaks function* to localize bright layers around the section where I want to merge the two images parts. Once the position is found, one image is cut off and added as an extension to the other one. As this method does not always work, due to multiple or similar peaks in the grayscale data, I include a picture around ± 2 *cm* of the stitching location for later verification. In cases of mismatches, I perform a manual correction afterwards. I find that this method excels in its simplicity and is quickly applicable to the 5000 line scan images acquired during processing.
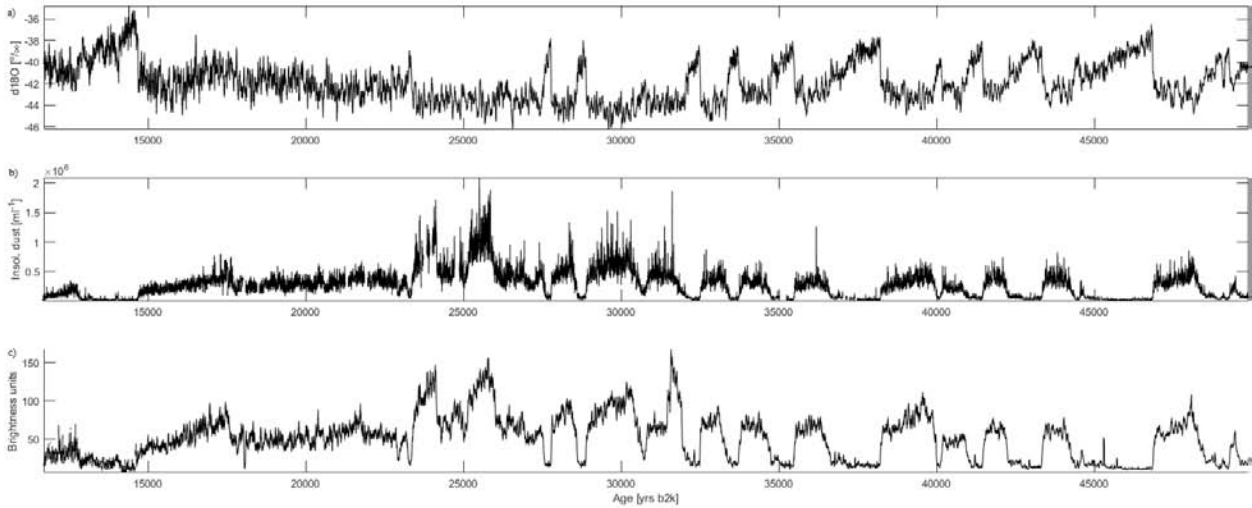
Figure 2.4: a) NorthGRIP $\delta^{18}O$ (NorthGRIPMembers, 2004), b) NorthGRIP concentration of insoluable dust particles (Ruth et al., 2003), c) EastGRIP visual stratigraphy image brightness against age (from this thesis, averaged over 10,000 data points). All plots on GICC05 (Vinther et al., 2006; Andersen et al., 2006; Svensson et al., 2006; Mojtabavi et al., 2020).

In the Holocene section, bubbles and core breaks are easily visible features. Here, the same grayscale method is applied to the scale at the side of the line scan image. This leads to errors, as the ice core can shift laterally due to the movement of the tray between two runs. Yet in most cases, the stitching worked fine with this method, and in case of mismatches, I corrected these manually.

2.4.3   Further Analysis Performed on the Images

The Assemblage of an Overview Booklet   To get an overview of all the line scan data available, I have assembled two overview booklets, which contains the line scan images: part I: the Holocene, and part II: the Glacial, including the Younger Dryas and Bølling–Allerød. These booklets contain information on the bag number and depth of the line scan image and can be found in Appendix A.2 and A.3.

Grayscale   The line scan images are grayscale images and each pixel can have a value from 0 to 255, resulting in 256 possible values. Plotting this brightness profile as a function of depth is the most common first analysis of line scan images (e.g. Svensson et al., 2005). As Svensson et al. (2005) have shown, the grayscale profile is very similar to the dust record, and when inverted, it matches the $\delta^{18}O$ record fairly well. To acquire a first overview of the ages of the line scan sections and their depth, I plot the grayscale values for EastGRIP as a function of age (fig. 2.4c). The age scale for EastGRIP is provided in the supplement of Mojtabavi et al. (2020). For comparison I plot the NorthGRIP $\delta^{18}O$ profile (fig. 2.4a, NorthGRIPMembers, 2004) and the NorthGRIP dust concentration (fig. 2.4b, Ruth et al., 2003), both on the GICC05 timescale (Vinther et al., 2006; Andersen et al., 2006; Svensson et al., 2006).

Layer tilt measurements   I measured the layer tilt of all line scan images from the Glacial section of EastGRIP (see chapter 4.2.5). During these measurements, I found a strong correlation between the tilt angle and the type of deformation features visible in the image. Thus, the idea for reconstructing the ice core orientation was born. I used three different approaches to measure the tilt of cloudy bands:

- (1) generating a grayscale plot along the left and right side of an image and calculating the offset of peaks. With a known distance between left and right side of the image, and the measured offset in peaks, I can then use simple trigonometry to determine the tilt of a layer.

- (2) I also tested the Hough Transform (Hough, 1962), a tool that detects, in my case, linear features in images. This proved to work well, yet had problems with perfectly horizontal layers.

- (3) My third approach was to use the Fast Fourier Transform.

All these methods have proven to work well, and deliver robust results. Limiting factor for all approaches, were deformation structures in the cloudy bands, from which option (2) and (3) suffered most. The simple trigonometrical approach (1) proved to be the most robust and thus suffice. More details on the three methods can be found in chapter 4.2.5 and a detailed discussion in chapter 4.4.2.

Flip-book For a quick overview and for presentations, I created a flip-book using the line scanner images throughout the EastGRIP ice core. While this was more a graphical excise, it did lay the basis for my work on melt layers and the bubble lock-in (chapter 6 and chapter 7, respectively). While "flipping" through the images, every once in a while dark, bubble-free layers raced by. This was my first contact with melt layers, which I then counted and characterized. Another feature I came across was in the upper 100 meters of the ice core: it is easy to see the change in visual appearance from firn to ice when quickly going through the images. With this change of appearance in the line scan images, I began to search for the firn to ice transition in detail and the work on chapter 7 began.
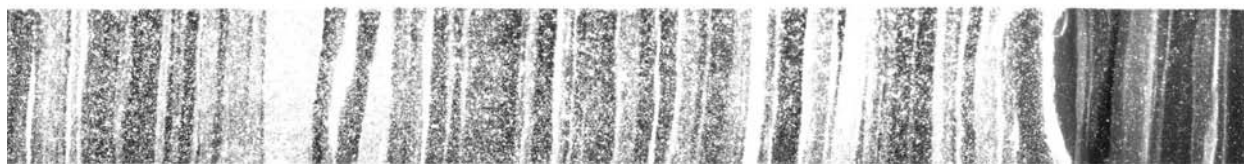
Figure 2.5: Bag 3214. Upper (left) three quarters drilled in 2018, bottom (right) part drilled in 2019. Both processed in 2019. The negative effect of one year core storage on image quality is clearly visible.

The effect of core storage over time The effect of core storage over one winter and later processing has been seen during the NorthGRIP drilling (Anders Svensson, pers. comm.). There is also a prominent example in the EastGRIP ice core, where the core was drilled in 2018, stored as a whole piece and then processed one year later in 2019 (fig. 2.5).

Bibliography - The Line Scanner

Alley, R. B., Gow, A. J., Meese, D. A., Fitzpatrick, J. J., and Waddington, E. D. (1997). "Grain-scale processes, folding, and stratigraphic". In: *Journal of Geophysical Research* 102.C12, pp. 26819–26830.

Alley, R. B. and Anandakrishnan, S. (1995). "Variations in melt-layer frequency in the GISP2 ice core: implications for Holocene summer temperatures in central Greenland". In: *Annals of Glaciology* 21, pp. 64–70. DOI: 10.3189/s0260305500015615.

Andersen, K. K., Svensson, A., Johnsen, S. J., Rasmussen, S. O., Bigler, M., Röthlisberger, R., Ruth, U., Siggaard-Andersen, M. L., Peder Steffensen, J., Dahl-Jensen, D., Vinther, B. M., and Clausen, H. B. (2006). "The Greenland Ice Core Chronology 2005, 15-42 ka. Part 1: constructing the time scale". In: *Quaternary Science Reviews* 25.23-24, pp. 3246–3257. DOI: 10.1016/j.quascirev.2006.08.002.

Faria, S. H., Freitag, J., and Kipfstuhl, S. (2010). "Polar ice structure and the integrity of ice-core paleoclimate records". In: *Quaternary Science Reviews* 29.1-2, pp. 338–351. DOI: 10.1016/j.quascirev.2009.10.016.

Faria, S. H., Kipfstuhl, S., and Lambrecht, A. (2018). *The EPICA-DML Deep Ice Core.* Berlin: Springer-Verlag GmbH Germany.

Fegyveresi, J. M., Fudge, T. J., Ferris, D. G., Winski, D. A., and Alley, R. B. (2019). "Visual Observations and Stratigraphy of the South Pole Ice Core (SPICEcore) Cold Regions Research and Engineering Laboratory". In: July.

Fegyveresi, J. M., Alley, R. B., Muto, A., Orsi, A. J., and Spencer, M. K. (2018). "Surface formation, preservation, and history of low-porosity crusts at the WAIS Divide site, West Antarctica". In: *Cryosphere* 12.1, pp. 325–341. DOI: 10.5194/tc-12-325-2018.

Fitzpatrick, J. J., Voigt, D. E., Fegyveresi, J. M., Stevens, N. T., Spencer, M. K., Cole-Dai, J., Alley, R. B., Jardine, G. E., Cravens, E. D., Wilen, L. A., Fudge, T. J., and McConnell, J. R. (2014). "Physical properties of the WAIS divide ice core". In: *Journal of Glaciology* 60.224, pp. 1140–1154. DOI: 10.3189/2014JoG14J100.

Herron, M. M., Herron, S. L., and Langway, C. C. (1981). "Climatic signal of ice melt features in southern Greenland". In: *Nature* 293.5831, pp. 389–391. DOI: 10.1038/293389a0.

Hough, P. V. (1962). *Method and means for recognizing complex patterns.* US Patent 3,069,654.

Jansen, D., Llorens, M. G., Westhoff, J., Steinbach, F., Kipfstuhl, S., Bons, P. D., Griera, A., and Weikusat, I. (2016). "Small-scale disturbances in the stratigraphy of the NEEM ice core: Observations and numerical model simulations". In: *Cryosphere* 10.1, pp. 359–370. DOI: 10.5194/tc-10-359-2016.

McGwire, K. C., Hargreaves, G. M., Alley, R. B., Popp, T. J., Reusch, D. B., Spencer, M. K., and Taylor, K. C. (2008). "An integrated system for optical imaging of ice cores". In: *Cold Regions Science and Technology* 53.2, pp. 216–228. DOI: 10.1016/j.coldregions.2007.08.007.

Mojtabavi, S., Wilhelms, F., Cook, E., Davies, S., Sinnl, G., Skov Jensen, M., Dahl-Jensen, D., Svensson, A., Vinther, B., Kipfstuhl, S., Jones, G., Karlsson, N., Faria, S. H., Gkinis, V., Kjær, H., Erhardt, T., Berben, S., Nisancioglu, K., Koldtoft, I., and Rasmussen, S. O. (2020). "A first chronology for the East GReenland Ice-core Project (EGRIP) over the Holocene and last glacial termination". In: *Climate of the Past Discussions* 16.December, pp. 2359–2380. DOI: 10.5194/cp-16-2359-2020.

Morcillo, G., Faria, S. H., and Kipfstuhl, S. (2020). "Unravelling Antarctica's past through the stratigraphy of a deep ice core: an image-analysis study of the EPICA-DML line-scan images". In: *Quaternary International* February. DOI: 10.1016/j.quaint.2020.07.011.

NorthGRIPMembers (2004). "High resolution climate record of the Northern Hemisphere reaching into the last Glacial Interglacial Period". In: *Nature* 431, pp. 147–151.

Ruth, U., Wagenbach, D., Steffensen, J. P., and Bigler, M. (2003). "Continuous record of microparticle concentration and size distribution in the central Greenland NGRIP ice core during the last glacial period". In: *Journal of Geophysical Research: Atmospheres* 108.D3.

Svensson, A., Andersen, K. K., Bigler, M., Clausen, H. B., Davies, D. D.-j. S. M., and Johnsen, S. J. (2008). "A 60000 year Greenland stratigraphic ice core chronology". In: *Climate of the Past* 4, pp. 47–57.

Svensson, A., Andersen, K. K., Bigler, M., Clausen, H. B., Dahl-Jensen, D., Davies, S. M., Johnsen, S. J., Muscheler, R., Rasmussen, S. O., Röthlisberger, R., Peder Steffensen, J., and Vinther, B. M. (2006). "The Greenland Ice Core Chronology 2005, 15-42 ka. Part 2: comparison to other records". In: *Quaternary Science Reviews* 25.23-24, pp. 3258–3267. DOI: `10.1016/j.quascirev.2006.08.003`.

Svensson, A., Nielsen, S. W., Kipfstuhl, S., Johnsen, S. J., Steffensen, J. P., Bigler, M., Ruth, U., and Röthlisberger, R. (2005). "Visual stratigraphy of the North Greenland Ice Core Project (NorthGRIP) ice core during the last glacial period". In: *Journal of Geophysical Research: Atmospheres* 110.2, pp. 1–11. DOI: `10.1029/2004JD005134`.

Taranczewski, T., Freitag, J., Eisen, O., Vinther, B., Wahl, S., and Kipfstuhl, S. (2019). "10,000 years of melt history of the 2015 Renland ice core, EastGreenland". In: *The Cryosphere Discussions* March, pp. 1–16. DOI: `10.5194/tc-2018-280`.

Thorsteinsson, T. (1996). "Textures and fabrics in the GRIP ice core, in relation to climate history and ice deformation Thorsteinn Thorsteinsson". PhD thesis, pp. 1–146.

Ueltzhöffer, K. J., Bendel, V., Freitag, J., Kipfstuhl, S., Wagenbach, D., Faria, S. H., and Garbe, C. S. (2010). "Distribution of air bubbles in the EDML and EDC (Antarctica) ice cores, using a new method of automatic image analysis". In: *Journal of Glaciology* 56.196, pp. 339–348. DOI: `10.3189/002214310791968511`.

Vinther, B. M., Clausen, H. B., Johnsen, S. J., Rasmussen, S. O., Andersen, K. K., Buchardt, S. L., Dahl-Jensen, D., Seierstad, I. K., Siggaard-Andersen, M. L., Steffensen, J. P., Svensson, A., Olsen, J., and Heinemeier, J. (2006). "A synchronized dating of three Greenland ice cores throughout the Holocene". In: *Journal of Geophysical Research Atmospheres* 111.13, pp. 1–11. DOI: `10.1029/2005JD006921`.

Westhoff, J., Sinnl, G., Svensson, A., Freitag, J., Kjær, H. A., Vallelonga, P., Vinther, B., Kipfstuhl, S., Dahl-jensen, D., and Weikusat, I. (2021). "Melt in the Greenland EastGRIP ice core reveals Holocene warming events". In: *Climate of the Past Discu* July, pp. 1–36. DOI: `10.5194/cp-2021-89`.

Westhoff, J., Stoll, N., Franke, S., Weikusat, I., Bons, P., Kerch, J., Jansen, D., Kipfstuhl, S., and Dahl-Jensen, D. (2020). "A Stratigraphy Based Method for Reconstructing Ice Core Orientation". In: *Annals of Glaciology* 62.85-86, pp. 191–202. DOI: `10.1017/aog.2020.76`.

Winstrup, M., Svensson, A. M., Rasmussen, S. O., Winther, O., Steig, E. J., and Axelrod, A. E. (2012). "An automated approach for annual layer counting in ice cores". In: *Climate of the Past* 8.6, pp. 1881–1895. DOI: `10.5194/cp-8-1881-2012`.

Chapter 3

Overview of Publications, Conferences, and Dissemination

3.1 First Author Publications

Publication #1 - chapter 4

A stratigraphy-based method for reconstructing ice core orientation

Authors: Westhoff, J., Stoll. N., Franke, S., Weikusat, I., Bons, P., Kerch, J., Jansen, D., Kipfstuhl, S., and Dahl-Jensen, D.

My contribution   Initial idea of method. Application of ice core orientation method to the EastGRIP line scan samples. Verification via "Swiss Saw"-rotation. Writing of all parts of the manuscript, except crystal orientation sections 4.3.4.2 and 4.4.4. Created figures: 2, 3, 5, 6, 7, 8, and 9.

State of the Art   So far, it has not been possible to reconstruct the in-situ orientation of visual ice core data, with a few exceptions. The first exception is by using the girdle fabric, derived from ice crystal orientations, to reconstruct two possible viewing options, dependent on ice flow direction (Faria et al., 2014; Weikusat et al., 2017). Another solution is to preserve the in-situ orientation by using mechanical solutions on the drill, such as adding a bolt close to the melt head (Talalay, 2020) or recording orientation and azimuth of non-rotational drill parts (Fitzpatrick et al., 2014). The latter two methods have worked well for short sections, but not continuously.

Summary   In chapter 4, I present the stratigraphy-based method for reconstructing ice core orientation. The method requires two input parameters: the borehole geometry (azimuth and inclination) and the line scan images. Based on the inclination of the layers, relative to the borehole inclination and the types of deformation structures visible in the cloudy bands, a precise reconstruction of the line scan image sample is possible. This orientation is persistent for other physical property image data, such as the fabric or LASM images.

Publication #2 - chapter 6

Melt in the Greenland EastGRIP ice core reveals Holocene warming events
Authors: Westhoff, J., Sinnl, G., Svensson, A., Freitag, J., Kjær, H. A., Vallelonga, P.,
    Vinther, B., Kipfstuhl, S., Dahl-Jensen, D., and Weikusat, I.
Journal: Climate of the Past
Doi: `https://doi.org/10.5194/cp-2021-89`
Status: in review
Received: 16 July 2021, Revision: in progress. Almost fully revised version included in
thesis.

My contribution   Counting of all melt layers, lenses, wind crusts, and other features.
Wrote all parts of manuscript, except 2012 snow pit study (section 6.1.4) and tree ring
sections (6.4.4). Created figures: 2 to 9 and 12 to 18.

State of the Art   Alley and Anandakrishnan (1995) published the so far first and only
melt layer from a deep ice core (depth > 600 m), namely GISP2. Shorter records from
Greenland have been created in the DYE-3 core (Herron et al., 1981), site A (Alley and
Koci, 1988), site J (Kameda et al., 1995), or Renland (Taranczewski et al., 2019). Melt layer
records also exist from Canada (Koerner and Fisher, 1990; Fisher et al., 1995; Fisher et al.,
2012), Alaska (Winski et al., 2018), and Arctic Russia (Fritzsche et al., 2005). Melt layer
records provide a robust record of past extreme warm events. Especially for sites in central
Greenland melt events are rare and Alley and Anandakrishnan (1995) only find one event
every 250 years at the GISP2 site. A melt layer record from another central Greenland site,
such as EastGRIP, proves to be very valuable. The formation of melt layers and the depth
of percolation of melt into the snow pack is still debated, e.g. Humphrey et al. (2012).

Summary   My co-authors and I have provided the second Holocene melt layer record from
central Greenland. We show how melt layers vary in thickness and distribution over the
Holocene. We find that our melt layer record matches established warm and cold periods, in
terms of frequency of melt events. We also compare melt events to the tree ring composite
from Sigl et al. (2015), and find a good alignment of some warm events, suggesting that
there is a partial correlation. In this work we also describe the brittle zone, by the number
of core breaks per meter. We also find sloping bubble-free layers, and suggest these to be
the result of rheology and not climate. Finally we discuss the the largest melt event found
in the EastGRIP record (from 986 CE). We compare the melt layers from 986 CE to the
coffee experiment and the 2012 CE melt and rain event. We also note that the 986 CE melt
layer and the Viking settlement voyage from Iceland to Greenland coincide.

Publication #3 - chapter 7

An optical approach to determine the bubble lock-in depth in ice cores
Authors: Westhoff, J., Dyonisius, M. N., Freitag, J., Weikusat, I., Martinerie, P., Fain, X.,
    and Blunier, T.
Journal: Journal of Glaciology
Status: ready to submit

My contribution Initial idea of manuscript. Data collection of line scan data. Compilation into a manuscript. Wrote all sections except firn-air pumping method and data (section 7.2.3) and discussion of modeling results (section 7.4.1).

State of the Art To determine the age of the trapped gas in ice cores, the firn air pumping method is usually applied. A bladder is inflated close to the bottom of a borehole and the amount of air that can be pumped out of the bottom section of the borehole is measured. Like this, the depth in which the air pathway connection to the atmosphere are sealed off is found. Additionally the depth is modeled by e.g. Witrant et al. (2012). In our manuscript, we present a novel, optical method to find the lock-in depth.

Summary chapter 7 describes an optical approach to determine the lock-in depth of air in ice cores. With this work, my co-authors and I show the importance of beginning the ice core processing, including the line scanning, as soon as possible on an ice core. Line scanning the firn section of the ice core can lead to various new discoveries, such as finding the first trapped bubbles by bright spots in the line scan images (chapter 7). In the paper, my co-authors and I, also include the results from the firn air pumping campaign at the S6 borehole (1 km from EastGRIP) and modeling results to determine the bubble lock- in and close-off depth.

Publication #4 - chapter 5

Small-scale Deformation Structures in the EastGRIP Ice Core
Authors: Westhoff, J.
Potential co-authors: Bons, P., Weikusat, I., Stoll, N., Streng, K., Jansen, D.,
    and Dahl-Jensen, D.
Journal: TBD
Status: first draft

My contribution Entire analysis and composition of manuscript, so far.

State of the Art The analysis of the GRIP and GISP2 physical properties marks the beginning of detailed analyses of deformation structures in the visual stratigraphy, i.e. folds in ice (Thorsteinsson et al., 1997; Alley et al., 1997). A description of why these small-scale folds are physically possible in deep ice cores followed by Waddington et al. (2001). With line scan images preserving the structures and covering continuous sections, the first complete overview of folds in ice cores was presented by Svensson et al. (2005) on the NorthGRIP core. An overview of the entire ice core and a detailed analysis of fold hinges was preented by Jansen et al. (2016) for NEEM and a full overview of the EDML ice core from Faria et al. (2018). The orientation of the EastGRIP ice core is a huge gain for analyzing deformation structures in the visual stratigraphy (Westhoff et al., 2020), as the alignment of structures with the ice flow direction is now possible, deformation structures can be described in more detail.

Summary In chapter 5, I investigate one specific deformation structure visible in the EastGRIP ice core. I analyze the sudden change of layer tilt on the bag-resolution and on the centimeter-scale resolution from line scan images. The structures I find have a great similarity to duplex structures, known from geology (Butler, 1982). The layers found inside these structures are displaced laterally and stacked between two shear zones. Stacking of

layers, and thus multiplying the signal could lead to inconsistencies for, e.g. annual layer, alignments between different records.

3.2 Co-author Publications

co-authored Publication #1 - (not included in this thesis):
Comment on "Exceptionally high heat flux needed to sustain the Northeast Greenland Ice Stream" by Smith-Johnsen et al., 2020
Authors: Bons, P. D., De Riese, T., Franke, S., Llorens, M. G., Sachau, T., Stoll, N., Weikusat, I., **Westhoff, J.**, and Zhang, Y.
Journal: The Cryosphere
Doi: `https://doi.org/10.5194/tc-15-2251-2021`
Status: published
Discussion started on 17 Dec 2020, published on 17 May 2021
My contribution: Contribution to discussions on heat fluxes and revision of manuscript.

co-authored Publication #2 - (not included in this thesis):
Ice-stream regime shift in Northeast Greenland
Authors: Franke, S., Bons, P.D., **Westhoff, J.**, Weikusat, I., Binder, T., Streng, K., Steinhage, D., Helm, V., Eisen, O., Paden, J.D., Eagles, G., and Jansen, D.
Journal: Nature Geoscience
Status: ready to submit
My contribution: I developed the idea for the visualization for the fold deformation stages and developed the folding hypothesis together with PB, DJ, IW and SF.

co-authored Publication #3 - (not included in this thesis):
Post-depositional processes visible in the integration of EGRIP high-resolution water isotope record and visual stratigraphy
Authors: Morris, V., **Westhoff, J.**, Vaughn, B., Weikusat, I., Jones, T., Markle, B., Hughes, A., Skorski, W., Brashear, C., Gkinis, V., Vinther, B., and White, J.
Journal: TBD
Status: in prep.
Doi to EGU abstract: `doi.org/10.5194/egusphere-egu21-14131`
My contribution: Contributions to discussions on the influence of melt layers on the water isotope signal. Responsible for visual stratigraphy section of work.

3.3 Conference Participation

Conference – Talk
Title: A stratigraphy-based method for reconstructing ice core orientation
Authors: Westhoff, J., Stoll, N., Franke, S., Weikusat, I., Bons, P. D., Kerch, J., Jansen, D., Kipfstuhl, S., and Dahl-Jensen, D.
Conference: vEGU General Assembly 2021, online
Date: 19 April 2021 - 30 April 2021
Link to EGU presentation: `https://doi.org/10.5194/egusphere-egu21-13150`

Conference – Talk
Title: Applications of the Line Scanner
Authors: Westhoff, J., Weikusat, I., Kipfstuhl, S., Svensson, A., Jansen, D.,
    and Dahl-Jensen, D.
Conference: EastGRIP Steering Committee, Copenhagen, Denmark
Date: 11 November 2019 - 15 November 2019

Conference – Poster
Title: Deformation Features and Disturbances in the Stratigraphy of the
    EastGRIP Ice Core
Auhtors: Westhoff, J., Weikusat, I., Kipfstuhl, S., Jansen, D., Svensson, A.,
    and Dahl-Jensen, D.
Conference: Deformation, Rheology, and Tectonics (DRT) 2019, Tübingen, Germany
Date: 11 June 2019 - 14 June 2019

Conference – Poster
Title: Deformation Features and Disturbances in the Stratigraphy of the
    EastGRIP Ice Core
Authors: Westhoff, J., Weikusat, I., Kipfstuhl, S., Jansen, D., Svensson, A.,
    and Dahl-Jensen, D.
Conference: EGU General Assembly 2019, Vienna, Austria
Date: 7 April 2019 - 12 April 2019
Link to poster: `https://epic.awi.de/id/eprint/49530/`

3.4   Co-authored Conference Talks and Posters

Conference – Talk
Title: Post-depositional processes visible in the integration of EGRIP high-resolution water
    isotope record and visual stratigraphy
Authors: Morris, V., **Westhoff, J.**, Vaughn, B., Weikusat, I., Jones, T., Markle, B., Hughes,
    A., Skorski, W., Brashear, C., Gkinis, V., Vinther, B., and White, J.
Conference: vEGU General Assembly 2021
Date: 19 April 2021 - 30 April 2021
Link: `https://doi.org/10.5194/egusphere-egu21-14131`

Conference – Talk
Title: Folded ice stratigraphy in North East Greenland: A three dimensional
    structural analysis
Authors: Franke, S., **Westhoff, J.**, Bons, P. D., Weikusat, I., Binder, T., Steinhage, D.,
    Helm, V., Eisen, O., and Jansen, D.
Conference: ESA - 2020 European Polar Science Week, Virtual Event
Date: 26 October 2020 - 30 October 2020
Link to poster: `https://epic.awi.de/id/eprint/53185/`

Conference – Talk
Title: The upper 2121 m at EastGRIP - Results from physical properties of NEGIS
Authors: Stoll, N., Weikusat, I., Kerch, J., Eichler, J., Shigeyama, W., Homma, T.,
    Jansen, D., Franke, S., Kuiper, E. J., Wallis, D., **Westhoff, J.**, Saruya, T.,
    Faria, S. H., Kipfstuhl, S., Goto-Azuma, K., Azuma, N., and Dahl-Jensen, D.
Conference: EGU General Assembly 2020, Vienna, Austria
Date: 4 May 2020 - 8 May 2020
Link to poster: `https://epic.awi.de/id/eprint/51896/`

Conference – Talk
Title: Issues with fracturing ice during an ice drilling project in Greenland (EastGRIP)
Authors: Weikusat, I., Wallis, D., Franke, S., Stoll, N., **Westhoff, J.**, Hansen, S. B.,
    Popp, T. J., Wilhelms, F., and Dahl-Jensen, D.
Conference: EGU General Assembly 2020, Vienna, Austria
Date: 4 May 2020 - 8 May 2020
Link to poster: `https://doi.org/10.5194/egusphere-egu2020-21768`

Conference – Talk
Title: EastGRIP ice down to 2121m - fabric and microstructure
Authors: Stoll, N., Weikusat, I., Kerch, J., Kleitz, I., Eichler, J., Shigeyama, W.,
    Homma, T., Jansen, D., Bayer-Giraldi, M., Kuiper, E. J., **Westhoff, J.**,
    Saruya, T., Hellmann, S., Franke, S., Götz, P., Goto-Azuma, K., Azuma, N.,
    Faria, S. H., Kipfstuhl, S., and Dahl-Jensen, D.
Conference: EastGRIP Steering Committee, Copenhagen, Denmark
Date: 11 November 2019 - 15 November 2019
Link to poster: `https://epic.awi.de/id/eprint/50620/`

Conference – Invited Talk
Title: Physical properties of the NEGIS ice core - The upper 1700 m in EGRIP
Authors: Stoll, N., Weikusat, I., Kerch, J., Kleitz, I., Eichler, J., Shigeyama, W.,
    Homma, T., Jansen, D., Bayer-Giraldi, M., Kuiper, E. J., **Westhoff, J.**,
    Saruya, T., Faria, S. H., Kipfstuhl, S., and Dahl-Jensen, D.
Conference: The Ninth Symposium on Polar Science, National Institute of Polar Research
    (NIPR), Tokyo, Japan
Date: 4 December 2018 - 7 December 2018
Link to talk: `https://epic.awi.de/id/eprint/48741/`

Conference – Poster
Title: An analysis of the influence of deformation and recrystallisation on microstructures
    of the EastGRIP ice core
Authors: Stoll, N., Kerch, J., Kleitz, I., Eichler, J., Shigeyama, W., Homma, T.,
    Jansen, D., Bayer-Giraldi, M., Kuiper, E. J., **Westhoff, J.**, Saruya, T.,
    Faria, S. H., Kipfstuhl, S., Dahl-Jensen, D., and Weikusat, I.
Conference: The Ninth Symposium on Polar Science, National Institute of Polar Research
    (NIPR), Tokyo, Japan
Date: 4 December 2018 - 7 December 2018
Link to poster: `https://epic.awi.de/id/eprint/48740/`

3.5 Talks, Posters, and Publications Prior to the PhD Period

Article
Title: Small-scale disturbances in the stratigraphy of the NEEM ice core:
 observations and numerical model simulations
Authors: Jansen, D., Llorens, M. G., **Westhoff, J.**, Steinbach, F., Kipfstuhl, S.,
 Bons, P. D., Griera, A., and Weikusat, I.
Journal: The Cryosphere, Volume: 10, Issue:1, pages: 359-370
Doi `https://doi.org/10.5194/tc-10-359-2016`

Conference – Talk
Title: Small-scale disturbances in the stratigraphy of ice cores:
 observations and numerical model simulations
Authors: Jansen, D., Llorens, M. G., **Westhoff, J.**, Steinbach, F., Kipfstuhl, S.,
 Bons, P. D., Griera, A., Eichler, J., and Weikusat, I.
Conference: EGU General Assembly 2016, Vienna, Austria
Date: 17 April 2016 - 22 April 2016
Link to talk: `https://epic.awi.de/id/eprint/40727/`

Conference – Poster
Title: Observations and modelling of centimetre-scale folding in the NEEM ice core
Authors: Jansen, D., Llorens, M. G., **Westhoff, J.**, Steinbach, F., Bons, P. D., Griera, A.,
 Weikusat, I., and Kipfstuhl, S.
Conference: International Symposium on contemporary ice sheet dynamics, Cambridge, UK
Date: 16 August 2015 - 21 August 2015
Link: `https://epic.awi.de/id/eprint/38756/`

Conference – Talk
Title: Small-scale folding observed in the NEEM ice core
Authors: Jansen, D., Llorens, M. G., **Westhoff, J.**, Steinbach, F., Bons, P. D.,
 Kipfstuhl, S., Griera, A., and Weikusat, I.
Conference: EGU General Assembly 2015, Vienna, Austria
Date: 12 April 2015 - 17 April 2015
Link: `https://epic.awi.de/id/eprint/37799/`

3.6 Dissemination

Ice Core Analysis Techniques (ICAT) PhD School
Position: Co-organizer of the events, together with Helle
Astrid Kjær.
Events: ICAT 2020, (2021), and 2022.
Task: I organized a large part of the 2020-event while
Helle Kjær was on maternity leave. I had invited speak-
ers, reserved hotel and lecture rooms, had the website and
registration ready, and more. Then the PhD school got

Figure 3.1: ICAT 2022 Logo.

canceled due to the global pandemic. Preparations for 2021 ran on a low scale, but we also
canceled the event due to ongoing travel restrictions. We aim to run ICAT 2022 in March

and preparations are ongoing. Collaborations with the DEEPICE project are present and we aim to include all PhD students from that project in our school.

EastGRIP International Spring/Summer Seminar Series (EISSSS) 2021
Position: Host of the event, with assistance from Iben Koldtoft.
Task: I organized the online seminar series, covering topics from EastGRIP, NEGIS, and Greenland. The seminar was held bi-weekly and online via zoom. The series included an ice breaker event via GatherTown before the first session. Invited speakers were: Ilka Weikusat, Niccolò Maffezzoli, Benjamin Keisling, Abigale Hughes, Yuki Komuro, Nan Zhang, Olaf Eisen, Valerie Morris, Mikkel Rasmus Schmidt, Prasad Gogineni and Drew Taylor.
Program: the program can be found here:

    `https://eastgrip.nbi.ku.dk/egrip-seminars/EISSSS_2021_program_v4.pdf`

Kulturnatten (Culture Night)
2018, 2019, and 2021
Position: Participant of the event.
Task: Guiding interested visitors through our exhibition under the umbrella of the Culture Night event, hosted by the City of Copenhagen. I attended our stand in the University building, with exhibition materials on ice core research. 2018 we included a tour through our ice core freezer, and 2021 we had a virtual tour around the East-GRIP camp, using VR-headsets.

Figure 3.2: Group picture of the Kulturnatten 2019 event

3.7 Overview Booklet of the Line Scan Images from EastGRIP

Authors: Westhoff, J., Kipfstuhl, S., Svensson, A., Dahl-Jensen, D., and Weikusat, I.
Part 1: Visual Stratigraphy of EastGRIP - Holocene
Overview booklet of line scans from the Holocene. An excerpt can be found in the appendix A.2, and the entire booklet here:

    `doi.org/10.17894/ucph.2f43d7c8-ae7f-47af-ad8a-4aaab2784b87`

Authors: Westhoff, J., Kipfstuhl, S., Svensson, A., Dahl-Jensen, D., and Weikusat, I.
Part 2: Visual Stratigraphy of EastGRIP
- Younger Dryas, Bølling-Allerød, and the Last Glacial
Overview booklet of line scans from the Younger Dryas, Bølling-Allerød, and the Last Glacial (until 50,000 yrs BP). An excerpt can be found in the appendix A.3, and the entire booklet here:

    `doi.org/10.17894/ucph.a1c27df7-ceac-4d2d-8d21-e6dc27afd5e7`

Bibliography - Overview of Publications

Alley, R. B., Gow, A. J., Meese, D. A., Fitzpatrick, J. J., and Waddington, E. D. (1997). "Grain-scale processes, folding, and stratigraphic". In: *Journal of Geophysical Research* 102.C12, pp. 26819–26830.

Alley, R. B. and Anandakrishnan, S. (1995). "Variations in melt-layer frequency in the GISP2 ice core: implications for Holocene summer temperatures in central Greenland". In: *Annals of Glaciology* 21, pp. 64–70. DOI: 10.3189/s0260305500015615.

Alley, R. and Koci, B. (1988). "Ice-Core Analysis at Site A, Greenland: Preliminary Results". In: *Annals of Glaciology* 10.May 2021, pp. 1–4. DOI: 10.3189/s0260305500004067.

Butler, R. W. (1982). "The terminology of structures in thrust belts". In: *Journal of Structural Geology* 4.3, pp. 239–245. DOI: 10.1016/0191-8141(82)90011-6.

Faria, S. H., Weikusat, I., and Azuma, N. (2014). "The microstructure of polar ice. Part II: State of the art". In: *Journal of Structural Geology* 61, pp. 21–49. DOI: 10.1016/j.jsg.2013.11.003.

Faria, S. H., Kipfstuhl, S., and Lambrecht, A. (2018). *The EPICA-DML Deep Ice Core*. Berlin: Springer-Verlag GmbH Germany.

Fisher, D. A., Koerner, R. M., and Reeh, N. (1995). "Holocene climatic records from Agassiz Ice Cap, Ellesmere Island, NWT, Canada". In: *Holocene* 5.1, pp. 19–24. DOI: 10.1177/095968369500500103.

Fisher, D., Zheng, J., Burgess, D., Zdanowicz, C., Kinnard, C., Sharp, M., and Bourgeois, J. (2012). "Recent melt rates of Canadian arctic ice caps are the highest in four millennia". In: *Global and Planetary Change* 84-85, pp. 3–7. DOI: 10.1016/j.gloplacha.2011.06.005.

Fitzpatrick, J. J., Voigt, D. E., Fegyveresi, J. M., Stevens, N. T., Spencer, M. K., Cole-Dai, J., Alley, R. B., Jardine, G. E., Cravens, E. D., Wilen, L. A., Fudge, T. J., and McConnell, J. R. (2014). "Physical properties of the WAIS divide ice core". In: *Journal of Glaciology* 60.224, pp. 1140–1154. DOI: 10.3189/2014JoG14J100.

Fritzsche, D., Schütt, R., Meyer, H., Miller, H., Wilhelms, F., Opel, T., and Savatyugin, L. M. (2005). "A 275 year ice-core record from Akademii Nauk ice cap, Severnaya Zemlya, Russian Arctic". In: *Annals of Glaciology* 42, pp. 361–366. DOI: 10.3189/172756405781812862.

Herron, M. M., Herron, S. L., and Langway, C. C. (1981). "Climatic signal of ice melt features in southern Greenland". In: *Nature* 293.5831, pp. 389–391. DOI: 10.1038/293389a0.

Humphrey, N. F., Harper, J. T., and Pfeffer, W. T. (2012). "Thermal tracking of meltwater retention in Greenland ' s accumulation area". In: *Journal of Geophysical Research* 117.October 2011, pp. 1–11. DOI: 10.1029/2011JF002083.

Jansen, D., Llorens, M. G., Westhoff, J., Steinbach, F., Kipfstuhl, S., Bons, P. D., Griera, A., and Weikusat, I. (2016). "Small-scale disturbances in the stratigraphy of the NEEM ice core: Observations and numerical model simulations". In: *Cryosphere* 10.1, pp. 359–370. DOI: 10.5194/tc-10-359-2016.

Kameda, T., Narita, H., Shoji, H., Nishio, F., Fujii, Y., and Watanabe, O. (1995). "Melt features in ice cores from site J, souther Greenland: some implications for summer cliamte since AD 1550". In: *Annals of Glaciology* May 2021, pp. 51–58.

Koerner, R. M. and Fisher, D. A. (1990). "A record of Holocene summer climate from a Canadian high-Arctic ice core". In: *Nature* 343.6259, pp. 630–631. DOI: 10.1038/343630a0.

Sigl, M. et al. (2015). "Timing and climate forcing of volcanic eruptions for the past 2,500 years". In: *Nature* 523.7562, pp. 543–549. DOI: 10.1038/nature14565.

Svensson, A., Nielsen, S. W., Kipfstuhl, S., Johnsen, S. J., Steffensen, J. P., Bigler, M., Ruth, U., and Röthlisberger, R. (2005). "Visual stratigraphy of the North Greenland Ice Core Project (NorthGRIP) ice core during the last glacial period". In: *Journal of Geophysical Research: Atmospheres* 110.2, pp. 1–11. DOI: 10.1029/2004JD005134.

Talalay, P. G. (2020). *Thermal Ice-Drilling Technology.* Springer, pp. 1–278. DOI: 10.1007/978-981-13-8848-4.

Taranczewski, T., Freitag, J., Eisen, O., Vinther, B., Wahl, S., and Kipfstuhl, S. (2019). "10,000 years of melt history of the 2015 Renland ice core, EastGreenland". In: *The Cryosphere Discussions* March, pp. 1–16. DOI: 10.5194/tc-2018-280.

Thorsteinsson, T., Kipfstuhl, J., and Miller, H. (1997). "Textures and fabrics in the GRIP ice core". In: *Journal of Geophysical Research* 102.C12, pp. 26583–26599. DOI: 10.1029/97JC00161.

Waddington, E. D., Bolzan, J. F., and Alley, R. B. (2001). "Potential for stratigraphic folding near ice-sheet centers". In: *Journal of Glaciology* 47.159, pp. 639–648. DOI: 10.3189/172756501781831756.

Weikusat, I., Jansen, D., Binder, T., Eichler, J., Faria, S. H., Wilhelms, F., Kipfstuhl, S., Sheldon, S., Miller, H., Dahl-Jensen, D., and Kleiner, T. (2017). "Physical analysis of an Antarctic ice core-towards an integration of micro-and macrodynamics of polar ice". In: *Philosophical Transactions of the Royal Society A: Mathematical, Physical and Engineering Sciences* 375.2086. DOI: 10.1098/rsta.2015.0347.

Westhoff, J., Stoll, N., Franke, S., Weikusat, I., Bons, P., Kerch, J., Jansen, D., Kipfstuhl, S., and Dahl-Jensen, D. (2020). "A Stratigraphy Based Method for Reconstructing Ice Core Orientation". In: *Annals of Glaciology* 62.85-86, pp. 191–202. DOI: 10.1017/aog.2020.76.

Winski, D., Osterberg, E., Kreutz, K., Wake, C., Ferris, D., Campbell, S., Baum, M., Bailey, A., Birkel, S., Introne, D., and Handley, M. (2018). "A 400-Year Ice Core Melt Layer Record of Summertime Warming in the Alaska Range". In: *Journal of Geophysical Research: Atmospheres* 123.7, pp. 3594–3611. DOI: 10.1002/2017JD027539.

Witrant, E., Martinerie, P., Hogan, C., Laube, J. C., Kawamura, K., Capron, E., Montzka, S. A., Dlugokencky, E. J., Etheridge, D., Blunier, T., and Sturges, W. T. (2012). "A new multi-gas constrained model of trace gas non-homogeneous transport in firn: Evaluation and behaviour at eleven polar sites". In: *Atmospheric Chemistry and Physics* 12.23, pp. 11465–11483. DOI: 10.5194/acp-12-11465-2012.

Chapter 4

A Stratigraphy-based Method for Reconstructing Ice Core Orientation

Julien WESTHOFF[1], Nicolas STOLL[2], Steven FRANKE[2], Ilka WEIKUSAT[2,3],
Paul BONS[3], Johanna KERCH[2], Daniela JANSEN[2], Sepp KIPFSTUHL[1,2],
Dorthe DAHL-JENSEN[1,4]

[1]*Physics of Ice, Climate, and Earth, Niels Bohr Institute, University of Copenhagen,
Copenhagen, Denmark*
[2]*Alfred Wegener Institute, Helmholtz Centre for Polar and Marine Research,
Bremerhaven, Germany*
[3]*Department of Geosciences, Eberhard Karls University Tübingen,
Tübingen, Germany*
[4]*Centre for Earth Observation Science, University of Manitoba,
Winnipeg, Canada*

Abstract Ever since the first deep ice cores were drilled, it has been a challenge to determine their original, in-situ orientation. In general, the orientation of an ice core is lost as the drill is free to rotate during transport to the surface. For shallow ice cores, it is usually possible to match the adjacent core breaks, which preserves the orientation of the ice column. However, this method fails for deep ice cores, such as the EastGRIP ice core in Northeast Greenland. This paper provides a method to reconstruct ice core orientation using visual stratigraphy and information about the borehole geometry. Because the EastGRIP ice core is drilled through the Northeast Greenland Ice Stream, we use information about the directional structures to perform a full geographical reorientation. We compared the core orientation with logging data from core break matching and the pattern of the stereographic projections of the crystals' c-axis orientations. Both comparisons agree very well with the proposed orientation method. The method works well for 441 out of 451 samples from a depth of 1375 m to 2120 m in the EastGRIP ice core. It can also be applied to other ice cores, providing a better foundation for interpreting physical properties and understanding the flow of ice.

4.1   Introduction

4.1.1   Why we Drill Ice Cores

Deep ice core drilling projects are usually undertaken for the purpose of climate reconstruction, which was first demonstrated by Dansgaard et al. (1969). The reconstruction of the past climate from ice core samples assumes that the snow in the ice sheet interior does not melt, and that annual layers accumulate horizontally, which leads to a continuous record (Cuffey and Paterson, 2010). The ice flow history can influence the reliability of ice core records and must be considered when reconstructing climate from ice cores (e.g., Jansen et al., 2016). As ice flows, the stratigraphic layers may be disturbed, which can lead to climate reconstruction errors, in particular for the deep parts of the ice column (NEEMCommunityMembers, 2013). Nevertheless, the visualization of stratigraphic deformation offers the possibility to decode past deformation in the bottom part of the ice sheet and to reconstruct ice core orientation.

4.1.2   Northeast Greenland Ice Stream and EastGRIP Drill Site
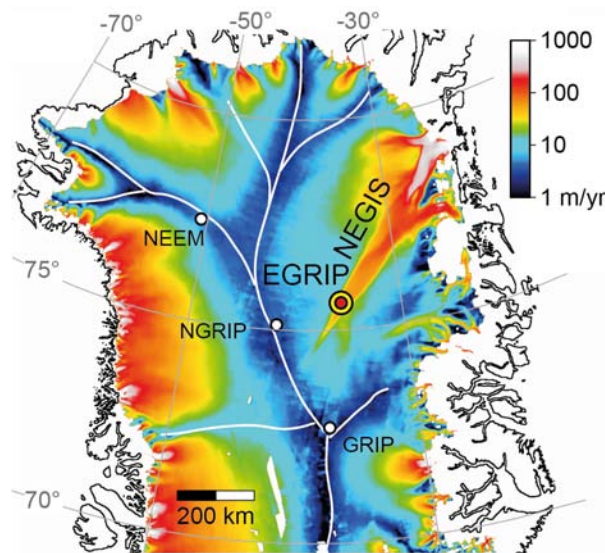
Figure 4.1: Surface velocity map of northern Greenland on a logarithmic scale. Locations of the EGRIP drill site in the upper part of NEGIS and other selected ice core drill sites on ice divides (white lines). NEGIS extends almost from the ice divide, Southwest of EastGRIP, to the coast. Surface velocities were obtained from the MEaSUREs velocity data set (Joughin et al., 2001, same as used by Bons et al., 2018) with data from the years 2000–2008.

The East Greenland Ice Core Project (EastGRIP or EGRIP) ice core is drilled in northern Greenland (fig. 4.1), at 75 38' N, 36 00' W, 2704 m a.s.l. (Vallelonga et al., 2014). This is a central location in the onset region of the Northeast Greenland Ice Stream (NEGIS). The NEGIS extends for more than 600 km almost from the ice divide to the coast. Unlike many ice streams where ice is entering the trunk of fast flow by a tributary system, the ice entering the NEGIS passes through the well-developed shear margins (Fahnestock et al., 2001; Joughin et al., 2001). At the drill site the ice on the surface flows with 55 m/a in an approximately 10 km wide central flow band (Hvidberg et al., 2020). Observations by Christianson et al. (2014) indicate soft and deformable subglacial sediment in the vicinity of the NEGIS, which facilitate sliding as well as a connection of the shear margins' positioning to the subglacial hydrology. Observations by Franke et al. (2020) support these findings and indicate the existence of subglacial landforms, shaped by the activity of the ice stream.

4.1.3 Determining Ice Core Orientation

In the visual stratigraphy images from EastGRIP, milky, impurity rich layers, known as cloudy bands, are found. These were observed and described for the first time by (Gow and Williamson, 1971) in Antarctica and (Hammer et al., 1978) in Greenland. These cloudy bands are only visible in ice from the last glacial period, i.e., below a depth of 1375 m (Mojtabavi et al., 2020). All previously drilled ice cores in Greenland show cloudy bands (Faria et al., 2010), but at EastGRIP, rapid changes from perfectly flat cloudy bands in one sample, to significantly folded layers in the next sample, were unexpected and unprecedented. These changes tend to occur at core breaks between two samples (sample length: 165 cm), collected in a single drill run. Thus these features could be a result of randomized and irregular core rotation occurring each time a core section was drilled.

During the process of core recovery, the orientation is lost due to rotation of the drill. See Johnsen et al. (2007) for a thorough description of electromechanical ice core drilling. Attempts to preserve this orientation, e.g., by using a spring to guide the drill, failed to work so far (pers. comm. Trevor Popp).

Borehole logging to determine borehole inclination (also referred to as plunge) and azimuth direction (also referred to as plunge direction) is common practice in ice core and rock drilling. For many methods, it is the first necessary step to retrieve core orientation. Further mechanical devices are required to orient the core fully (Davis and Cowan, 2012). From rock drilling, many methods for reorienting a core are known. Methods such as "the spear", sending a heavy spear with a sharp point or wax-pencil tip downhole after every run that marks the bottom edge of the core (Davis and Cowan, 2012), were not used in ice core drilling due to lack of time in the short drill season in summer and concerns about damage to the ice sample. Furthermore, this method only delivers relaible results in boreholes with an inclination greater than 15°. Many newer methods have evolved over the last decades, such as, Ezy-Mark, Ballmark, and Reflex systems, but have not been applied to ice core drilling. Paulsen et al. (2002) describe reorienting features using a downhole camera and matching these to features in the drill core. This is not applicable to EastGRIP, as there are no images of the borehole so far. Downhole imaging has been applied to the upper part (top 630 m) of the North Greenland Eemian Ice Drilling (NEEM) ice core, but not used for determining orientations (Hubbard and Malone, 2013).

First oriented ice cores were drilled with a thermal drill at Vostok Station in 1972 (Talalay, 2020). A horizontal bolt was screwed near the thermal head and melted a groove on the core surface during drilling. An inclinometer section was embedded in the meltwater tank. Like this, three oriented core sections, of approximately one metre each, were recovered. This method works well with thermal drills, as there is no internal rotation of drill sections. It becomes more complicated with electromechanical and thermal cable-suspended drills as the bottom drill parts rotate while drilling.

Recording azimuth and inclination of the non-rotational drill parts at the moment of core breaking are suggested by Talalay (2014). This provides the spatial position of the pressure chamber, which can be related to the rotational parts of the drill section, thus retrieving the core orientation. Fitzpatrick et al. (2014) applied this idea and retrieved core orientations relative to magnetic North, which were marked using an azimuth line on the core just before extraction from the drill barrel. These marks did not always line up, either due to rotation of the core in the core barrel (Fitzpatrick et al., 2014) or due to problems with the azimuth measurements (pers. comm. Pavel Talalay).

4.1.4 Motivation

In this study, we introduce a new method to determine ice core orientation. The main innovation is the usage of geological drilling know-how, such as the combination of borehole inclination with the apparent layer dip and applying this to directional features visible in ice cores. This is the first time, that directional features are used for thorough and complete reconstruction of ice core orientation.

To understand the flow of ice, we depend on directional information. The spatial orientation of large-scale radar images, showing the ice sheet's internal structure, is linked to the flight or ground path from which they were acquired. Thus, the direction can readily be implemented. However, due to the loss of ice core orientation during core recovery, all measurements done on an ice core are interpreted without directional information. However, this information about an ice core's orientation is crucial and a necessity for interpreting physical and flow properties of ice, and all other image data taken from the ice core. If the orientation is known, ambiguous observations are avoided, which allows for a more confident interpretation of the data.

As drills that preserve or record ice core orientation for the entire core have not been applied yet, other methods are required to determine core orientation. The method presented here supplies a technique, independent of the relative orientation obtained during logging by core break-matching (discussed later) and independent of stereographic projections of c-axis distribution (Weikusat et al., 2017, also discussed later). We determine the orientation of 451 samples from 1375 m to 2120 m depth, i.e., ice from the last glacial period (Mojtabavi et al., 2020), characterized by the occurrence of cloudy bands (Hammer et al., 1978). These cloudy bands are necessary for the application of the method, as well as a certain amount of flow, to detect directional deformation. Additionally, some borehole inclination is necessary, as this method will not provide results in a perfectly vertical borehole, which would be a rare case in the electromechanical ice core drilling. We then compare our results to core break matching and c-axis orientations, for verification of our method.

4.2 Methods

4.2.1 Journey of an Ice Core - From the Bottom of the Ice Sheet to the Measurement Table

During drilling and core preparation, many steps change the orientation of the sample before measurements are made. The drill (fig. 4.2A) cuts a cylinder out of the ice, with the bottom still attached to the bulk ice (fig. 4.2B). The core catchers engage the ice, and the pull of the winch breaks the cylinder of ice off the bottom. The length of this cylinder, obtained in one run, can be up to 3.6 m, depending on core barrel length. It is then lifted to the surface (fig. 4.2C), while the drill and core barrel rotate freely, and the in-situ core orientation is lost.

When the core reaches the surface, its top is matched to the bottom break of the previous ice core section (fig. 4.2D). In most cases, this match is possible, thus retrieving the relative orientation of the drill core. The logger's mark, a continuous line on the core, represents this relative orientation. For ease of handling, the core is cut into regular sample lengths, e.g., 165 cm pieces at EastGRIP (fig. 4.2E).

In cases of shattered ice, core quality is affected and samples are rotated to provide undamaged ice for all necessary measurements. It is rotated relative to the line marked on the core (γ, fig. 4.2F).
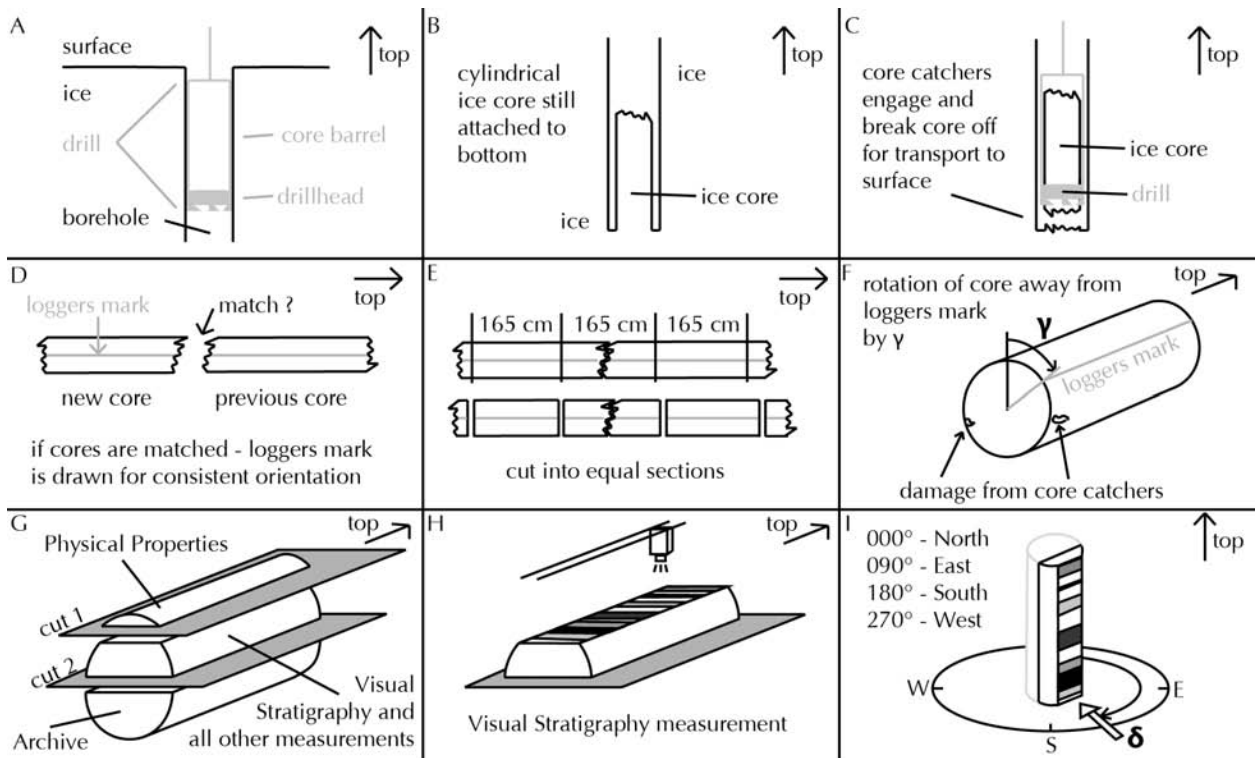
Figure 4.2: Steps to recover an ice core until the measurement of visual stratigraphy (A to H). Spatial orientation of the direction of view, defined here as δ, is measured clockwise from North (I).

Now two cuts are made along the long axis of the core (fig. 4.2G). This provides three 165 cm-long pieces, one for physical properties measurements, one for visual stratigraphy and most other measurements, and one as an archive piece for future purposes. The visual stratigraphy sample is created by an optical 2D scan from the top (fig. 4.2H) while being illuminated from below. Figure 4.2I illustrates the spatial orientation of the ice core, described as δ from now on. It is measured clockwise from geographic North.

4.2.2 The Line Scanner

The line scanner, used at EastGRIP, has been developed by Schäfter+Kirchhoff GmbH, in cooperation with Alfred Wegener Institute, Helmholtz Centre for Polar and Marine Research (AWI). Details can be found in, e.g., Svensson et al. (2005) or Faria et al. (2018). On Greenland, the line scanner was applied to obtain a line scan profile for sections of the North Greenland Eemian Ice Drilling (NEEM) deep ice core during the field campaign seasons 2009 to 2011 (unpublished data). An older version of this device was used for the drilling campaign at the Northern Greenland Ice Core Project (NorthGRIP), in the 2000s Svensson et al. (2005). At NorthGRIP, the line scan was only done on the second NorthGRIP core, below 1300 m. The first visual archives of an ice core from Greenland were created on the Greenland Ice Core Project (GRIP) and the Greenland Ice Sheet Project (GISP2) ice cores in the 1990s, in an enormous effort, using pencil and paper (Grootes et al., 1993; Alley et al., 1997).

Faria et al. (2010) and Jansen et al. (2016) show the potential of visual stratigraphy images, e.g., complementary to other methods for deciphering deformation mechanisms, novel for identifying structures in ice such as tilted-lattice bands. Other applications are stratigraphic dating of ice cores, as done by, e.g., Svensson et al. (2005).

To acquire the line scan images, a polished slab of ice is illuminated at an angle from below, often referred to as 'dark field' imaging. Impurities, dust, bubbles, and fractures will

scatter the light, thus making these features visible. While the core is illuminated, a camera scans the surface and detects areas where light is scattered (fig. 4.2H). Where light travels through "clean" ice and is not scattered, a dark field below the ice core is detected (Svensson et al., 2005; Faria et al., 2010). The main cause of light scattering in ice from the last glacial period, other than fractures, are cloudy bands. These are layers with a high mineral dust concentration (Hammer et al., 1978), and micro-inclusions (Faria et al., 2010).

4.2.3　Borehole Logging
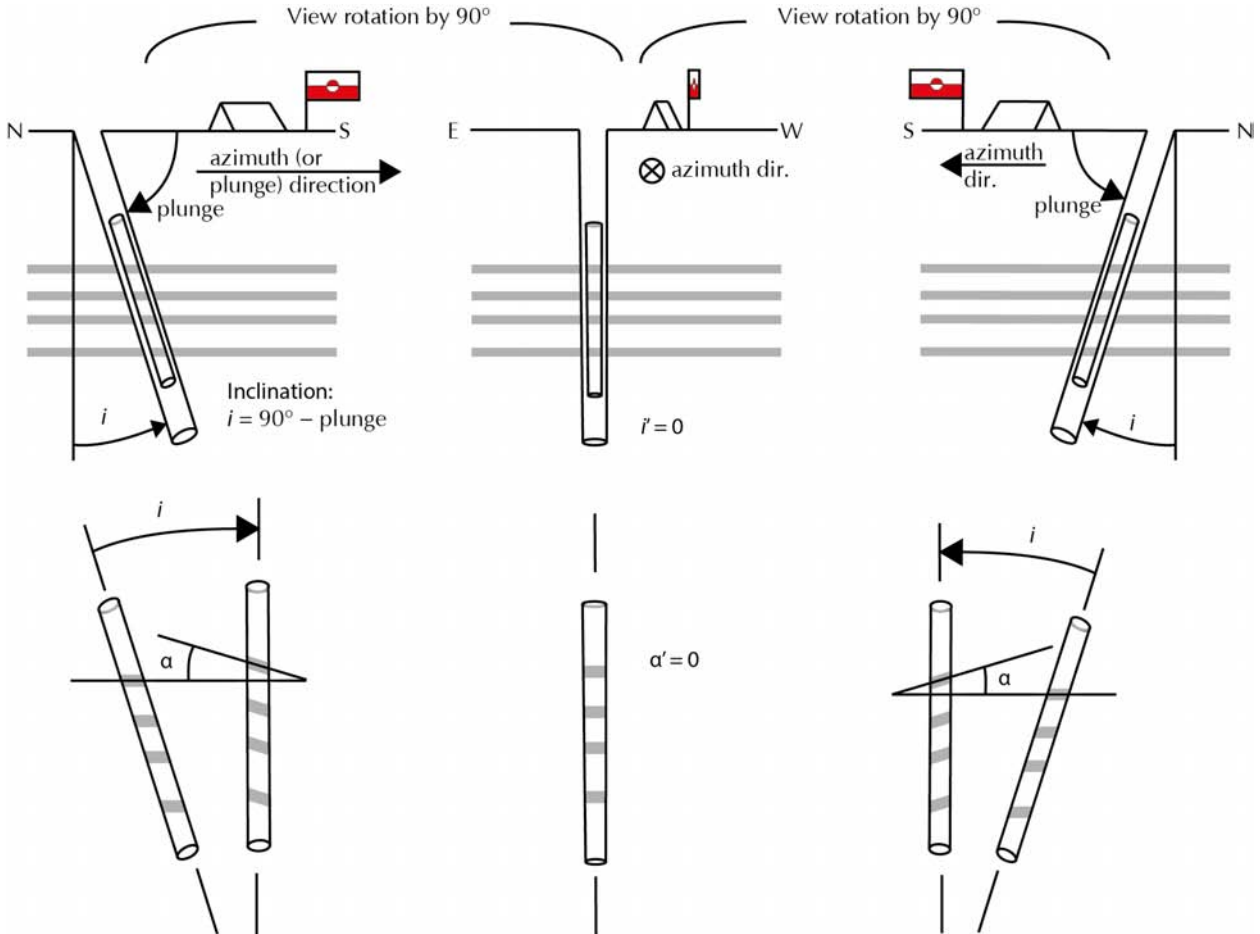
Figure 4.3: Three viewing directions of the same borehole. In the top row, the angles i and i' represent the true and apparent borehole inclination ($90° - plunge$), respectively. i and i' in the bottom row are the angles necessary to tilt the ice core to vertical. Assuming horizontal layering, i is equal to α, the dip angle of inclined layers in the ice core and i' is equal to α', the apparent dip angle.

The Danish Borehole Logger (Gundestrup et al., 1994) provides the boreholes inclination and spatial azimuth orientation. The inclination (i) of a borehole can be defined as the angle between the vertical and the borehole axis, or its plunge, which is the angle it makes with the horizontal plane (fig. 4.3). The plunge (or azimuth) direction, is the geographic direction in which the borehole points when projected on the horizontal plane. For consistency we will from now on refer to plunge direction as azimuth direction (φ). We use the convention that $N = 000°$, $E = 090°$, etc., up to $360° = 000°$ (fig. 4.2I).

In this study, we do not include other measurements by the logger (temperature, borehole diameter, and liquid pressure). The EastGRIP borehole has been drilled with inclinations up to 6° from vertical. The borehole is logged at the beginning and end of every field season with the purpose of observing undisturbed borehole temperatures, changes of diameter, and

borehole geometry due to ice deformation. The measurements from the end of the 2019 field season are used here.

4.2.4 Tilt of Cloudy Bands due to Borehole Tilt

An observer looking at an arbitrarily oriented borehole, will see an apparent inclination of $i' = 0°$ (or a vertical plunge of 090°) when looking in the borehole azimuth direction, or in the opposite direction (fig. 4.3 middle). Any other viewing direction results in an apparent inclination between 0° and the true inclination, when the viewing direction is ±090° to the azimuth direction ($i' = i$, fig. 2, left and right). The same is observed when considering the tilt of layers (usually cloudy bands) in an extracted drill core.

The orientation of the true horizontal plane in a core is not known if the core is not oriented and, therefore, only its inclination and azimuth direction are known. We therefore define the horizontal in a core as the plane perpendicular to the core axis. When the core transects layering at an angle less than 090°, layering will appear tilted. The true tilt α will only be observed when looking at the core perpendicular to the material line in the core that was originally parallel to the plunge direction. The observed tilt α will then be identical to i, but with opposite sign. Here we use the sign convention that α is positive when layers appear to be tilted clockwise, i.e., to the right. When the core is observed from an arbitrary direction, the layers will have an apparent tilt angle α', which can range from $-i$ to $+i$.

4.2.5 Measuring a Cloudy Band's Tilt
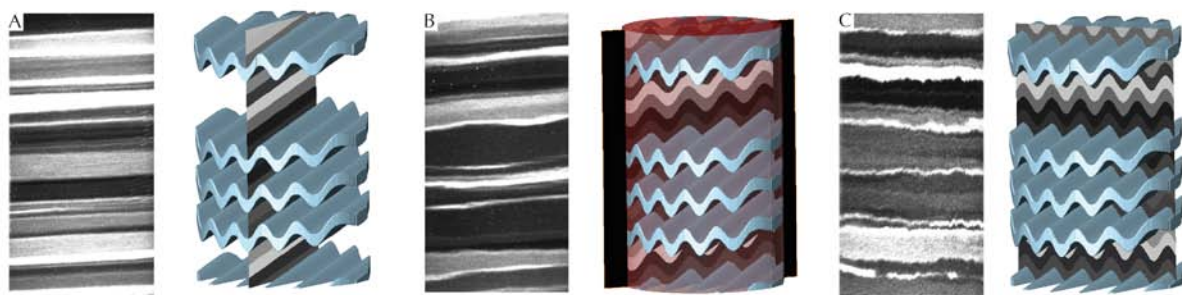
Figure 4.4: Three types of deformation features. (A) No features and flat layering, (B) long wavelength undulations, and (C) crenulations (symmetric upright folds), overprinting other features. Visible structures depend on direction of view, illustrated by the cylinder with several folded layers next to every image.

We automatically measured the layer tilt of all 451 visual stratigraphy samples (equivalent to 745 m of core) using Matlab (MATLAB, 2018). Other methods for measuring a layer's tilt are discussed later. We created a brightness-intensity profile along the left and right side of each image. Bright sections caused a peak in the signal and dark sections valleys. Using the built-in function for signal processing, "alignsignals" the offset (D) of the left and right brightness-intensity curves was determined. With a known distance between the left and right side (x), the angle is calculated with simple trigonometry:

$$\alpha' = \tan(\frac{D}{x}).$$ (4.1)

Manual verification was necessary because irregularities in the layers may prevent the proper alignment of the same layer. In the samples, we observe three types of layering. Straight,

regular layers with (fig. 4.4A), long wavelength undulations (fig. 4.4B), and small-scale folds with approximately vertical axial planes, termed crenulations in geology (Cosgrove, 1976, fig. 4.4C). Crenulations form by lateral shortening of thin laminations in rocks or a foliation defined by strongly anisotropic minerals, such as micas (Cosgrove, 1976; Ran et al., 2019) or ice (Bons et al., 2016).

The automated method for tilt measurements was verified manually on 30 random samples. It provides good ($\pm 0.1°$) results on featureless layers (fig. 4.4A), but the measured tilt scatters in case of samples with folded or undulating layers (fig. 4.4B). Using the median of up to 288 tilt measurements on one sample delivered results very similar (within $\pm 0.3°$) to manual measurement. All angles greater than $8°$ (or smaller than $-8°$) were removed after manual verification that no layers have such a large inclination.

4.2.6   Reconstructing the Core Orientation
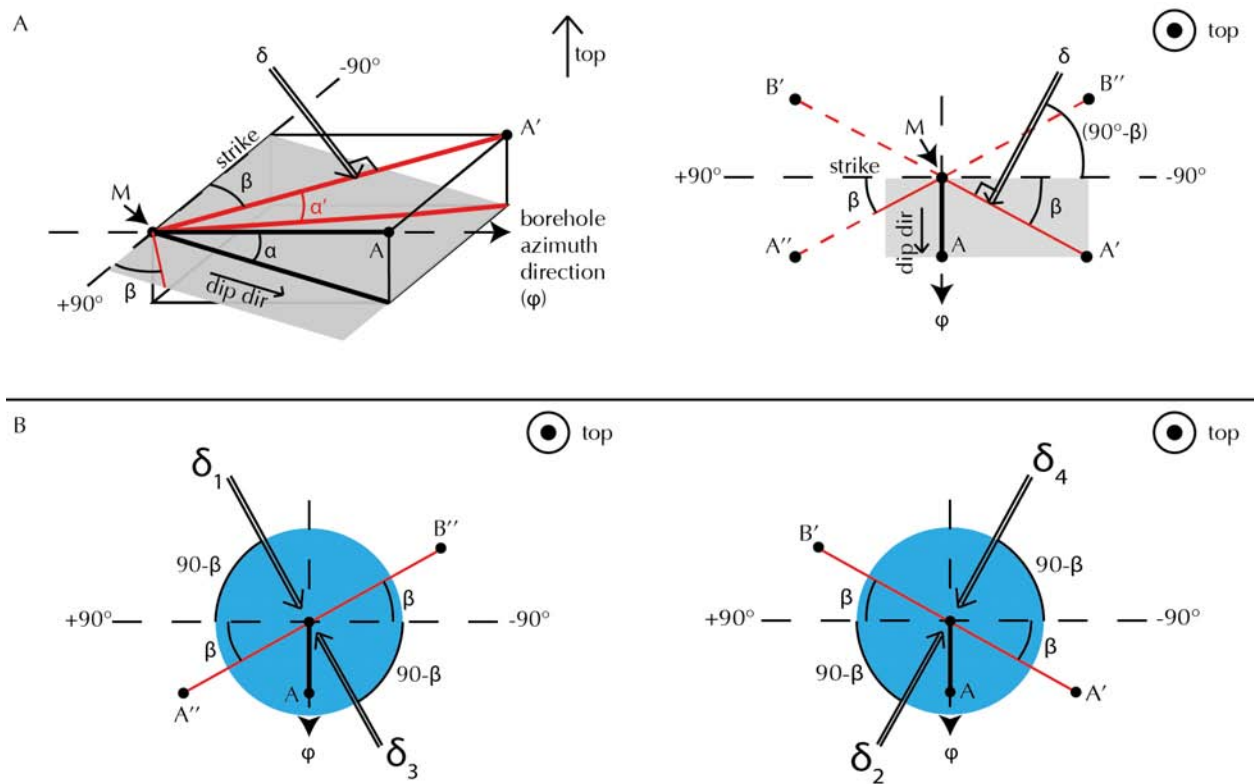
Figure 4.5: (A) An inclined plane (gray square), e.g., a layer in an ice core, with the dip angle α on the steepest profile $\overline{MA}$. Same dip of gray layer, but smaller apparent dip angle α' on profile $\overline{MA'}$. Profile $\overline{MA'}$ is β away from strike. For one apparent dip angle α' there are four possible positions for β, spanning profiles from M to A', A", B', and B". (B) Ice core (blue circle) viewed along the vertical axis. Surface of "cut 2" (fig. 4.2G) is either along $\overline{A'B'}$ or $\overline{A''B''}$. $\delta_{(1-4)}$ represent the possible viewing directions. All red lines, extended vertically, could be possible image planes.

Figure 4.5 illustrates terms explained in the following section. The tilt or dip direction (labeled as "dip dir") is the direction of the steepest inclined line on a tilted plane. The dip angle (α) is the declination of this plane, measured from a horizontal projection ($\overline{MA}$). The angle α is the largest possible plunge angle of a line on this plane. Strike is the unique non-inclined line on an inclined plane. Dip direction is $90°$ to strike and when viewed from the top, as in fig. 4.5A (right), $\overline{MA}$ and "dip dir" have the same orientation.

The apparent dip (α') is the dip angle that is actually observed when a core is sectioned. Apparent dip direction (fig. 4.5, red line $\overline{MA'}$) is the geographic orientation of this intersec-

tion on a horizontal plane. α' ranges between α and 0 (absolute values). For further details about apparent dip consult, e.g., Fossen (2010). The dip direction relative to strike, of any apparent dip angle α' is given by β:

$$\sin(\beta) = \frac{\tan(|\alpha'|)}{\tan(\alpha)}. \tag{4.2}$$

In our case, α is given by the maximum inclination of the borehole (i, fig. 4.3) and α' represents the measured tilt of a cloudy band in a visual stratigraphy sample. The angle β is defined as the angle between the strike and the intersection of the section and horizontal plane, $\overline{MA'}$ (red line in fig. 4.5). It is also the angle between strike and $\overline{A'B'}$ and $\overline{A''B''}$. The lines $\overline{A'B'}$ and $\overline{A''B''}$ extended as planes parallel to the ice core axis, are two possible section orientations for a given angle β (fig. 4.2G). Visual stratigraphy is scanned from a 90° angle to the section plane (fig. 4.2H). For such a given angle β, these two planes can be viewed from two opposite directions, giving a total of four possible viewing directions $\delta_{(1-4)}$:

$$\delta_{(1,2)} = \varphi + 90 \pm (90 - \beta), \tag{4.3}$$

$$\delta_{(3,4)} = \varphi - 90 \pm (90 - \beta). \tag{4.4}$$

The borehole azimuth direction (φ) was logged at the end of the 2019 field season and is required to determine the other angles that link the coordinate system from fig. 4.5 to a fixed geographical orientation, as in fig. 4.3.

$\delta_{(1,2)}$ have a positive layer tilt (downward sloping to the right), both are on the $+90°$ side in fig. 4.5, bottom panel. Negative tilts (to the left) are represented by $\delta_{(3,4)}$, lying on the $-90°$ side. Knowing the sign of the layer tilt reduces the number of possible orientations from four to two, as either eq. 4.3 or 4.4 would apply.

We will show that $\delta_{(1,2)}$ (or $\delta_{(3,4)}$) are connected to the type of deformation structure seen in the visual stratigraphy. This makes each δ unique to distinguish and enables the reconstruction of the true direction of view.

4.3   Results

4.3.1   Input Parameters for EastGRIP Core Orientation Reconstruction

The analyzed samples range from a depth of 1375 m to 2120 m. We measured the tilt of cloudy bands (α') for every visual stratigraphy sample, and plot one point per 165 cm-long sample (fig. 4.6A). Measured layer tilts vary between $-4°$ and $+4°$, and are randomly distributed. In fig. 4.6A some clusters are visible and these will be discussed later.

The borehole inclination i ranges from 2.7° to 3.6° (fig. 4.6B). Assuming horizontal layers in the ice sheet, i of the borehole is equal to the maximum layer tilt α in the ice core (fig. 4.3). For $i = 3.5°$, we expect to see an apparent layer tilt α' ranging from 0 to $\pm 3.5°$, depending on the viewing direction.

In the analyzed depth range, the borehole azimuth direction ranges from 190° to 150°, meaning it shifts from plunging towards South to a Southeast direction (fig. 4.6C). This information is the input for eq. 4.3 and eq. 4.4 to retrieve an absolute orientation for the ice core.
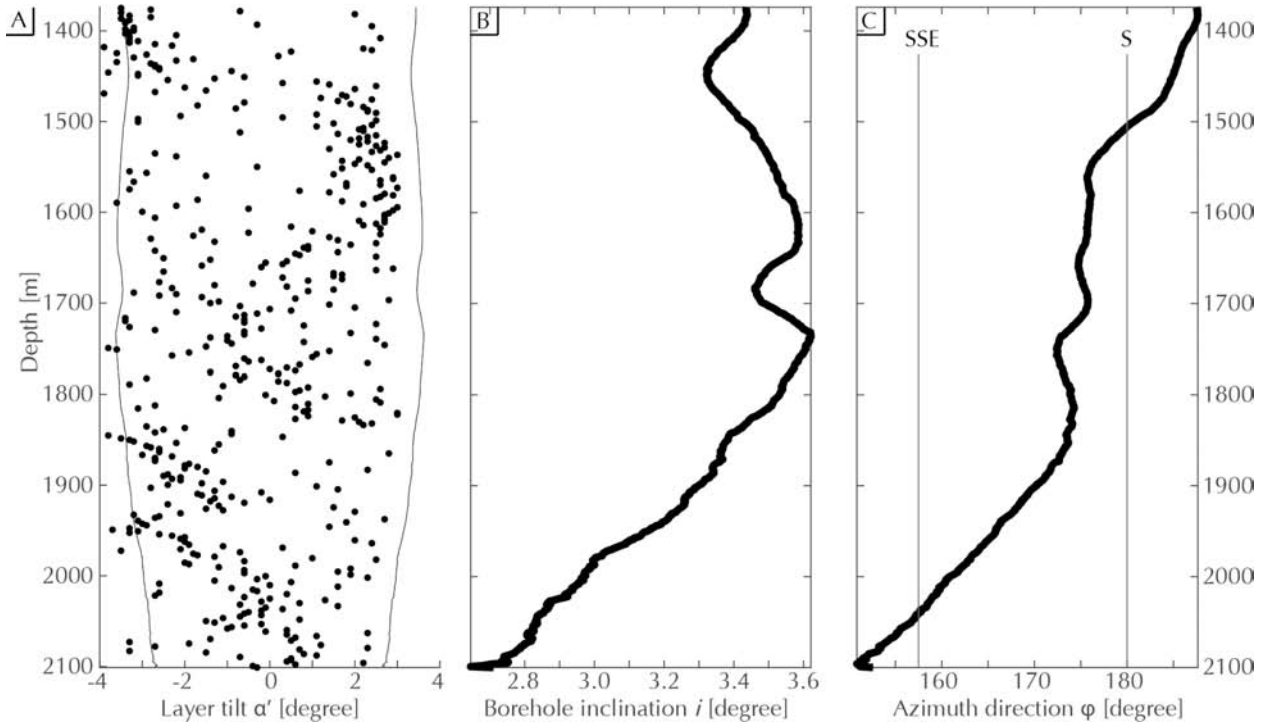
Figure 4.6: (A) Tilt of cloudy bands (α') from 1375 m to 2120 m (bag 2500 to 3856), each circle is the median value of 288 measurements for each 165 cm-long sample. (B) Inclination i and (C) azimuth direction φ of the EastGRIP borehole against depth. Inclination angle from (B) also shown as a thin line in (A).

4.3.2   Deformation Structure Matched to Layer Tilt

To differentiate the two potential δ, we make use of observed deformation structures, as explained above (fig. 4.4). When plotting the cloudy band's inclination against depth, color-coded for specific deformation structures, a systematic arrangement is visible (fig. 4.7). Above 1900 m, the flat layers with no features (fig. 4.7A, mean as dashed line) are located at the high and low values of the tilt. In the same depth range, cloudy bands with crenulations (fig. 4.7C) have values closer to 0°. Cloudy bands with long-wavelength folds and undulations (fig. 4.7B) scatter over the full spectrum of layer tilts.

Borehole inclination and azimuth direction change significantly below 1900 m (fig. 4.6). The tilt of layers with no features (fig. 4.7A) gradually shifts to values around 0°. Layers with crenulations (fig. 4.7C) now incline at larger values. Thus, these specific deformation features are linked to specific layer tilts.

4.3.3   Work Flow Diagram

The flow diagram (fig. 4.8, left side) supplies the user with a step by step instruction on how to use the presented method. It requires the input of borehole geometry (#1) and visual stratigraphy images (#2), and knowledge about ice flow direction (step 5). All other parameters are obtained from these. In the following, to illustrate the method, two consecutive visual stratigraphy images from a depth of around 1634 m (bag 2971 and 2972), with different deformation structures, are compared and reoriented (fig. 4.8, right side).

Input #1 defines the reference system, i.e., the azimuth direction and inclination of the borehole. Azimuth direction φ is 175.5°, and borehole inclination i is 3.6° for bag 2971 and 2972. Thus, this is also the dip direction and dip angle of our layers.

The apparent dip α', i.e., the visible tilt of the layers, in bag 2971 and 2972 is −1.3° and 2.5°, respectively. We apply eq. 4.2 to calculate β, which is 12° and 56° respectively. For a negative layer tilt α' eq. 4.4 is used for bag 2971. For the positive tilt α' in bag 2972, we
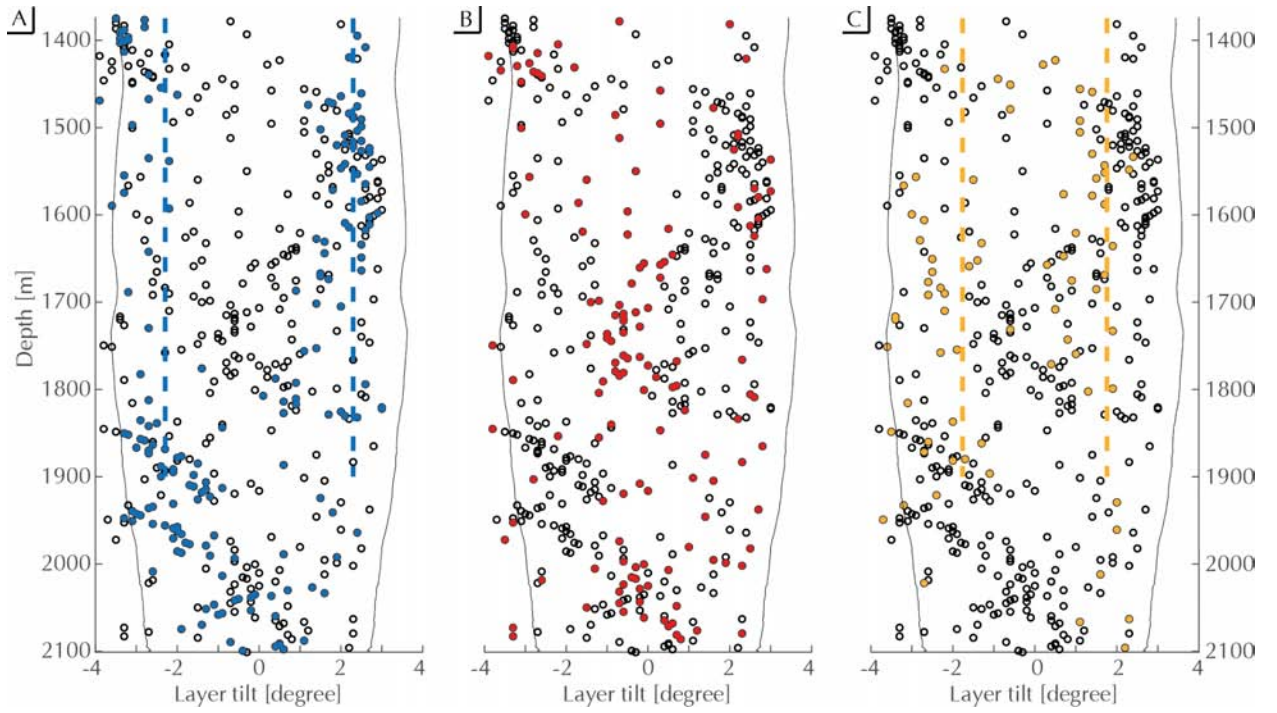
Figure 4.7: Deformation-structure types and the corresponding layer tilt of cloudy bands against depth. Cloudy bands with no or flat features (A, blue), long wavelength undulations and folds (B, red), and crenulations (C, orange). Dashed lines are means for 1375 m to 1900 m separated for positive and negative tilt. No features mean: ±2.3 and crenulations mean: ±1.6.

apply eq. 4.3. Both provide two possible viewing directions $\delta = 008°$ and $\delta = 163°$ for bag 2971 and $\delta = 232°$ and $\delta = 299°$ for bag 2972 (see fig. 4.8).

In the visual stratigraphy of bag 2971, we can clearly identify crenulations, linked to compression folds, and thus, the direction of view for δ must be close to perpendicular to ice flow direction of NEGIS (flow towards 025°). In this case, the position at 008° fulfills this requirement. A viewing direction of 163° would not represent an angle where compressional folds would be visible in the stratigraphy, and can therefore be eliminated as a possible viewing direction.

Cloudy bands in bag 2972 show no deformation features. Thus, the cut plane must be oriented approximately parallel to flow direction. At $\delta = 232°$, we would expect to see deformation features in the cloudy bands. The second option $\delta = 299°$ however, is closer to the anticipated value parallel to the ice flow direction. Therefore, the first value (232°) can be ruled out.

4.3.4 Comparison of Viewing Direction δ to Other Methods

Relative Orientation from Core Recovery

Before cutting the ice core for visual stratigraphy analysis, it is rotated at an angle γ, relative to the loggers mark (illustrated in fig. 4.2F). This rotation defines the relative core orientation γ, which is continuously documented (fig. 4.9, red). We calculate the absolute orientation δ (fig. 4.9, black) for all samples, which represents the orientation relative to geographic North. We observe a strong correlation in the difference of absolute and relative orientation $\delta - \gamma$ (fig. 4.9, blue). Subtracting γ from δ determines the deviation of the loggers mark from geographic North (compare to fig. 4.2).

Figure 4.9 also indicates the loss of relative core orientation (vertical black lines) due to mismatches of core breaks (illustrated in fig. 4.2D). For each mismatch in a core break,

Input #1: borehole geometry
- azimuth direction (φ) and
- inclination (i)

Input #2:
visual stratigraphy image

Step 1:
determine tilt
of cloudy bands (α')

Step 2:
calculate β
[eq. 2]

is α' positive
or negative?

Step 3:
calculate δ
[eq. 3 and 4]

Step 4:
analyze deformation features:
- crenulations,
- folds with long wavelength,
- or no structures.
[e.g., right side]

Step 5:
determine better fit in respect
to ice flow direction
– positive: δ_1 or δ_2
– negative: δ_3 or δ_4

Result:
δ represents the orientation of
a sample's cut plane

Examples:
φ: 175.5°
i: 3.6°

bag 2971
depth
1633.95m

bag 2972
depth
1634.05m

$\alpha' = -1.3°$

$\alpha' = 2.5°$

$\beta = 12°$

$\beta = 56°$

negative

positive

$\delta_3 = 163°$
$\delta_4 = 008°$

$\delta_1 = 299°$
$\delta_2 = 232°$

crenulations

no structures

δ_4

δ_1

↑top

↑top

S   W

E   S

E   N
$\delta = 008°$

N   W
$\delta = 299°$

1633.95m   ↑top   Bag 2971

1634.00m

1634.05m   Bag 2972

1634.10m

1634.15m

top

N
δ_1 δ_4
W   90-β -90°
+90° β E
δ_2 δ_3
azimuth
direction
S   (175.5°)

top

N
δ_1 δ_4
W   90-β -90°
+90° β E
δ_2 δ_3
azimuth
direction
S   (175.5°)

000° = North, 090° = East,
180° = South, 270° = West

Figure 4.8: Left: flow diagram to determine ice core absolute orientation, applied on bag 2971 and 2972. Middle: visual stratigraphy images of the two consecutive bags, including a depth scale. Right: sketch of visual stratigraphy plane, including relevant angles to obtain the orientation. Blue: spatial orientation of δ. Red: visual stratigraphy plane.

a new loggers mark is created, which has a random but continuous orientation for a range of matching core breaks. In sections with a preserved relative core orientation, very small rotations (of γ) are aimed for prior to cutting the ice core for visual stratigraphy. This results in many layer tilt measurements clustering around a certain value as this is the preferred cut orientation during core preparation.

All core mismatches in this section are documented in the field protocol as "probably lost", except break number three, 16, and 19, which are labeled as "not-matched". "Not-matched" means that the relative orientation is lost, but the mismatches at breaks three and 19 do not show this mismatch in our data (fig. 4.9). On the other hand, the mismatch at break 16 is clearly visible. In many of the assumed core mismatches, the orientation is, in fact, not lost (e.g., break one, seven, nine, and 26). A prominent example of a loss of core orientation is break 27, where the orientation ($\delta - \gamma$) changes abruptly.

Orientation of Crystal-Scale Directional Features

The orientation of a single ice crystal can easily be described by its c-axis, which is the vector perpendicular to the crystal's basal plane (e.g., Petrenko and Whitworth, 1999). C-axis orientation has been measured continuously, every 10 to 15 m, throughout the EastGRIP
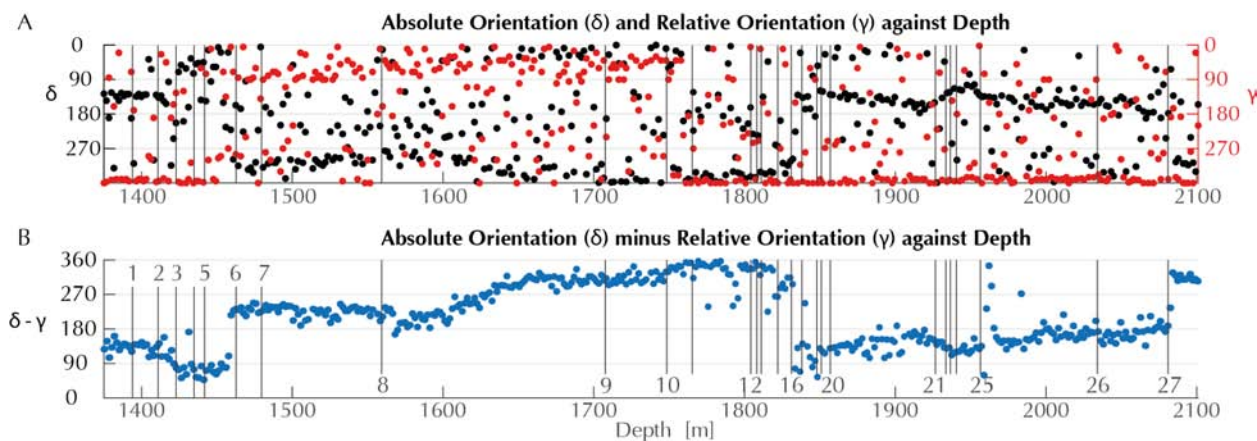
Figure 4.9: (A) Absolute spatial orientation δ (black) and relative orientation γ (red) against depth. (B) $\delta - \gamma$ (blue) describes the offset angle of the relative orientation from geographic North. Vertical lines show core breaks where a match was not possible.

core. Between 1375 m and 2120 m, we use 34 c-axis plots. They show a c-axis distribution that is classified as a girdle in varying strengths.

Each projection alone shows a developed girdle with various orientations (fig. 4.10A). These plots have a random orientation, when all are plotted together without rotational correction (fig. 4.10B$_1$). This is also visible in the rose-diagram and histogram (fig. 4.10B$_{2,3}$). Each c-axis plot may be rotated by δ as determined by the method reported here (fig. 4.10A). A systematic directional feature, i.e., a girdle with the same orientation for all samples, is visible when all samples are oriented (fig. 4.10 bottom panel). The vertical girdle is now clearly orientated towards 120° and 300°, which is approximately perpendicular to the assumed flow direction at 030°.

4.4 Discussion

4.4.1 Statistical Overview

Reorientation of the EastGRIP ice core worked well for 396 of 451 samples (88%). These 451 samples cover 745 core metres, which covers the full interval of interest from 1375 m to 2120 m depth. After a comparison with the relative orientation γ, a good agreement was found for 441 of 451 samples (98%). In the remaining ten samples, the layer tilt is very close to 0°, so the sample can be viewed from two opposing sides, allowing two possible orientations, which cannot be distinguished further.

4.4.2 Cloudy Band Tilt Measurement

The limited accuracy in measuring the inclination of a cloudy band is the largest source of uncertainty. The measurements in featureless samples are the most accurate, as every cloudy band is parallel to the one above and below.

As deformation of the visual stratigraphy increases, the accuracy of the tilt measurement declines. The approach by Drews et al. (2012), who used the Hough Transform (Hough, 1962) on visual stratigraphy data from the European Project for Ice Coring in Antarctica, Dronning Maud Land Deep Drilling (EDML), was tested on our data. We added a pre-processing step to the Hough Transform, using the built-in Matlab skeleton function for binary images, which greatly improved the outcome (MATLAB, 2018). The skeleton function finds the centerline between two edges, providing the average tilt of the top and bottom edge of a
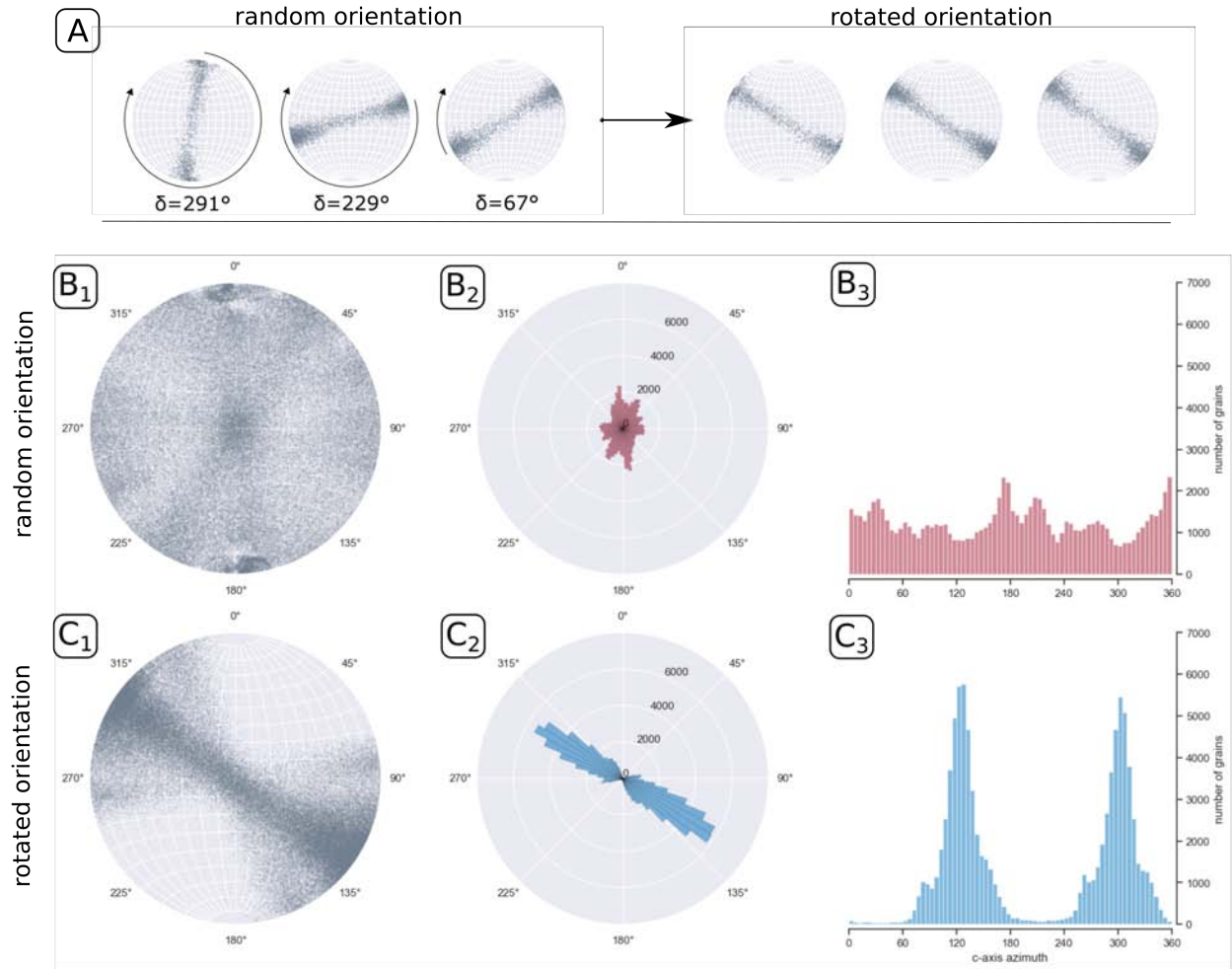
Figure 4.10: Comparison of stereographic projections of crystallographic oriented fabric c-axis of an un-rotated and rotated ice core. Panel (A) shows three individual stereographic projections before and after the rotation. A comparison of 34 c-axis data sets are shown in panel (B) and (C), with: (1) stereographic projections of the c-axis of all ice crystals, (2) a rose diagram and (3) a histogram showing the distribution of the azimuth of all ice crystals binned in 5 degree units, respectively before and after re-orientation.

cloudy band. Still, a large number of detected lines in the image did not match stratigraphic layers. Therefore, for our approach, we determined a cloudy band's inclination by using left-right grayscale signal alignment (see method section).

Another approach to detecting the layer tilt is using Fast Fourier Transform (FFT). This method is suggested by McGwire et al. (2008) and applied on the West Antarctic Ice Sheet (WAIS) Divide Deep ice core (Fitzpatrick et al., 2014). However, it holds the same limitations as the Hough Transform and our grayscale alignment, as undulations and folds in the cloudy bands scatter the result.

An increase of disturbances in the cloudy bands correlates with variations of layer tilt within one sample. The top edge of a cloudy band can have a different tilt to the bottom one, as the layer thickness can vary within the width of one sample (fig. 4.8, cloudy band at 1633.98 m). This means that any method to determine layer tilt will suffer an increase the more layers are disturbed. We therefore assume that the straightforward comparison between left and right side of a sample suffices.

4.4.3 Relative and Absolute Orientation

To estimate the uncertainty in the tilt measurement, we compare the absolute orientation δ to the relative orientation γ. The latter was collected over three field seasons, by approximately nine different operators, and rounded to the next 5° or 10°, therefore, we expect a certain range of scattering. Figure 4.9B shows that the difference of absolute orientation minus relative orientation $(\delta - \gamma)$ align. If we assume γ to be very precise (to the closest 5°), the noise in this alignment is caused by inaccuracies in δ. Although there are uncertainties in tilt measurements of cloudy bands, the results show that the general orientation δ agrees with the relative orientation γ taken during ice core processing in the field.

The presented results are a rare opportunity to analyze the quality of core break matching (fig. 4.2D) during ice core logging in the field. Mistakes made can be identified by comparing the relative orientation γ (fig. 4.2F) to the absolute orientation δ. A loss of relative core orientation is indicated as a sudden change of $\delta - \gamma$. Three of these are easily spotted between break five and six, at break 16, and break 27. While break 16 and 27 are located exactly at the change of angle, the change of angle at 1459 m depth is located four metres above mismatch six. As this agrees well with the length of core retrieved in one drill run, we can interpret an inconsistency in documenting the depth while logging. This interpretation is most likely not valid for mismatch eight, where the small change in $\delta - \gamma$ is observed seven metres deeper.

An interesting feature is the slow shift of $\delta - \gamma$ between 1600 m and 1650 m (from 210° to 300°). The relative orientation is assumed to have been kept constant and borehole inclination and azimuth barely change (fig. 4.6). However, an observed gradual shift over 90° could be the sum of tiny shifts in orientation during ice core logging. We find inconsistencies in the loggers field protocol for this depth range, where although all core breaks are labeled as matched, smaller core sections are missing or out of place. This gradual shift of relative orientation could be the result of small core break mismatches, due to these missing or too small sections. A more apprupt change in $\delta - \gamma$ is observed between mismatch 11 and 12, where $\delta - \gamma$ decreases sharply and then returns to the previous level. Again, the loggers field protocol shows inconsistencies for this part of the core, however, without mentioning further details. We argue that the deviations of five samples after mismatch 25 are most likely related to an incorrect measurement of γ because the correlation works well before and after this section and no errors in the tilt measurements were found.

Problems with core break matching seem to cluster. They are located between mismatch 12 to 20 and 21 to 25. While this could be related to variations in the drill setup and difficulties in drilling, leading to a reduced core quality, it could also be related to personal preferences of the core logging operators.

In the cluster between mismatch 12 and 20 there are several occasions where a mismatch was assumed, but the orientation was actually preserved, e.g., at mismatches 12, 13, 14, and 20. The challenges for continuous and precise core break matching can be observed between mismatch 15 and 19, where the values show a large variability and two mismatches are labeled as "not-matched".

There are many sections where core break matching worked very well. Between mismatch seven and eight, 20 and 21, and 25 and 27, $\delta - \gamma$ does not change over longer periods. Even with a number of different personnel acquiring the data, core break matching works very well in the analyzed depth region. The field protocol seems to be more on the conservative side, as at most of the mismatches labeled with "probably lost" the relative core orientation is actually preserved. Also, the documentation of core rotation prior to cutting (γ, fig. 4.2F) was done in an diligent manner, with very few exceptions.

4.4.4   Direction of Flow Inferred from the Crystal Orientation

The orientation distribution of the c-axes of crystals in one sample are called fabric, or crystal preferred orientation (CPO). When ice is deformed, the CPO changes, with its type depending on the dominating deformation mode (e.g., Kamb, 1972). The two main processes impacting the fabric pattern are 1) rotation of c-axes towards the direction of maximum finite shortening (Alley, 1992; Qi et al., 2019) and 2) recrystallization leading to the formation of new grains with different orientations, compared to the host grain (Llorens et al., 2017). Information on the deformational history can therefore, to a certain extent, be derived from the fabric of a sample (Kamb, 1972; Thorsteinsson et al., 1997; Wang et al., 2002; Montagnat et al., 2014; Weikusat et al., 2017).

According to (e.g., Cuffey and Paterson, 2010), the observed developed vertical girdle between 1375 m and 2120 m indicates extensional deformation along flow direction. If the dominating stress regime is axial extension, crystals rotate and basal planes shift towards paralelllism with the direction of extension (Thorsteinsson et al., 1997; Wang et al., 2002). Hence, c-axes rotate away from the direction of extension, producing girdle fabrics. Depending on their strength, patterns are classified as developing, developed, or strong girdle. The stronger a girdle, the more c-axes are aligned in the girdle, and the thinner the girdle becomes (Cuffey and Paterson, 2010).

The use of visual stratigraphy data enabled us to rotate the c-axis orientation data in a structured way. Doing so results in girdles that are aligned perpendicular to the observed flow direction of 030° of NEGIS. Our data confirm that the ice stream's extensional deformation results in a vertical girdle perpendicular to the flow direction.

Some scatter remains, which can be explained by unavoidable difficulties in measuring the angle of undulations and folds in stratigraphic layers and small-scale changes in the crystal fabric. However, the rotation of the fabric data using the correction we derived with our method turned out to be successful and indicates a deformation pattern, which agrees very well with the observed flow direction of NEGIS (Hvidberg et al., 2020).

4.4.5   Interpretation of Visible Deformation Structures

The schematic image of folds in a cylinder, as done in fig. 4.4, is an idealization, as it shows the grayscale variation within an infinitely thin slice. Ice is a transparent material, and the image obtained in a line scanner is the product of light passing through a thick slice and is averaged over the focus depth. The sharpest image is obtained when layer boundaries align in the direction of observation. This is always the case in undisturbed layers. However, when layers are folded, this is only the case when looking along the fold axes. We therefore only observe sharp, thin layers with clear crenulation folds in sections at a large angle (δ around 025° or 205°) to the fold axis or extension direction. Cutting the folds obliquely results in more wavy patterns that may resemble extensional structures, such as boudins, shear bands, and truncations.

Field geologists are acutely aware that structures may look very different, depending on how they are intersected by the outcrop surface. The true nature and style of folds, for example, is only seen in surface that are approximately perpendicular to the fold axis. The same applies here. After having established the true orientation of all drill-core section, assuming a consistent fold-axis orientation, those sections that have the proper orientation can be selected to analyze the deformation structures. Care should be taken not to over-interpret other sections, as the oblique sections through structures may be misleading.

A variation of cloudy-band morphology with depth could reflect a true variation in type or frequency of deformation structures. However, orientation of the drill-core sections should first be carried out to ascertain that this is not an artifact of sectioning. In the current case,

it appears that variations that range from straight layers to folds can be explained by this sectioning effect. Approximately straight layering is observed in sections close to parallel to the flow direction, while folds are observed in those perpendicular to it. This is consistent with extension of the ice sheet in the direction of flow and lateral constriction, which is expected to result in the observed fold orientations (Bons et al., 2016). The surface velocity fields at the EastGRIP drill site (Hvidberg et al., 2020) support this deformation regime as surface flow lines converge into the ice stream. Inside NEGIS the ice flow is parallel and the velocity is a magnitude higher than outside of the stream. Velocity at EastGRIP increases downstream, implying extension in the flow direction.

4.5 Conclusions

We present a simple method to determine the in-situ orientation of an ice core (summarized in a flow chart in fig. 4.8). Knowledge of this orientation of an ice core sample and the associated orientated physical properties is a major advance for the interpretation of deformation structures. Macroscopic folds in the visual cloudy-band stratigraphy, as well as deformation-related micro-structures and crystal fabrics can now be described with consideration of their spatial orientation. This leads to a high gain in information about the direction in which ice deforms and how it flows. This will greatly facilitate and improve the interpretation of deformation structures and the kinematic framework of that deformation.

This method contributes to the application of computational models, as visible 3D structures from the ice core are now comparable to the result of 3D models. This is possible as the direction of view δ covers the full 360° of possible orientations, so throughout core depth every direction is visible with its corresponding deformation structures. Using many 2D images, with different orientations, the 3D structure of an ice core can now be constructed.

Including other methods, such as analyzing the crystal-fabric orientation, we can further improve this method and enhance the accuracy. However, this study shows that the fabric is not a necessary input parameter for reconstructing the ice core orientation.

Information about ice core orientation is a necessity when interpreting structures seen in the ice core. This ranges from micro-scale features in the ice core lattice to macro-scale features seen in centimetre-scale folds. Neglecting the ice core orientation can lead to incomplete, and possibly misleading, interpretations of the physical processes related to ice flow and more generally, any analyses based on 2D images of an ice core.

Acknowledgements

Bibliography - Ice Core Orientation

Alley, R. B., Gow, A. J., Meese, D. A., Fitzpatrick, J. J., and Waddington, E. D. (1997). "Grain-scale processes, folding, and stratigraphic". In: *Journal of Geophysical Research* 102.C12, pp. 26819–26830.

Alley, R. B. (1992). "Flow-law hypotheses for ice-sheet modeling". In: *Journal of Glaciology* 38.129, pp. 245–256. DOI: 10.3189/s0022143000003658.

Bons, P. D., Kleiner, T., Llorens, M. G., Prior, D. J., Sachau, T., Weikusat, I., and Jansen, D. (2018). "Greenland Ice Sheet: Higher Nonlinearity of Ice Flow Significantly Reduces Estimated Basal Motion". In: *Geophysical Research Letters* 45.13, pp. 6542–6548. DOI: 10.1029/2018GL078356.

Bons, P. D., Jansen, D., Mundel, F., Bauer, C. C., Binder, T., Eisen, O., Jessell, M. W., Llorens, M. G., Steinbach, F., Steinhage, D., and Weikusat, I. (2016). "Converging flow and anisotropy cause large-scale folding in Greenland's ice sheet". In: *Nature Communications* 7, pp. 1–6. DOI: 10.1038/ncomms11427.

Christianson, K., Peters, L. E., Alley, R. B., Anandakrishnan, S., Jacobel, R. W., Riverman, K. L., Muto, A., and Keisling, B. A. (2014). "Dilatant till facilitates ice-stream flow in northeast Greenland". In: *Earth and Planetary Science Letters* 401, pp. 57–69. DOI: 10.1016/j.epsl.2014.05.060.

Cosgrove, J. (1976). "The formation of crenulation cleavage". In: *Journal of the Geological Society* 132.2, pp. 155–178.

Cuffey, K. M. and Paterson, W. S. B. (2010). *The Physics of Glaciers*, p. 722.

Dansgaard, W. ., Johnsen, S. . J. ., Møller, J. ., and Langway, C. J. (1969). "One Thousand Centuries of Climatic Record from Camp Century on the Greenland Ice Sheet". In: *Science* 166.3903, pp. 377–381.

Davis, B. K. and Cowan, E. J. U. N. (2012). "Oriented Core - What the ... ?" In: pp. 61–63.

Drews, R., Eisen, O., Steinhage, D., Weikusat, I., Kipfstuhl, S., and Wilhelms, F. (2012). "Potential mechanisms for anisotropy in ice-penetrating radar data". In: *Journal of Glaciology* 58.209, pp. 613–624. DOI: 10.3189/2012JoG11J114.

Fahnestock, M., Abdalati, W., Joughin, I., Brozena, J., and Gogineni, P. (2001). "High geothermal heat flow, basal melt, and the origin of rapid ice flow in central Greenland". In: *Science* 294.5550, pp. 2338–2342. DOI: 10.1029/2001JD900194.

Faria, S. H., Freitag, J., and Kipfstuhl, S. (2010). "Polar ice structure and the integrity of ice-core paleoclimate records". In: *Quaternary Science Reviews* 29.1-2, pp. 338–351. DOI: 10.1016/j.quascirev.2009.10.016.

Faria, S. H., Kipfstuhl, S., and Lambrecht, A. (2018). *The EPICA-DML Deep Ice Core*. Berlin: Springer-Verlag GmbH Germany.

Fitzpatrick, J. J., Voigt, D. E., Fegyveresi, J. M., Stevens, N. T., Spencer, M. K., Cole-Dai, J., Alley, R. B., Jardine, G. E., Cravens, E. D., Wilen, L. A., Fudge, T. J., and McConnell, J. R. (2014). "Physical properties of the WAIS divide ice core". In: *Journal of Glaciology* 60.224, pp. 1140–1154. DOI: 10.3189/2014JoG14J100.

Fossen, H. (2010). *Structural Geology*, p. 463. arXiv: arXiv:1011.1669v3.

Franke, S., Jansen, D., Binder, T., Dörr, N., Helm, V., Paden, J., Steinhage, D., and Eisen, O. (2020). "Bed topography and subglacial landforms in the onset region of the Northeast Greenland Ice Stream". In: *Annals of Glaciology* 61.81, pp. 143–153. DOI: 10.1017/aog. 2020.12.

Gow, A. J. and Williamson, T. (1971). "Volcanic ash in the Antarctic ice sheet and its possible climatic implications". In: *Earth and Planetary Science Letters* 13.1, pp. 210–218.

Grootes, P. M., Stuiver, M., White, J. W. C., Johnsen, S., and Jouzel, J. (1993). "Comparsion of oxygen isotope records from the GISP2 and GRIP Greenland ice cores". In: *Nature* 366.33, pp. 552–554.

Gundestrup, N. S., Clausen, H. B., and Hansen, B. L. (1994). "The UCPH borehole logger". In: *Mem. Natl. Inst. Polar Res.* 49, pp. 224–233.

Hammer, C. U., Clausen, H. B., Dansgaard, W., Gundestrup, N. S., Johnsen, S. J., and Reeh, N. (1978). "Dating of greenland ice cores by flow models, isotopes, volcanic debris, and continental dust". In: *Journal of Glaciology* 20.82, pp. 3–26.

Hough, P. V. (1962). *Method and means for recognizing complex patterns.* US Patent 3,069,654.

Hubbard, B. and Malone, T. (2013). "Optical-televiewer-based logging of the uppermost 630m of the NEEM deep ice borehole, Greenland". In: *Annals of Glaciology* 54.64, pp. 83–89. DOI: 10.3189/2013AoG64A201.

Hvidberg, C. S., Grinsted, A., Dahl-Jensen, D., Khan, S. A., Kusk, A., Andersen, J. K., Neckel, N., Solgaard, A., Karlsson, N. B., Kjar, H. A., and Vallelonga, P. (2020). "Surface velocity of the Northeast Greenland Ice Stream (NEGIS): Assessment of interior velocities derived from satellite data by GPS". In: *Cryosphere* 14.10, pp. 3487–3502. DOI: 10.5194/ tc-14-3487-2020.

Jansen, D., Llorens, M. G., Westhoff, J., Steinbach, F., Kipfstuhl, S., Bons, P. D., Griera, A., and Weikusat, I. (2016). "Small-scale disturbances in the stratigraphy of the NEEM ice core: Observations and numerical model simulations". In: *Cryosphere* 10.1, pp. 359–370. DOI: 10.5194/tc-10-359-2016.

Johnsen, S. J., Hansen, S. B., Sheldon, S. G., Dahl-Jensen, D., Steffensen, J. P., Augustin, L. J., Journé, P., Alemany, O., Rufli, H., Schwander, J., Azuma, N., Motoyama, H., Popp, T., Talalay, P. G., Thorsteinsson, T., Wilhelms, F., and Zagorodnov, V. (2007). "The Hans Tausen drill: Design, performance, further developments and some lessons learned". In: *Annals of Glaciology* 47, pp. 89–98. DOI: 10.3189/172756407786857686.

Joughin, I., Fahnestock, M., MacAyeal, D., Bamber, J. L., and Gogineni, P. (2001). "Observation and analysis of ice flow in the largest Greenland ice stream". In: *Journal of Geophysical Research: Atmospheres* 106.D24, pp. 34021–34034.

Kamb, B. (1972). "Experimental recrystallization of ice under stress". In: *Washington DC American Geophysical Union Geophysical Monograph Series* 16, pp. 211–241.

Llorens, M. G., Griera, A., Steinbach, F., Bons, P. D., Gomez-Rivas, E., Jansen, D., Roessiger, J., Lebensohn, R. A., and Weikusat, I. (2017). "Dynamic recrystallization during deformation of polycrystalline ice: Insights from numerical simulations". In: *Philosophical Transactions of the Royal Society A: Mathematical, Physical and Engineering Sciences* 375.2086. DOI: 10.1098/rsta.2015.0346.

MATLAB (2018). *9.7.0.1190202 (R2019b).* Natick, Massachusetts: The MathWorks Inc.

McGwire, K. C., Hargreaves, G. M., Alley, R. B., Popp, T. J., Reusch, D. B., Spencer, M. K., and Taylor, K. C. (2008). "An integrated system for optical imaging of ice cores". In: *Cold Regions Science and Technology* 53.2, pp. 216–228. DOI: 10.1016/j.coldregions. 2007.08.007.

Mojtabavi, S., Wilhelms, F., Cook, E., Davies, S., Sinnl, G., Skov Jensen, M., Dahl-Jensen, D., Svensson, A., Vinther, B., Kipfstuhl, S., Jones, G., Karlsson, N., Faria, S. H., Gkinis,

V., Kjær, H., Erhardt, T., Berben, S., Nisancioglu, K., Koldtoft, I., and Rasmussen, S. O. (2020). "A first chronology for the East GReenland Ice-core Project (EGRIP) over the Holocene and last glacial termination". In: *Climate of the Past Discussions* 16.December, pp. 2359–2380. DOI: `10.5194/cp-16-2359-2020`.

Montagnat, M., Azuma, N., Dahl-Jensen, D., Eichler, J., Fujita, S., Gillet-Chaulet, F., Kipfstuhl, S., Samyn, D., Svensson, A., and Weikusat, I. (2014). "Fabric along the NEEM ice core, Greenland, and its comparison with GRIP and NGRIP ice cores". In: *Cryosphere* 8.4, pp. 1129–1138. DOI: `10.5194/tc-8-1129-2014`.

NEEMCommunityMembers (2013). "Eemian interglacial reconstructed from a Greenland folded ice core". In: *Nature* 493.7433, pp. 489–494. DOI: `10.1038/nature11789`.

Paulsen, T. S., Jarrard, R. D., and Wilson, T. J. (2002). "A simple method for orienting drill core by correlating features in whole-core scans and oriented borehole-wall imagery". In: *Journal of Structural Geology* 24.8, pp. 1233–1238. DOI: `10.1016/S0191-8141(01)00133-X`.

Petrenko, V. F. and Whitworth, R. W. (1999). *Physics of ice.* OUP Oxford.

Qi, C., Prior, D. J., Craw, L., Fan, S., Llorens, M.-G., Griera, A., Negrini, M., Bons, P. D., and Goldsby, D. L. (2019). "Crystallographic preferred orientations of ice deformed in direct-shear experiments at low temperatures." In: *Cryosphere* 13.1. DOI: `10.5194/tc-13-351-2019`.

Ran, H., Riese, T. de, Llorens, M. G., Finch, M. A., Evans, L. A., Gomez-Rivas, E., Griera, A., Jessell, M. W., Lebensohn, R. A., Piazolo, S., and Bons, P. D. (2019). "Time for anisotropy: The significance of mechanical anisotropy for the development of deformation structures". In: *Journal of Structural Geology* 125.January 2018, pp. 41–47. DOI: `10.1016/j.jsg.2018.04.019`.

Svensson, A., Nielsen, S. W., Kipfstuhl, S., Johnsen, S. J., Steffensen, J. P., Bigler, M., Ruth, U., and Röthlisberger, R. (2005). "Visual stratigraphy of the North Greenland Ice Core Project (NorthGRIP) ice core during the last glacial period". In: *Journal of Geophysical Research: Atmospheres* 110.2, pp. 1–11. DOI: `10.1029/2004JD005134`.

Talalay, P. G. (2014). "Perspectives for development of ice-core drilling technology: A discussion". In: *Annals of Glaciology* 55.68, pp. 339–350. DOI: `10.3189/2014AoG68A007`.

Talalay, P. G. (2020). *Thermal Ice-Drilling Technology.* Springer, pp. 1–278. DOI: `10.1007/978-981-13-8848-4`.

Thorsteinsson, T., Kipfstuhl, J., and Miller, H. (1997). "Textures and fabrics in the GRIP ice core". In: *Journal of Geophysical Research* 102.C12, pp. 26583–26599. DOI: `10.1029/97JC00161`.

Vallelonga, P. et al. (2014). "Initial results from geophysical surveys and shallow coring of the Northeast Greenland Ice Stream (NEGIS)". In: *Cryosphere* 8.4, pp. 1275–1287. DOI: `10.5194/tc-8-1275-2014`.

Wang, Y., Thorsteinsson, T., Kipfstuhl, J., Miller, H., Dahl-Jensen, D., and Shoji, H. (2002). "A vertical girdle fabric in the NorthGRIP deep ice core, North Greenland". In: *Annals of Glaciology* 35, pp. 515–520. DOI: `10.3189/172756402781817301`.

Weikusat, I., Jansen, D., Binder, T., Eichler, J., Faria, S. H., Wilhelms, F., Kipfstuhl, S., Sheldon, S., Miller, H., Dahl-Jensen, D., and Kleiner, T. (2017). "Physical analysis of an Antarctic ice core-towards an integration of micro-and macrodynamics of polar ice". In: *Philosophical Transactions of the Royal Society A: Mathematical, Physical and Engineering Sciences* 375.2086. DOI: `10.1098/rsta.2015.0347`.

Chapter 5

Small-scale Deformation Structures in the EastGRIP Ice Core

Julien WESTHOFF[1],
Potential co-authors:
Paul BONS[2], Ilka WEIKUSAT[2,3], Nicolas STOLL[3], Kyra STRENG[2],
Daniela JANSEN[3], and Dorthe DAHL-JENSEN[1,4]

[1]*Niels Bohr Institute, University of Copenhagen, Copenhagen, Denmark*
[2]*Department of Geosciences, Eberhard Karls University Tübingen, Tübingen, Germany*
[3]*Alfred Wegener Institute, Helmholtz Centre for Polar and Marine Research,
Bremerhaven, Germany*
[4]*Centre for Earth Observation Science, University of Manitoba, Winnipeg, Canada*

Abstract   The EastGRIP ice core is drilled through the Northeast Greenland Ice Stream, which has a surface velocity of 55 m/yr towards NNE (or 025°) at the drill site. We analyze the the depth region from 1375 to 2120 m covering a large part of the Glacial Period. We use the line scanner to make the stratigraphy visible and document disturbances in the layering. Disturbances are visible in cuts perpendicular to the ice flow direction, and not in cuts parallel to flow. Between these two extremes, we have a gradual change in type and amount of disturbances. The disturbances, or deformation structures, are the result of strain caused by the stress field at the EastGRIP site, which is described by a compressional component perpendicular to and an extensional component parallel to the ice flow direction. As with all other ice cores, the ice in the EastGRIP ice core is thinned vertically. Due to the advanced thinning of layers, it is clear that the visible structures are not the remnants of surface features, such as sastrugi. In most samples cut perpendicular to ice flow, i.e. with the compressional setting visible, we find structures, very similar to geological duplex structures. We identify duplex structures by the sudden change of layer tilt within one sample and discuss one example, from a depth of 1651 m, in detail. Duplex structures are confined by layer parallel shear zones, with tilted layers in between them. The small-scale shear zones only become evident due to the deformation they cause, and can extend well beyond these visible structures. We furthermore suggest, that shear zones are present parallel to layering, but do not show up, as a lateral displacement of layers, does not disrupt the vertical profiles.

Disclaimer   This chapter is a draft version, without any thorough reviews by the co-authors. The list of potential co-authors is a suggestion, including people that could potentially provide input for later stages of the manuscript. The current version has only been very briefly reviewed by the suggested co-authors, mainly for approving it to be included to the thesis at this stage. Thus, the main author (JW) is solely responsible for the text provided in this chapter.

5.1 Introduction

5.1.1 EastGRIP, the Special Ice Stream Ice Core
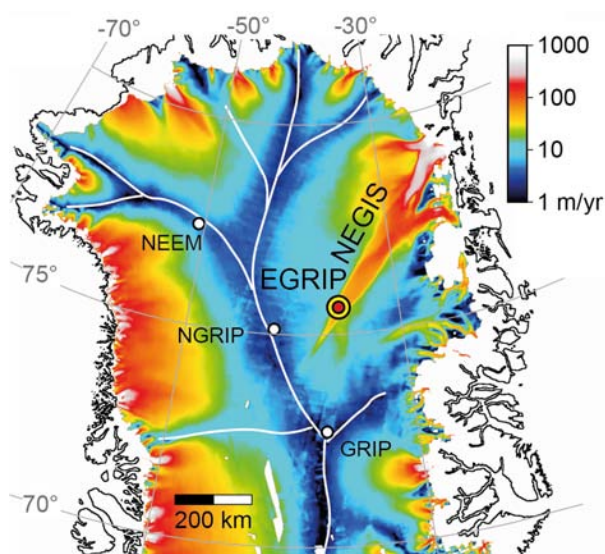
Figure 5.1: Overview of surface velocities and drill sites in Northern Greenland (modified from Bons et al., 2018, on the basis of the MEaSUREs velocity data set (Joughin et al., 2010). NEGIS flow direction at EastGRIP is NNE, or 025°.

The East Greenland Ice Core Project (East-GRIP) ice core is unique concerning its location on the ice sheet. It is drilled through the Northeast Greenland Ice Stream (NEGIS), which has a surface velocity of 55 m per year towards the NNE (or 025°, Hvidberg et al., 2020). The ice sheet surface velocity is facilitated by sliding at the ice-rock interface as well as, internal deformation and a flow parallel elongation component (e.g. Dansgaard and Johnsen, 1969). Unique to NEGIS is a strong compression component perpendicular to flow at the EastGRIP drill site, (Hvidberg et al.,2020, Westhoff et al., 2020).

Jansen et al. (2016) present a detailed overview of folds, describing the fold hinges as tilted lattice bands, in the NEEM ice core. When comparing a number of deep ice cores, the authors also suggest that folding occurs at different depths of ice cores, but is rarely seen shallower than in the upper third of the ice cores. The difficulty is, that folds only become visible, when optical markers, such as cloudy bands, are present. Cloudy bands regularly appear in ice older than the Holocene, i.e. the Last Glacial Period. In the EastGRIP ice core, Glacial ice is found in a depth of 1375 m and below (Mojtabavi et al., 2020). Modeling studies suggest deformation structures to be visible in the upper part of the ice column (e.g. Steinbach et al., 2016; Llorens et al., 2017) but evidence has only been found by Westhoff et al. (2021).

We investigate deformation structures found in the EastGRIP ice core. Evidence of deformation is immediately visible, with the first appearance of cloudy bands in a depth around 1375 m. This is a much shallower depth than in other ice core records (Jansen et al., 2016). Additionally, these folds have a very different appearance than those described by Svensson et al. (2005, NorthGIRP), Jansen et al. (2016, NEEM), or Faria et al. (2010, 2018, EDML).

5.1.2 A Brief Summary of Ice Core Orientation

Orientation describes the direction from which we look at an ice-core image-sample, e.g. a line scan image. We reference the image sample to geographic North, where we imagine the ice core to be in-situ in the ice sheet (fig. 5.2). We then view a plane along the ice core's long axis, where the normal to this plane, projected into the horizontal is the viewing direction δ, as in fig. 5.2.
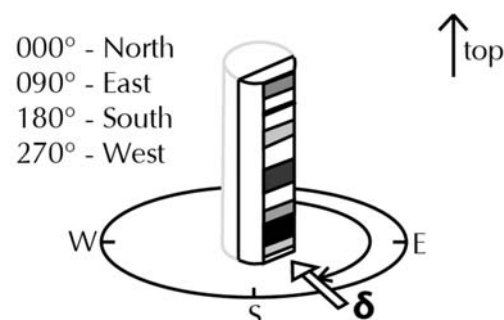
Figure 5.2: The orientation of an ice core referred to as viewing direction δ (Westhoff et al., 2020).

Figure 5.3: The visual appearance of deformation features is dependent on the orientation of the plane analyzed. a) no features visible, b) long-wavelength undulations, and c) crenulation folds and very disturbed layers. d) Rose diagram 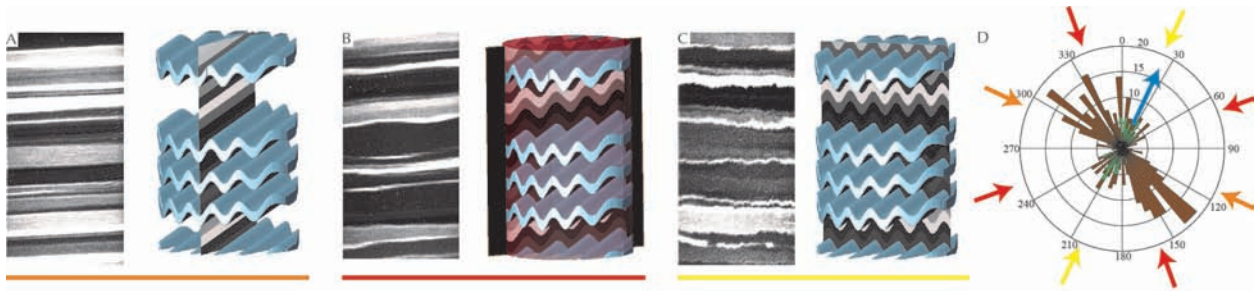of all line scan image orientations. Orange is viewed perpendicular on a cut parallel to ice flow (folds like a), yellow arrow is facing into the ice stream, with an image plane perpendicular to flow (folds like c), and the red arrows show an intermediate viewing possibilities (folds like b). The blue arrow (in d) indicates the flow ice direction.

Reconstructions of the ice core orientation have been made by Faria et al. (2014) and Weikusat et al. (2017), who rely on the girdle fabric where the orientation relative to flow direction can be pinned down to two possibilities. The fabric is expressed by the orientation of the c-axes of single ice crystals in an ice core sample. The composite of c-axes is then displayed in a stereographic projection (Kamb, 1972; Thorsteinsson et al., 1997; Wang et al., 2002; Montagnat et al., 2014; Weikusat et al., 2017). This method only works when the fabric has a specific pattern (e.g. a girdle) and leaves two possible orientations for the sample.

Another attempt was taken by Fudge et al. (2016) using the inclination of layers to see if the ice core had been rotated. They do not reconstruct the orientation, but find mismatches and thus positions where core break matching did not work.

Westhoff et al. (2020) describe a method to reconstruct the ice core orientation and provide an orientation for 441, of 451 samples, from the Glacial section of the EastGRIP ice core. They show that the visible deformation structures in the EastGRIP ice core are dependent on the direction of the cutting plane which is scanned (fig. 5.3a,b,c).

To verify their method, Westhoff et al. (2020) compare their results to the fabric orientation and to the logging protocols that contain information on the quality of core break matching and the rotation prior to cutting. If core break matching would work perfectly and the core would not be rotated before cutting, then we would only see the ice core from one direction. Core break matching works extremely well and only failed four times between 1375 m and 2120 m depth (Westhoff et al., 2020). Due to damages on the ice core from e.g. the drill's core catchers, the ice core is deliberately being rotated prior to cutting. This implies, that the ice core is scanned from a different orientation every time. This orientation is not random, as rotations prior to cutting are kept small. We therefore have certain viewing orientations dominating (fig. 5.3d).

5.2   Methods

5.2.1   The Line Scanner and Visual Stratigraphy

The line scanner creates a grayscale image of an ice core slab. The ice core slab is polished on both sides, and by introducing light at an angle from below, features inside the ice, such as core breaks, bubbles, or dust-rich layers, are made visible. Dust-rich layers appear bright, as they scatter light, and layers with less dust appear dark, as the dark field below the ice core slab is imaged. Most commonly the bright layers are referred to as dust layers or cloudy

bands, deposited by storms occurring mainly in spring (Hammer et al., 1978; Svensson et al., 2005; Winstrup et al., 2012). In the EastGRIP line scan images, from top to bottom, the first cloudy bands are found at a depth of 1375 m, which corresponds to the age of around 11.700 years before today (Mojtabavi et al., 2020). For more details on the way the line scanner works, consult Svensson et al. (2005), Faria et al. (2018), Westhoff et al. (2020), or Westhoff et al. (2021).

5.2.2 Investigation of Deformation Structures

To create an overview of deformation structures in an ice core, we manually assessed the line scan images. Manually creating an overview of deformation features is the state of the art method in the visual stratigraphy of ice cores (e.g. Alley et al., 1997; Svensson et al., 2005; Jansen et al., 2016; Weikusat et al., 2017). Exceptional structures were marked, sorted, and documented. For the overview of changes in the tilt of cloudy bands (from here on called layers), we manually analyzed every sample and take notes. The results are divided into change of tilt detected, not detected, and uncertain.

5.3 Results

5.3.1 Deformation Structures in the EastGRIP Ice Core

When viewing visual stratigraphy images of the ice core, e.g. cuts parallel to the ice flow direction (close to $\delta = 115°$ *or* $295°$, see fig. 5.2) we find well-layered stratigraphy. An example of this is fig. 5.4a, which shows no indications of being disturbed by flow. Figure 5.4a is from 2119.3 m depth and despite the sample being from the bottom-most part of the core drilled so far, it shows less disturbance than the other examples from further up in the stratigraphic column. This is because structures appear different, depending on the direction we visualize them, i.e. the orientation of the sample (fig. 5.3). Visual stratigraphy images with no deformation structures (fig. 5.3a and 5.4a) are the most abundant ones, occurring in 237 of 452 samples (52%). They are, by chance, imaged the most often (see fig. 5.3d).

When viewing images from cuts perpendicular to flow direction (close to $\delta = 025°$ *or* $205°$), we find many instances of folded layers throughout the visual stratigraphy of EastGRIP (fig. 5.4b to i). Figure 5.4b,c show a layer that has the appearance of a porphyroclast. In geology, a prophyroclast would be a more competent grain, or compound, which is rotated in a softer matrix during simple shear (Fossen, 2010). Yet this explanation is unlikely as layers in ice have a very similar competency.

Figures 5.4d,e,f show boudin-like structures (green arrows), which are all from cuts perpendicular to ice flow direction. Boudins in rocks are the result of an extensional regime, where stretching of a stronger layer creates thickness variations across that layer. These variations can make the layer too thin to see in some sections and bulge out in others. We do not have an extensional regime in the images shown, but the resulting structures look similar. Thus, a feasible explanation is still missing. We also find a disturbed band in a thick layer (fig. 5.4e, yellow arrow) which does not disrupt the stratigraphy, but follows the slope of the layer boundary below.

The bottom row of fig. 5.4(g,h,i) displays sections where the tilt of layer stacks suddenly changes and layers thin out and disappear. The mechanisms of these types of folds will be highlighted in the next sections and a suggested structural setting will be presented in the discussion.

a) 2119.3 m (bag 3854, $\delta = 280°$) b) 1752.5 m (bag 3185, $\delta = 50°$) c) 1691.50 m (bag 3076, $\delta = 26°$)*

d) 1427.9 m (bag 2597, $\delta = 200°$) e) 1428.0 m (bag 2597, $\delta = 200°$)* f) 1394.5 m (bag 2534, $\delta = 190°$)

g) 1405.2 m (bag 2555, $\delta = 40°$)* i) 1422.0 m (bag 2585, $\delta = 245°$) h) 1690.65 m (bag 3074, $\delta = 26°$)
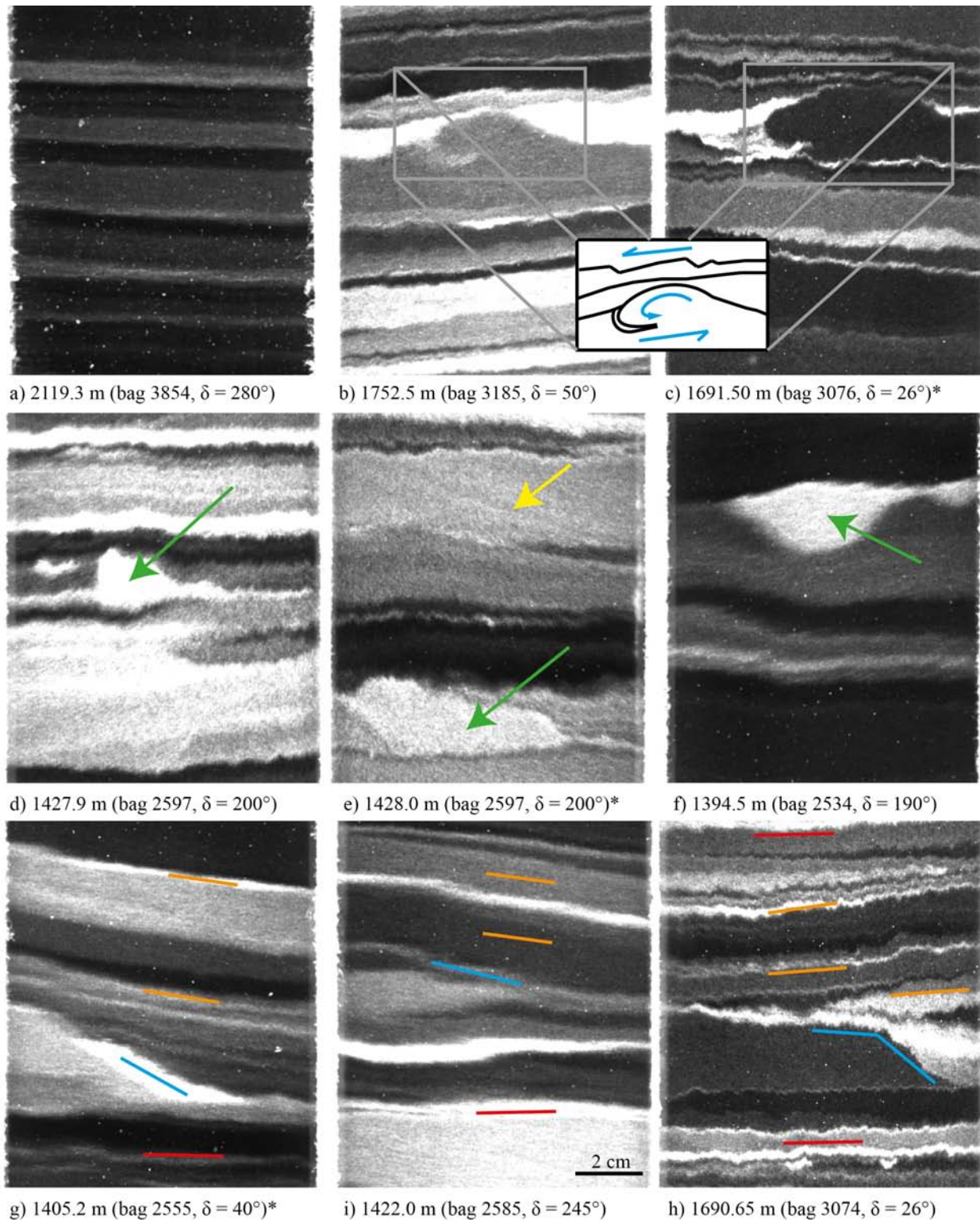
Figure 5.4: Deformation structures in the EastGRIP ice core. Visible deformation features are highly dependent on the viewing direction (δ). a) bottom-most scan of the EastGRIP ice core (before the year 2021). b,c) Porphyroclastic appearance of a sheared layer. d,e,f) Boudin-like structures (indicated in green) and deformation band (yellow) in e). g,h,i) Duplex structures with sudden changes of tilt and abruptly ending layers. Visualized are the ramp (in blue), general layering of section (red), and changed layer tilt (orange). Images with (*) are mirrored.

5.3.2 Sudden Change in Layer Tilt
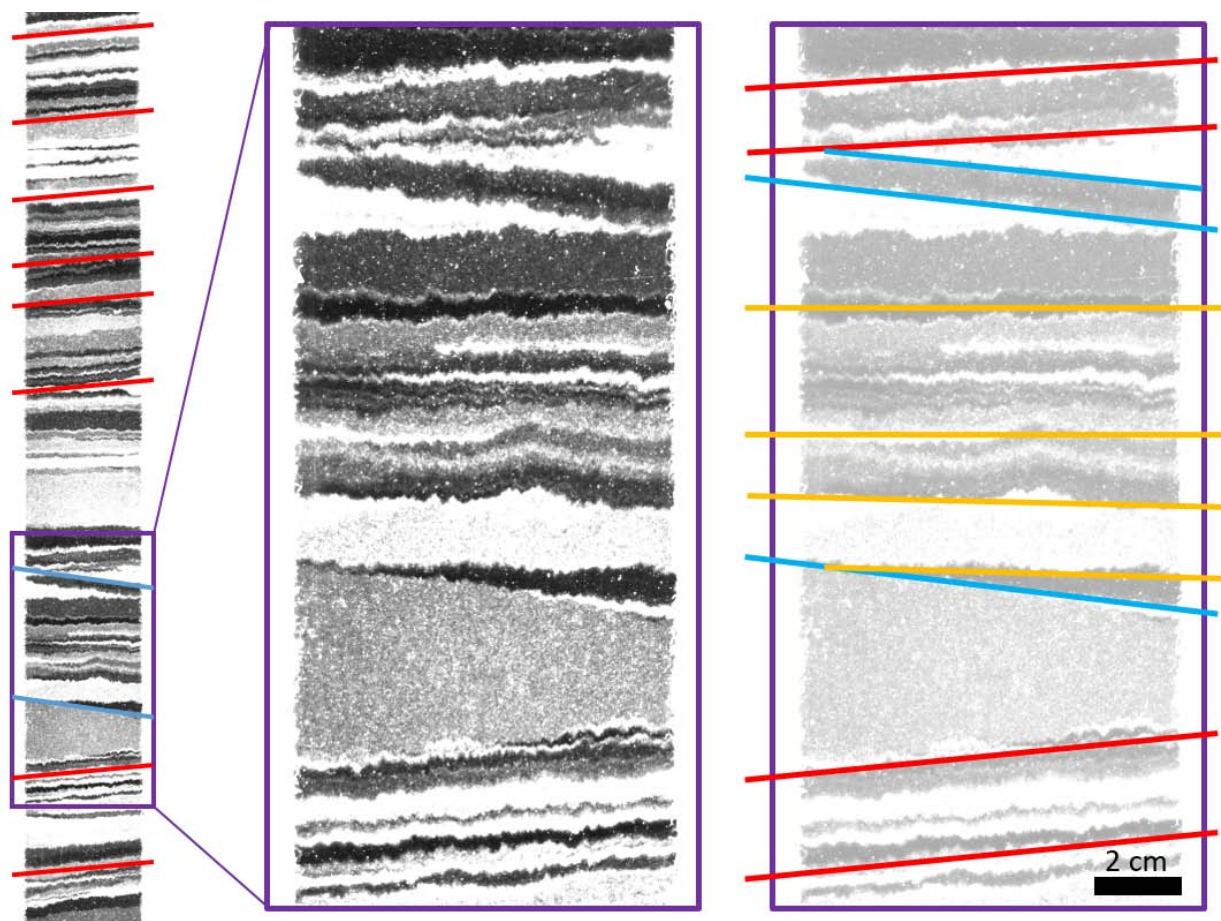
Figure 5.5: Change of layer tilt within one sample. General tilt is to the left (red), but an upper and lower boundary layer are tilted to the right (blue), with horizontal layers in between (yellow). Full bag 3516 (1933.25 to 1933.80 m) on left (8 x 55 cm), and details on right (scale in figure).
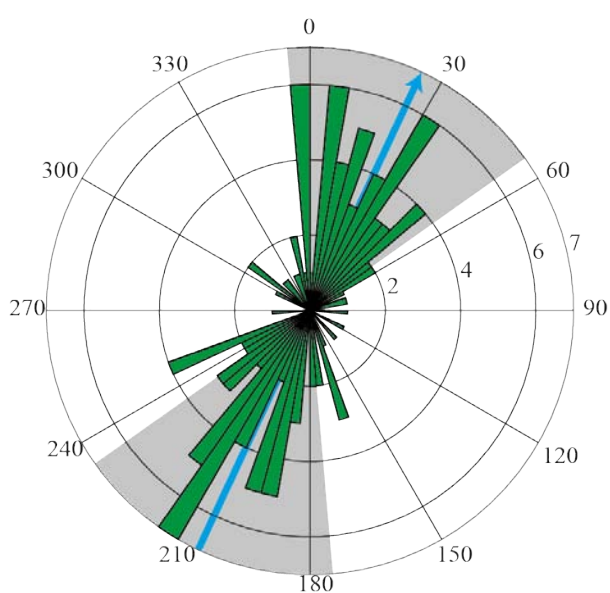
Figure 5.6: Spatial orientation of samples where we find a sudden change of layer tilt. Total number of events: 121. Blue: NEGIS and gray: ±30° of ice flow direction.

fig. 5.5 is an example of how the tilt of layers can change throughout one sample. The general tilt for the sample is towards the left (red), while a small section of ten centimeters in length has horizontal layers (yellow). These horizontal layers are between two wedges sloping to the right (blue). The crucial aspect of these structures is that there is a zone where layers are tilted relative to the layers below and above that have the same orientation (red).

Of 448 samples, from 1375 m to 2120 m depth, we find 121 samples (fig. 5.6) that clearly show a change of layer tilt within one sample (like in fig. 5.5). In another 94 cases, the change of tilt is either not as sudden or not as clear (smaller tilt angle change).

We find that these 121 samples with changing layer tilt have a preferred viewing direction δ (fig. 5.6). Analysis of figure 5.6
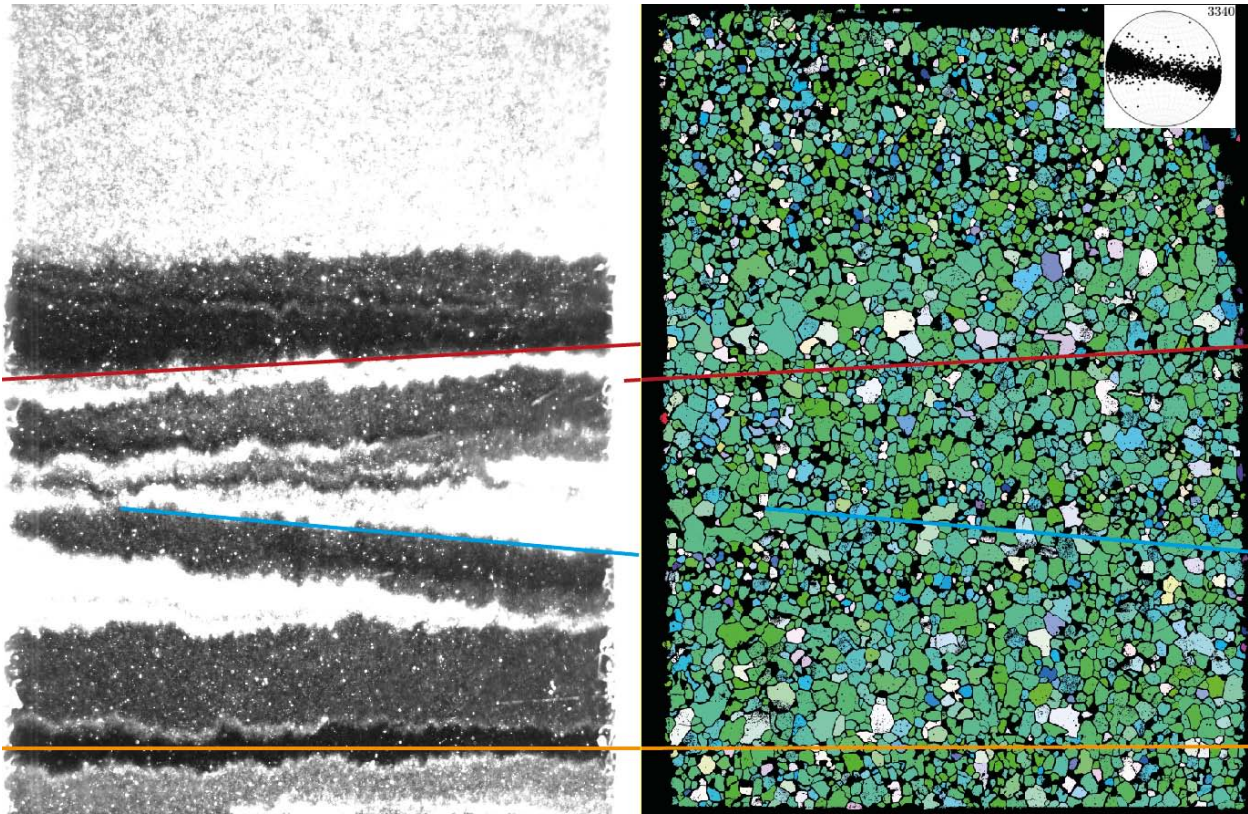
Figure 5.7: Close up of the upper edge of the purple box in fig. 5.5. Visual stratigraphy (left) and grain orientation or fabric (right) around the area of a sudden change of tilt. Crystal orientation of the sample in the stereo projection (top right). Tilt of layers follow the same trend in both images.

suggests, that the majority of layers that show a sudden change of layer tilt become visible around $\pm 30°$ of ice flow direction. Within $\pm 30°$ of ice flow direction, i.e. between 355° to 055° and 185° to 245°, we find 92 samples, of 149 in total, that show a change of layer tilt, corresponding to more than 60% (fig. 5.6).

Figure 5.7 is a zoomed-in section of the upper part of the sudden change of tilt shown in fig. 5.5(purple box). Line scan and fabric images (fig. 5.7, left and right, respectively) are aligned via the bag and depth registration. Dark line scan layers, with few solid impurities correspond to layers with larger grain size and vice versa. Thus, line scan and fabric images can be aligned very well. The limitation is that different surfaces of the ice core are imaged for the different methods and a gap of at least one millimeter lays between the line scan and the fabric image (fig. 5.7, left and right, respectively).

The fabric pattern of the sample is a girdle with a maximum in the horizontal (fig. 5.7, top right). A girdle resembles a pattern, where all c-axes of ice crystals lay on a line (in 2D) or a circle (3D), and the preferred easy-glide direction is 90° to either side of the circle. Westhoff et al. (2020) find a viewing direction (δ) of 043° degree for this sample. This corresponds to looking upstream into the ice stream on an image cut perpendicular to ice flow direction.

5.4 Discussion

The observed and described structures throughout this work, cannot be remnants of surface features, as thinning has reduced the layer thickness to 10% of its initial thickness (Gerber et al., 2021). To reproduce the assumed initial shape of the layers, one would need to stretch the images in fig. 5.4 by a factor of 10 in the vertical. This would create slopes unfeasible for the ice sheet's surface. Thus, the structures described in the following must be the result of deformation. Waddington et al. (2001) describes this effect in more detail.

5.4.1 Small-scale Duplex Structures

Duplex structures are well-known in structural geology from large-scale mountain-building processes and smaller, outcrop-scale compressional settings (Fossen, 2010). The Crow's Nest Pass in the Canadian Rocky Mountains is a textbook example of such a structure (fig. 5.8a,b, McClay and Insley, 1986). Hereby compressional stress imbricates a former well-bedded layer with a number of lenses, or horses, which are commonly bounded by a fault or shear zone on both sides.

The Crow's Nest Pass duplex consists of many small horses, that make a progressively bigger angle with the roof- and floor-fault from left to right (fig. 5.8c, McClay and Insley, 1986). This means that the youngest horses are at the leading end in the front (left). The oldest horses on the right have been steepened by riding piggyback on the younger horses on the left. Experiments to visualize this effect have been performed by Mulugeta and Koyi (1987).

Duplex structures are known to form in well-bedded rocks, where thrusts follow bedding planes (flats) and occasionally cut trough layers (ramps). Limestone beds separated by thin marly layers (Crows Nest) for a composite anisotropy (layer-dependent mechanical properties, fig. 5.8a,b) and it is expected that an intrinsic anisotropy (such as a strong crystal preferred orientation, CPO, in ice, fig. 5.8g,h) can cause similar structures (see Griera et al., 2013 for a discussion on composite and intrinsic anisotropy).

The sequential development of piggyback horses in fig. 5.8d, shows the over steepening of the older horses, with proceeding deformation in thrusts (Butler, 1982). Layers parallel to initial layering (flats) are connected by ramps, which cut off arbitrary surfaces (Butler, 1982). These ramps can either be a footwall ramp or a hangingwall ramp (fig. 5.8e). The layers on the left and right side of fig. 5.8e are in stratigraphic order, while the ones in the middle duplicate at some point. A stack of thrusts is then referred to as a duplex structure (fig. 5.8f).

On the outcrop scale, the duplex structure is easy to see (fig. 5.8a), but if we were to drill a narrow core perpendicular to the layering, the occurrence of a duplex in our core would be rare. This narrow drill core is what we have from EastGRIP (fig. 5.8g,h). Despite the limited core diameter of only 10 cm, we find a number of duplex structures throughout the 800 meters of the analyzed ice core. The duplex described in fig. 5.8g,h is most likely a hinterland-dipping duplex, where the oldest horses piggyback ride the younger ones.

Duplex structures require a compressional stress regime. This compressional setting can be found at the EastGRIP site, perpendicular to ice flow direction (Hvidberg et al., 2020; Westhoff et al., 2020). The structures visible in an ice-sample (fig. 5.8g) have strong similarities to duplex structures, including footwall ramps, cutting off the inital layering, horses with different inclinations, and hangingwall ramps. These flats and ramps (red in fig. 5.8h) resemble thin layers of enhanced deformation, and could thus be small shear zones. The similarities of known structures (fig. 5.8a to f) to those found in ice (fig. 5.8g,h) make duplex structures a feasible explanation. The crenulation folds (short upright folds) found by
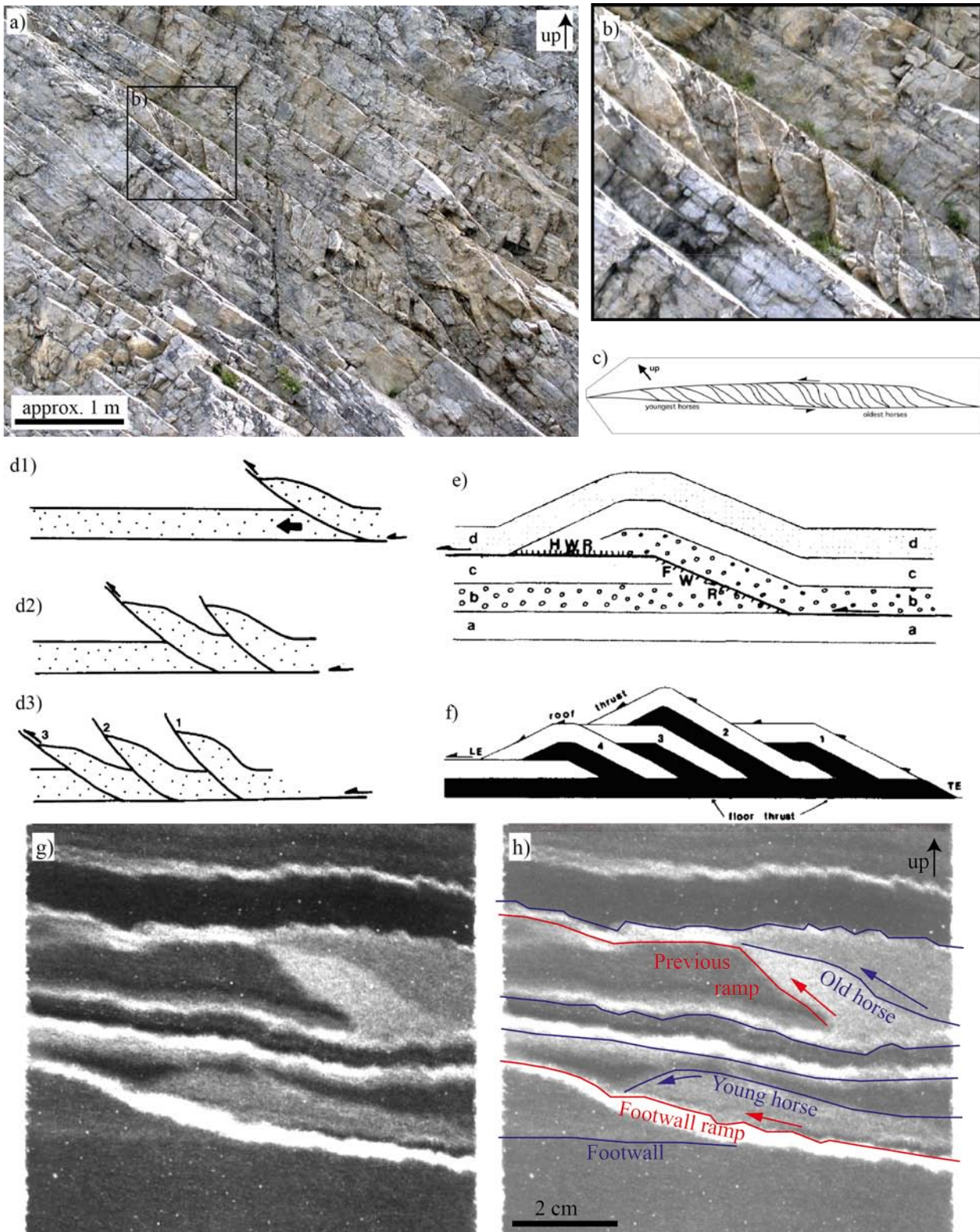
Figure 5.8: a,b) Duplex structure in a limestone outcrop from Crow's Nest Pass in the Canadian Rocky Mountains (picture credits: Paul Bons). c) Outline of the structures from (a). d) Development of a piggyback thrust sequence in time (d1 to d3), with propagation direction (black arrow) and order of development (1 to 3, in d3). e) Relationship of frontal hanging wall ramp (HWR) and footwall ramp (FWR), including layers from a to d. f) Cross section through a duplex parallel to the transport direction. Trailing edge (TE) and leading edge (LE), and horses labeled in order of development (d,e,f from Butler, 1982). g,h) Line scan image from 1651.65 m depth (bag 3004, $\delta = 030°$). Duplex structure within a ten-by-ten-centimeter image of ice.

Westhoff et al. (2020), or fig. 5.3c) are also the result of compression and are found in images samples with the same orientation as those containing duplex structures. These crenulations are also clearly visible in the thin layers in fig. 5.8g.

5.4.2 Duplex Structures Throughout the Ice Core

The footwall ramp extending across the image (fig. 5.8h) suggests that duplex structures are also visible on the larger scale, exceeding the core diameter. We use the sudden change of layer tilt as an indication for these duplex structures exceeding the core diameter. We thus assume, that a sudden change of layer tilt, as seen in fig. 5.5, is a duplex structure. In 60% of all line scan samples viewed perpendicular into ice flow direction, we see a sudden change of layer tilt (see results). Duplex structures are therefore a rather common feature in NEGIS.

The thin shear zones above and below a set of horses (fig. 5.8d) probably extend well beyond the visible deformation structure. Shear zones parallel to cloudy bands, i.e. the layering, will not become visible. Also, the lateral shift of layers does not become visible using other methods, such as $\delta^{18}O$ or other climatic reconstructions, as the stratigraphic order is not disturbed vertically, but only shifted horizontally.

5.4.3 Deformation Structures can be Hard to See...
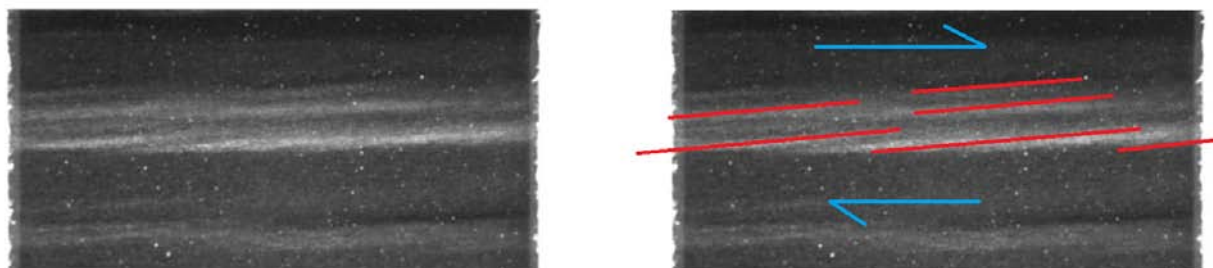
Figure 5.9: An apparently undisturbed layer from 1587 m depth (bag 2885) viewed almost parallel to the ice flow direction ($\delta = 156$). Sense of shear is indicated in blue and potential shear bands in red.

Structural disturbances in ice cores can be hard to see. At first sight, fig. 5.9a seems like a perfectly flat cloudy band. With more careful observation, we find the layer to be disturbed. The selected layer is from a depth of 1587 m (bag 2885) and has an orientation of $\delta = 156$. This means the section is cut almost parallel to the ice flow direction, which is roughly represented by the upper blue arrow (fig. 5.9b). The bright sections in the layer (red lines) could thus be shear bands of a yet undiscovered additional deformation mechanism in the NEGIS.

Bibliography - Deformation Structures

Alley, R. B., Gow, A. J., Meese, D. A., Fitzpatrick, J. J., and Waddington, E. D. (1997). "Grain-scale processes, folding, and stratigraphic". In: *Journal of Geophysical Research* 102.C12, pp. 26819–26830.

Bons, P. D., Kleiner, T., Llorens, M. G., Prior, D. J., Sachau, T., Weikusat, I., and Jansen, D. (2018). "Greenland Ice Sheet: Higher Nonlinearity of Ice Flow Significantly Reduces Estimated Basal Motion". In: *Geophysical Research Letters* 45.13, pp. 6542–6548. DOI: 10.1029/2018GL078356.

Butler, R. W. (1982). "The terminology of structures in thrust belts". In: *Journal of Structural Geology* 4.3, pp. 239–245. DOI: 10.1016/0191-8141(82)90011-6.

Dansgaard, W. and Johnsen, S. J. (1969). "A Flow model and a time scale for the ice core from camp century , Greenland". In: *Journal of Glaciology* 8.53, pp. 215–223.

Faria, S. H., Freitag, J., and Kipfstuhl, S. (2010). "Polar ice structure and the integrity of ice-core paleoclimate records". In: *Quaternary Science Reviews* 29.1-2, pp. 338–351. DOI: 10.1016/j.quascirev.2009.10.016.

Faria, S. H., Weikusat, I., and Azuma, N. (2014). "The microstructure of polar ice. Part II: State of the art". In: *Journal of Structural Geology* 61, pp. 21–49. DOI: 10.1016/j.jsg.2013.11.003.

Faria, S. H., Kipfstuhl, S., and Lambrecht, A. (2018). *The EPICA-DML Deep Ice Core.* Berlin: Springer-Verlag GmbH Germany.

Fossen, H. (2010). *Structural Geology*, p. 463. arXiv: arXiv:1011.1669v3.

Fudge, T. J., Taylor, K. C., Waddington, E. D., Fitzpatrick, J. J., and Conway, H. (2016). "Electrical stratigraphy of the WAIS Divide ice core: Identification of centimeter-scale irregular layering". In: *Journal of Geophysical Research: Earth Surface RESEARCH* 121, pp. 1218–1229. DOI: 10.1002/2013JF002871.Received.

Gerber, T. A., Hvidberg, C. S., Rasmussen, S. O., Franke, S., Sinnl, G., Grinsted, A., Jansen, D., and Dahl-jensen, D. (2021). "Upstream flow effects revealed in the EastGRIP ice core using a Monte Carlo inversion of a two-dimensional ice-flow model". In: *The Cryosphere* February.

Griera, A., Llorens, M. G., Gomez-Rivas, E., Bons, P. D., Jessell, M. W., Evans, L. A., and Lebensohn, R. (2013). "Numerical modelling of porphyroclast and porphyroblast rotation in anisotropic rocks". In: *Tectonophysics* 587, pp. 4–29. DOI: 10.1016/j.tecto.2012.10.008.

Hammer, C. U., Clausen, H. B., Dansgaard, W., Gundestrup, N. S., Johnsen, S. J., and Reeh, N. (1978). "Dating of greenland ice cores by flow models, isotopes, volcanic debris, and continental dust". In: *Journal of Glaciology* 20.82, pp. 3–26.

Hvidberg, C. S., Grinsted, A., Dahl-Jensen, D., Khan, S. A., Kusk, A., Andersen, J. K., Neckel, N., Solgaard, A., Karlsson, N. B., Kjar, H. A., and Vallelonga, P. (2020). "Surface velocity of the Northeast Greenland Ice Stream (NEGIS): Assessment of interior velocities derived from satellite data by GPS". In: *Cryosphere* 14.10, pp. 3487–3502. DOI: 10.5194/tc-14-3487-2020.

Jansen, D., Llorens, M. G., Westhoff, J., Steinbach, F., Kipfstuhl, S., Bons, P. D., Griera, A., and Weikusat, I. (2016). "Small-scale disturbances in the stratigraphy of the NEEM ice core: Observations and numerical model simulations". In: *Cryosphere* 10.1, pp. 359–370. DOI: 10.5194/tc-10-359-2016.

Joughin, I., Smith, B. E., Howat, I. M., Scambos, T., and Moon, T. (2010). "Greenland flow variability from ice-sheet-wide velocity mapping". In: *Journal of Glaciology* 56.197, pp. 415–430. DOI: 10.3189/002214310792447734.

Kamb, B. (1972). "Experimental recrystallization of ice under stress". In: *Washington DC American Geophysical Union Geophysical Monograph Series* 16, pp. 211–241.

Llorens, M. G., Griera, A., Steinbach, F., Bons, P. D., Gomez-Rivas, E., Jansen, D., Roessiger, J., Lebensohn, R. A., and Weikusat, I. (2017). "Dynamic recrystallization during deformation of polycrystalline ice: Insights from numerical simulations". In: *Philosophical Transactions of the Royal Society A: Mathematical, Physical and Engineering Sciences* 375.2086. DOI: 10.1098/rsta.2015.0346.

McClay, K. R. and Insley, M. W. (1986). "Duplex structures in the lewis thrust sheet, crowsnest pass, rocky mountains, Alberta, Canada". In: *Journal of Structural Geology* 8.8, pp. 911–922. DOI: 10.1016/0191-8141(86)90036-2.

Mojtabavi, S., Wilhelms, F., Cook, E., Davies, S., Sinnl, G., Skov Jensen, M., Dahl-Jensen, D., Svensson, A., Vinther, B., Kipfstuhl, S., Jones, G., Karlsson, N., Faria, S. H., Gkinis,

V., Kjær, H., Erhardt, T., Berben, S., Nisancioglu, K., Koldtoft, I., and Rasmussen, S. O. (2020). "A first chronology for the East GReenland Ice-core Project (EGRIP) over the Holocene and last glacial termination". In: *Climate of the Past Discussions* 16.December, pp. 2359–2380. DOI: 10.5194/cp-16-2359-2020.

Montagnat, M., Azuma, N., Dahl-Jensen, D., Eichler, J., Fujita, S., Gillet-Chaulet, F., Kipfstuhl, S., Samyn, D., Svensson, A., and Weikusat, I. (2014). "Fabric along the NEEM ice core, Greenland, and its comparison with GRIP and NGRIP ice cores". In: *Cryosphere* 8.4, pp. 1129–1138. DOI: 10.5194/tc-8-1129-2014.

Mulugeta, G. and Koyi, H. (1987). "Three-dimensional geometry and kinematics of experimental piggyback thrusting". In: *Geology* 15.11, pp. 1052–1056. DOI: 10.1130/0091-7613(1987)15<1052:TGAKOE>2.0.CO;2.

Steinbach, F., Bons, P. D., Griera, A., Jansen, D., Llorens, M. G., Roessiger, J., and Weikusat, I. (2016). "Strain localization and dynamic recrystallization in the ice-air aggregate: A numerical study". In: *Cryosphere* 10.6, pp. 3071–3089. DOI: 10.5194/tc-10-3071-2016.

Svensson, A., Nielsen, S. W., Kipfstuhl, S., Johnsen, S. J., Steffensen, J. P., Bigler, M., Ruth, U., and Röthlisberger, R. (2005). "Visual stratigraphy of the North Greenland Ice Core Project (NorthGRIP) ice core during the last glacial period". In: *Journal of Geophysical Research: Atmospheres* 110.2, pp. 1–11. DOI: 10.1029/2004JD005134.

Thorsteinsson, T., Kipfstuhl, J., and Miller, H. (1997). "Textures and fabrics in the GRIP ice core". In: *Journal of Geophysical Research* 102.C12, pp. 26583–26599. DOI: 10.1029/97JC00161.

Waddington, E. D., Bolzan, J. F., and Alley, R. B. (2001). "Potential for stratigraphic folding near ice-sheet centers". In: *Journal of Glaciology* 47.159, pp. 639–648. DOI: 10.3189/172756501781831756.

Wang, Y., Thorsteinsson, T., Kipfstuhl, J., Miller, H., Dahl-Jensen, D., and Shoji, H. (2002). "A vertical girdle fabric in the NorthGRIP deep ice core, North Greenland". In: *Annals of Glaciology* 35, pp. 515–520. DOI: 10.3189/172756402781817301.

Weikusat, I., Jansen, D., Binder, T., Eichler, J., Faria, S. H., Wilhelms, F., Kipfstuhl, S., Sheldon, S., Miller, H., Dahl-Jensen, D., and Kleiner, T. (2017). "Physical analysis of an Antarctic ice core-towards an integration of micro-and macrodynamics of polar ice". In: *Philosophical Transactions of the Royal Society A: Mathematical, Physical and Engineering Sciences* 375.2086. DOI: 10.1098/rsta.2015.0347.

Westhoff, J., Sinnl, G., Svensson, A., Freitag, J., Kjær, H. A., Vallelonga, P., Vinther, B., Kipfstuhl, S., Dahl-jensen, D., and Weikusat, I. (2021). "Melt in the Greenland EastGRIP ice core reveals Holocene warming events". In: *Climate of the Past Discu* July, pp. 1–36. DOI: 10.5194/cp-2021-89.

Westhoff, J., Stoll, N., Franke, S., Weikusat, I., Bons, P., Kerch, J., Jansen, D., Kipfstuhl, S., and Dahl-Jensen, D. (2020). "A Stratigraphy Based Method for Reconstructing Ice Core Orientation". In: *Annals of Glaciology* 62.85-86, pp. 191–202. DOI: 10.1017/aog.2020.76.

Winstrup, M., Svensson, A. M., Rasmussen, S. O., Winther, O., Steig, E. J., and Axelrod, A. E. (2012). "An automated approach for annual layer counting in ice cores". In: *Climate of the Past* 8.6, pp. 1881–1895. DOI: 10.5194/cp-8-1881-2012.

Chapter 6

Melt in the Greenland EastGRIP Ice Core Reveals Holocene Warm Events

Julien WESTHOFF[1], Giulia SINNL[1], Anders SVENSSON[1], Johannes FREITAG[2], Helle Astrid KJÆR[1], Paul VALLELONGA[1], Bo VINTHER[1], Sepp KIPFHSTUHL[2], Dorthe DAHL-JENSEN[1,3], and Ilka WEIKUSAT[2,4]

[1]*Niels Bohr Institute, University of Copenhagen, Copenhagen, Denmark*
[2]*Alfred Wegener Institute, Helmholtz Centre for Polar and Marine Research, Bremerhaven, Germany*
[3]*Centre for Earth Observation Science, University of Manitoba, Canada*
[4]*Department of Geosciences, Eberhard Karls University Tübingen, Germany*

Abstract We present a record of melt events obtained from the EastGRIP ice core, in central north eastern Greenland, covering the largest part of the Holocene. The data were acquired visually using an optical dark-field line scanner. We detect and describe bubble-free layers and -lenses throughout the ice above the bubble-clathrate transition, located at 1150 m in the EastGRIP ice core, corresponding to an age of 9720 years b2k. We define the brittle zone in the EastGRIP ice core from 650 m to 950 m depth, where we count on average more than three core breaks per meter. We analyze melt layer thicknesses, correct for ice thinning, and we account for missing layers due to core breaks. Our record of melt events shows a large, distinct peak around 1014 years b2k (986 CE) and a broad peak around 7000 years b2k corresponding to the Holocene Climatic Optimum. In total we can identify approximately 831 mm of melt (corrected for thinning) over the past 10,000 years. Our climatic interpretation matches well with the Little Ice Age, the Medieval and Roman Warm Periods, the Holocene Climatic Optimum, and the 8.2 kyr event. We also compare the most recent 2500 years to a tree ring composite and find an overlap between melt events and tree ring anomalies indicating warm summers. We open the discussion for sloping bubble-free layers (tilt angle off horizontal > 10°) being the effect of rheology and not climate. We also discuss our melt layers in connection to a coffee experiment (coffee as a colored substitute for melt infiltration into the snow pack) and the real time observations of the 2012 CE rain event at NEEM. We find that the melt event from 986 CE is most likely a large rain event, similar to 2012 CE, and that these two events are unprecedented throughout the Holocene. Furthermore, we observe that the summer of 986 CE, which hosts an exceptional warm event in Greenland, coincides with the Viking settlement voyage from Iceland to Greenland.

6.1   Introduction

6.1.1   Greenland Melt Layer Records

Melt layers provide a robust record of warm summer days on the Greenland ice sheet, i.e. days the surface temperature exceeded the melting point and/or that insolation was very high (Langway and Shoji, 1990). A 10,000 year melt layer record from a Greenlandic ice core was presented by Alley and Anandakrishnan (1995) on the Greenland Ice Sheet Project 2 (GISP2) ice core, who applied visual inspection during ice core processing. Herron et al. (1981) also use visual inspection on the DYE3 ice core from southern Greenland, to create a 2200 year melt record. Similar visual methods, in addition to density measurements, were used by Freitag et al. (2014 EGU poster) on two shallow cores around DYE3 and South Dome in Greenland. Shorter records have been established at other southern Greenland sites, such as site A (70,8 °N, 36,0 °W, 3145 m, Alley and Koci, 1988) or site J (66°51.9'N, 46°15.9'W, 2030 m, Kameda et al., 1995).

A range of techniques have been applied to investigate melt layers in ice cores from Greenland and other locations: Keegan et al. (2014) compared multiple shallow cores across the dry zone in Greenland and show a spatial variability of melt layers, with only the warm summer event from 1889 CE being visible in all cores (cores were drilled before 2012 CE). Studies of melt features in the ablation zone of the Greenland ice sheet have been conducted using multiple shallow ice cores (e.g. Graeter et al., 2018), or snow pits (e.g. Humphrey et al., 2012). Combined computer tomography (CT, Schaller et al., 2016) and visual analysis using line scan images (see methods section) for melt layer detection was applied on the Renland Ice Cap (RECAP) ice core, coastal eastern Greenland, by Taranczewski et al. (2019), combining one deep and two shallow cores. Melt layer records have been established for many glaciated sites around the world, e.g. in Canada (Koerner and Fisher, 1990; Fisher et al., 1995; Fisher et al., 2012), Alaska (Winski et al., 2018), and Arctic Russia (Fritzsche et al., 2005).

There are several methods to detect melt layers in ice. They can be detected using noble gases (NEEMCommunityMembers, 2013; Orsi et al., 2015), irregularities in the Electronic Conductivity Measurements (ECM, pers. comm. Sune Rasmussen), or by identifying anomalies in stable water isotope records (Valerie Morris, in prep.). More recent melt events can be detected using satellite images: as an example Steen-Larsen et al. (2011) describe six recent melt events at the North Greenland Eemian Ice Drilling (NEEM) site. Combining satellite and ice core data to create a melt archive is done in several studies such as Mote (2007), Keegan et al. (2014), or Trusel et al. (2018). Melt layers, i.e. bubble-free layers, can easily be confused with wind crusts (see method section), that are studied by Fegyveresi et al. (2018) and Weinhart et al. (2021).

The 2012 CE melt and rain event in Greenland is very well observed and documented, e.g. Nghiem et al. (2012), Tedesco et al. (2013), Nilsson et al. (2015), or Bonne et al. (2015). Bonne et al. (2015) provide a detailed study on the atmospheric conditions leading to the rain event, in combination with field observations, e.g. from Steen-Larsen et al. (2011). Nilsson et al. (2015) present a detailed study on the 2012 melt event using CryoSat-2 radar altimetry. Observations at the NEEM drill site show, that the surface temperature exceeded the melting point over five days, and that melt layers formed at approximately 5, 20, and 69 cm depth (Nghiem et al., 2012). Using the words of Trusel et al. (2018): "For the most recent 350 years in Greenland ice core, 2012 melt is unambiguously the strongest melt season on record."
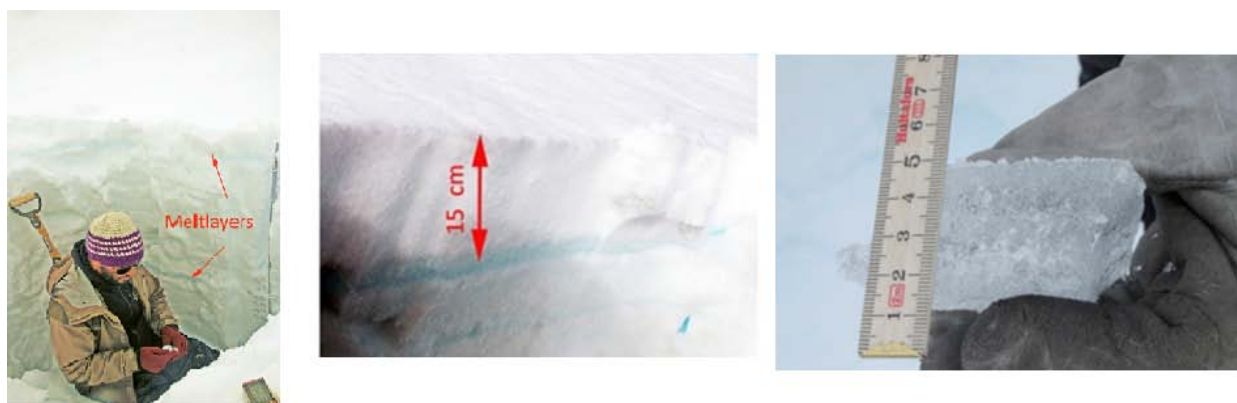
Figure 6.1: a) View into the snowpit dug just after the 2012-rain/melt event at NEEM. The resulting melt layers occur in depths of around 15 and 70 cm below surface. b) close up on the upper melt layer and c) the 3.5 centimeter thick layer.

6.1.2 What are Melt Layers?

Melt layers are commonly thought of as events with surface melt due to intense solar radiation and/or high temperature leading to the formation of superficial liquid melt puddles followed by their percolation into the snowpack (e.g. Shoji and Langway, 1987; Humphrey et al., 2012). Occurring less frequently, rain events over an ice sheet can lead to the same type of features, which was e.g. observed at NEEM in 2012 CE (fig. 6.1).

Polar ice sheets are colder under clear-sky conditions, as snow absorbs and radiates effectively in the longwave but reflects in the shortwave. Eye witnesses from NEEM, DYE3, and South Dome in Greenland verify that thick clouds brought in the high air temperatures leading to the 2012 CE warm event across Greenland.

For recent melt events, it has been shown that these are spatially highly variable and only a widspread melt event from 1889 CE can be found in almost all shallow ice cores across Greenland (Keegan et al., 2014). Melt, or bubble-free, layer records for the past 10,000 years have only been identified for the GISP2 (Alley and Anandakrishnan, 1995) and the RECAP (Taranczewski et al., 2019) ice cores. In deep ice cores, such as GISP2, bubbles transform to clathrates and become difficult to detect visually (Kipfstuhl et al., 2001). Methods to detect melt layers from clathrate distributions have not succeeded yet. In the RECAP ice core, the Holocene ice covers 533 of a total core length of 584 meters (Simonsen et al., 2019). Here the stratigraphy of the deepest layers of the Holocene (Early Holocene) are thinned too much to detect single melt layers. Therefore, all analysis to date are limited to the past 10,000 years, with the exception of NEEMCommunityMembers (2013) and Orsi et al. (2015), who investigated noble gas (isotopes) on selected samples of the NEEM ice core.

The features in the snowpack resulting from a melt event can be distinguished into: melt layers, melt lenses (Das and Alley, 2005), and melt pipes (Pfeffer and Humphrey, 1998). Layers and lenses are horizontal structures with different lateral extensions and melt pipes are vertical pathways formed by the melt water (more details in the methods section). It is also possible for water to refreeze homogeneously, in the absence of a low-permeability layer. These refrozen sections will not appear as a single layer, and remain unseen in our analysis. In the next section, we present a simple experiment to reconstruct melt features in the snowpack.
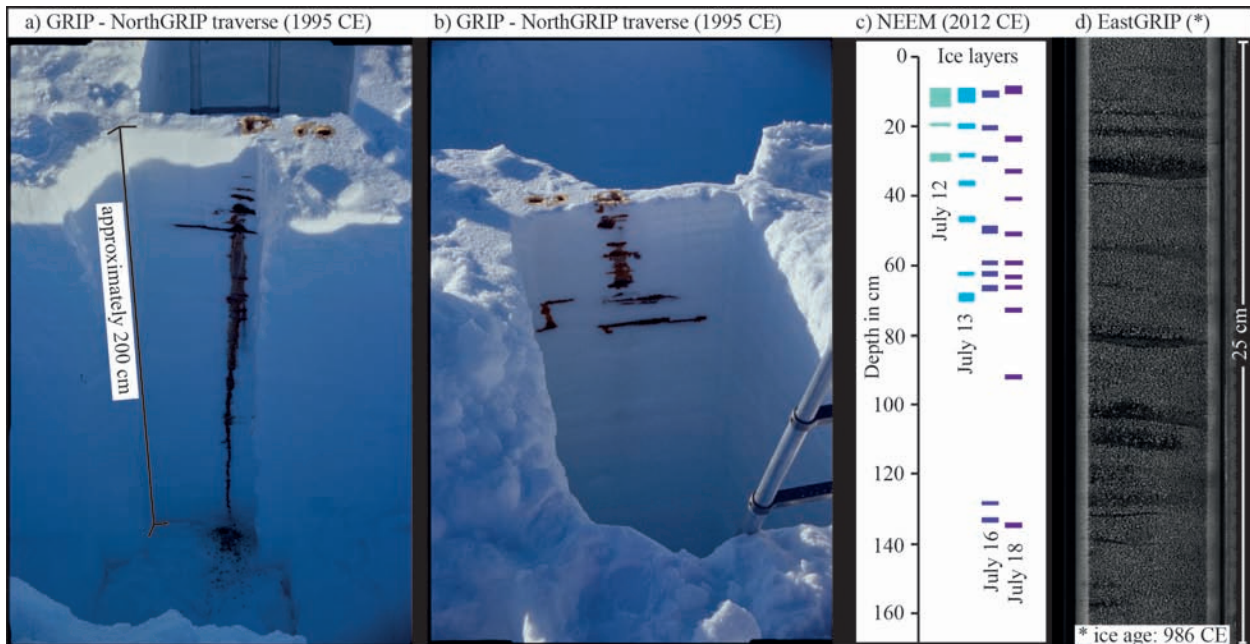
6.1.3   The Coffee Experiment

Figure 6.2: a,b) Two sides of the same double trench, with three coffee injection points visible on the surface of the trench wall. Vertical coffee-pipes are not always visible, but the horizontal coffee layers and lenses are very pronounced. The long vertical pipe reaching the bottom in a) is due to the ex-filtration of coffee from the trench wall. The trench's depth is approximately two meters. c) Appearance of ice layers in different depths during the warm event 2012 at NEEM. Measurements were made by extending the same snow pit, which was revisited over the days of the warm event. d) Upper half of line scan of bag 252 (top at 138.05 m depth, years 986 to 989 CE) with multiple melt lenses and layers.

We present the result from a simple rain-melt-event-experiment performed in April 1995, on a traverse from the Greenland Ice Core Project (GRIP) site to the Northern Greenland Ice Core Project (NorthGRIP) site in Greenland (fig. 6.2a,b). A double trench was dug, leaving an approximately 30 cm thick wall between the two trenches. This is commonly done to visualize different structures in the snowpack (e.g. Fegyveresi et al., 2018). Three shots of cold coffee were poured at the top of the trench wall simulating a melt event. The coffee percolates through the snowpack, leaving a brown trace representing melt layers, -lenses and -pipes. A more sophisticated version of this experiment was performed a decade later, between 2007 and 2009, by Humphrey et al. (2012) in western Greenland.

Vertical melt pipes remain mostly invisible, but the horizontal expansion of the coffee into layers and lenses is very pronounced. It is worth noting that this represents one event, which creates multiple layers in the snowpack. Furthermore, these melt layers are not at the surface, but penetrate 40 cm deep. It is also easily visible, that melt layers from the same event (coffee injection) can appear very differently, despite the fact they are only 30 cm apart, i.e. on either side of the trench wall (compare fig. 6.2a,b). Having multiple melt layers and lenses in such close vertical proximity thus indicates a rain event on the ice sheet.

A limitation to this experiment, is that we are not able to reconstruct the lateral extension of the coffee layers. Due to the thin wall between the pits the coffee left the wall and cannot extend in the vertical. The vertical percolation is also limited by the thin walls, as vertical pathways must be found within this wall. Within the unconfined snow pack, the vertical percolation could thus reach greater depths.

6.1.4 Real-time Observations of the 2012 Melt Event

While ice core studies on melt events show the finished picture of melt layers, lenses, and pipes (see methods) in the snowpack, the 2012 melt event at NEEM offered a unique chance to observe the creation of these structures in real-time. The warm event in 2012 lasted from July 12th to 15th, with varying temperatures around 0°C (Bonne et al., 2015). During these days, snowpits reveal the appearance of ice layers at different depths over time (fig. 6.2c). Depth is relative to the snow surface and due to the warming of the snowpack, the whole surface level lowered about 10 to 15 cm over the course of the warm event. This explains the apparent "rise" of the uppermost ice level over time - the surface was actually lowering. To acquire undisturbed data, the trench was widened by approximately 0.5 m every measurement day. This widening slightly changes the depth registration of each ice layer. This shows the high spatial variability of ice- or melt layers in the snowpack.

By July 12, a substantial warming of the surface snowpack was observed, with the top 12 cm of snowpack close to melting point (-0.2°C) and the development of more ice or refrozen melt layers at depths 22 and 32 cm. The surface snowpack had warmed considerably by July 13, with further thickening of melt layers and the development of a 3.5 cm-thick melt layer at 70 cm depth (fig. 6.1c). Local rain contributed to this rapid warming of the top 65 cm of snowpack to near-melting temperatures. Somewhat cooler conditions on July 14 saw some cooling of the lower part of the snowpack. July 15 was the last day of warming observed in the snowpack, with the uppermost 80 cm of snowpack near melting point, warming of deeper snow down to 1.5 m depth, and the deeper percolation of melt water to 1.5 m depth. Observations of July 16 indicate a cooling of the snowpack from both above and below, with complete refreezing of the surface snow by July 18.

Experimental simulations of melt events have been performed by (Das and Alley, 2005; Humphrey et al., 2012), but in-situ observations have only been conducted at NEEM (e.g. Bonne et al., 2015) and Summit in 2012 (e.g. Bennartz et al., 2013). Older melt events can be found in ice cores using visual methods (fig. 6.2d), such as the line scanner (see methods section).

6.1.5 Integrity of Our (and Other) Melt Layer Records

"How likely is it to miss an event?" This question can be addressed in two ways: either by missing an event in our analysis or because the refrozen melt water is not in the 10 cm section of the ice core. If a melt lens is behind bubbles it becomes hard to see in our 2D images, and will probably be classified as uncertain, or missed completely (fig. 6.13). The prominent and big events will not be missed with our analysis as they are very obvious in line scan images. To further reduce the likeliness of missing events, our analysis was done twice, minimizing operator errors.

On the other hand, we miss bubble-free layers in the ice sheet's stratigraphy due to the ice core's restricted diameter. Studies such as Keegan et al. (2014), Schaller (2018), Fegyveresi et al. (2018), Taranczewski et al. (2019), or our coffee experiment (fig. 6.2) show the high spatial variability of melt lenses in trenches or shallow cores. While the spatial distribution of a melt lens or a layer is not homogeneous over larger areas, our ice core with a diameter of 10 cm is a very narrow sample of the ice column. Keegan et al. (2014) show that that big melt events, such as the 1889 event are visible in most shallow cores and snowpits and thus prove a widespread distribution. For bigger events, we can therefore assume that our analysis is representative of the largest part of Northern Greenland, while smaller events might be restricted to local areas.

Another problem with interpreting melt layers is shown in the snowpit sampling during the 2012 melt event at NEEM (fig. 6.1 and fig. 6.2c). When a melt event creates multiple

melt layers, the uppermost melt layers remain in the snow of that year and the lower ones may percolate into snow from the previous years. This is also true for melt events which only form one layer, yet larger melt events seem to percolate deeper into the snow pack. Pfeffer and Humphrey (1998) perform a very detailed study on melt water infiltration into the snowpack which highlights this effect. Therefore, interpretations of melt events on an annual time scale should be handled with care, and the uppermost layer should be taken as a reference. This effect can be neglected on the decadal and upwards resolution.

6.1.6   Climate of the Holocene and the Drill Site
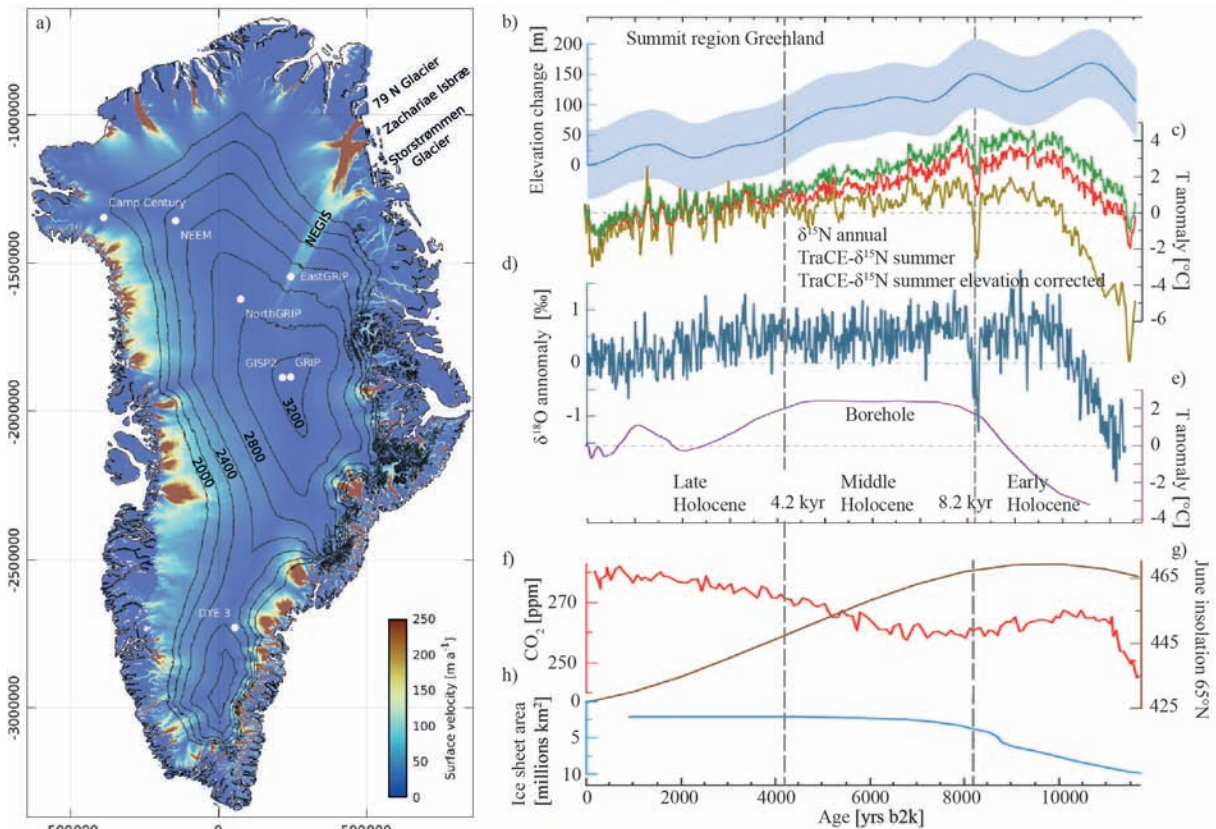
Figure 6.3: a) Overview map of Greenland, including relevant ice core drill sites and surface velocities from Gerber et al. (2021). b) to h) Modified from Axford et al. (2021, fig. 2 and 3e). The vertical dashed lines mark the boundary between Early and Middle, and Middle and Late Holocene at 8.2 kyr and 4.2 kyr, respectively. All proxies are shown as anomalies relative to the 1930–1970. b) Estimated surface elevation change at Summit (dark blue, Vinther et al., 2009) and uncertainty (faded blue shading, Lecavalier et al., 2013), c) annual $\delta15N$ (dark yellow) and summer (red) and elevation-corrected summer (green) Summit temperature anomalies from TraCE-$\delta15N$ (Buizert et al., 2018), d) GRIP oxygen isotopes (Rasmussen et al., 2006; Vinther et al., 2006), and e) GRIP borehole temperature reconstruction (Dahl-Jensen et al., 1998). f) Climate forcings and influences including June insolation (Berger and Loutre, 1991), g) atmospheric CO_2 (Monnin et al., 2004), and h) decline of the Laurentide-Innuitian-Cordilleran ice sheet complex (Dalton et al., 2020), y-axis reversed.

Melt layers, such as those resulting from the 2012 CE warm event, can be found in ice cores throughout the Holocene. To analyze and understand these, a climatic overview is necessary: Axford et al. (2021) have put together different records of the Holocene climate in Greenland (fig. 6.3), including the GISP2 melt layer record (Alley and Anandakrishnan, 1995). Their study offers two possible climatic reconstructions: A climatic optimum around the Early Holocene, as shown by pollen, geological records, and $\delta15N$ from ice cores (e.g. fig. 6.3c), or a damped climatic optimum, as shown by the $\delta18O$ from ice cores (fig. 6.3d).

The dampening of these warm temperatures at the end of the Last Glacial Period and the Early Holocene, is due to a larger ice sheet with higher surface elevation (fig. 6.3a,h), and therefore cooler temperatures, from ice core reconstructions, due to a higher lapse rate (e.g. Brunt, 1933; Gardner et al., 2009; Vinther et al., 2009).

The timing and intensity of the Holocene Climatic Optimum is still debated: e.g. Lecavalier et al. (2017) find an early and intense HCO, while e.g. Badgeley et al. (2020) argue for a later HCO. Bova et al. (2021) argue that the warm temperatures at the beginning of the Holocene are a bias caused by proxies mostly affected by warmer summer temperatures (fig. 6.3g), and larger seasonal variations, while the annual mean temperature remained lower and gradually climbed to today's value more or less following atmospheric CO_2 concentrations (fig. 6.3f).

The East Greenland Ice Core Project (EastGRIP) ice core, on which we create our melt layer record, is drilled through the Northeast Greenland Ice Stream (NEGIS, fig. 6.3a). This ice stream flows from the ice divide, between NorthGRIP and the summit area, towards the NNE until it terminates at the coast (Vallelonga et al., 2014). Today's position of the EastGRIP drill site moves with approximately 55 m/yr (Hvidberg et al., 2020), i.e. approximately 15 cm per day.

6.2 Methods

6.2.1 Depth of Interest

Our analysis covers the upper 1090 m of the EastGRIP ice core, corresponding to the years 1965 CE to 7604 BCE, i.e. 9569 years. We use the age scale provided by Mojtabavi et al. (2020), with a maximum counting error of one to two years. We use the time reference "years before the year 2000 CE" (yrs b2k).

The depth notation in this work refers to the depth below the 2017 ice sheet surface, the year in which ice core drilling began. Ice core processing started 13.75 m below the surface, which corresponds to the year 1965 CE (44 yrs b2k, Mojtabavi et al., 2020). Thus, this is the youngest material available for our analysis.

We terminate our investigation of bubble-free layers at a depth of 1090 m, approximately 9604 yr b2k. The most challenging aspect of this depth is the almost complete transition from air bubbles to clathrates (e.g. Shoji and Langway, 1987; Kipfstuhl et al., 2001; Uchida et al., 2014). With bubbles transforming to clathrates under pressure and thus becoming smaller, the spacing between bubbles increases, and bubble-free layers become increasingly difficult to identify. This bubble-clathrate transformation is not a gradual process over depth, but has variable rates for different layers due to their physical properties and the resulting complex crystallization of air hydrates (Weikusat et al., 2015). We use the line scan images to find that the conversion from bubbles to clathrates is fully completed in a depth of 1150 m, but end our analysis 60 m above that depth.

6.2.2 The Line Scanner and its Images

The line scanner is a well-established and powerful tool for high resolution analysis of ice stratigraphy, making use of contrast enhancement by the optical dark-field method (Faria et al., 2018). Different devices with similar setups have been used on many deep ice core since the NorthGRIP drilling in 1995 (Svensson et al., 2005; McGwire et al., 2008; Jansen et al., 2016; Faria et al., 2018; Morcillo et al., 2020; Westhoff et al., 2020). The device used at EastGRIP is the second generation Alfred-Wegener-Institute (AWI) line scanner. Images are obtained with a camera moving along the top of a 165 cm long and 3.6 cm thick ice

core slab. Two light sources illuminate the polished ice core slab at an angle from below (for details consult Svensson et al., 2005; Westhoff et al., 2020).

The appearance of line scan images is substantially different from firn to ice (fig. 6.4 left and right, respectively). In firn and snow, the bright sections of the image represent the solid parts, such as snow crystals or ice layers. Dark sections of the image represent voids, i.e. air. When firn has been compressed to ice, the appearance of features is inverted: ice now appears dark and bubbles, i.e. air, are now represented by bright pixels. This inversion of appearance is caused by firn-grains being non-transparent, thus reflecting light. Ice on the other hand is transparent and allows light to travel through without any reflections, thus a dark field below the ice core slab is imaged. Bubbles appear bright, as their rounded ice-air interface offers perfect conditions for light scattering in all directions.

The firn-ice transition is situated at around 70 m depth (e.g. Buizert et al., 2012), so the largest part of our investigation is conducted on ice with bubbles, where bubble-free layers are easy to identify (e.g. fig. 6.4d).

6.2.3   Types of Events
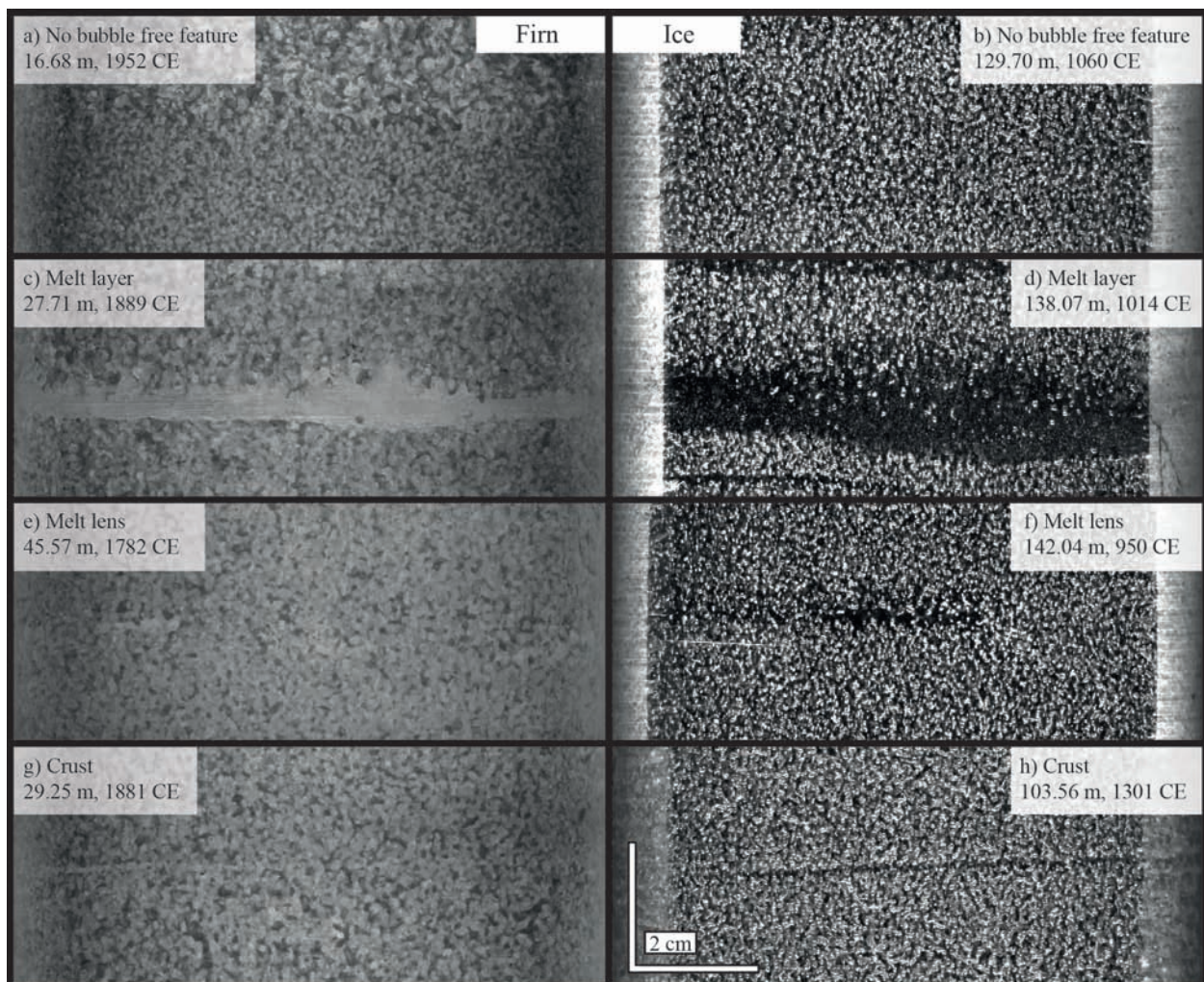
Figure 6.4: The appearance of different structures in line scan images in firn (left) and ice (right). a,b) Typical examples of appearance of firn and ice. c,d) bubble-free layers interpreted as melt layers. These are continuous horizontally across the ice core. e,f) bubble-free lenses interpreted as melt lenses, which are discontinuous patches mostly with a horizontal elongation. g,h) Very thin and straight bubble-free layers with sharp edges. These structures are hard to see in line scan images and are interpreted as crusts, the result of surface hardening by the wind.

In the upper 1100 m of the EastGRIP ice core the majority of the ice contains bubbles, and thus the "normal" appearance of firn and ice (fig. 6.4a,b). Firn and ice can be bubble-free for two reasons: either snow melted and refroze close to the surface, creating a melt layer or lens, or a surface hardening took place e.g. by wind which forms hard (wind-)crusts. On this basis we define three types of bubble-free features: melt layers (fig. 6.4c,d), melt lenses (fig. 6.4e,f), and crusts (fig. 6.4g,h). Within our three categories, we note the certainty of our labeling as either "certain" or "uncertain". We add a fourth category for features that hint to bubble-free layers but are not completely distinguishable, these can be considered "very uncertain".
We define the different types as follows:

- Melt layers are in general continuous features ranging across the entire horizontal core width (10 cm). The melt layer thickness can vary within one layer, but we define, that it should always be greater than one millimeter at its narrowest point ($1\ mm = 18.6\ pixels$). They can have sharp edges (fig. 6.4c bottom left) or smooth edges, where bubbles are within the melt layer (fig. 6.4d top edge).

- Melt lenses have the same appearance as melt layers, yet are of smaller dimensions and not continuous across the width of the core. The definition of layer and lens is therefore determined by the core diameter, which in the EastGRIP ice core is approximately 10 cm. Lenses can have a rounded shape, yet in general, they show an elongation along the horizontal.

- Crusts are very thin bubble-free layers, around one millimeter, and in general continuous from one side of the core to the other. They have a sharp border to the bubbles around them. These thin layers can be identified reasonably well and distinguished from melt layers in the upper 250 m. Yet as thinning of layers proceeds, a distinction is no longer possible. We therefore assume that below 250 m, all layers with the appearance of crusts are actually thinned melt layers. Thinning would be influential to such a degree that crusts are eventually no longer detectable using line scan images.

6.2.4   Core Breaks and the Brittle Zone

Core breaks influence the counting of melt layers and lenses. Core breaks are fractures in the core, mainly occurring for two reasons: either from breaking the ice core free at the bottom of the borehole (see Westhoff et al., 2020), or from fractures in the brittle-zone ice (Neff, 2014).

- The drilling-related core-breaks are usually approximately horizontal. During smooth drilling operations and good ice quality, core breaks occur every few meters, depending on the length of the core barrel chamber which is implemented in the deployed drilling system.

- In the brittle zone, where the internal pressure of the trapped air bubbles is very high and exceeds the tensile strength of the ice core, the ice core samples will break up and sometimes even explode. This is an effect of pressure-temperature relaxation after core recovery at the surface. Core breaks in the brittle zone could have any orientation and thus tend to run diagonally across the core and line scan image.

During line scanning, light is introduced at an angle from below the core slab. As core breaks usually have a rough break-surface, followed by a gap and another rough break-surface, the light intensity will drop when crossing the void. This intensity loss casts shadows
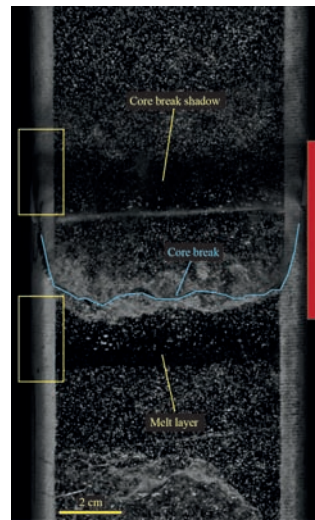
Figure 6.5: A core break casting a shadow and a melt layer have a very similar appearance in the line scan images. A distinction is made first by the proximity to the break, and then by differences of brightness along the ice core's round drilling edge (yellow boxes). Core break shadows darken the edge of a sample. Minimum section not suited for analysis is indicated by red bar.

on either side of the core breaks. These shadows greatly depend on the geometry of the core break and can easily be mistaken for a bubble-free layer. A rare occasion (one of two in total) is fig. 6.5, where a melt layer is very close to a break. The core break is distinguishable from a melt layer, because the core break casts a shadow on the edge of the core slab, while the edge remains at a constant brightness in the presence of a melt layer (yellow boxes in fig. 6.5). Similar to the core break shadows are the saw-cut shadows, which appear at the ends of each 165 cm-long line scan.

To account for this difficulty, features close to core breaks and the edge of the images are in general disregarded. This implies, that the more core breaks we have, the more bubble-free events we may miss and the more we underestimate the number of events. It is, therefore, necessary to obtain an overview of core breaks throughout the depth of interest. We estimate the chance of missing a bubble-free event by assuming a 4 cm-sample loss for each break. In general, a shadow is cast 1.5 cm to either side of the break and the break itself disturbs the image across at least 1 cm, adding up to 4 cm in total (fig. 6.5, red bar).

6.2.5   Northern Hemisphere Tree Rings

Sigl et al. (2015) created a Northern Hemisphere temperature reconstruction using the tree ring composite record (N-Tree), which we compare to melt events. The tree ring record comprises tree ring growth anomalies from five different locations across the Northern Hemisphere, where temperature is the limiting factor to growth. The N-Tree record is presented on its independent annual ring-width timescale (NS1-2011), carrying no uncertainty according to Sigl et al. (2015). The individual records from northern locations in Finland, Sweden, Siberia, Central Europe, and USA almost always overlap, providing a composite average of the tree growth in response to temperature.

For the comparison of melt events to the tree ring data, we translate the EastGRIP (GICC05) ages to the tree ring timescale (NS1-2011). We verified good alignment of East-GRIP and N-Tree data as many volcanic eruptions align to drastic cooling events within one to two years. We refer to ages and events using the GICC05 timescale, for consitency throughout the manuscript.
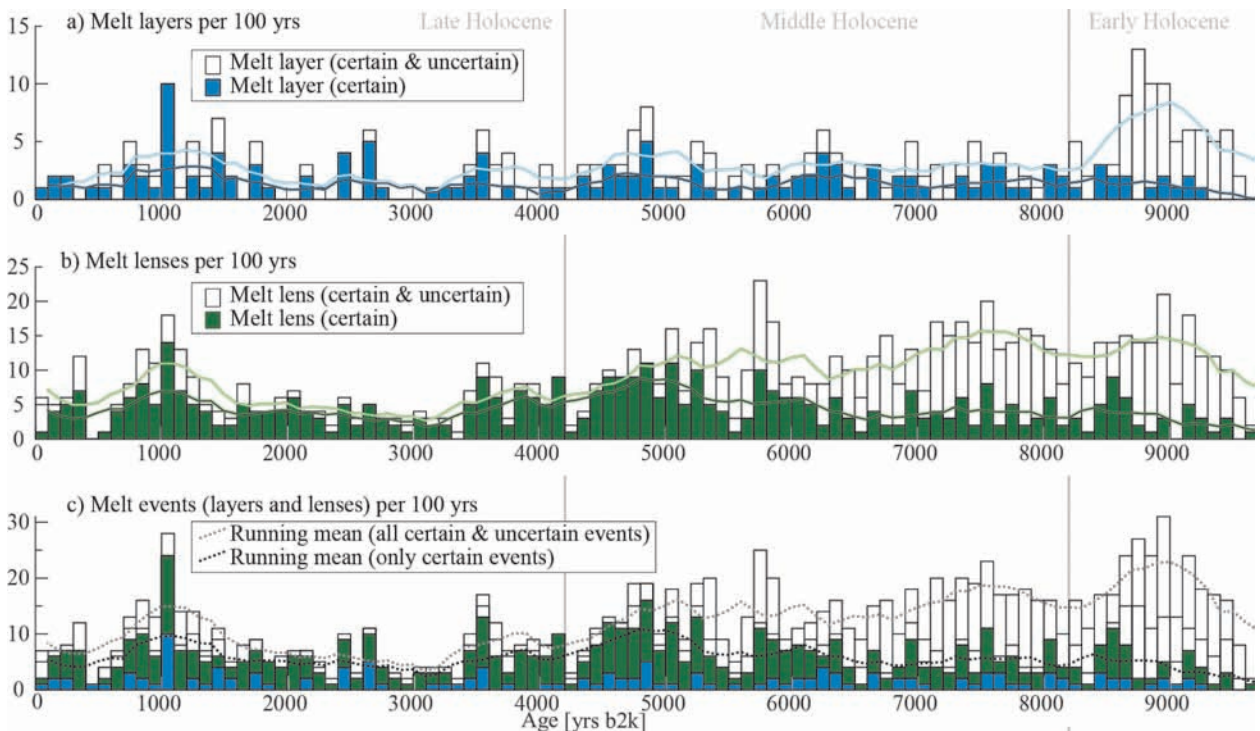
6.3 Results

6.3.1 Melt Events

Figure 6.6: Number of melt layers and lenses per century throughout the last 9700 years in the EastGRIP ice core. Running means are shown as solid lines. a) Melt layers (dark blue) and uncertain melt layers (white), b) melt lenses (dark green) and uncertain melt lenses (white), c) melt events, i.e., stack of panels a) and b), including their uncertainties. Note that the bar representing the period from 0 to 100 yrs b2k only represents 56 years, and not 100 like the other bars, as our analysis only begins in 1956 CE.

We find 561 melt events throughout the last 9700 years in the EastGRIP record (fig. 6.6c), which can be separated into 137 melt layers (fig. 6.6a) and 424 melt lenses (fig. 6.6b). Melt lenses are thus almost three times more frequent and represent smaller events. We find another 622 uncertain events, of which 157 are uncertain melt layers and 465 uncertain melt lenses.

Both melt lenses and layers follow the same trend and are most abundant during the same periods. As both features represent refrozen melt water, we can consequently group them together as melt events (fig. 6.6). For events we are certain of, we see a gradual decrease in number of events towards the Early Holocene. We find very few or no melt layers around the years 500, 2000, and 3000 b2k, and also melt lenses are less frequent. We find many certain melt events (dark blue and dark green in fig. 6.6), around the years 1000, 3500 to 4000, 4500 to 5200, and around 6000 b2k. We then continuously find melt events in between 6000 and 9000 yrs b2k, yet in varying number.

Including uncertain events, the number of events plateaus towards the Early Holocene, and even shows a slight increase. These are melt layers and lenses that are difficult to see in the line scan data, and should thus be treated with caution.

Events older than 9000 years become difficult to detect due to progressive bubble to clathrate transformation, therefore values gradually decrease. Slightly before 9000 yrs b2k the ratio of uncertain to certain layers increases, indicating the difficulty in detecting melt

layers. Also, we do not capture the most recent years, younger than 44 yrs b2k (1956 CE). Therefore the bar representing the period from 0 to 100 yrs b2k only represents 56 years, and not 100 like the other bars (fig. 6.6).

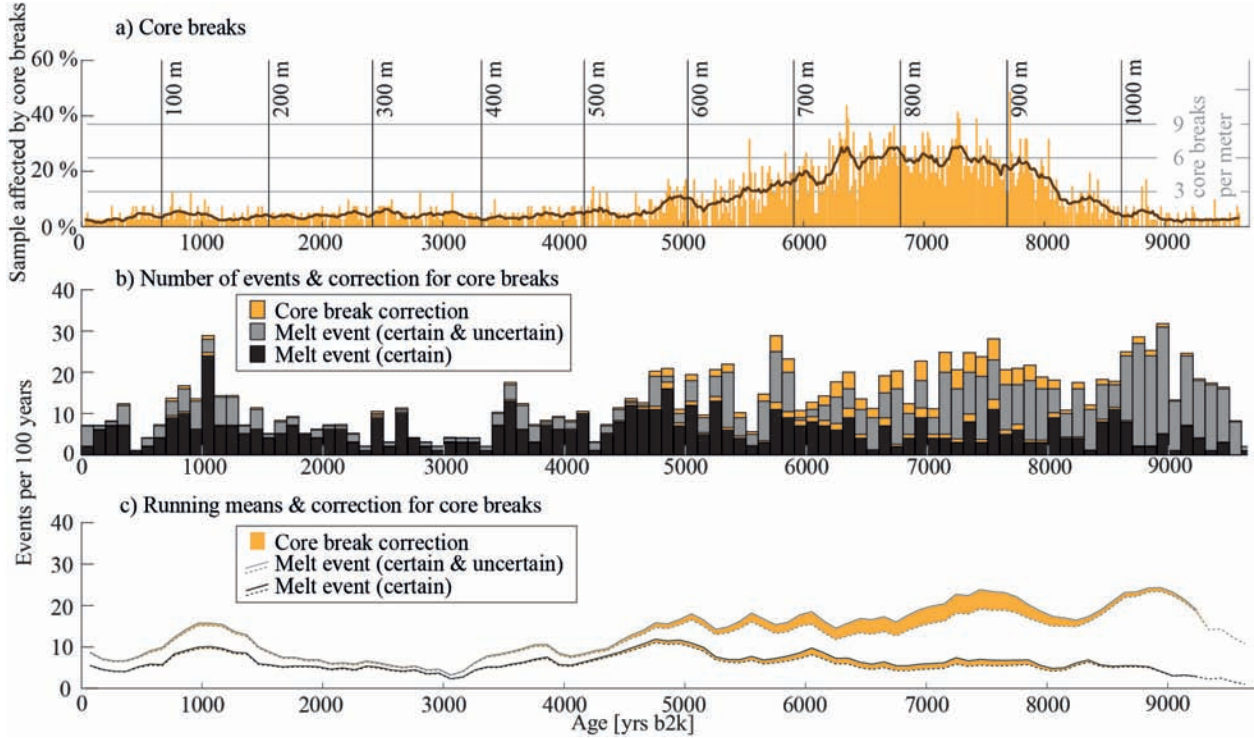## 6.3.2   Core Breaks and their Implications

Figure 6.7: a) Percentage of 165 cm-sample affected by core breaks (orange bars, scale left side), amount of core breaks per meter (orange bars, scale right side), and running mean over 16.5 meters (brown line). The broad peak between 650 and 950 m depth indicates the brittle zone. b) Certain melt events (black) and uncertain melt events (gray) corrected for potentially missed events in proximity of core breaks (orange). c) Running means of melt events, from fig. 6.6c (dashed lines) and core break corrected means (solid line).

We count core breaks (fig. 6.7a, orange bars) in the upper 1100 m of the EastGRIP ice core and show the corresponding ages and depths. The running mean over 16.5 meters (fig. 6.7a, brown line) clearly locates the brittle zone between 650 and 950 m depth. In the brittle zone, the number of core breaks greatly increases and exceeds three breaks per meter (or five breaks per 165-cm sample). As a core break masks four centimeters, we lose almost 25% of the sample in sections with six core breaks per meter.

As we know the number of melt events per sample, we can estimate the number of events missed due to core break shadows (see methods section). Events per 100 years are shown by vertical bars and the potentially missed melt events, i.e. our core break correction, in orange (fig. 6.7b, mean values in fig. 6.7c). The largest corrections are therefore performed in the brittle zone where we add around 25% to the number of melt events. This does not change the overall picture much but shows that we probably underestimate melt events in the time between 6000 and 8000 yrs b2k.

Our correction described above, assumes no correlation between the location of core breaks and melt layers. This correlation could be expected as melt layers might affect the crystal structure or other physical properties of the core. We perform a non quantitative visual inspection and do not find any connection of melt layers weakening, or strengthening, the ice and thus affecting the initiation and location of core breaks in the brittle zone.

6.3.3 Melt Layer Thickness and Total Melt

For the 137 certain melt layers, we have documented their thickness (M_0, fig. 6.8). Melt lenses are excluded from this analysis, as their average thickness is below one millimeter, and has not been measured. The layer thickness of melt layers is shown by the yellow, orange, and red bars, and to distinguish events within a short period, the thickness is indicated by circles. Cases of multiple events within five years are marked with a star (fig. 6.8c). We find three cases with three or more events within five years (black star) and 13 cases with two layers in five years (blue star).

We correct the melt layer thickness for thinning (initial thickness, M_0, open circles to corrected thickness, M, filled circles, fig. 6.8a,b,c), using the thinning function from Gerber et al. (2021, fig. 6.8d). Here we must keep in mind that the thinning is an average of all layers, derived from radar data. It is thus an upper limit assumption for the thinning of melt layers, which are denser, due to the lack of bubbles, and should therefore thin less than the surrounding ice.

Thin melt layers ($M < 4mm$, yellow) are found throughout the Holocene, yet seem to be more abundant in the Late Holocene (last 4200 years before today). Thick melt layers ($M > 8mm$, red) become more frequent further back in time. This trend is also highlighted by the blue curves (running means). The thinning-corrected running mean (solid blue line, fig. 6.8b,c) points to an average melt layer thickness of around 5 mm for the past 4500 years. Going back further in time, we see a gradual increase in melt layer-thickness in ice older than 4500 years (fig. 6.8c), peaking at an average thickness of 8 mm around 6500 to 7000 yrs b2k (solid blue line). In events older than 7000 years, the mean gradually drops and the last melt layer found is in ice deposited 9235 yrs b2k.

We expect to miss thinner melt layers the further back we go in time, which is represented by our results (fig. 6.8c) where we only find seven thin melt layers ($M < 4mm$, yellow) between 7000 and 9700 yrs b2k. In the same period we find 15 medium ($4mm < M < 8mm$, orange) and nine thick melt layers ($M > 8mm$, red). Assuming we miss thin layers but not thicker ones, we would expect a continuous increase in average melt layer thickness. Yet this average gradually drops below 7500 yrs while we approach Holocene Climatic Optimum (HCO). A possible reason for this gradual drop could be the two cooling events 8200 and 9300 years ago (Alley et al., 1997; Rasmussen et al., 2007; Thomas et al., 2007).

We only find melt layers exceeding a thickness of 15 mm between 6100 and 8100 yrs b2k, with one exception at 1014 yrs b2k (fig. 6.8c). This allocates the majority of thick melt layers to the Middle Holocene (Northgrippian Period, Cohen et al., 2016).

Derived from melt layer thicknesses, we present a melt layer record of the total amount of melt per century and millenium (fig. 6.8e,f, respectively). This record is corrected for thinning, using values from fig. 6.8c and we account for potentially missed layers due to core breaks (orange, from fig. 6.7). Layers thinner than 1.54 mm have been removed for consistency (see supplement fig. 6.16).

Millimeters of melt per century (fig. 6.8e) displays the high variability of melt events, as some centuries do not contain any events. Yet, the running mean (black line) shows distinct spikes, around 4500 to 5000 yrs b2k, 6000 to 6500 yrs b2k and around 7500 yrs b2k. These coincide with the period of the HCO. The HCO is also pronounced in the amount of melt per millennial (fig. 6.8f), with a peak in the interval between 6000 and 7000 yrs b2k.

Outstanding in both plots, centuries and millennia, is the peak around 1000 yrs b2k. The melt event from this period, i.e. 1014 yrs b2k or 986 CE, was of such an intensity, that it leaves an unprecedented spike in the melt record of the past 10,000 years. Here, it is important to note, that this is an event confined to a short period over one or a few summers, and not a signal representative for the entire century or millennium.
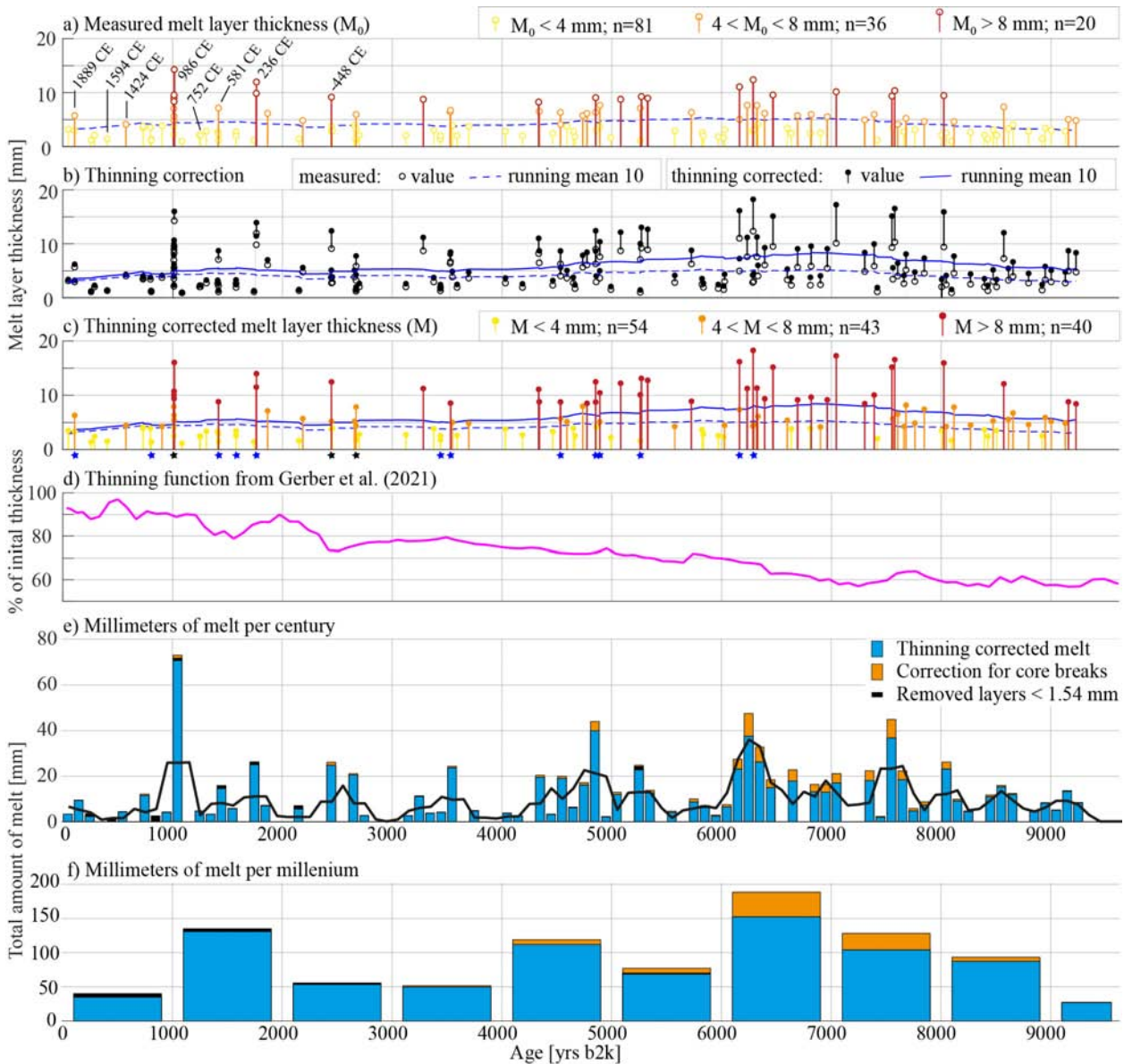
Figure 6.8: Measured (M_0, a) and thinning-corrected (M, c) melt layer thickness shown with open and filled circles respectively. Running mean over 10 events with dashed (measured) and solid blue line (thinning-corrected). Individual correction for thinning (b) using the thinning function from Gerber et al. (2021) shown in d). Yellow, orange, and red bars with circles indicate melt layers with a thickness smaller than 4 mm, between 4 and 8 mm, and greater than 8 mm, respectively. Labeled in panel a) are events later compared to tree rings with ages in [CE] notation. Stars in c) mark multiple events within five years (blue two events, black three or more). Millimeters of melt per century (e) and millenium (f) (blue bars, calculated from melt layer thicknesses), potentially missed events due to core breaks (orange), removed layers smaller than 1.54 mm (black, see fig. 6.16), and running mean (black line).

6.4 Discussion

6.4.1 The Highly Dynamic EastGRIP Site

The EastGRIP ice core is drilled though the NEGIS (fig. 6.9a), with a surface velocity of 55 m/yr. Gerber et al. (2021) backtrack the location of ice from EastGRIP over time and show that, e.g., 9000 years old ice was deposited 170 ($\pm$ 17) km further southwest and at a 270 m higher elevation. For their calculations Gerber et al. (2021) use today's ice sheet dimensions, but as Vinther et al. (2009) show, the ice sheet elevation has not been constant over the Holocene (fig. 6.3b). Vinther et al. (2009) suggest that NEGIS' origin, the area somewhere between the NorthGRIP and GRIP sites, was at 150 to 200 m higher elevation at the beginning of the Holocene, compared to today.

Adding the values from Vinther et al. (2009) and Gerber et al. (2021), the true elevation change over the past 9000 years could lie around 400 m. Using the lapse rate estimate of temperatures decreasing by 0.6 to 0.9°C every 100 m of elevation gain (Gardner et al., 2009), we can observe a temperature change at the EastGRIP drill site of 3°C solely by waiting 9000 years, flowing downstream, and without considering any climatic changes. Thus, when analyzing EastGRIP-ice we must take into account the spatial variations with time.

Alley and Anandakrishnan (1995) suggest that an increase in 2°C causes a 7.5-fold increase in melt frequency, by comparing their GISP2 melt layer frequencies to a record from site A (see introduction, Alley and Koci, 1988). Assuming this linear relationship between melt layers and temperature to be correct, we would expect a more than 10-fold increase in melt frequency for EastGRIP over the Holocene, solely due to the lowering of the site elevation (see above). An increase of frequency in such magnitude, from the Early to Late Holocene, is not supported by our data. On the contrary, the amount of melt decreases from the Early Holocene to today (see fig. 6.8f), and thus other parameters must play a key role. This suggests that the site elevation lowering, i.e. potential temperature increase, is more than compensated by gradual cooling over the Holocene.

6.4.2 The Climatic Picture of the Holocene Derived from Melt Events

Our climatic interpretation (fig. 6.9a) is derived, by eye, from the number of melt events, their thickness, and melt event frequency (fig. 6.9 b,c,d respectively). In the central Northeastern part of the Greenland ice sheet, i.e. the EastGRIP site, we see strong variations in these melt layer proxies over time, suggesting a fluctuating climate over the past 10,000 years. The most recent 4000 years show a gradual decrease of melt events with the last peak at around 1000 yrs before today, probably caused by a single event. The trend in the Middle and Early Holocene appears to plateau with some fluctuations. This climatic interpretation fits well with the generally accepted theory, that summer temperatures decrease throughout the Holocene, e.g. Axford et al. (2021) and also follows the trend of the stable water isotopes, a proxy for temperature (fig. 6.9a). As melt events generally occur during summer, our interpretation is consistent with recent results by Bova et al. (2021), who state that annual temperatures increase and summer temperatures decrease throughout the Holocene.

We clearly see the Medieval Warm Period around the year 1000 yrs b2k, identified by a number of melt layers and lenses. Concerning the Roman Warm Period, only the second half (2000 to 1600 yrs b2k) is visible in the number of melt events and the melt layer thickness (fig. 6.9b,c, respectively), while the full period (between 2250 and 1600 yrs b2k) is represented by melt event frequencies (fig. 6.9d). Based on fig. 6.9a, we see the warm HCO from 5800 to 7000 yrs b2k, 7200 to 8100 yrs b2k, and from 8500 to 8700 yrs b2k, with cooler periods
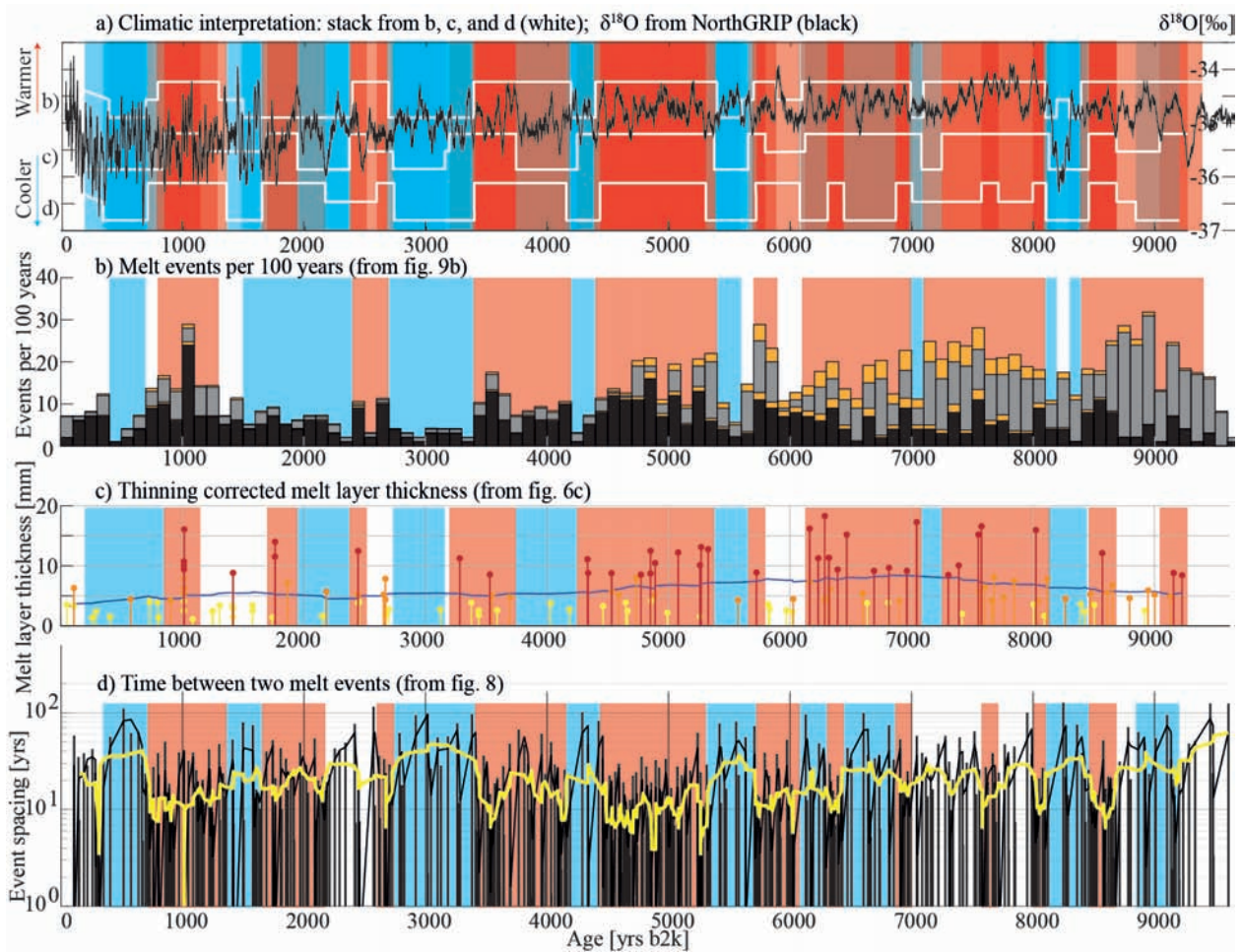
Figure 6.9: a) A climatic interpretation of melt layer distribution over the Holocene. Without absolute values, red represents warmer periods and blue colder ones. The white lines are a climatic interpretation from b,c,d and red and blue shadings are a stack of b,c,d. Stable Oxygen Isotope ($\delta^{18}O$) record from NorthGRIP in black (NorthGRIPmembers, 2004). b) Melt events per 100 years (fig. 6.7b) with red shading in periods with many events, and blue in periods with fewer events. c) Melt layer thickness (fig. 6.8c), with red shading in periods with thick melt layers. d) Melt event frequencies, with short time spans between melt events in red and long time spans in blue. Running mean in yellow.

in-between.

We find distinct cold periods around the year 500, 3000, 5600, and 8200 b2k. In all our measurements (fig. 6.9) the 8.2 kyr event (Alley et al., 1997; Rasmussen et al., 2007; Thomas et al., 2007) stands out as a period with very few melt events and only one melt layer. Our analysis does not show the 9.3 kyr event, as this is where we lose the signal due to the disappearance of bubbles.

Periods that are neither explicitly warm nor cold, are left with a white shading (fig. 6.9), e.g. the very recent past, i.e. younger than 100 yrs b2k. In these youngest 100 years of our record, we see a clear increase in the stable water isotope signal (NorthGRIPmembers, 2004, fig. 6.9a), displaying an increase of temperature over the Greenland ice sheet. We remind the reader that our melt layer analysis ends in the year 1956 CE. For the more recent period, we rely on other data sources, e.g. Steen-Larsen et al. (2011), who suggest that we have five melt events in the past 15 years. These melt events are derived from satellite-based microwaves observations and their existence in the snowpack is not confirmed, thus must be treated with caution. These five events would translate into 33 events per 100 years and would create a peak slightly higher than the one at around 1014 yrs b2k, to which we from here on refer to as the 986 CE event.

6.4.3 The Melt Layers of the 986 CE Event

We can find a set of melt layers, corresponding to a large melt or rain event (see coffee experiment) in the EastGRIP ice core around the year 986 CE, or slightly after, in a depth of 138.05 m (fig. 6.2d, bag 252). Here we count nine melt layers and 12 melt lenses over 60 cm, which represent five years. Seven of these melt layers are visible in fig. 6.2d. The nine melt layers might not represent nine separate events, but could have been created in one single event. We can assume that the rainwater percolated 1.5 m deep into the snowpack and left nine melt layers. All of these layers thus may have formed within a few days, similar to the 2012 warm event at NEEM (fig. 6.2c). The depth of 1.5 m roughly covers five years making this assumption feasible.

Rain events are rare on the Greenland ice sheet and the 986 CE event stands out as a huge melt event with probably very high surface temperatures and rain. It is also worth noting, that the 1889 CE melt event, which is present in most areas and ice cores across Greenland and therefore considered a big event, consists of only two melt layers, and must therefore not have been as intense as the 986 CE event. The only melt event comparable to the 968 CE event, yet with significantly thinner layers, happened around the year 675 BCE (2675 yrs b2k and 328 m depth) with four melt layers and three melt lenses within the stratigraphy of one year. Thus, these events are rare in Greenland, even over the course of the entire Holocene.

The exceptional warm event (986 CE) found in the ice core, coincides with the settlement voyage of Erik the Red from Iceland to Greenland. According to the book of Icelanders (Íslendingabók), which was written in 1133: "And Eiríkr began to settle the country fourteen or fifteen years before Christianity came here to Iceland, according to what a man who had himself accompanied Eiríkr the Red there told Thorkell Gellisson in Greenland" (Þorgilsson, 1968). Christianity was adopted in Iceland either in 999 or 1000 CE, so fourteen or fifteen years before that could refer to either 984, 985 or 986 CE.

Due to uncertainties in the historical record, in ice core dating, and melt water percolation depth, an alignment of the events is challenging. Yet, if these two events aligned, then the warm event could have contributed to the success of the passage from Iceland to Greenland. Deeper investigation on this coincidence is necessary and we cannot claim any causality here. But whether or not the viking voyages and melt events are connected, the 986 CE event is by far the most outstanding melt event found in the visual stratigraphy of the EastGRIP ice core.

6.4.4 Melt Layers and Northern Hemisphere Tree Rings

We evaluated the age offset of seven melt events (see fig. 6.8a) to the highest peak in the tree ring record (fig. 6.10a), within a ±6-year window around the melt event (fig. 6.10b to h). Melt events lay very close to a tree ring peak, in most cases within the same year. Two events show an offset of four to five years to the highest peak within the ±6-year window (E4 and E6, fig. 6.10e,g, respectively). We find a slightly smaller peak around the same year as the melt layers. Thus, we attribute this offset to incorrect peak assignment. All highlighted events (black boxes, E1 to E7) have at least one tree ring peak (warm anomaly) in very close proximity. For the 986 CE event (fig. 6.10d), the most outstanding melt event in our record, we find a tree ring warm-year which is about 2.4 years older.

Melting at EastGRIP might not be synchronous with all tree ring peaks, but still offers some insight to the correlation of melt and tree ring growth on a larger geographic scale. This is also the case for volcanic eruptions: many volcanic events do not correspond to deep cooling in the tree ring records, although local minima are often observed in correspondence. Due to the age uncertainty of melt events and difficulties in time-scale translations, we cannot
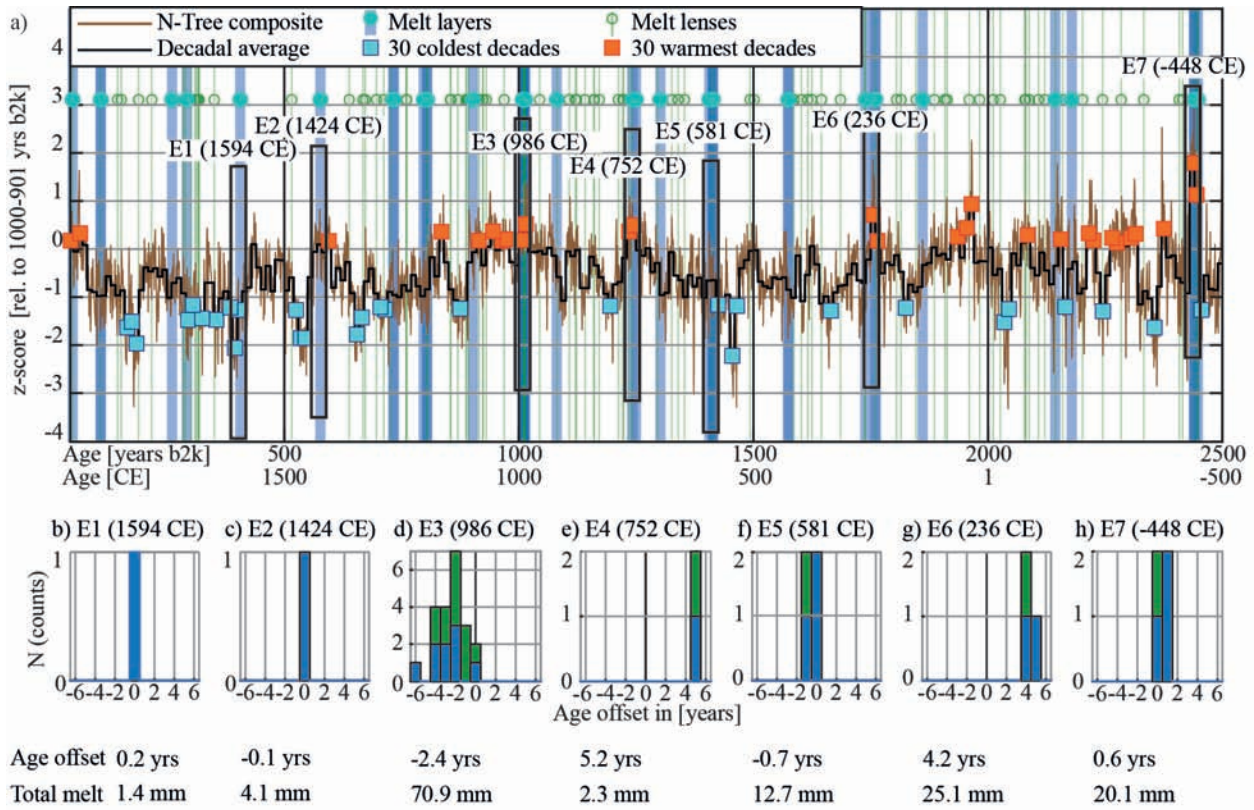
Figure 6.10: a) Tree ring growth anomaly (brown, Sigl et al., 2015) compared to melt from 44 to 2500 yrs b2k. Melt layers (blue) and lenses (green) are highlighted at the corresponding age by vertical bars. Seven melt events (E1 to E7) are highlighted with black boxes. Decadal average (black line), 30 warmest and coldest decades as orange and light blue boxes, respectively. b -h) histograms of age offset form the melt events (layers in blue, lenses in green) to the largest tree ring growth year, within ±6 years. The exceptional 986 CE event (E3) is younger than the tree ring maximum by about 2.4 years.

evaluate a more precise age-offset. Moreover, even though more melting occurs during tree ring warm-decades, not every prominent peak in the tree ring record has melt events in its proximity.

The location of EastGRIP might not represent the complexity of the climatic dynamics that produces tree ring growth anomalies at scattered locations around the Northern Hemisphere, but the occurrence of more melt in warm periods and in proximity of some of the warmest years suggests a partial correlation. We expect that future studies could improve the results we have presented, in particular for the correlation of the melt events at EastGRIP with other ice cores and with more temperature records from around the globe.

We test the hypothesis that warmer periods contain more melt events than colder ones (fig. 6.11). For this, we remove outliers and test the amount of melt per decade (in the last 2500 years) against Poisson distributions. We find, that in the 50 warmer decades the occurrence of melt is 0.82 events/per decade, while in the other decades it is on average 0.55. However, the attribution of warm/cold depends on the N-Tree record used as a temperature-proxy, so we are forced to stop our analysis at 2500 yrs b2k. For the rest of the Holocene, we observe that the occurrence of melt is highest in the older millennia (4000 to 8000 yrs b2k), on average about 1.5/decade, compared to about 0.7 in the younger Holocene millennia (compare to fig. 6.8f).
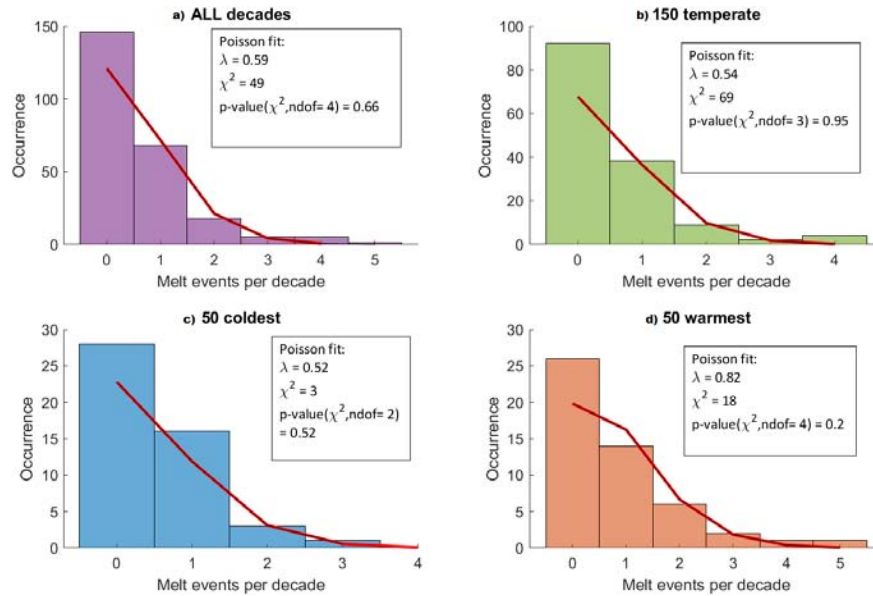
Figure 6.11: Histograms of melt events per decade, over the last 2500 years. To highlight a correlation between melt and Northern Hemisphere temperatures, we distinguish cold, warm, or temperate decades (b,c, or d, respectively). We fit the occurrence of melt per decade to Poisson distributions, and obtain satisfactory p-values. The warmest decades (d) show an occurrence of melt 18% higher than the general value (a). Melt in cold decades is not substantially different from the temperate value.

6.4.5 A First Attempt to Interpret Sloping Bubble-free Layers

Sloping bubble-free layers (fig. 6.12) become more frequent in the lower half of our investigation depth, i.e. below 600 m, or older than 5000 yrs b2k (fig. 6.14). These are layers that have a tilt greater than 10° from horizontal, mostly between 30° and 60° (fig. 6.12). In general, they are discontinuous, giving them the appearance of a lens, rather than a layer. These thin and hard-to-see structures are very dependent on which plane, by chance, was cut to produce the 2D line scan image (Westhoff et al., 2020). A layer like in fig. 6.12 can easily be missed if it is located just a few millimeters below the surface.

These layers cannot be leftovers of sloping surface structures, due to their steep tilt. Resolving the initial shape of the layer, i.e. by stretching in the vertical, the layers would become even steeper and be too steep for ice sheet surface structures.

Figure 6.12a is an almost vertical structure and thus could be a melt pipe. Yet this fails to explain why we only see these structures in great depths and not in the upper half of our depth of interest.

Sloping layers at around 15° and 45°, fig. 6.12b,c, respectively, appear to be sets of conjugate bands, thus they could be the result of rheology. Steinbach et al. (2016) and Llorens et al. (2017) show sets of conjugate shear bands as a result of pure shear in ice in their numerical simulations. In nature so far, all sloping layers allocated to deformation, are the result of simple shear (Alley et al., 1997; Jansen et al., 2016) and not pure shear. A challenge is that we expect to find shear bands where ice is softer, thus brighter, and containing more bubbles. Our results show that these shear bands appear in dark, bubble-free layers, contradicting the established theory. While discussing these deformation structures in detail is beyond the scope of this work, it is worth mentioning these for future investigations.
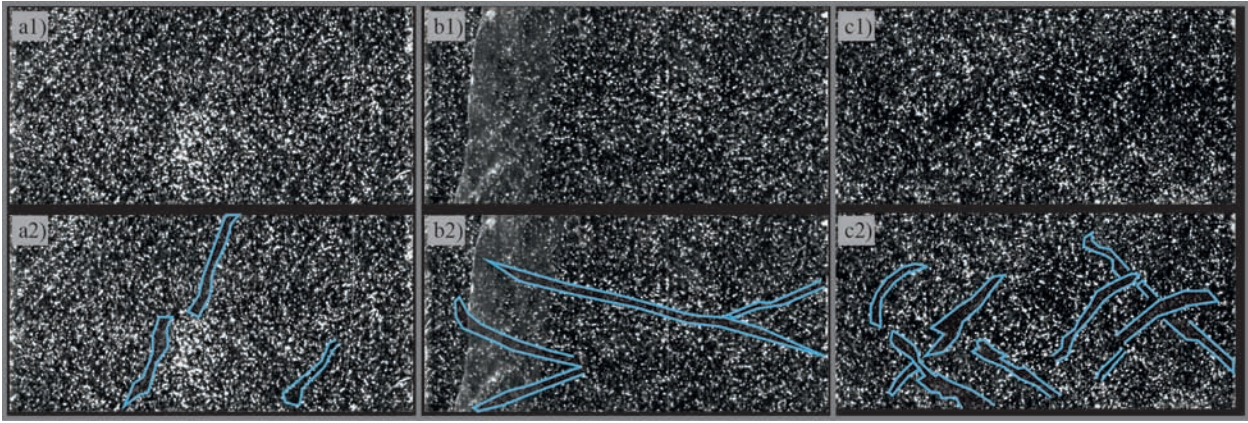
Figure 6.12: Top row: Line scan images, bottom row: same image as top row, with highlighted sloping bubble-free layers. a) 459.60 m, 3840 yrs b2k, very steep structures, melt pipe-like appearance. b) 696.26 m, 5886 yrs b2k, continuous bubble-free structure appear as a set of conjugate deformation bands. c) 998.73 m, 8625 yrs b2k, many sloping bubble-free layers all at angles around 45°.

6.5   Conclusion

In comparison with ice core melt layer records from Renland, coastal Greenland (Taranczewski et al., 2019) or northern Canada (Fisher et al., 2012), the record of 831 mm melt in 10,000 yrs of the Eastgrip ice core is rather low. Here we must keep in mind that the average summer temperature at EastGRIP lays around -25°C, making melt events a rare phenomenon. It is therefore almost surprising that we find 137 melt layers and 424 melt lenses at a site with such cold summers.

We correct for thinning of layers due to vertical compression with depth, but including the upstream effects remains a challenge. It is possible that temperatures rise by 3°C soley due to EastGRIP site flowing downstream with NEGIS, but the number of melt layers per 100 years does not increase in the expected rate (Alley and Anandakrishnan, 1995). With a gradual cooling throughout the Holocene (Axford et al., 2021), the temperature changes caused by a lowering of the elevation at EastGRIP are hard to quantify. Nevertheless, warm and cold periods throughout the Holocene stand out in our record. The climatic warm and cold periods derived from melt layers (fig. 6.9), match generally accepted climatic periods such as the Medieval and Roman warm periods, the HCO, or the 8.2 kyr cooling event.

When analyzing melt layers on an annual time scale, the well-studied 2012-melt event in Greenland (e.g. Nghiem et al., 2012; Bonne et al., 2015; Nilsson et al., 2015) helps our understanding of natural melt events. The infiltration of melt layers from different years into the stratigraphy, could potentially ruin the consistency of, e.g. isotope records assuming the stratigraphy to be linear in time. This certainly adds another factor of complication to the tempo-spatial variability recently observed and discussed (e.g. Steen-Larsen et al., 2011; Münch and Laepple, 2018). In hindsight it is not possible to distinguish between two scenarios: 1) five consecutive years with surface melting each summer, which then create a melt layer in each of the corresponding snow layers, or 2) one large melt and rain event, which creates melt layers scattered across all the snow from the last five years below. For smaller events the first options seems likely. For larger events, creating thick melt layers, the chances are high that melt percolates deep into the wet and warm snow pack, disrupting the stratigraphic order.

We compare the melt layer record to tree rings (Sigl et al., 2015), and find that some peaks in the melt layer and tree ring data align (with an offset of a few years, see above). The large melt events also stand out in the tree ring record and hint to outstanding warm summers being a phenomenon over the entire Northern Hemisphere. While this is not strictly

in agreement with our understanding of atmospheric circulations (e.g. Bonne et al. (2015); Hanna et al., 2016; Graeter et al., 2018), the effect could also be restricted to some trees used in the tree ring composite, introducing a warm bias for these certain years.

So far, the 986 CE and 2012 CE melt events are unprecedented in the Holocene. Although the 2012-melt, and rain, event is considered an exception it could be a hint to what we can expect for future summers in Greenland as global warming proceeds.

Author Contribution

Initial idea of manuscript and data acquisition by JW. Support on melt layers in ice cores in general came from AS, JF, SK, and DDJ. Coffee experiment and melt layer definition by SK and JW. Tree ring to melt comparison by GS, idea by AS. Viking voyages and melt events by AS and JW. NEEM snowpit data and text by HAK and PV. Climatic interpretations and ice sheet evolution by BMV, AS, and JW. Comments on physical properties of melt layers and their appearance by IW and SK. JW prepared the manuscript with contributions and revisions from all co-authors.

Competing Interests

The authors declare that they have no conflict of interest.

Acknowledgements

Data Availability

Once published, the data can be downloaded on the Centre for Ice and Climate home page: www.iceandclimate.nbi.ku.dk.

Bibliography - EastGRIP Melt Layers

Alley, R. B., Gow, A. J., Meese, D. A., Fitzpatrick, J. J., and Waddington, E. D. (1997). "Grain-scale processes, folding, and stratigraphic". In: *Journal of Geophysical Research* 102.C12, pp. 26819–26830.

Alley, R. B. and Anandakrishnan, S. (1995). "Variations in melt-layer frequency in the GISP2 ice core: implications for Holocene summer temperatures in central Greenland". In: *Annals of Glaciology* 21, pp. 64–70. DOI: 10.3189/s0260305500015615.

Alley, R. and Koci, B. (1988). "Ice-Core Analysis at Site A, Greenland: Preliminary Results". In: *Annals of Glaciology* 10.May 2021, pp. 1–4. DOI: 10.3189/s0260305500004067.

Axford, Y., Vernal, A. de, and Osterberg, E. C. (2021). "Past Warmth and Its Impacts During the Holocene Thermal Maximum in Greenland". In: *Annual Review of Earth and Planetary Sciences* 49.1, pp. 279–307. DOI: 10.1146/annurev-earth-081420-063858.

Badgeley, J. A., Steig, E. J., Hakim, G. J., and Fudge, T. J. (2020). "Greenland temperature and precipitation over the last 20000 years using data assimilation". In: *Climate of the Past* 16.4, pp. 1325–1346. DOI: 10.5194/cp-16-1325-2020.

Bennartz, R., Shupe, M. D., Turner, D. D., Walden, V. P., Steffen, K., Cox, C. J., Kulie, M. S., Miller, N. B., and Pettersen, C. (2013). "July 2012 Greenland melt extent enhanced by low-level liquid clouds". In: *Nature* 496.7443, pp. 83–86. DOI: 10.1038/nature12002.

Berger, A. and Loutre, M. F. (1991). "Insolation values for the climate of the last 10 million years". In: *Quaternary Science Reviews* 10.4, pp. 297–317. DOI: 10.1016/0277-3791(91)90033-Q.

Bonne, J. L., Steen-Larsen, H. C., Risi, C., Werner, M., Sodemann, H., Lacour, J. L., Fettweis, X., Cesana, G., Delmotte, M., Cattani, O., Vallelonga, P., Kjær, H. A., Clerbaux, C., Sveinbjörnsdóttir, Á. E., and Masson-Delmotte, V. (2015). "The summer 2012 Greenland heat wave: In situ and remote sensing observations of water vapor isotopic composition during an atmospheric river event". In: *Journal of Geophysical Research* 120.7, pp. 2970–2989. DOI: 10.1002/2014JD022602.

Bova, S., Rosenthal, Y., Liu, Z., Godad, S. P., and Yan, M. (2021). "Seasonal origin of the thermal maxima at the Holocene and the last interglacial". In: *Nature* 589.7843, pp. 548–553. DOI: 10.1038/s41586-020-03155-x.

Brunt, D. (1933). "The adiabatic lapse-rate for dry and saturated air". In: *Quarterly Journal of the Royal Meteorological Society* 59, pp. 351–360. DOI: https://doi.org/10.1002/qj.49705925204.

Buizert, C., Keisling, B. A., Box, J. E., He, F., Carlson, A. E., Sinclair, G., and DeConto, R. M. (2018). "Greenland-Wide Seasonal Temperatures During the Last Deglaciation". In: *Geophysical Research Letters* 45.4, pp. 1905–1914. DOI: 10.1002/2017GL075601.

Buizert, C. et al. (2012). "Gas transport in firn: Multiple-tracer characterisation and model intercomparison for NEEM, Northern Greenland". In: *Atmospheric Chemistry and Physics* 12.9, pp. 4259–4277. DOI: 10.5194/acp-12-4259-2012.

Cohen, K. M., Finney, S. C., Gibbard, P. L., and Fan, J. .-. (2016). "International Chronostratigraphic Chart". In: *The ICS International Chronostratigraphic Chart* 36.3, pp. 199–204.

Dahl-Jensen, D., Mosegaard, K., Gundestrup, N., Clow, G. D., Johnsen, S. J., Hansen, A. W., and Balling, N. (1998). "Past temperatures directly from the Greenland Ice Sheet". In: *Science* 282.5387, pp. 268–271. DOI: 10.1126/science.282.5387.268.

Dalton, A. S. et al. (2020). "An updated radiocarbon-based ice margin chronology for the last deglaciation of the North American Ice Sheet Complex". In: *Quaternary Science Reviews* 234. DOI: 10.1016/j.quascirev.2020.106223.

Das, S. B. and Alley, R. B. (2005). "Characterization and formation of melt layers in polar snow : observations and experiments from West Antarctica". In: *Journal of Glaciology* 51.173, pp. 307–312.

Dash, J. G., Rempel, A. W., and Wettlaufer, J. S. (2006). "The physics of premelted ice and its geophysical consequences". In: *Reviews of Modern Physics* 78.3, pp. 695–741. DOI: 10.1103/RevModPhys.78.695.

Faria, S. H., Kipfstuhl, S., and Lambrecht, A. (2018). *The EPICA-DML Deep Ice Core*. Berlin: Springer-Verlag GmbH Germany.

Fegyveresi, J. M., Alley, R. B., Muto, A., Orsi, A. J., and Spencer, M. K. (2018). "Surface formation, preservation, and history of low-porosity crusts at the WAIS Divide site, West Antarctica". In: *Cryosphere* 12.1, pp. 325–341. DOI: 10.5194/tc-12-325-2018.

Fisher, D. A., Koerner, R. M., and Reeh, N. (1995). "Holocene climatic records from Agassiz Ice Cap, Ellesmere Island, NWT, Canada". In: *Holocene* 5.1, pp. 19–24. DOI: 10.1177/095968369500500103.

Fisher, D., Zheng, J., Burgess, D., Zdanowicz, C., Kinnard, C., Sharp, M., and Bourgeois, J. (2012). "Recent melt rates of Canadian arctic ice caps are the highest in four millennia". In: *Global and Planetary Change* 84-85, pp. 3–7. DOI: `10.1016/j.gloplacha.2011.06.005`.

Fritzsche, D., Schütt, R., Meyer, H., Miller, H., Wilhelms, F., Opel, T., and Savatyugin, L. M. (2005). "A 275 year ice-core record from Akademii Nauk ice cap, Severnaya Zemlya, Russian Arctic". In: *Annals of Glaciology* 42, pp. 361–366. DOI: `10.3189/172756405781812862`.

Gardner, A. S., Sharp, M. J., Koerner, R. M., Labine, C., Boon, S., Marshall, S. J., Burgess, D. O., and Lewis, D. (2009). "Near-surface temperature lapse rates over arctic glaciers and their implications for temperature downscaling". In: *Journal of Climate* 22.16, pp. 4281–4298. DOI: `10.1175/2009JCLI2845.1`.

Gerber, T. A., Hvidberg, C. S., Rasmussen, S. O., Franke, S., Sinnl, G., Grinsted, A., Jansen, D., and Dahl-jensen, D. (2021). "Upstream flow effects revealed in the EastGRIP ice core using a Monte Carlo inversion of a two-dimensional ice-flow model". In: *The Cryosphere* February.

Graeter, K. A., Osterberg, E. C., Ferris, D. G., Hawley, R. L., Marshall, H. P., Lewis, G., Meehan, T., McCarthy, F., Overly, T., and Birkel, S. D. (2018). "Ice Core Records of West Greenland Melt and Climate Forcing". In: *Geophysical Research Letters* 45.7, pp. 3164–3172. DOI: `10.1002/2017GL076641`.

Hanna, E., Cropper, T. E., Hall, R. J., and Cappelen, J. (2016). "Greenland Blocking Index 1851–2015: a regional climate change signal". In: *International Journal of Climatology* 36.15, pp. 4847–4861. DOI: `10.1002/joc.4673`.

Herron, M. M., Herron, S. L., and Langway, C. C. (1981). "Climatic signal of ice melt features in southern Greenland". In: *Nature* 293.5831, pp. 389–391. DOI: `10.1038/293389a0`.

Humphrey, N. F., Harper, J. T., and Pfeffer, W. T. (2012). "Thermal tracking of meltwater retention in Greenland ' s accumulation area". In: *Journal of Geophysical Research* 117.October 2011, pp. 1–11. DOI: `10.1029/2011JF002083`.

Hvidberg, C. S., Grinsted, A., Dahl-Jensen, D., Khan, S. A., Kusk, A., Andersen, J. K., Neckel, N., Solgaard, A., Karlsson, N. B., Kjar, H. A., and Vallelonga, P. (2020). "Surface velocity of the Northeast Greenland Ice Stream (NEGIS): Assessment of interior velocities derived from satellite data by GPS". In: *Cryosphere* 14.10, pp. 3487–3502. DOI: `10.5194/tc-14-3487-2020`.

Jansen, D., Llorens, M. G., Westhoff, J., Steinbach, F., Kipfstuhl, S., Bons, P. D., Griera, A., and Weikusat, I. (2016). "Small-scale disturbances in the stratigraphy of the NEEM ice core: Observations and numerical model simulations". In: *Cryosphere* 10.1, pp. 359–370. DOI: `10.5194/tc-10-359-2016`.

Kameda, T., Narita, H., Shoji, H., Nishio, F., Fujii, Y., and Watanabe, O. (1995). "Melt features in ice cores from site J, souther Greenland: some implications for summer cliamte since AD 1550". In: *Annals of Glaciology* May 2021, pp. 51–58.

Keegan, K. M., Albert, M. R., McConnell, J. R., and Baker, I. (2014). "Climate change and forest fires synergistically drive widespread melt events of the Greenland Ice Sheet". In: *Proceedings of the National Academy of Sciences of the United States of America* 111.22, pp. 7964–7967. DOI: `10.1073/pnas.1405397111`.

Kipfstuhl, S., Pauer, F., Kuhs, W. F., and Shoji, H. (2001). "Air bubbles and clathrate hydrates in the transition zone ofthe NGRIP deep ice core". In: *Geophysical Research Letters* 28.4, pp. 591–594. DOI: `10.1029/1999GL006094`.

Koerner, R. M. and Fisher, D. A. (1990). "A record of Holocene summer climate from a Canadian high-Arctic ice core". In: *Nature* 343.6259, pp. 630–631. DOI: `10.1038/343630a0`.

Langway, C. C. and Shoji, H. (1990). "Past temperature record from the analysis of melt features in the DYE3, Grennland, ice core". In: *Annals of Glaciology* 14, pp. 343–344.

Lecavalier, B. S., Fisher, D. A., Milne, G. A., Vinther, B. M., Tarasov, L., Huybrechts, P., Lacelle, D., Main, B., Zheng, J., Bourgeois, J., and Dyke, A. S. (2017). "High Arctic Holocene temperature record from the Agassiz ice cap and Greenland ice sheet evolution". In: *Proceedings of the National Academy of Sciences of the United States of America* 114.23, pp. 5952–5957. DOI: `10.1073/pnas.1616287114`.

Lecavalier, B. S., Milne, G. A., Vinther, B. M., Fisher, D. A., Dyke, A. S., and Simpson, M. J. (2013). "Revised estimates of Greenland ice sheet thinning histories based on ice-core records". In: *Quaternary Science Reviews* 63, pp. 73–82. DOI: `10.1016/j.quascirev.2012.11.030`.

Llorens, M. G., Griera, A., Steinbach, F., Bons, P. D., Gomez-Rivas, E., Jansen, D., Roessiger, J., Lebensohn, R. A., and Weikusat, I. (2017). "Dynamic recrystallization during deformation of polycrystalline ice: Insights from numerical simulations". In: *Philosophical Transactions of the Royal Society A: Mathematical, Physical and Engineering Sciences* 375.2086. DOI: `10.1098/rsta.2015.0346`.

McGwire, K. C., Hargreaves, G. M., Alley, R. B., Popp, T. J., Reusch, D. B., Spencer, M. K., and Taylor, K. C. (2008). "An integrated system for optical imaging of ice cores". In: *Cold Regions Science and Technology* 53.2, pp. 216–228. DOI: `10.1016/j.coldregions.2007.08.007`.

Mojtabavi, S., Wilhelms, F., Cook, E., Davies, S., Sinnl, G., Skov Jensen, M., Dahl-Jensen, D., Svensson, A., Vinther, B., Kipfstuhl, S., Jones, G., Karlsson, N., Faria, S. H., Gkinis, V., Kjær, H., Erhardt, T., Berben, S., Nisancioglu, K., Koldtoft, I., and Rasmussen, S. O. (2020). "A first chronology for the East GReenland Ice-core Project (EGRIP) over the Holocene and last glacial termination". In: *Climate of the Past Discussions* 16.December, pp. 2359–2380. DOI: `10.5194/cp-16-2359-2020`.

Monnin, E., Steig, E. J., Siegenthaler, U., Kawamura, K., Schwander, J., Stauffer, B., Stocker, T. F., Morse, D. L., Barnola, J. M., Bellier, B., Raynaud, D., and Fischer, H. (2004). "Evidence for substantial accumulation rate variability in Antarctica during the Holocene, through synchronization of CO2 in the Taylor Dome, Dome C and DML ice cores". In: *Earth and Planetary Science Letters* 224.1-2, pp. 45–54. DOI: `10.1016/j.epsl.2004.05.007`.

Morcillo, G., Faria, S. H., and Kipfstuhl, S. (2020). "Unravelling Antarctica's past through the stratigraphy of a deep ice core: an image-analysis study of the EPICA-DML line-scan images". In: *Quaternary International* February. DOI: `10.1016/j.quaint.2020.07.011`.

Mote, T. L. (2007). "Greenland surface melt trends 1973-2007: Evidence of a large increase in 2007". In: *Geophysical Research Letters* 34.22, pp. 1–5. DOI: `10.1029/2007GL031976`.

Münch, T. and Laepple, T. (2018). "What climate signal is contained in decadal - To centennial-scale isotope variations from Antarctic ice cores?" In: *Climate of the Past* 14.12, pp. 2053–2070. DOI: `10.5194/cp-14-2053-2018`.

NEEMCommunityMembers (2013). "Eemian interglacial reconstructed from a Greenland folded ice core". In: *Nature* 493.7433, pp. 489–494. DOI: `10.1038/nature11789`.

Neff, P. D. (2014). "A review of the brittle ice zone in polar ice cores". In: *Annals of Glaciology* 55.68, pp. 72–82. DOI: `10.3189/2014AoG68A023`.

Nghiem, S. V., Hall, D. K., Mote, T. L., Tedesco, M., Albert, M. R., Keegan, K., Shuman, C. A., DiGirolamo, N. E., and Neumann, G. (2012). "The extreme melt across the Greenland ice sheet in 2012". In: *Geophysical Research Letters* 39.20, pp. 6–11. DOI: `10.1029/2012GL053611`.

Nilsson, J., Vallelonga, P., Simonsen, S. B., Sørensen, L. S., Forsberg, R., Dahl-Jensen, D., Hirabayashi, M., Goto-Azuma, K., Hvidberg, C. S., Kjær, H. A., and Satow, K.

(2015). "Greenland 2012 melt event effects on CryoSat-2 radar altimetry". In: *Geophysical Research Letters* 42.10, pp. 3919–3926. DOI: `10.1002/2015GL063296`.

NorthGRIPmembers (2004). "High-resolution record of Northern Hemisphere climate extending into the last interglacial period". In: *Nature* 431.September, pp. 147–151.

Orsi, A. J., Kawamura, K., Fegyveresi, J. M., Headly, M. A., Alley, R. B., and Severinghaus, J. P. (2015). "Differentiating bubble-free layers from Melt layers in ice cores using noble gases". In: *Journal of Glaciology* 61.227, pp. 585–594. DOI: `10.3189/2015JoG14J237`.

Pfeffer, W. T. and Humphrey, N. F. (1998). "Fortmation of ice layers by infiltration and refreezing of meltwater". In: *Annals of Glaciology* 26, pp. 83–91.

Rasmussen, S. O., Andersen, K. K., Svensson, A. M., Steffensen, J. P., Vinther, B. M., Clausen, H. B., Siggaard-Andersen, M. L., Johnsen, S. J., Larsen, L. B., Dahl-Jensen, D., Bigler, M., Röthlisberger, R., Fischer, H., Goto-Azuma, K., Hansson, M. E., and Ruth, U. (2006). "A new Greenland ice core chronology for the last glacial termination". In: *Journal of Geophysical Research Atmospheres* 111.6, pp. 1–16. DOI: `10.1029/2005JD006079`.

Rasmussen, S. O., Vinther, B. M., Clausen, H. B., and Andersen, K. K. (2007). "Early Holocene climate oscillations recorded in three Greenland ice cores". In: *Quaternary Science Reviews* 26.15-16, pp. 1907–1914. DOI: `10.1016/j.quascirev.2007.06.015`.

Schaller, C. F. (2018). "Towards understanding the signal formation in polar snow, firn and ice using X-ray computed tomography". In: *PhD Thesis*, p. 68. DOI: `10.1088/1751-8113/44/8/085201`. arXiv: `1011.1669`.

Schaller, C. F., Freitag, J., Kipfstuhl, S., Laepple, T., Christian Steen-Larsen, H., and Eisen, O. (2016). "A representative density profile of the North Greenland snowpack". In: *Cryosphere* 10.5, pp. 1991–2002. DOI: `10.5194/tc-10-1991-2016`.

Shoji, H. and Langway, C. (1987). "HYDRATE-BUBBLE . TRANSFORMATION PROCESS IN GLACIER ICE". In: *Journal de Physique* 3.48, pp. 551–556.

Sigl, M. et al. (2015). "Timing and climate forcing of volcanic eruptions for the past 2,500 years". In: *Nature* 523.7562, pp. 543–549. DOI: `10.1038/nature14565`.

Simonsen, M. F., Baccolo, G., Blunier, T., Borunda, A., Delmonte, B., Frei, R., Goldstein, S., Grinsted, A., Kjær, H. A., Sowers, T., Svensson, A., Vinther, B., Vladimirova, D., Winckler, G., Winstrup, M., and Vallelonga, P. (2019). "East Greenland ice core dust record reveals timing of Greenland ice sheet advance and retreat". In: *Nature Communications* 10.1. DOI: `10.1038/s41467-019-12546-2`.

Steen-Larsen, H. C. et al. (2011). "Understanding the climatic signal in the water stable isotope records from the NEEM shallow firn/ice cores in northwest Greenland". In: *Journal of Geophysical Research Atmospheres* 116.6, pp. 1–20. DOI: `10.1029/2010JD014311`.

Steinbach, F., Bons, P. D., Griera, A., Jansen, D., Llorens, M. G., Roessiger, J., and Weikusat, I. (2016). "Strain localization and dynamic recrystallization in the ice-air aggregate: A numerical study". In: *Cryosphere* 10.6, pp. 3071–3089. DOI: `10.5194/tc-10-3071-2016`.

Svensson, A., Nielsen, S. W., Kipfstuhl, S., Johnsen, S. J., Steffensen, J. P., Bigler, M., Ruth, U., and Röthlisberger, R. (2005). "Visual stratigraphy of the North Greenland Ice Core Project (NorthGRIP) ice core during the last glacial period". In: *Journal of Geophysical Research: Atmospheres* 110.2, pp. 1–11. DOI: `10.1029/2004JD005134`.

Taranczewski, T., Freitag, J., Eisen, O., Vinther, B., Wahl, S., and Kipfstuhl, S. (2019). "10,000 years of melt history of the 2015 Renland ice core, EastGreenland". In: *The Cryosphere Discussions* March, pp. 1–16. DOI: `10.5194/tc-2018-280`.

Tedesco, M., Fettweis, X., Mote, T., Wahr, J., Alexander, P., Box, J. E., and Wouters, B. (2013). "Evidence and analysis of 2012 Greenland records from spaceborne observations, a regional climate model and reanalysis data". In: *The Cryosphere* 7.2, pp. 615–630. DOI: `10.5194/tc-7-615-2013`.

Thomas, E. R., Wolff, E. W., Mulvaney, R., Steffensen, J. P., Johnsen, S. J., Arrowsmith, C., White, J. W., Vaughn, B., and Popp, T. (2007). "The 8.2 ka event from Greenland ice cores". In: *Quaternary Science Reviews* 26.1-2, pp. 70–81. DOI: 10.1016/j.quascirev.2006.07.017.

Trusel, L. D., Das, S. B., Osman, M. B., Evans, M. J., Smith, B. E., Fettweis, X., McConnell, J. R., Noël, B. P., and Broeke, M. R. van den (2018). "Nonlinear rise in Greenland runoff in response to post-industrial Arctic warming". In: *Nature* 564.7734, pp. 104–108. DOI: 10.1038/s41586-018-0752-4.

Uchida, T., Yasuda, K., Oto, Y., Shen, R., and Ohmura, R. (2014). "Natural supersaturation conditions needed for nucleation of air-clathrate hydrates in deep ice sheets". In: *Journal of Glaciology* 60.224, pp. 1135–1139. DOI: 10.3189/2014JoG13J232.

Vallelonga, P. et al. (2014). "Initial results from geophysical surveys and shallow coring of the Northeast Greenland Ice Stream (NEGIS)". In: *Cryosphere* 8.4, pp. 1275–1287. DOI: 10.5194/tc-8-1275-2014.

Vinther, B. M., Buchardt, S. L., Clausen, H. B., Dahl-Jensen, D., Johnsen, S. J., Fisher, D. A., Koerner, R. M., Raynaud, D., Lipenkov, V., Andersen, K. K., Blunier, T., Rasmussen, S. O., Steffensen, J. P., and Svensson, A. M. (2009). "Holocene thinning of the Greenland ice sheet". In: *Nature* 461.7262, pp. 385–388. DOI: 10.1038/nature08355.

Vinther, B. M., Clausen, H. B., Johnsen, S. J., Rasmussen, S. O., Andersen, K. K., Buchardt, S. L., Dahl-Jensen, D., Seierstad, I. K., Siggaard-Andersen, M. L., Steffensen, J. P., Svensson, A., Olsen, J., and Heinemeier, J. (2006). "A synchronized dating of three Greenland ice cores throughout the Holocene". In: *Journal of Geophysical Research Atmospheres* 111.13, pp. 1–11. DOI: 10.1029/2005JD006921.

Weikusat, C., Kipfstuhl, S., and Weikusat, I. (2015). "Raman tomography of natural air hydrates". In: *Journal of Glaciology* 61.229, pp. 923–930. DOI: 10.3189/2015JoG15J009.

Weinhart, A. H., Kipfstuhl, S., Hörhold, M., Eisen, O., and Freitag, J. (2021). "Spatial Distribution of Crusts in Antarctic and Greenland Snowpacks and Implications for Snow and Firn Studies". In: *Frontiers in Earth Science* 9.March, pp. 1–16. DOI: 10.3389/feart.2021.630070.

Westhoff, J., Stoll, N., Franke, S., Weikusat, I., Bons, P., Kerch, J., Jansen, D., Kipfstuhl, S., and Dahl-Jensen, D. (2020). "A Stratigraphy Based Method for Reconstructing Ice Core Orientation". In: *Annals of Glaciology* 62.85-86, pp. 191–202. DOI: 10.1017/aog.2020.76.

Winski, D., Osterberg, E., Kreutz, K., Wake, C., Ferris, D., Campbell, S., Baum, M., Bailey, A., Birkel, S., Introne, D., and Handley, M. (2018). "A 400-Year Ice Core Melt Layer Record of Summertime Warming in the Alaska Range". In: *Journal of Geophysical Research: Atmospheres* 123.7, pp. 3594–3611. DOI: 10.1002/2017JD027539.

Þorgilsson, A. (1968). *Íslendingabók (The Book of Icelanders)*. Ed. by J. Benediktsson.

6.6 Supplement

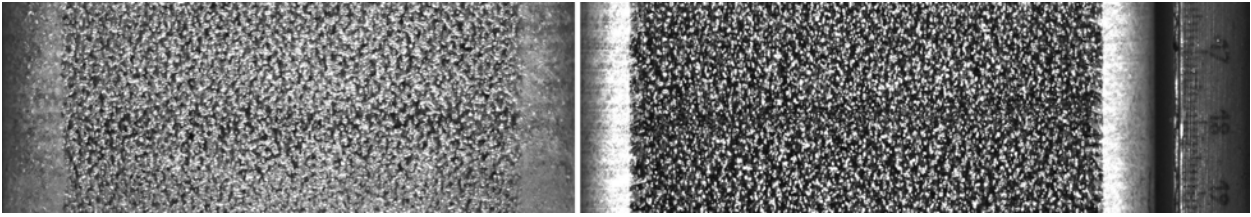### 6.6.1 Uncertain Melt Events

Figure 6.13: Uncertain melt layers from 102 and 187 m depth. Scale on right

Melt layers are not always as clear as shown in the examples in fig. 6.4. Figure 6.13 shows two examples of melt layers, which we have labeled as uncertain. The layers are not free from bubbles, yet one could assume that there is a bubble-free layer behind, or in front of, a thin section of ice with bubbles.
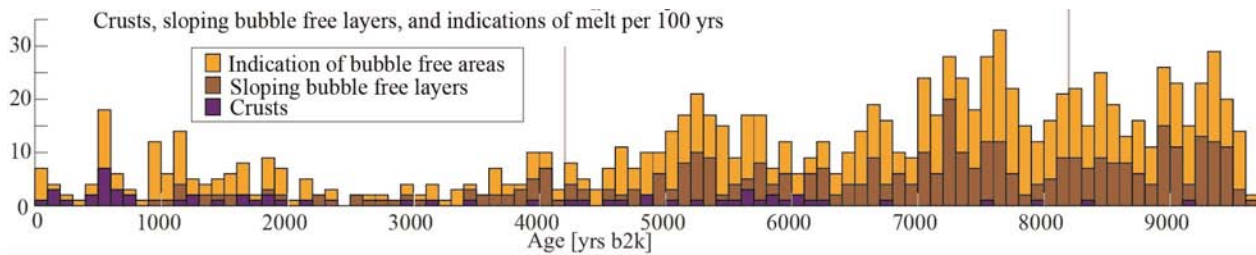
6.6.2 Very Uncertain Melt Layers

Figure 6.14: Number of bubble-free layers and lenses per century throughout the last 9700 years in the EastGRIP ice core. Indications of bubble-free areas (orange), which are very uncertain melt layers and -lenses that only hint to bubble-free areas. Sloping bubble-free layers (brown) with a tilt of more than 10 degrees from horizontal, which are in general very thin and not always continuous. Crusts (purple) are only certain/clearly identifiable in the last 2000 years (upper 250 m). Crusts shown beyond 2000 years were thought to be crusts during analysis, and later changed to uncertain melt layers. Note that the bar representing the period from 0 to 100 yrs b2k only represents 56 years, and not 100 like the other bars, as our analysis only begins in 1956 CE.

Other than melt events, we find crusts, sloping bubble-free layers, and indications of melt events (fig. 6.14). In total, we find 60 crusts (purple in fig. 6.14), of which we are certain about 17. These certain crusts are all in the last 2000 years, i.e. the upper 250 m. Crusts found below this depth are classified as uncertain and were added as uncertain melt layers. We find 410 cases of sloping bubble-free layers, mainly in a depth below 600 m (approximately 5000 yrs b2k). These bubble-free layers with an inclination over 10° are discussed in chapter 6.4.5. We also find 579 cases where the line scan images hint at an area or layer without bubbles, but cannot be seen with full certainty. These could represent warm summer days, on which small amounts of surface melt occur, yet not sufficient to classify as melting. These small amount of water on the air-ice interfaces can cause a change in the porosity of the firn. Dash et al. (2006) describe these as enhanced pre-melting and discuss incomplete vs. complete surface melting. These pre-melt events are hard to identify in line scan images, or even under a microscope, and only become visible when comparing the brightness changes over a long section ($> 10cm$). We, therefore, classify these brightness changes as "very uncertain melt layers", or as in fig. 6.14, as "indications of bubble-free

layers". They are added to the overview for the sake of completeness and might be useful for comparison to other methods (e.g. Morris et al., in prep.).

6.6.3 Data Acquisition

The data were collected in a semi-automated fashion using Matlab. We run a script, which divides the line scan image (length 165 cm) into ten equal sections, with two centimeters overlap. Thus, we display 16.5 (+ 2) cm of the core at a time. We display three different color maps: a "hot" map, a "cool" map of the inverted image, and the original grayscale line scan image. Using a tool that records pixel coordinates by clicking on the image, we select the layers of interest. The position of the layer is then immediately converted to depth using

$$depth[m] = ((bagNumber * 0.55) - 0.55) + (pixels/(186 * 100)). \qquad (6.1)$$

A bag is the standard unit in ice coring samples, corresponding to 55 cm. $BagNumber$ refers to the line scan bag number, where only every third bag is listed, meaning one sample (165 cm) corresponds to three bags (55 cm each). We convert pixels to depth, using the value $1cm = 186px$. This means that the depth is referenced to the top of every third bag, not to every bag as is the standard for most other methods. For melt layers we record the upper and lower boundary, for all other features we only record the center value for depth. We did the analysis twice to minimize operator errors and mismatches between were reassessed.

6.6.4 Melt Layer Thickness
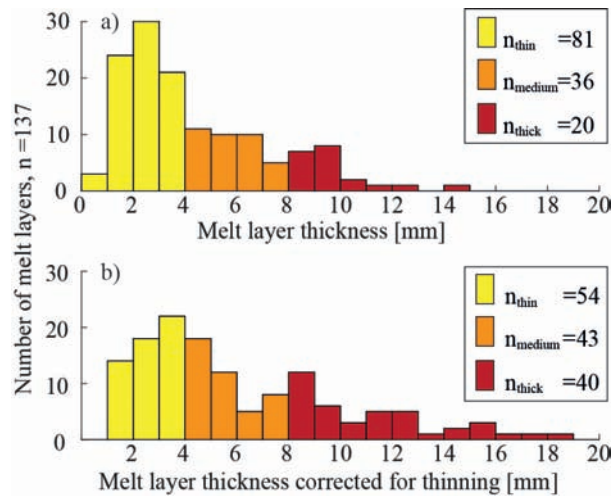
Figure 6.15: Histogram of melt layer thicknesses with the same color-code as fig. 6.8. a) Measured values, b) corrected for thinning using the thinning function from Gerber et al. (2021).

Over the Holocene, the range of melt layer thicknesses varies between 1 and 14 mm (fig. 6.15a). Although following the definition, a melt layer cannot be thinner than two millimeters, we find 27 layers below this threshold, before correcting for thinning. These are events that are included for one of two reasons: they vary in thickness and an estimated average was taken or they have the distinct appearance of a melt layer and can clearly be differentiated from a crust. Correcting for thinning removes the layers between zero and one millimeter and increases the number of thick melt layers.

We see that most melt layers ($n = 81$, fig. 6.15a) are thin melt layers ($M < 4mm$, yellow). Even after correcting for thinning, this remains the same, although the size of the groups are more equal now (fig. 6.15b). Thick melt layers ($M > 8mm$, red) remain the fewest, although

their number doubles when correcting for thinning. We find 40 thick melt layers in almost 10,000 years, giving an average of one big melt layer in 250 years. On average we find one melt layer every 70 years, but not regularly (compare to fig. 6.8).

6.6.5   Too Thin Melt Layers

Figure 6.16: Thinning corrected melt layer thicknesses (circles). Black-colored circles are removed from the record, due to cut off at 1.54 mm (pink circle and line).

The time averaged total melt record is corrected for thinning and for potentially missed layers due to core breaks (fig. 6.8e,f). For consistency, we cut out layers that are thinner than 1.54 mm. This is the th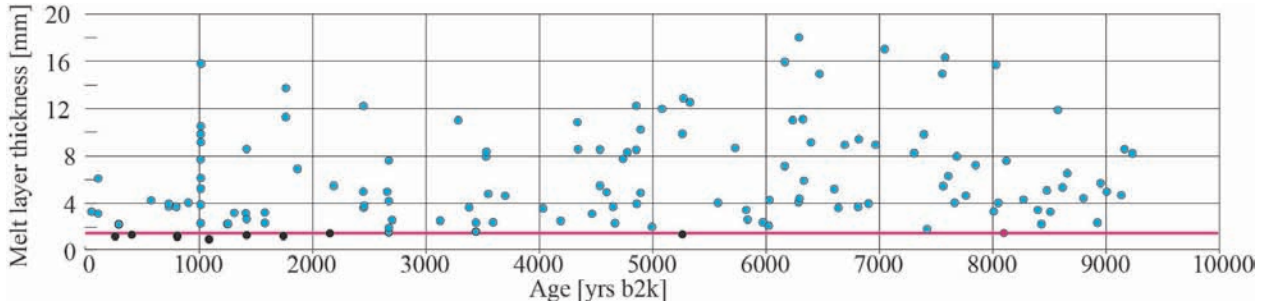innest layer found in the oldest section, with an age of 8101 yrs b2k (fig. 6.16a, pink circle). We apply the threshold on thinning-corrected layers (fig. 6.16a, pink line). Excluding these thin layers from older ice, removes the bias of counting more thin layers in younger sections, compared to older sections.

6.6.6   Melt Layer and Lens Frequency

We analyze the duration between melt layer and melt lenses, representing the time from an older event, to the next younger event (fig. 6.17). We distinguish between melt layers (blue bars, fig. 6.17a) and melt lenses (green bars, fig. 6.17b). Running means for 2, 10, and 50-year events show the long-term variations. Due to melt lenses being approximately three times more frequent, their spacing is much smaller than that of melt layers.

In fig. 6.17b (melt lenses), around 1000, 3500 to 4000, 4500 to 5500, around 6000, 8000 to 8200, and around 8500 yrs b2k the time between two melt lenses is between 10 to 15 years (orange running mean), therefore very short (red bars). We find a very large spacing (blue bars) of events around 500 yrs b2k, where the spacing exceeds 100 years and in the period from 3000 to 3500 yrs b2k, where the spacing between two melt lenses is around 60 years. Such a large spacing between two melt lens events only becomes visible again in ice older than 9000 years, where bubble-free layers become more difficult to see and we end our analysis.

A similar pattern is also visible in fig. 6.17a (melt layers), yet with fewer details, as melt layers occur less frequently. Time spans with high melt lens frequencies roughly match periods with high frequencies of melt layers. An outstanding difference is the period from 5800 to 6200 yrs b2k, where the time between two melt lenses is short, but between melt layers it is long. The opposite is visible around 6400 yrs b2k, where the time between two melt layers is short, but long between the lenses.

In both records (fig. 6.17a,b) we find three shorter time spans around 7800, 8100, and 8500 yrs b2k which have a very short spacing between two events.

The long term trend (fig. 6.17b, purple line) which is the running mean over 50 events suggests the largest spacing between two events around 3000 yrs b2k with approximately 30 to 35 years and the lowest around 5000 yrs b2k with 12 years spacing. Older than 5000
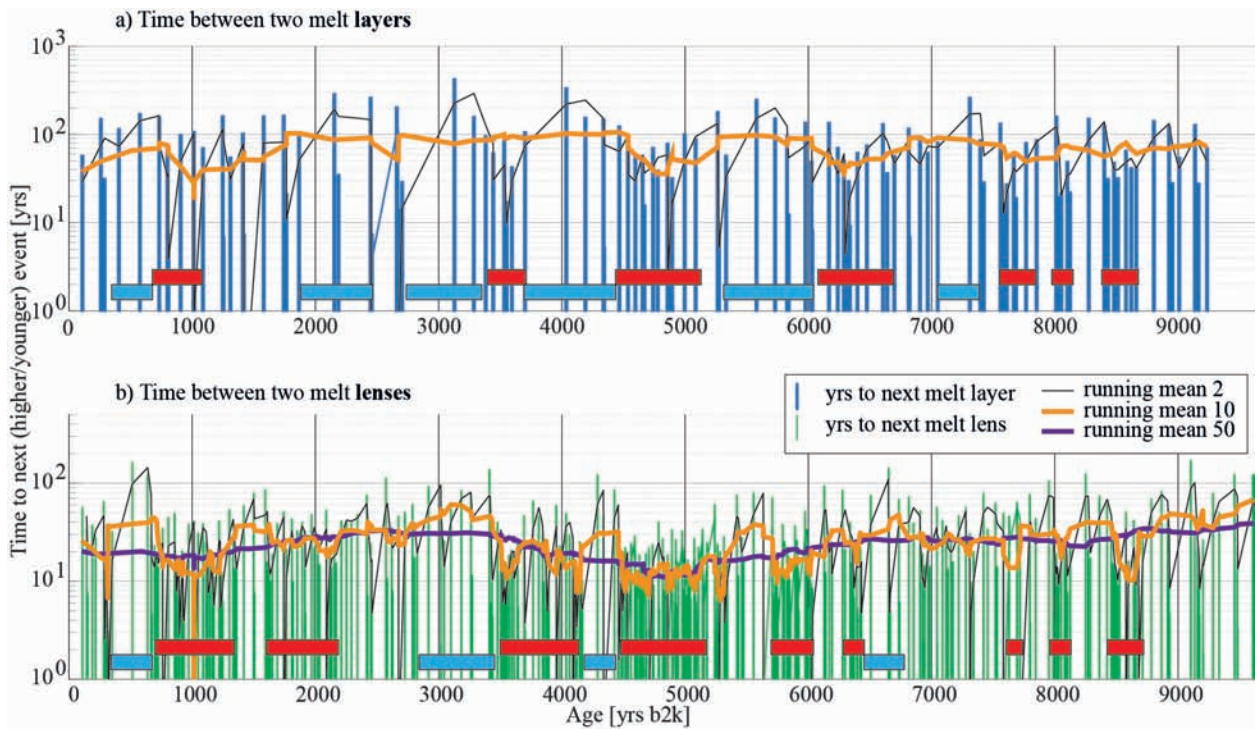
Figure 6.17: Time from older event to next younger event, a) for 137 melt layers (vertical blue bars) and b) 424 melt lenses (green bars). Different running means (averages with moving window) to visualize long-term variations. Red bars highlight periods with a short spacing between events, and blue bars represent a long spacing.

years the trend gradually increases, showing greater spacing between two melt events, with a small drop around 7500 yrs b2k. The highest value of 35 years between two events is only reached at the very bottom of our analysis depth, older than 9000 years, where the likelihood of missing an event greatly increases.

6.6.7 Statistics

We show the time between two melt layers, melt lenses, melt events and random events (fig. 6.18) on a logarithmic x-axis. The graph is a straight line, proving the exponential distribution, which we expect to find in a naturally occurring and homogeneous Poisson process.

6.6.8 Comparison to Other Melt Layer Records

GISP2

To compare our work, we use the only other melt layer record from a central Greenland ice core covering large parts of the Holocene. Alley and Anandakrishnan (1995) analyzed the GISP2 ice core using visual inspection and to some degree photography, the state-of-the-art method at that time. On average they find one melt event every 153 years. We find one melt event every 17.3 years in the EastGRIP ice core (561 melt events in total, fig. 6.6c). We can dedicate our increase in finding melt events by a factor of 10 to the better optical methods nowadays.

The sites GISP2 (Alley and Anandakrishnan, 1995) and EastGRIP (this work) are both in a central region on the Greenland ice sheet and the ice recovered at EastGRIP, inside the NEGIS, originates upstream from the GRIP and GISP2 area (Gerber et al., 2021). While
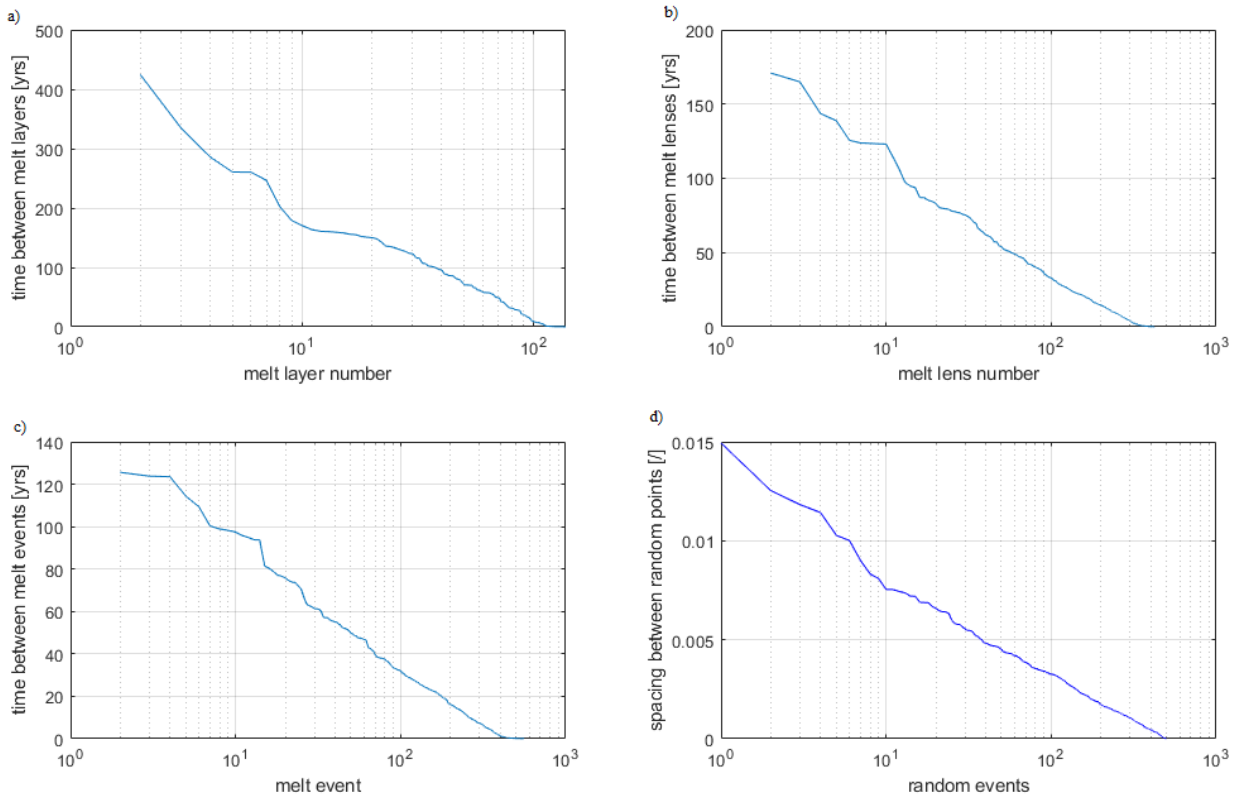
Figure 6.18: Time between two a) melt layers, b) melt lenses, c) melt events, and d) random events

ice flows downstream the site elevation decreases and temperature gradually increases (see chapter 6.4.1). For the Early Holocene, we can therefore assume the records must be in some way similar, but the number of events should gradually increase towards present day. This holds, as the GISP2 record has a very pronounced HCO (between 6000 and 8000 yrs b2k), while our record (of certain events, fig. 6.6c, dark colors) shows melt events to be slightly more evenly distributed over the past 10,000 years. When we include uncertain events (fig. 6.6c, bright colors), the GISP2 and EastGRIP records are very similar and their peaks align well.

RECAP Ice Core

Another available, but not peer reviewed, melt layer record is assembled by Taranczewski et al. (2019) of the RECAP ice core. The authors present a melt layer record for the last 10,000 years on Renland, eastern Greenland. In this ice core, the Holocene covers 533 of the 584 meters of total core length (Simonsen et al., 2019). As the Holocene ice reaches almost to bedrock, it is subjected to high amounts of thinning in the bottom parts. As thinning equally affects bubble-free ice and bubbly ice (for ice, no study has shown the opposite so far), the signal is lost at a much shallower depth than at EastGRIP or GISP2. The RECAP record, therefore, provides a very robust melt layer record for the Late Holocene (past 4200 years before today), but probably not for the Middle and Early Holocene.

Taranczewski et al. (2019) find a broad peak of melt events around 4000 years b2k, which is not visible in the GISP2 (Alley and Anandakrishnan, 1995) or EastGRIP (this study) melt layer record. The RECAP melt layer record is thus likely a regional record of Eastern Greenland, but not fully comparable with the central ice sheet.

Chapter 7

An Optical Approach to Determine the Bubble Lock-in Depth in Ice Cores

Julien WESTHOFF [1], Michael N. DYONISIUS [1], Johannes FREITAG [2],
Ilka WEIKUSAT [2,3], Patricia MARTINERIE [4], Xavier FAIN [4],
and Thomas BLUNIER [1]

[1]Physics of Ice, Climate, and Earth, University of Copenhagen,
Copenhagen, Denmark
[2]Alfred Wegener Institute, Helmholtz Centre for Polar and Marine Research,
Bremerhaven, Germany
[3]Department of Geosciences, Eberhard Karls University Tübingen,
Tübingen Germany
[4]Univ. Grenoble Alpes, CNRS, IRD, Grenoble INP, IGE,
Grenoble, France

Abstract   We present a novel technique to find the bubble lock-in and close-off depth in polar ice using the visual stratigraphy obtained from line scan images from the EastGRIP ice core. We compare our results to the 2018 firn air pumping campaign, which was done one kilometer from the EastGRIP drill site. We use the line scan images from 13.75 to 101.05 m depth of the EastGRIP ice core and run a grayscale analysis on brightness intensities and additionally count the number of bright spots. We analyze one sample every 55 cm for the entire depth of interest and enhance the resolution to one centimeter for a section over 16 m around the lock-in depth. We suggest that the lock-in depth begins around 58.30 m depth, where we see the first formation of rounded air pathways, and we find the first fully enclosed air bubbles at a depth of 66.55 m. Our results match those from the firn air campaign, including later experimental and modeling studies, very well and show that our optical approach works.

7.1   Introduction

7.1.1   Trapping Gases in Ice Cores

Ice cores, from polar ice sheets, provide a rare opportunity to directly measure the composition of the air from our past atmosphere far back in time (Petit et al., 1999). As snow accumulates on top of the polar ice sheets, it densifies into firn and ice (Herron and Langway, 1980). In the upper firn column, the air in the interstitial space between the snow grains is still connected to the open atmosphere. As the snow grains compact under the weight of overlying accumulation, the air in the interstitial space becomes isolated from the open atmosphere, slowly trapped, and occluded into the bubbles.

The top part of the ice core, before the brittle ice zone, annual layer counting of chemical markers provide the best age estimates (e.g. Sigl et al., 2016). The gas age is often tied to the ice age through calculation of delta age offset with firn models, which require good quantification of the close-off depth and firn densification model

On the bottom part of the ice core, when annual layer counting error accumulates and becomes difficult, it is better to establish the gas age first through synchronization of well-mixed gas such as CH_4 and $\delta^{18}O(atm.)$ (e.g., Buizert et al., 2015), then develop the delta age offset and calculate the ice age difference between the host-ice and the air trapped inside the ice. This age difference is a first starting point to determine the age of trapped gases.

The age of ice can be determined by e.g. layer counting techniques using results from continuous flow analysis Andersen et al. (e.g. 2006) or translating the age scale from other ice cores using volcanic markers, e.g. Rasmussen et al. (2006) or Mojtabavi et al. (2020).

With regards to gas, the firn column is divided into three zones (Sowers et al., 1992). Blunier and Schwander (2000) describe three zones derived from the succession of δ^{15}N of atmosphere: an upper convection zone, a static air column (the diffusive zone), and the non-diffusive zone. Between the diffusive and non-diffusive zone we find the firn-ice transition. In this transition open pores of the firn gradually close and become trapped air bubbles inside solid ice.

To find the bubble close-off depth (BCD) it is important to understand firn and densification processes. Many authors have investigated these topics: Herron and Langway (1980) developed a simple model based on accumulation, density, and temperature to find the BCD. Martinerie et al. (1992) provide details on each of these parameters and their influence at different sites. Birner et al. (2018) present a 2D model to investigate layering in the lock-in depth, as this plays a key role in the closure of air pathways. Lipenkov (2018) presents sketches and X-ray tomography of firn pores, and a semi-empirical model to relate bubble size and number with snow accumulation rate and temperature during ice formation. Ueltzhöffer et al. (2010) develop a tool to detect bubbles in images from scanned thick sections of selected samples from different Antarctic ice cores. On the EPICA Dronning Maud Land (EDML) ice core, Morcillo et al. (2020) take this one step further and show how continuous images of an ice core can be used to create a bubble record (details in method section).

In this study, we investigate the firn-ice transition and present a novel, optical approach to precisely determine the depth of bubble lock-in. We investigate layering and the influence of melt layers. We further present the results from the firn-air pumping campaign and modeling results to reconstruct bubble close-off depth at the East Greenland Ice Core Project (EastGRIP) site.

7.1.2 Drill Sites and Variation Between Cores

For our optical measurements we use the EastGRIP ice core and for validation, we use the results from the firn air pumping campaign, which was conducted on the S6 borehole. These two sites lay approximately one kilometer apart, inside the Northeast Greenland Ice Stream (NEGIS) in Northeastern Greenland (EastGRIP coordinates: 75°38'N, 36°00'W, 2704 m a.s.l., Vallelonga et al., 2014). The EastGRIP site has a fairly stable accumulation rate of 0.11 m ice eq. yr^{-1} over the past 400 years (Vallelonga et al., 2014). Riverman et al. (2019) and Oraschewski and Grinsted (2021) suggest that ice inside NEGIS is subjected to enhanced densification from the sides, due to flow, and and not only vertically by gravity.

When analyzing and comparing the results from two different locations, we must keep in mind that spatial variations can occur. At the Northern Greenland Eemian Ice Drilling (NEEM) site, Buizert et al. (2012) describe two shallow cores which are only 64 m apart from each other. Despite the close proximity of these two shallow cores, they show differences in measured mixing ratio profiles that exceed the experimental error and the BCD differs by approximately half a meter (Buizert et al., 2012).

7.2 Methods

7.2.1 The Line Scan Images

The line scanner images a 165 cm-long polished ice core slab from above, while illuminating the ice from below (Svensson et al., 2005; Faria et al., 2018; Westhoff et al., 2020). This causes light to be reflected on various features, such as snow and firn grains, core breaks, bubbles, dust-rich layers, and others. In ice from the Holocene period, the main cause of reflections and scattering are air bubbles within the ice and core breaks. These features then appear as bright sections in the line scan.
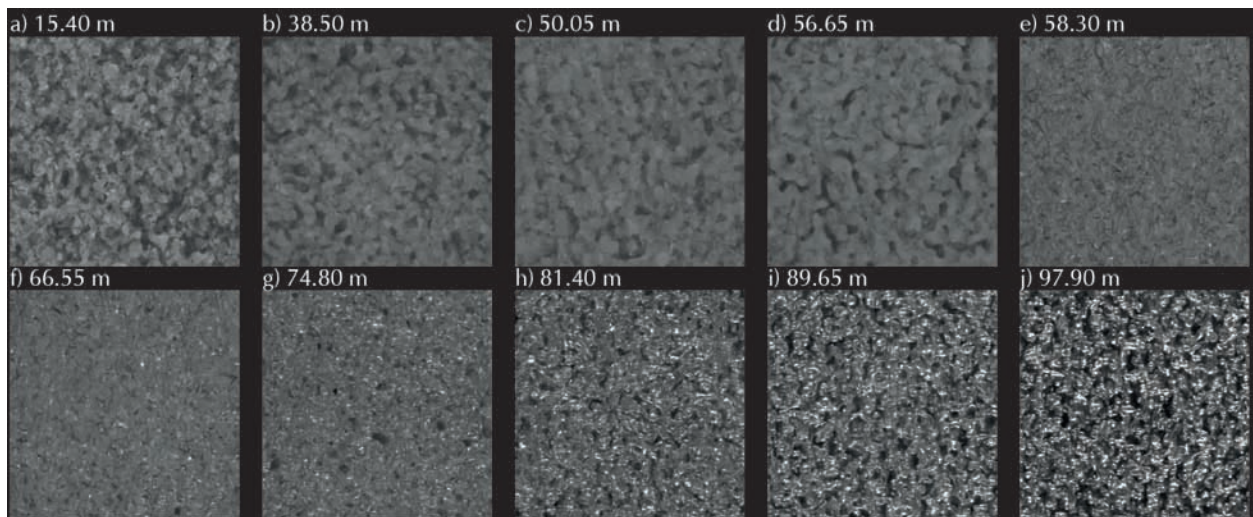
Figure 7.1: Two by two centimeter images from the line scanner. Examples of the optical appearance in line scanner image, with enhanced brightness for visualization.

Between firn and ice, there is an inversion of bright and dark sections (Westhoff et al., 2021). Grains of snow and firn appear bright as these grains are not transparent and thus reflect or scatter light. Voids, i.e. air, between grains then appear dark (fig. 7.1a to d). In ice, bright and dark are inverted, as ice is transparent and the dark background is imaged. Air, in the form of bubbles, reflects light and thus appears bright (fig. 7.1h to j). In the transition from firn to ice, we see mixed elements of both appearances (fig. 7.1e to g). For

more details on the different appearances of firn and ice in line scan images, see Westhoff et al. (2021).

Line scan images provide a 2D picture of the structure of the ice cores. The focus depth is set to a few millimeters below the ice core's polished surface. While these 2D images cannot provide a full 3D reconstruction such as e.g. a computer tomography scan (e.g. Freitag et al., 2013 or Lipenkov, 2018), it does reveal some structures and we can get a hint of how the 3D structure could look like. Experience in using the line scanner reveals that when using the camera settings as done in fig. 7.1, we have approximately half a centimeter in focus, which is then visible in the image. As light is introduced at an angle from below, the ice below and above our focus depth remains invisible.

Figure 7.1a (depth below the ice sheet surface: 15.40 m) shows one of the first samples that was scanned. We see firn grains in different shadings of gray and voids scattered across the two by two-centimeter image. From fig. 7.1a to d, the firn grains remain bright and the voids connect to more elongated structures.

Our image analysis shows a significant change in the appearance of texture at 58.30 m depth (between fig. 7.1d and e). This change is represented by the first appearance of white spots in the images, which are evidence of the first formation of rounded continuous ice-air interfaces, i.e. trapped air bubbles. The lighting from below the ice core slab is reflected on these rounded solid-gas interfaces causing bright reflections, white spots, or, using the terminology from Morcillo et al. (2020), bright spots.

Further analysis of sections below the firn-ice transition show an increase in bright spots, which reveals the gradual closure of air pathways. As this is a 2D analysis, connections into the y-axis (into the page) can easily be missed. Yet, analyzing the x- and z-axis (lateral extension and depth-axis, respectively) gives an idea of the distribution and scale of air pathways.

While fig. 7.1e shows bright spots, these do not only represent closed bubbles but could also be pathways evolving into a rounded shape. The first definite evidence of closed bubbles can be found in a depth of 66.5 m, where on a 2D appearance some bubbles appear fully enclosed (fig. 7.1f).

In a depth of 74.8 m (fig. 7.1g) we can identify closed bubbles, together with tubes of bubbles, which are still connected. These tubes and bubbles decrease in size, causing a further closure of pathways within the ice (fig. 7.1h).

In a depth of 89.65 m (fig. 7.1i) all bubbles are fully closed off, without any sub-cm-scale pathways in the x- and z-axis. Pathways may still appear in the y-direction. While bubbles form, the space of the image occupied by dark areas, i.e. clean ice, starts to increase.

7.2.2   Grayscale and Bubble Analysis

The grayscale analysis of line scan images is common practice in glaciology (Svensson et al., 2005; Morcillo et al., 2020). We perform a grayscale analysis on 1x5 cm-increments by measuring the intensity values for pixels (px) in the selected area. One centimeter is represented by 186 px, each increment thus has a size of 186 by 930 px. The pixel values range from 0 to 255, representing 256 possibilities. We measure the minimum value, median, and maximum value of each increment.

We investigate the uppermost section of the EastGRIP ice core, i.e. from 13.75 m below surface to 101.05 m (examples shown in fig. 7.1). We measure one 1x5 cm-sample every 55 cm, i.e. every bag, for the upper 100 meters. For 16 meters around the lock-in depth, we measure continuous, i.e. without gaps, 1x5 cm-samples for higher resolution. For each line scan, we remove two centimeters from the top, around sections with core breaks, and the bottom.

Furthermore, we count the bright spots as a proxy for the number of bubbles in our samples. Bright spots are clusters of bright pixels in a binary image. To convert the grayscale image (pixel range from 0 to 255) to a binary image (0 or 255), we use three different cut-offs: 60, 150, and 250. We do not use the method of Ueltzhöffer et al. (2010) due to complicated 3D effects from our thick line scans (discussed later). Neither do we use a blur function (or similar) to correct for gaps in bright pixels belonging to the same bright spot and might therefore overestimate the number of bubbles. Yet, our analysis is simple and sufficient to detect the first formation of bubbles, and also makes layering visible within the BCD depth (see discussion).

7.2.3 Firn-air Data Collection

Firn air sampling took place at 75°37'14.0"N, 35°58'16.1"W approximately one kilometer out of the EGRIP camp between June 12 to 21, 2018. We drilled with the Copenhagen 3" shallow drill to a depth just below 66 m. The ice core retrieved is called the 'S6 firn core'. Then the French firn air sampling system was lowered into the hole and inflated. Flask samples were taken at 22 depth levels from the surface to 66m depth. In parallel to the flask samples, a Picarro cavity ring-down instrument (Type G1301) was used to monitor the concentrations of CO_2 and CH_4. Before the instrument the air was pulled through a magnesium perchlorate trap to remove water vapor, making the water vapor correction obsolete. Although the measurements have been calibrated with our working standard, their purpose was monitoring during the sampling process. The data do not have the same quality as laboratory measurements, thus, some offsets are to be expected. The flow rate during sampling was about 4.3 l per minute down to 61 m below the surface and then decreased to below 1 l per minute at 66 m below the surface where we stopped sampling. The low flow rate at the lowest level indicates that the pores in the firn are almost closed off.

7.3 Results

To quantify our optical impression from the line scan images, we analyze the pixel values (fig. 7.2a,c). The minimum pixel values (yellow line) of each 1x5 cm-increment remain relatively constant over the upper 100 meters of the EastGRIP ice core. This ensures constant camera settings without any adjustments made to the brightness. The maximum pixel values (brown) rapidly rise below a depth of 58 m, while the median value (red) remains at a constant value. This indicates that very bright pixels remain an exception.

From the first processed ice core section (13.75 m) to 58 m, minimum, median, and maximum values do not vary much (fig. 7.2a). We see a small peak at 50 m, and two troughs at around 54 and 58 m. Below 58 m, we see a trend of linearly increasing maximum pixel values (fig. 7.2a, dashed brown line) from 58 m to 85 m, where they remain at 255 over several samples. We identify a drop at around 90 m and then the value remains at a maximum of 255. During the increase of pixel values from 58 m, we identify peaks, indicating some sort of layering in this section (discussed later). fig. 7.2a has a resolution of one 1x5 cm-sample every 55 cm (i.e. in the center of every bag).

We find the first evidence of bubble layering in a depth of 58 m, the beginning of lock-in zone at 66.6 m, and the close off depth at approximately 89 m depth, at which the bubbles start to get squeezed and dark areas become larger

fig. 7.2b is an attempt to determine the number of bubbles from the bright spot proxy. Between 58 m and 85 m, we see an exponential increase (purple dashed line) in bright spots. Between 85 and 90 m, we find two drops to very low bright spot numbers and then a sudden
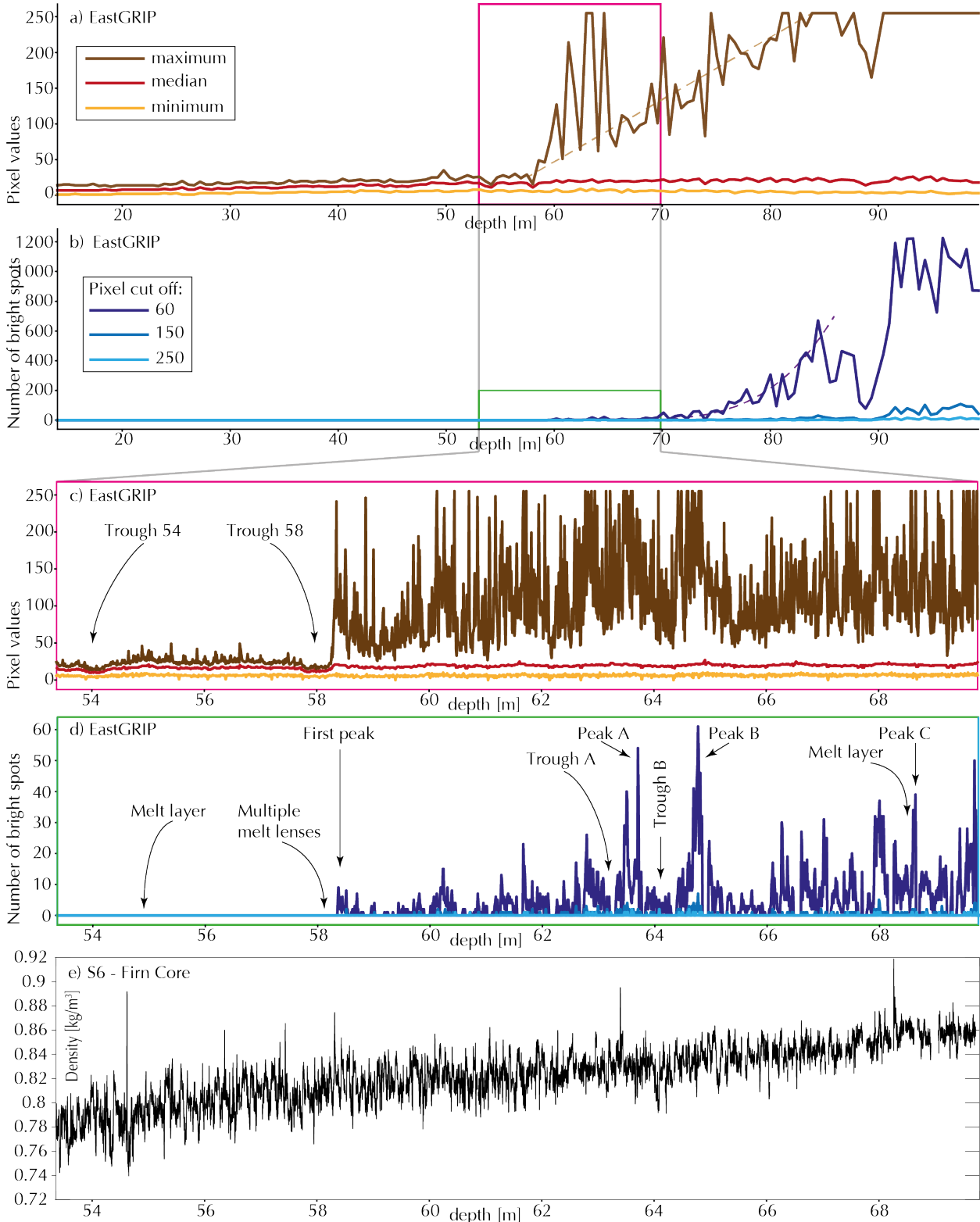
Figure 7.2: Depth of investigation from 13.75 m to 101.05 m below surface with one measurement every 55 cm (a and b). Detailed analysis from 53.35 to 69.85 m, with continuous measurements every centimeter (c and d). Our analysis locates the bubble close-off at 58.30 m depth. We find a linear increase in maximum brightness of bubble reflections in a) and a roughly exponential increase in bubbles in b) (dashed lines). Both c) and d) show a sudden appearance of bubbles below 58.30 m with layering well visible in d. e) Density profile from the S6 firn core. Full profile will be published in Freitag et al. (in prep.).

increase to between 800 and 1200 bright spots per 1x5 cm-image, where it remains constant with depth.

For detailed inspection of the close-off depth, we analyze continuously between 53.35 to 69.85 m (fig. 7.2c, pink box in fig. 7.2a). The drops of all pixel values around 54 m and 58 m (trough 54 and trough 58, respectively) have a width of approximately 30 cm. Below the last trough, at 58.30 m, the maximum pixel values (brown) greatly increase, almost reaching the maximum of 255. Higher maximum pixel values than the average of shallow depths represent the first appearance of bright spots in the line scan images (fig. 7.1e). The detailed inspection does not show a gradual increase in maximum pixel values, but rather multiple peaks and troughs, representing layers containing more and fewer bubbles.

fig. 7.2d (green box in fig. 7.2b) also shows the sudden appearance of bright spots at a depth of 58.3 m. The peaks in fig. 7.2c,d align, but peaks become more visible in d. The number of bright spots does not show a gradual increase, but just like fig. 7.2c, multiple peaks and troughs. This means that a 1x5 cm increment with many bright spots is in general found below an increment with very few bright spots. A prominent example of this alternation is peak B (fig. 7.2d) where we find a prominent trough followed by a peak.

We compare our results with the density data from the S6 firn core (fig. 7.2e). The S6 core is located one kilometer away from the EastGRIP camp (see methods), but both, the EastGRIP and S6 core, should have a rather similar density profile, which is dependent on temperature, and follows a gradual increase over the depth of investigation, without any significant changes in our proposed lock-in depth. Yet at exactly 58.3 m depth, the density profile (fig. 7.2e) has a thick and very dense layer. This could be the impermeable layer, below which diffusion is increasingly limited. We will discuss below, whether we see bubbles closing off, the impermeable layer, or other features in our bright spots analysis.

7.4 Discussion

7.4.1 Experimental and Modeled Bubble Close-off Depth

The air flow during firn air pumping started to decrease from 60 m. At 66 m the air flow had decreased to below one quarter indicating that the close off depth was close by. The kink in the concentration and $\delta^{15}N$ isotope ratios slopes versus depth defined as the top of the close off zone (called slope break in Witrant et al., 2012) is found between 58 to 60 m. Continuous flow measurements of methane (e.g. Stowasser et al., 2012) show that layers with not fully closed pores can be found down to 71.5 m while from around 66.5 m the bubbles are essentially closed off.

We compare our results to the expected results derived from the IGE firn model (Witrant et al., 2012). Constant temperature and accumulation for isothermal firn might be offset for EGRIP due to the effect of strain-densification (Riverman et al., 2019; Oraschewski and Grinsted, 2021). The basic parameterization (Witrant et al., 2012, Eqs. 4 and 6, blue in fig. 7.3b,c,d) results in too high CH_4 concentration in the model versus the data below close off. To improve the model to data match we modified the open/closed porosity ratio parameterization by changing the exponential factor from 7.6 to 3.0 (green in fig. 7.3b,c,d). While this improves the overall match of the model with the CH_4 data, the beginning of the bubble closure moves significantly upwards resulting in 50% closed porosity at around 64.8 m compared to around 61.3 m in the basic (green in fig. 7.3d) configuration.
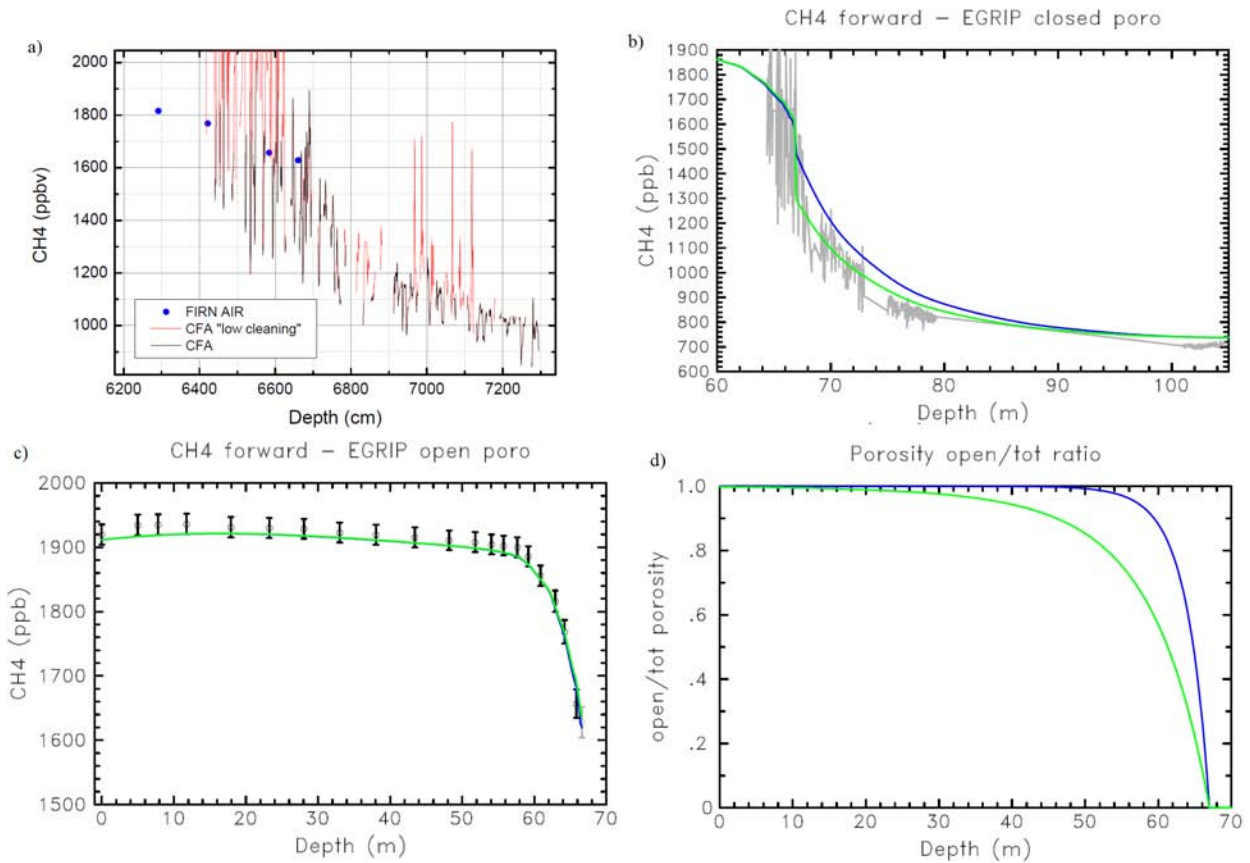
Figure 7.3: a) CH_4 as a function of depth around the bubble close-off. Values from the firn air pumping campaign are included as blue circles. b,c) Forward modeling of CH_4 for closed and open porosity. d) Ratio of open vs. total porosity as a result of the firn air pumping campaign.

7.4.2   Comparison of our Results with the Experimental and Modeled Depths

From our analysis we find that first rounded pathways appear around 58.30 m. This matches very well the results from methane and $\delta^{15}N$ data that suggest the depth to lie between 58 and 60 m. We assume that our method has a higher precision than the modeled depth, as we can pinpoint the exact depth where the first bubbles occur.

Our suggestion of finding the first closed-off bubbles around 66.55 m depth (fig. 7.1f in methods section) also goes hand in hand with the results from the firn-air pumping-campaign, suggesting the full closure of pathways to be around 66.6 m depth. Continuous flow analysis (CFA) measurements propose essentially full closure at around 66.5 m, matching our observations. In places where the CFA measurements indicate isolated layers of open pores (between 69.5 to 71.5 m) we find high pixel values (fig. 7.2a) just above, hinting to a layer where bubble closure has proceeded quite far.

Comparing the 50% open/closed porosity ratio from Martinerie el al. (fig. 7.3d) to lay at 64.8 m depth matches "peak B" (fig. 7.2d) very well, thus suggesting that a peak in our bubble number can very likely influence the porosity ratios.

7.4.3   Melt Layers Around the Lock-in Depth

The study by Westhoff et al. (2021) provides an overview of melt events in the EastGRIP ice core. In the following, we analyze the melt layers and -lenses in the proximity of the lock-in depth. As Blunier and Schwander (2000) state: All mixing processes are strongly influenced
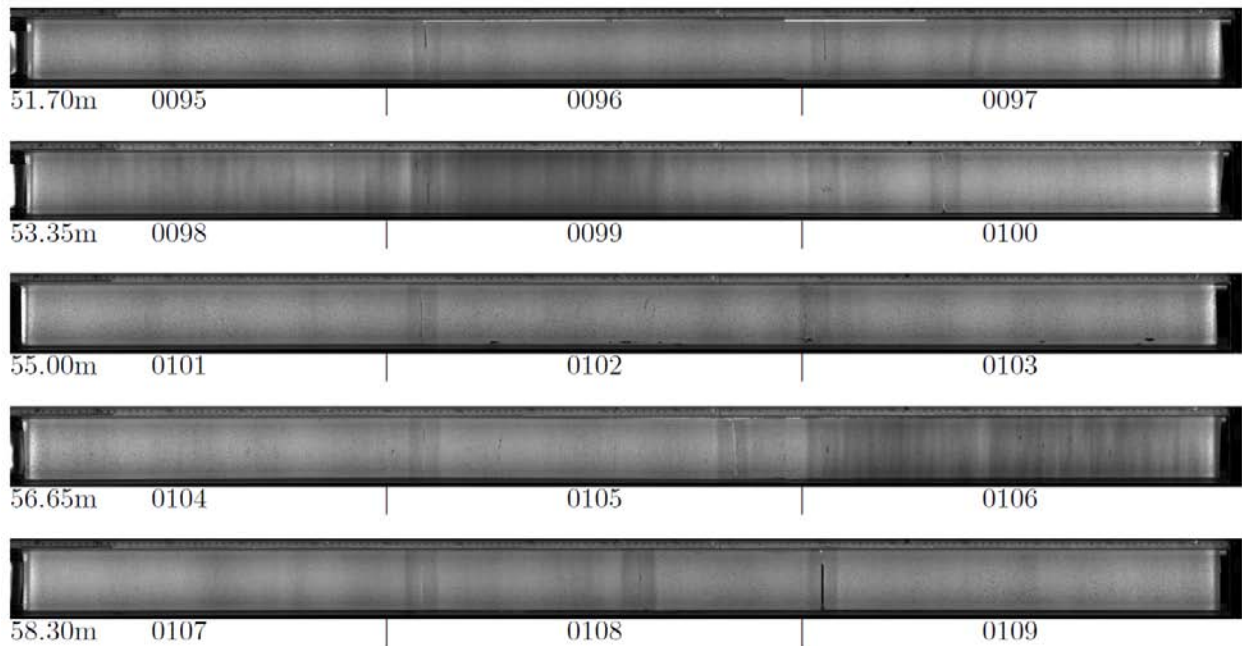
Figure 7.4: Bag 95 to 109, showing brightness variations in the line scan images and melt layers.

by the presence or absence of icy layers resulting from surface melting during summer. In the 16 m around the BCD (fig. 7.2c,d) we find two melt layers in total: in 54.80 and 68.60 m depth. The upper one should be treated with caution, as it is located next to a core break and could be an imaging artifact, rather than a true layer (top of bag 99, fig. 7.4, Westhoff et al., 2021). In the following 30 cm below this melt layer (bag 99), we find the section with significantly darker line scan images (i.e., lower grayscale values, compare to fig. 7.2c, trough 54). Darker layers such as these have been influenced by summer surface melting, or pre-melting (Dash et al., 2006). They probably have an increased density with less permittivity, but to which degree has not been quantified yet.

The ice in 55 to 58 m depth is characterized by the occurrence of eleven melt lenses in total. These are small melt patches with a horizontal extent less than the core width, i.e. less than 10 cm. Four of these lie between 58.00 and 58.16 cm depth (fig. 7.2d), just above the lock-in depth and inside the darker line scan image section (bag 106, fig. 7.4). Melt lenses are evidence for strong surface melting, most likely during summer, and thus an alteration of the physical properties of the snowpack. This alteration can work as a block for vertical diffusion and thus enhance the formation of the first bubbles below this depth.

The influence of a melt layer at 68.6 m is visible in our data (fig. 7.2d), but not to an outstanding degree. Just below the melt layer, we find a layer containing many bubbles, probably an effect of reduced diffusivity due to the icy layer above. Yet this peak (peak C, fig. 7.2d) is equally high as other bubble-rich layers and thus indicates that melt layers must not cause an outstanding effect on bubble close-off. A reason for this uncertainty could be the limited size of the core or image, and therefore the inability to quantify the extent of the melt layer over more than ten centimeters.

7.4.4 Layering Around the Bubble Close-off depth

The idea, that some sort of layering in the lock-in depth can influence the closure of bubbles, has been around for a long time (e.g. Blunier and Schwander, 2000; Mitchell et al., 2015). This idea motivated Birner et al. (2018) to establish a 2D model which includes layering, in order to better reproduce the lock-in of air bubbles. With the line scan images of the

EastGRIP firn section, we now have a unique chance to further investigate this layering.

If we expect the closing-off of bubbles to be a gradual process with depth, fig. 7.2 proves us wrong. We see a sudden appearance of bubbles, or bright spots (a proxy for bubbles), just below a dark layer (trough 58 in fig. 7.2c). fig. 7.2d shows a continuation of this trend with depth. We see alternating layers, with more and fewer bubbles. When the bubble number drops to zero, the reason is mostly missing data due to core breaks. Yet the height of the peaks, i.e. number of bright spots, varies below the BCD.

We find two outstanding layers with more bubbles than in other peaks around 63.5 and 64.5 meters (fig. 7.2d, peak A and B, respectively), in which air has been occulated and diffusion is absolutely limited. Just above both these layers, we find layers with few bubbles, where diffusion is possible to a higher degree because pathways are not fully blocked yet.

7.4.5 Do we Really See the First Bubbles in our Analysis?

Our analysis shows bright spots below a depth of 58.3 m. Yet some layers with closed off bubbles, or rounded pathways, should already be visible well above a depth of 58.3 m. This therefore suggests, that it is not just bubbles that we see, but maybe a connection of multiple effects. In a depth of 58.3 m in the density profile (fig. 7.2e), we find the potential impermeable layer which could have an effect on closed off bubbles.

We therefore suggest, that below the impermeable layer, bubbles are sealed-off from the atmosphere and under a pressure, that the physical properties change. This change causes reflections, i.e. bright spots. The change could also lead to a change in crystal properties, such as connected ice-crystal planes, being the surface for reflections. Our analysis thus, does not necessarily show only rounded bubble pathways, but could also be a method to find the impermeable layer, below which diffusion is limited and the lock-in depth begins.

7.5 Summary and Outlook

Using data from the visual stratigraphy of EastGRIP, we have defined the depth of bubble lock-in to begin at 58.30 m. In this depth bubbles are formed and diffusion become increasingly difficult. This depth matches well with results from the firn air pumping campaign and the modeled results.

The ice from 58.3 m depth was deposited in the year 1681 CE and we thus have a gas age difference of 338 years (year of drilling: 2018 CE).

We also find strong evidence for layering in the firn-ice transition having an effect on the formation of air bubbles and disrupting a gradual bubble close-off.

As accumulation proceeds and annual layers get buried by more recent ones, the depth of bubble lock-in rises relative to a fixed layer. On a meter scale, we can assume that the depth of bubble lock-in will not progress upward gradually, but rather jump to the depth of approximately 54 m, where we see another set of dark layers (fig. 7.4, bag 99).

Our analysis reveals the first bubbles in the EastGRIP ice core, and can be used on any other ice core where optical line scanning was done. We therefore hope that all ice cores drilled in the future will be line scanned all the way from the surface to the bottom.

Acknowledgements

Bibliography - Bubble Lock-in

Andersen, K. K., Svensson, A., Johnsen, S. J., Rasmussen, S. O., Bigler, M., Röthlisberger, R., Ruth, U., Siggaard-Andersen, M. L., Peder Steffensen, J., Dahl-Jensen, D., Vinther, B. M., and Clausen, H. B. (2006). "The Greenland Ice Core Chronology 2005, 15-42 ka. Part 1: constructing the time scale". In: *Quaternary Science Reviews* 25.23-24, pp. 3246–3257. DOI: `10.1016/j.quascirev.2006.08.002`.

Birner, B., Buizert, C., Wagner, T. J., and Severinghaus, J. P. (2018). "The influence of layering and barometric pumping on firn air transport in a 2-D model". In: *Cryosphere* 12.6, pp. 2021–2037. DOI: `10.5194/tc-12-2021-2018`.

Blunier, T. and Schwander, J. (2000). "Gas enclosure in ice: age difference and fractionation". In: *Physics of Ice Core Records*, pp. 307–326.

Buizert, C., Cuffey, K., Severinghaus, J., Baggenstos, D., Fudge, T., Steig, E., Markle, B., Winstrup, M., Rhodes, R. H., Brook, E. J., et al. (2015). "The WAIS Divide deep ice core WD2014 chronology–Part 1: Methane synchronization (68–31 ka BP) and the gas age–ice age difference". In: *Climate of the Past* 11.2, pp. 153–173. DOI: `doi:10.5194/cp-11-153-2015`.

Buizert, C. et al. (2012). "Gas transport in firn: Multiple-tracer characterisation and model intercomparison for NEEM, Northern Greenland". In: *Atmospheric Chemistry and Physics* 12.9, pp. 4259–4277. DOI: `10.5194/acp-12-4259-2012`.

Dash, J. G., Rempel, A. W., and Wettlaufer, J. S. (2006). "The physics of premelted ice and its geophysical consequences". In: *Reviews of Modern Physics* 78.3, pp. 695–741. DOI: `10.1103/RevModPhys.78.695`.

Faria, S. H., Kipfstuhl, S., and Lambrecht, A. (2018). *The EPICA-DML Deep Ice Core*. Berlin: Springer-Verlag GmbH Germany.

Freitag, J., Kipfstuhl, S., and Laepple, T. (2013). "Core-scale radioscopic imaging: A new method reveals density-calcium link in Antarctic firn". In: *Journal of Glaciology* 59.218, pp. 1009–1014. DOI: `10.3189/2013JoG13J028`.

Herron, M. M. and Langway, C. C. (1980). "Firn densification: an empirical model". In: *Journal of Glaciology* 25.93.

Lipenkov, V. Y. (2018). "How air bubbles form in polar ice". In: *Earth's Cryosphere* 22.2, pp. 16–28. DOI: `10.21782/KZ1560-7496-2018-2`.

Martinerie, P., Raynaud, D., Etheridge, D. M., Barnola, J. M., and Mazaudier, D. (1992). "Physical and climatic parameters which influence the air content in polar ice". In: *Earth and Planetary Science Letters* 112.1-4, pp. 1–13. DOI: `10.1016/0012-821X(92)90002-D`.

Mitchell, L. E., Buizert, C., Brook, E. J., Breton, D. J., Fegyveresi, J., Baggenstos, D., Orsi, A., Severinghaus, J., Alley, R. B., Albert, M., Rhodes, R. H., Mcconnell, J. R., Sigl, M., Maselli, O., and Gregory, S. (2015). "Observing and modeling the influence of layering on bubble trapping in polar firn". In: *Journal of Geophysical Research : Atmospheres*, pp. 2558–2574. DOI: `10.1002/2014JD022766.Received`.

Mojtabavi, S., Wilhelms, F., Cook, E., Davies, S., Sinnl, G., Skov Jensen, M., Dahl-Jensen, D., Svensson, A., Vinther, B., Kipfstuhl, S., Jones, G., Karlsson, N., Faria, S. H., Gkinis, V., Kjær, H., Erhardt, T., Berben, S., Nisancioglu, K., Koldtoft, I., and Rasmussen, S. O. (2020). "A first chronology for the East GReenland Ice-core Project (EGRIP) over the Holocene and last glacial termination". In: *Climate of the Past Discussions* 16.December, pp. 2359–2380. DOI: `10.5194/cp-16-2359-2020`.

Morcillo, G., Faria, S. H., and Kipfstuhl, S. (2020). "Unravelling Antarctica's past through the stratigraphy of a deep ice core: an image-analysis study of the EPICA-DML line-scan images". In: *Quaternary International* February. DOI: `10.1016/j.quaint.2020.07.011`.

Oraschewski, F. M. and Grinsted, A. (2021). "Modeling enhanced firn densification due to strain softening". In: *The Cryosphere* September, pp. 1–24.

Petit, J. R., Jouzel, J., Raynaud, D., Barkov, N. I., Barnola, J.-M., Basile, I., Bender, M., Chappellaz, J., Davisk, M., Delaygue, G., Delmotte, M., Kotlyakov, V. M., Legrand, M., Lipenkov, V. Y., Lorius, C., Pépin, L., Ritz, C., Saltzmank, E., and Stievenard, M. (1999). "Climate and atmospheric history of the past 420,000 years from the Vostok ice core, Antarctica The recent completion of drilling at Vostok station in East". In: *Nature* 399, pp. 429–436.

Rasmussen, S. O., Andersen, K. K., Svensson, A. M., Steffensen, J. P., Vinther, B. M., Clausen, H. B., Siggaard-Andersen, M. L., Johnsen, S. J., Larsen, L. B., Dahl-Jensen, D., Bigler, M., Röthlisberger, R., Fischer, H., Goto-Azuma, K., Hansson, M. E., and Ruth, U. (2006). "A new Greenland ice core chronology for the last glacial termination". In: *Journal of Geophysical Research Atmospheres* 111.6, pp. 1–16. DOI: `10.1029/2005JD006079`.

Riverman, K. L., Alley, R. B., Anandakrishnan, S., Christianson, K., Holschuh, N. D., Medley, B., Muto, A., and Peters, L. E. (2019). "Enhanced Firn Densification in High-Accumulation Shear Margins of the NE Greenland Ice Stream". In: *Journal of Geophysical Research: Earth Surface* 124.2, pp. 365–382. DOI: `10.1029/2017JF004604`.

Sigl, M. et al. (2016). "The WAIS Divide deep ice core WD2014 chronology - Part 2: Annual-layer counting (0-31 ka BP)". In: *Climate of the Past* 12.3, pp. 769–786. DOI: `10.5194/cp-12-769-2016`.

Sowers, T., Bender, M., Raynaud, D., and Korotkevich, Y. S. (1992). "δ15N of N2 in air trapped in polar ice: a tracer of gas transport in the firn and a possible constraint on ice age-gas age differences". In: *Journal of Geophysical Research* 97.D14. DOI: `10.1029/92jd01297`.

Stowasser, C., Buizert, C., Gkinis, V., Chappellaz, J., Schapbach, S., Bigler, M., Fan, X., Sperlich, P., Baumgartner, M., Schilt, A., and Blunier, T. (2012). "Continuous measurements of methane mixing ratios from ice cores". In: *Atmospheric Measurement Techniques* 5.5, pp. 999–1013. DOI: `10.5194/amt-5-999-2012`.

Svensson, A., Nielsen, S. W., Kipfstuhl, S., Johnsen, S. J., Steffensen, J. P., Bigler, M., Ruth, U., and Röthlisberger, R. (2005). "Visual stratigraphy of the North Greenland Ice Core Project (NorthGRIP) ice core during the last glacial period". In: *Journal of Geophysical Research: Atmospheres* 110.2, pp. 1–11. DOI: `10.1029/2004JD005134`.

Ueltzhöffer, K. J., Bendel, V., Freitag, J., Kipfstuhl, S., Wagenbach, D., Faria, S. H., and Garbe, C. S. (2010). "Distribution of air bubbles in the EDML and EDC (Antarctica) ice cores, using a new method of automatic image analysis". In: *Journal of Glaciology* 56.196, pp. 339–348. DOI: `10.3189/002214310791968511`.

Vallelonga, P. et al. (2014). "Initial results from geophysical surveys and shallow coring of the Northeast Greenland Ice Stream (NEGIS)". In: *Cryosphere* 8.4, pp. 1275–1287. DOI: `10.5194/tc-8-1275-2014`.

Westhoff, J., Sinnl, G., Svensson, A., Freitag, J., Kjær, H. A., Vallelonga, P., Vinther, B., Kipfstuhl, S., Dahl-jensen, D., and Weikusat, I. (2021). "Melt in the Greenland EastGRIP ice core reveals Holocene warming events". In: *Climate of the Past Discu* July, pp. 1–36. DOI: `10.5194/cp-2021-89`.

Westhoff, J., Stoll, N., Franke, S., Weikusat, I., Bons, P., Kerch, J., Jansen, D., Kipfstuhl, S., and Dahl-Jensen, D. (2020). "A Stratigraphy Based Method for Reconstructing Ice Core Orientation". In: *Annals of Glaciology* 62.85-86, pp. 191–202. DOI: `10.1017/aog.2020.76`.

Witrant, E., Martinerie, P., Hogan, C., Laube, J. C., Kawamura, K., Capron, E., Montzka, S. A., Dlugokencky, E. J., Etheridge, D., Blunier, T., and Sturges, W. T. (2012). "A new multi-gas constrained model of trace gas non-homogeneous transport in firn: Evaluation and behaviour at eleven polar sites". In: *Atmospheric Chemistry and Physics* 12.23, pp. 11465–11483. DOI: `10.5194/acp-12-11465-2012`.

Chapter 8

Conclusion and Outlook

8.1 The Upper 80% of the EastGRIP Ice Core

So far 80%, 2120 of the expected 2650 m, of the EastGRIP ice core have been drilled over three seasons. The upper 1375 m, covering the Holocene, Younger Dryas, and Bølling-Allerød periods have proven to be well-layered and well-suited for climate reconstructions. Thus, one of the aims of the EastGRIP project is fulfilled: to retrieve an ice core containing an undisturbed record of the Holocene.

But is this upper section really undisturbed? Evidence for deformation comes from the line scan images, e.g. in sloping bubble-free layers (chapter 6.4.5) and by the fact, that the first visible cloudy bands already contain deformation structures, i.e. small upright folds (chapter 4). While these folds are interesting for the study of rheology, they do not seem to disturb the vertical stratigraphy.

Deformation structures found in the Glacial Section drilled so far (1375 m to 2120 m), with the bottom most core corresponding to an age of approximately 50,000 yrs before today, tell a different story. chapter 5 suggests, that duplex structures disturb the integrity on a small scale, as visible in fig. 5.8h. The appearance of sudden changes in layer tilt (fig. 5.5) suggests that these duplex structures are also visible on the larger scale, disrupting centimeter to decimeter-long sections of the stratigraphy, by rotating and stacking them over each other. Following the theory of duplex structures, the stacks of layers are not removed in other places, but only doubled within the structure (fig. 5.8e).

8.2 Outlook to the Bottom 20% of the EastGRIP Ice Core

For the bottom 20% of the ice core I expect folds, disturbances and very exciting studies on the flow of ice. It is not clear how much flow and deformation is compensated by sliding over the bedrock and how much by internal deformation. The parallel to flow radargrams (fig. 8.1 from Franke et al., 2021) suggest relatively undisturbed stratigraphic layers towards the bedrock. The flight path to acquire the radargram begins South, outside of NEGIS, crosses the Southern shear margin, takes a slight turn and follows NEGIS parallel to flow downstream (for exact path and overview see Franke et al., 2021).

In the EDML ice core, Faria et al. (2010) find many meters of ice that has a very horizontal layering at 85% of the ice cores depth. They attribute these horizontal layers to large amounts of simple shear, shearing all folds so far to the horizontal, that they appear to be horizontal layers. Below this depth, they find strongly disturbed layers and display some of the structures, which show z-folds exceeding the width of the ice core. In other ice cores,
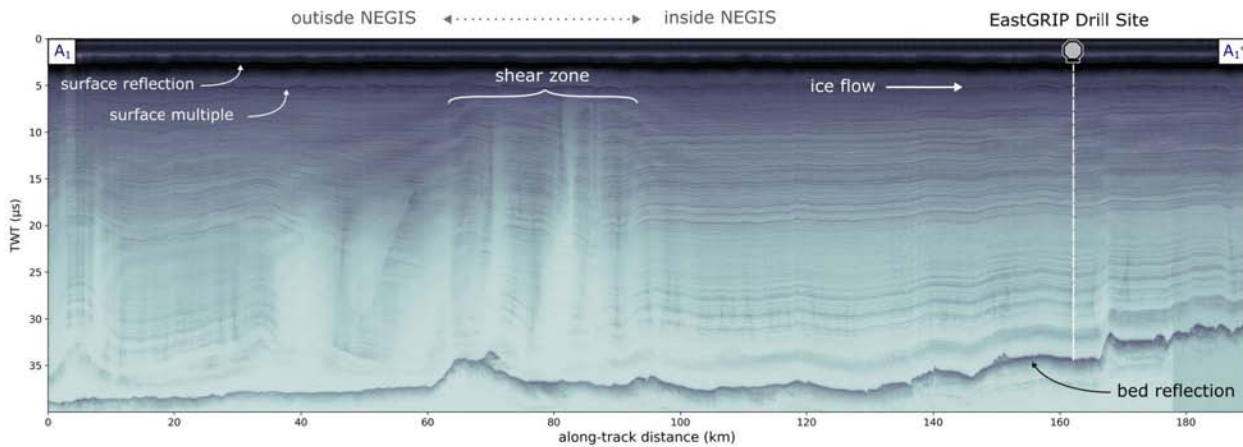
Figure 8.1: Radargram from outside NEGIS, across the Southern shear margin, and parallel to ice flow downstream (Franke et al., 2021).

such as NorthGRIP or NEEM, the bottom parts are handled off quickly, by describing them as extremely folded (Svensson et al., 2005; Jansen et al., 2016).

The main aim for my PhD was to analyze the "bottom parts" (not specifically defined) of the ice core. I will do so during my upcoming PostDoc within the Ice Flow Project, as soon as the sections have been drilled and visualized with the line scanner. Until then, I have a number of follow-up projects that resulted from my work presented in this thesis, which I briefly elaborate on in the following sections.

8.3   Future Perspectives

My findings presented in this thesis can be considered a large boost in ice coring knowledge. Not only have I further extended the application range of the line scan device, I have also solved the problem of determining ice core orientation, which had persisted for decades, and applied the newly won knowledge to deformation structures. I have created a valuable melt layer archive, and found a novel, optical solution to determine the lock-in depth of air into the ice matrix.

The reconstruction of the orienation of the EastGRIP ice core beholds unique chances to further understand the physical properties of ice. I have presented one application in chapter 5 and few applications and ideas will follow in 8.3.1.

Many of the topics presented in the paper about melt layers (chapter 6) are just scratching the surface and deserve more detailed studies. The first obvious choice is to analyze the NEEM line scan data and search for melt events in the same manner as in the work presented here (more details in chapter 8.3.4). Another interesting study would evaluate the core breaks in the brittle zone, concerning their orientation and structural appearance (see chapter 8.3.3). And finally, a detailed analysis of the 986 CE melt event, comparing it to the 2012 and 1889 CE melt events and historical events, would be of great interest (see chapter 8.3.6).

8.3.1   Physical Properties with a Known Ice Core Orientation

My method for reconstructing ice core orientation did not only solve the problem of missing core orientation. but also sparked interest in the drill group, to advance methods in preserving ice core orientation directly from the drill. This will prove to be useful in sections of the ice core with no cloudy bands.

Knowledge of ice core orientation is a great advance for the interpretation of physical properties of ice cores. Line scan-, fabric-, and LASM-images can now be interpreted including directional information. We can now include ice flow direction, to further investigate grain elongations visible in the LASM images, which will be useful for Johanna Kerch and Ilka Weikusat. Furthermore, we can apply the core orientation to the newly built XXL-LASM, which scans a full bag, and where Miguel Moreno will be working on.

Ilka Weikusat's work on fracture patterns from core breaks, caused by the drill's core catchers, can also be put into directional perspective, explaining preferred propagation of fractures in one direction over others. While preferred propagation directions of fractures are obvious to inspect, the challenge is to interpret these features, which are visible in one sample, and missing in another. Hence, the orientation of the image data is crucial.

Including orientation of fabric-image samples can be useful to further understand the spatial structures of ice crystals, relative to their c-axis orientations (PhD work of Nicholas Stoll).

By understanding deformation structures on the small scale, i.e. knowing their spatial properties, we can compare them to large scale deformation structures visible in radargrams, adding to the work of Steven Franke.

Further investigating the undulations, or long wavelength folds, we see in the EastGRIP ice core and comparing them to the effect on reflections in radar data, is a task I want to approach with Tamara Gerber.

The orientation of structures and a better understanding of them, can help in evaluate the outcome of ice flow models, such as those that Nicholas Rathman is working on.

8.3.2 More Deformation Structures Awaiting to be Discovered

Apart from those described in chapter 5, many more structures are visible in the line scan data of EastGRIP (fig. 5.4), which I will investigate further in the future. Some of them, such as the duplex structures, could have an impact on climate reconstructions, and thus deserve more attention throughout the ice coring community.

8.3.3 A Detailed Analysis of Core Breaks in the Brittle Zone

While counting core breaks in the Holocene section of the EastGRIP ice core (see chapter 6.3.2), the directional orientation of core breaks throughout the brittle zone caught my attention. The core breaks caused by fracture due to expansion of trapped air, not those caused by drilling operations, run diagonally across the ice core (fig. 8.2). I plan to investigate, whether there is a systematic direction of core breaks, influenced by the physical properties, or weather they are randomly oriented. The ice core orientation of the brittle zone is not known, thus interpreting a certain preferred direction of fracture propagation will be challenging. On the other hand, exactly this could be the chance to determine ice core orientation, namely by the direction of core break propagation.

8.3.4 The NEEM Melt Layer Record

Melt layers are a rare opportunity to identify extreme warm weather events from the past. These melt events are caused by exceptionally warm temperateness occurring over the central ice sheet and their frequency could be a good indicator for climate change. Furthermore, the information on frequency of melt layers can be used to fine-tune climate models. With this motivation I plan to investigate the melt layers from the NEEM line scan images. Line scan images have been obtained continuously from around 100 m depth to the bottom of the ice
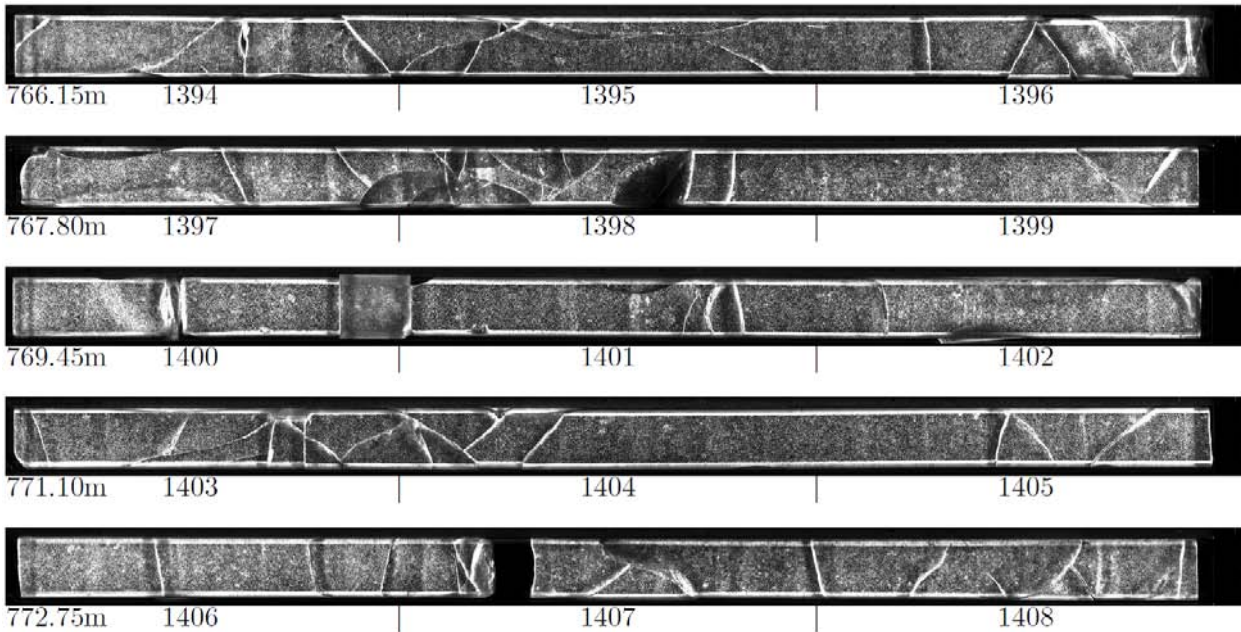
Figure 8.2: Line scan samples from bag 1394 to 1408, in the central part of the EastGRIP brittle zone. Core breaks are bright linear features in the line scan images.

core more than 2500 m below the surface. By analyzing them in the same manner as done in chapter 6, the two records can be compared.

I want to address the following questions: How similar is the NEEM melt layer record to the one from EastGRIP? Do we find the same events? If not, where are the differences, and why?

A first step would be to establish a melt layer record of the NEEM visual stratigraphy. I have the script ready to do it in the same manner as for EastGRIP (see chapter 6). I have created an overview of the NEEM line scan data, concerning what is available and processed, with which line scanner it was done, and the file format of the saved images (table 8.1). Challenges here are that the file names, file size, and file type are not consistent throughout the ice core. Also stitching is required for images from bags 1191 to 1575, with the great problem, that the bag-tag was moved on the core, and therefore covers the section of overlap. This means that the images that require stitching have a very small overlapping section and the scripts I used for EastGRIP is not immediately applicable. An easy challenge, but not be missed, is that all files are saved with the top to the bottom, so a 180° rotation is necessary.

When this project is accomplished, other archives for melt layer reconstructions could include the notes on the ECM record of the DYE-3 ice core.

Table 8.1: Overview of line scanner data collection from NEEM. Including number of scans for one sample and number of bags in one scan, i.e. length of scan.

Bag	Scanner	Comment	Bags in one scan	File type
180 to 1092	Old line scanner	1 file per sample	3	.png
1092 to 1191	*missing*	-	-	
1191 to 1575	New line scanner	8-12 files per sample, stitching needed	3	.bmp
2100 and 2283	New line scanner	4 scans per sample	3	.bmp
1575 to 2331	*missing*	-	-	
2331 to 3197	Old line scanner	1-3 file(s) per sample	3	.png
3198 to 4606	New scanner	6 scans per sample	2	.bmp

8.3.5 Influence of Melt Layers on the Water Isotope Signal
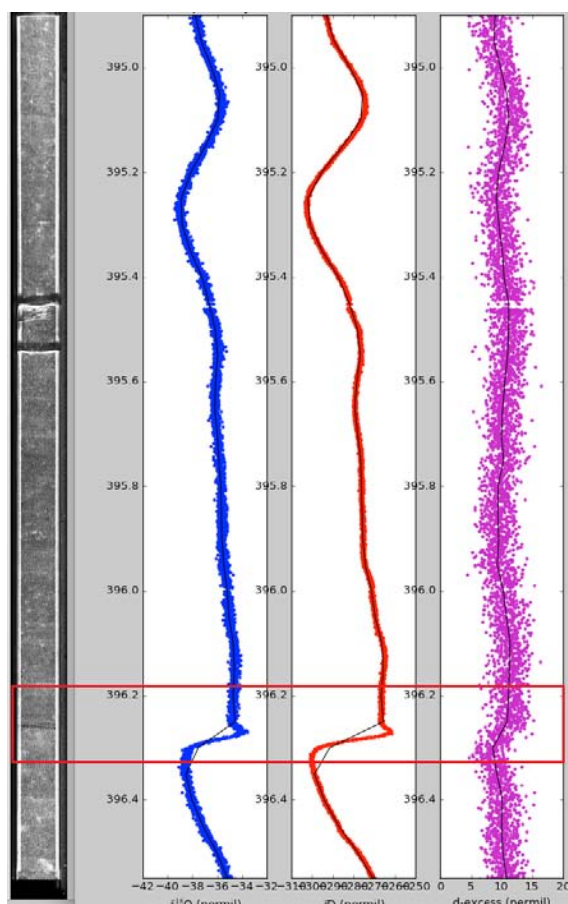
Figure 8.3: Bag 719 (depth from 395 m) showing the line scan images, the $\delta^{18}O$, δD, and the d-excess record for the EastGRIP ice core (Morris et al., 2021). Red box indicates the melt layer.

That percolating and refreezing melt can disrupt the stratigraphy is well accepted. Yet, the traces that these melt layers leave in other records have not been studied in detail. The first attempt to investigate these was taken by Johannes Freitag (2014, EGU Poster). Building up on this, Valerie Morris and I plan to investigate the influence of melt layers on the stable water isotope signal in more detail. Basis for their analysis are on one hand the melt layer record derived from line scan images (Westhoff et al., 2021), and on the other hand the Holocene isotope record from Morris et al. (in prep.).

Melt layers identified in the EastGRIP ice core align with spikes in the stable water isotope records (fig. 8.3, red box in a depth of 396.25 m). Many layers analyzed so far align, but a detailed overview and analysis is still work in progress. Noticeable so far is that many melt layers labeled as very uncertain, i.e. with a very low confidence in the line scan images, are visible in the stable water isotopes record. Which melt layers align and how they appear in the line scanner compared to spikes visible in the $\delta^{18}O$ and δD still needs to be analyzed in detail. Also the direction of the excursion, i.e. to more positive or negative values, of the $\delta^{18}O$ record, still needs to be evaluated.
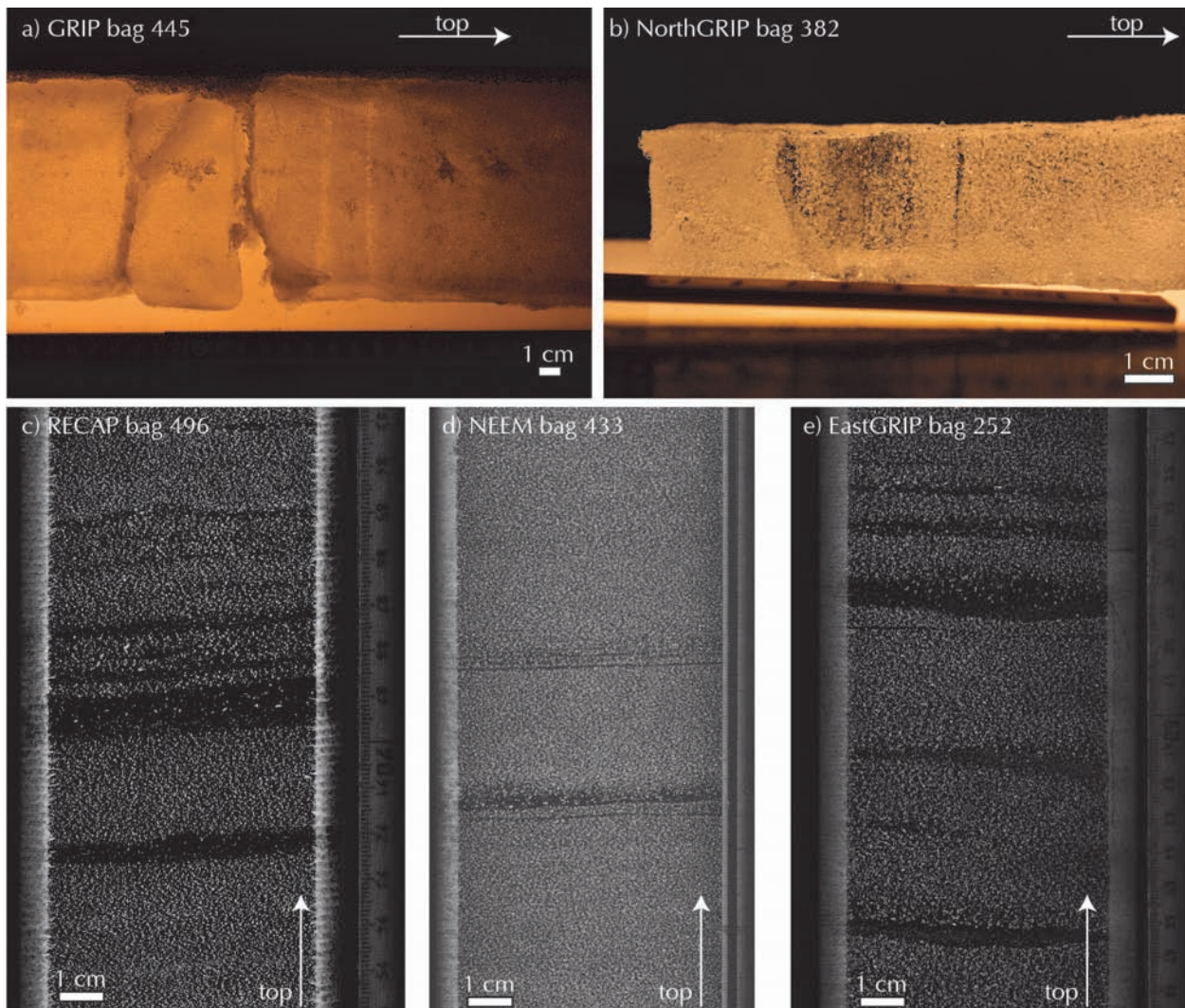
Figure 8.4: The 986 CE melt layer in different Greenland ice cores. a) GRIP, b) NorthGRIP1, c) RECAP, d) NEEM, and e) EastGRIP. a,b) are photographic images, taken in Oct. 2021, c,d,e) are line scan images.

8.3.6 The 986 CE Melt Event and the Viking Settlement Voyage to Greenland

In chapter 6 my co-authors and I find an impressive melt layer in the depth of 138.05 m of the EastGRIP ice core (fig. 6.2). This depth corresponds to a GICC05 age of 986 CE (Mojtabavi et al., 2020). The layer from 986 CE had already been noticed by Þorsteinn Þorsteinsson during the NorthGRIP drilling, and finding a melt layer that dates to the same year in the EastGRIP ice core is exciting already on its own. Furthermore, the year 986 CE is the year that Erik the Red sailed from Iceland to Greenland and thus marks the first Viking settlement voyages to Greenland (Þorgilsson, 1968). In chapter 6 we present the coincidence of the Viking voyages and the melt layers, suggesting that the favorable warm weather might have lead to the success of the voyage. The viking section of the melt layer paper sparked a lot of interest as it connects historic events to a layer we can actually see in the ice core. I therefore plan to investigate this melt layer in more depth.

To start this investigation, I searched for the melt layer from the same year in the line scan data of NEEM and RECAP and in the actual ice cores from NorthGRIP and GRIP. The corresponding years were provided by Giulia Sinnl, and support in the freezer by Iben Koldtoft. Iben and I eventually found the corresponding layers (fig. 8.4).

Now I plan to further investigate the questions: How large is this event compared to the

2012 and the 1889 melt event? Could this warm event really be connected to the Viking voyages to Greenland? I plan to do so with the following team: Þorsteinn Þorsteinsson, Anders Svensson, Ilka Weikusat, Dorthe Dahl-Jensen and potentially others.

Challenges include an ongoing revision of the GICC05 timescale. This revision could cause a shift of some years and then melt layer and Viking voyage don't align anymore. The first attempt to align the events, is based on the GICC05 timescale (fig. 8.5).
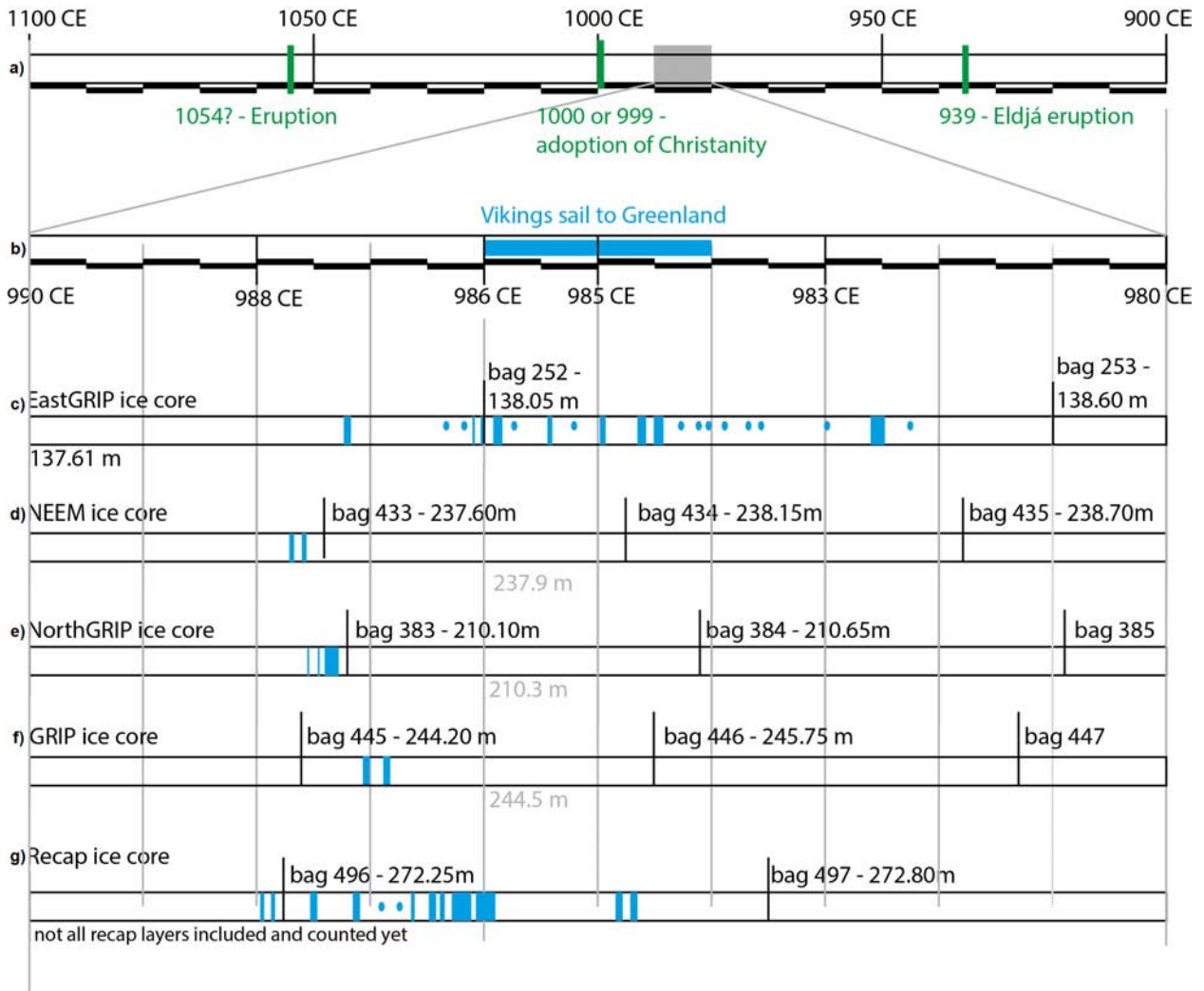
Figure 8.5: A first attempt to align the 986 CE melt layer from different ice cores. a) Time line of relevant events between 900 CE and 1100 CE. b) Zoom in between 980 CE and 990 CE with melt layer in different ice cores: c) EastGRIP, d) NEEM, e) NorthGRIP1, f) GRIP, and g) RECAP

An additional challenge is the uncertainty in the historic time scale as stated in the Íslendingabók (The Book of Icelanders) from 1133 CE (Þorgilsson, 1968): "and Eiríkr began to settle the country fourteen or fifteen years before Christianity came here to Iceland, according to what a man who had himself accompanied Eiríkr the Red there told Þorkell Gellisson in Greenland." Christianity was adopted in Iceland either in 999 or 1000 CE, so fourteen or fifteen years before that could refer to either 984, 985 or 986, depending on which timing one adheres to for the adoption of Christianity (pers. comm. Þorsteinn Þorsteinsson).

While aligning the melt layers from the ice cores, I found the melt layers at the bottom of bag 382 and the top of bag 382 in NorthGRIP one and two, respectively. This leads to a depth difference of around 40 to 50 cm. But, the difference between the two NorthGRIP cores should be smaller (Hvidberg et al., 2002). Maybe one of the cores was inserted the wrong way into the bag after some processing in last 25 years, this seems unlikely but possible. A

problem was also finding the melt layer in NorthGRIP 2, as there is only very little ice left to analyze, there are many core breaks in the bag, and the melt layer is potentially close to the end of a bag.

Despite the challenges in the time scale uncertainties, a study on the 986 CE melt event would still be interesting, as the melt layer is visible in all Greenland ice cores (which I have looked at so far, fig. 8.4), and could thus be exciting to compare to the 1889 CE and 2012 CE melt events.

8.3.7   The Future of an Optical Bubble Lock-in Method

The newly described optical method to determine the lock-in depth can be used to assist the various teams around the world working on gas measurements in ice cores. The method is a quick way to determine the bubble lock-in depth, leading to the age difference between deposited snow/ice and the age of trapped air bubbles.

For future investigations, we can also use line scan data of firn sections of ice cores, or shallow cores. There are countless oportunities in the firn sections, where seasonal variations of physical properties are visible in the line scan images. We can use this, and other information from the line scan data to further complement the work of Johannes Freitag on the CT. The line scan images of firn sections could be useful, as they might show different properties than CT measurements. This is worth investigating further.

8.4   The Line Scanner
- One Thousand and One Opportunities

The line scanner is a treasure chest, where the lid has barely been opened! In this thesis, I have presented an overview of possibilities using data from the line scanner. I have covered the entire length of the, so far drilled, EastGRIP ice core. This length covers time from the year 1956 CE until 50,000 years before today. I have used the line scanner to analyze firn and to find the bubble lock-in depth. The line scanning of firn sections of ice cores is not commonly done and this should be changed. There are countless discoveries to be made in these sections, that have just been ignored so far.

As I have shown, the line scan data is very well suited to identify melt layers throughout long sections of an ice core. Due to the high resolution of the line scan images, there are countless more opportunities to investigate melt layers, including their shape, the inclusion of bubbles in melt layers and many other features.

Furthermore, the line scan data can be used to enhance our understanding of folded stratigraphy. When we understand the mechanisms that drive deformation in ice, we can use these to reconstruct folded layers. Folded layers in the bottom sections of ice cores usually disturb the continuity of climatic records, and with knowledge won from line scan images, we can learn to unfold these sections. This might prove to be especially useful for the upcoming Beyond-EPICA project in Antarctica. The aim of the project is to drill one million year old ice and the bottom sections are expected to be folded and disturbed. With the help of the line scanner we can try to unfold these parts of the ice core and maybe win the race to be first to have a continuous one million year climate record from ice cores.

Bibliography - Outlook

Faria, S. H., Freitag, J., and Kipfstuhl, S. (2010). "Polar ice structure and the integrity of ice-core paleoclimate records". In: *Quaternary Science Reviews* 29.1-2, pp. 338–351. DOI: `10.1016/j.quascirev.2009.10.016`.

Franke, S., Jansen, D., Binder, T., Paden, J., Dörr, N., Gerber, T., Miller, H., Dahl-Jensen, D., Helm, V., Steinhage, D., Weikusat, I., Wilhelms, F., and Eisen, O. (2021). "Airborne ultra-wideband radar sounding over the shear margins and along flow lines at the onset region of the Northeast Greenland Ice Stream". In: *Earth System Science Data Discussions* April, pp. 1–24. DOI: `10.5194/essd-2021-91`.

Hvidberg, C. S., Steffensen, J. P., Clausen, H. B., Shoji, H., and Kipfstuhl, J. (2002). "The NorthGRIP ice-core logging procedure: Description and evaluation". In: *Annals of Glaciology* 35.1, pp. 5–8. DOI: `10.3189/172756402781817293`.

Jansen, D., Llorens, M. G., Westhoff, J., Steinbach, F., Kipfstuhl, S., Bons, P. D., Griera, A., and Weikusat, I. (2016). "Small-scale disturbances in the stratigraphy of the NEEM ice core: Observations and numerical model simulations". In: *Cryosphere* 10.1, pp. 359–370. DOI: `10.5194/tc-10-359-2016`.

Mojtabavi, S., Wilhelms, F., Cook, E., Davies, S., Sinnl, G., Skov Jensen, M., Dahl-Jensen, D., Svensson, A., Vinther, B., Kipfstuhl, S., Jones, G., Karlsson, N., Faria, S. H., Gkinis, V., Kjær, H., Erhardt, T., Berben, S., Nisancioglu, K., Koldtoft, I., and Rasmussen, S. O. (2020). "A first chronology for the East GReenland Ice-core Project (EGRIP) over the Holocene and last glacial termination". In: *Climate of the Past Discussions* 16.December, pp. 2359–2380. DOI: `10.5194/cp-16-2359-2020`.

Morris, V., Westhoff, J., Vaughn, B., Weikusat, I., Jones, T., Markle, B., Hughes, A., Skorski, W., Brashear, C., Gkinis, V., Vinther, B., and White, J. (2021). "Post-depositional processes visible in the integration of EGRIP high-resolution water isotope record and visual stratigraphy". In: DOI: `10.5194/egusphere-egu21-14131`.

Svensson, A., Nielsen, S. W., Kipfstuhl, S., Johnsen, S. J., Steffensen, J. P., Bigler, M., Ruth, U., and Röthlisberger, R. (2005). "Visual stratigraphy of the North Greenland Ice Core Project (NorthGRIP) ice core during the last glacial period". In: *Journal of Geophysical Research: Atmospheres* 110.2, pp. 1–11. DOI: `10.1029/2004JD005134`.

Westhoff, J., Sinnl, G., Svensson, A., Freitag, J., Kjær, H. A., Vallelonga, P., Vinther, B., Kipfstuhl, S., Dahl-jensen, D., and Weikusat, I. (2021). "Melt in the Greenland EastGRIP ice core reveals Holocene warming events". In: *Climate of the Past Discu* July, pp. 1–36. DOI: `10.5194/cp-2021-89`.

Þorgilsson, A. (1968). *Íslendingabók (The Book of Icelanders)*. Ed. by J. Benediktsson.

Appendix A

Appendix

A.1: Line Scanner Settings for 2019
Shows the one-page overview-sheet I provided to the 2019 EastGRIP processing team, with a brief instruction on the line scanner settings.

A.2: Visual Stratigraphy of EastGRIP - Holocene
Overview booklet of line scans from the Holocene. Displayed here are: title page, first page with notes, and two example pages. Example pages are the uppermost scans from the EastGRIP ice core (page 2) and an example from the brittle zone (page 33 from booklet). The entire overview can be found here:

    `doi.org/10.17894/ucph.2f43d7c8-ae7f-47af-ad8a-4aaab2784b87`

A.3: Visual Stratigraphy of EastGRIP
- Younger Dryas, Bølling-Allerød, and the Last Glacial
Overview booklet of line scans from the Younger Dryas, Bølling-Allerød, and the Last Glacial (until 50,000 yrs BP). Displayed here are: title page, first page with methods and results, and two example pages. Example pages are pages 7 and 21 from booklet. Page 7 covers the last nine bags of the Glacial (2509 to 2501) and the transition into the Bølling-Allerød warm period (from bag 2501). Page 21 covers the Dansgaard-Oeschger event three, dark line scan samples in upper half of page (GI-3, Rasmussen et al., 2006).
The entire overview can be found here:

    `doi.org/10.17894/ucph.a1c27df7-ceac-4d2d-8d21-e6dc27afd5e7`

A.1   Line Scanner Settings for 2019

ALWAYS do all scans and take your time to properly prepare the scan surface and bottom surface of core.
Back up on line scan hard drives AND EastGRIP shared drive.

Table A.1: Suggested settings for line scanner throughout the Glacial section of the EastGRIP ice core, i.e. from bag 3197.

	File Name (bag + code)	Integration time	Aperture	Focus Depth [mm]
1	3197___1.bmp	0.505 ms	4	40
2	3197_1_32mm.bmp	0.505 ms	4	32
3	3197_1_24mm.bmp	0.505 ms	4	24
4	3197_1_1_32mm.bmp	0.201 ms	4	32

Table A.2: Suggested settings for line scanner from bag 1643 to 1931.

	File Name (bag + code)	Integration time	Aperture	Focus Depth [mm]
1	1646___1.bmp	0.022 ms	8	40
2	1646_1_1.bmp	0.097 ms	8	40
3	1646_1_2_32mm.bmp	0.097 ms	4	32

To the operator: if you get the impression that the images after bag 3197 onward become too bright and bright layers merge into each other as they have the maximum white value and cannot be distinguished anymore then: divide all integration times for all four scans by 2 and continue procedure as before.

In other words:
    never change aperture or focus depths
    never change only one integration time
when a change of values should be necessary:
    change ALL integration time values by the SAME factor
    (e.g. divided by 2 or times 1.5 or whatever)
but only for bags below 3200!

A.2 Visual Stratigraphy of EastGRIP - Holocene

Westhoff, J., Kipfstuhl, S., Svensson, A., Dahl-Jensen, D., and
Weikusat, I.
with special thanks to the processing teams

Bag 35 to 37

Bag 251 to 253

Image: Bag 422
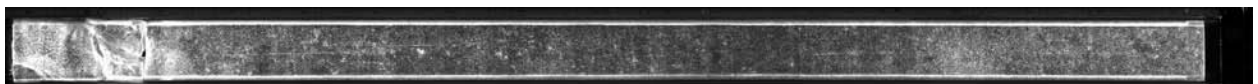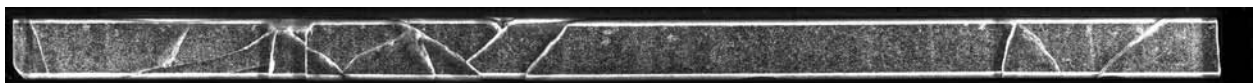

Bag 785 to 787

Bag 1403 to 1405

For questions and remarks contact: julien.westhoff@nbi.ku.dk

Notes:

This overview covers the Holocene section of EastGRIP:
    From bag 26 (upper most) to bag 2266, or
    13.75 m to 1246.30 m depth, or
    1965 AD to 9753 BC, or
    35 yrs b2k to 11753 yrs b2k.

Younger Dryas – Holocene transition (11,700 yrs b2k) just above 1244 m depth, in bag 2262.

13.75m   0026   0027   0028

15.40m   0029   0030   0031

17.05m   0032   0033   0034

18.70m   0035   0036   0037

20.35m   0038   0039   0040

22.00m   0041   0042   0043

23.65m   0044   0045   0046

25.30m   0047   0048   0049

26.95m   0050   0051   0052

28.60m   0053   0054   0055

30.25m   0056   0057   0058

31.90m   0059   0060   0061

33.55m   0062   0063   0064

35.20m   0065   0066   0067

36.85m   0068   0069   0070
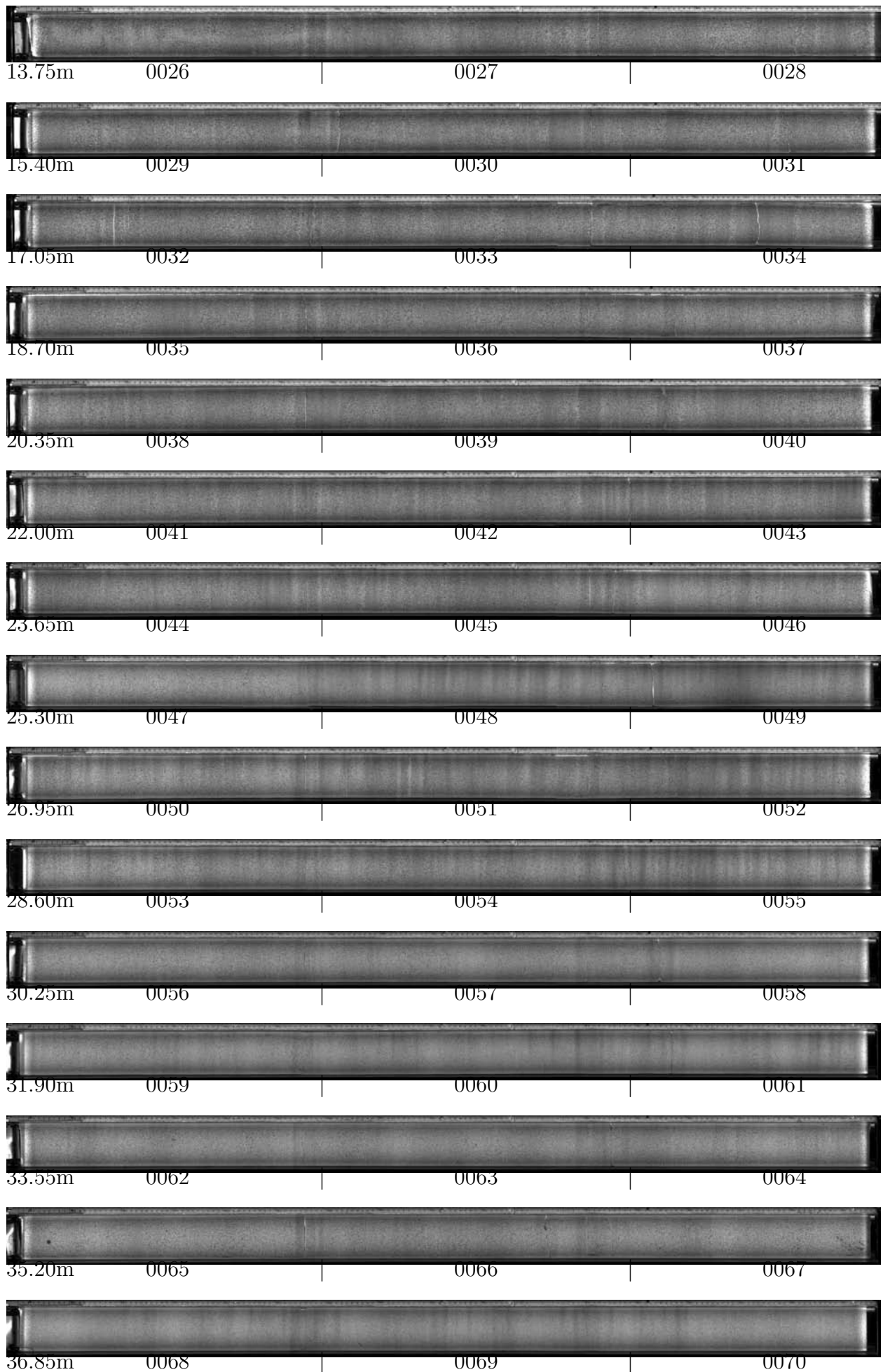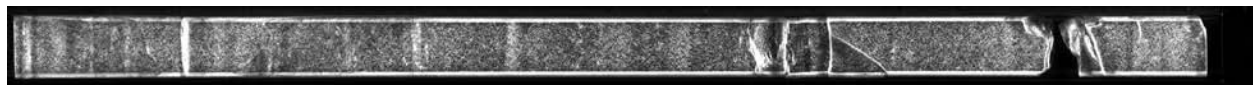
734.80m   1337 | 1338 | 1339
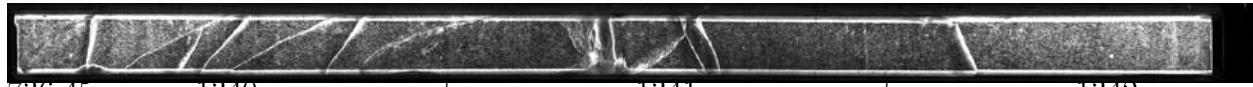
736.45m   1340 | 1341 | 1342
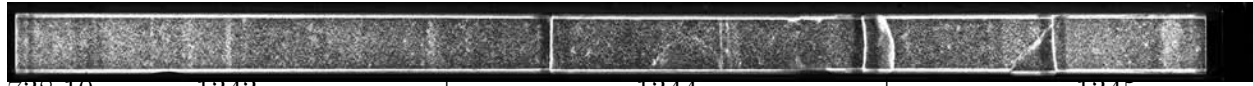
738.10m   1343 | 1344 | 1345
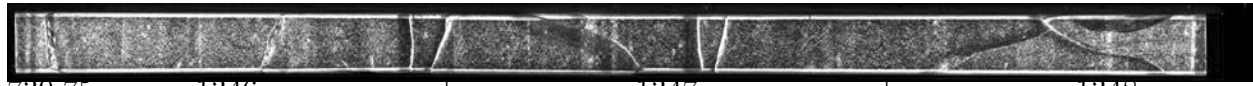
739.75m   1346 | 1347 | 1348
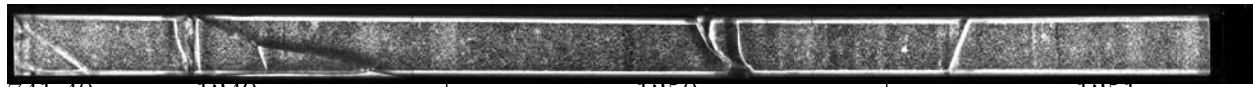
741.40m   1349 | 1350 | 1351

743.05m   1352 | 1353 | 1354
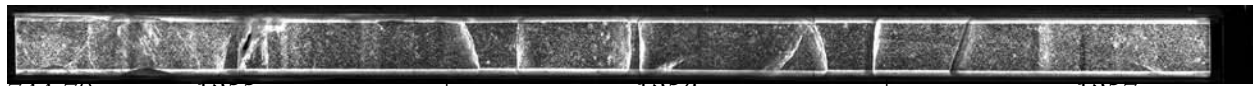
744.70m   1355 | 1356 | 1357

746.35m   1358 | 1359 | 1360
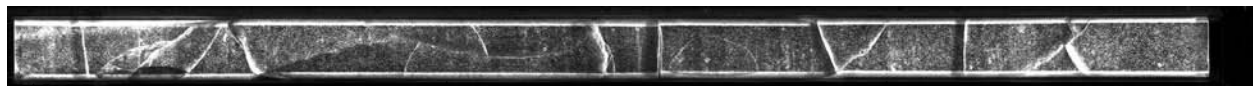
748.00m   1361 | 1362 | 1363
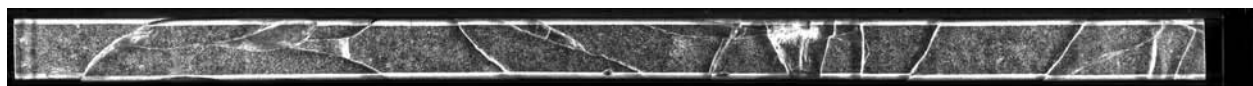
749.65m   1364 | 1365 | 1366
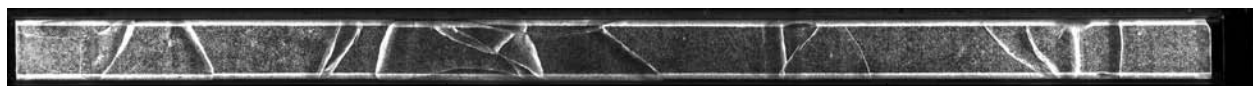
751.30m   1367 | 1368 | 1369

752.95m   1370 | 1371 | 1372
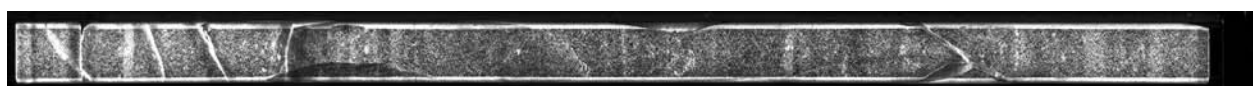
754.60m   1373 | 1374 | 1375

756.25m   1376 | 1377 | 1378

A.3   Visual Stratigraphy of EastGRIP - Younger Dryas, Bølling-Allerød, and the Last Glacial

Westhoff, J., Kipfstuhl, S., Svensson, A., Dahl-Jensen, D., and Weikusat, I.

with special thanks to the processing teams
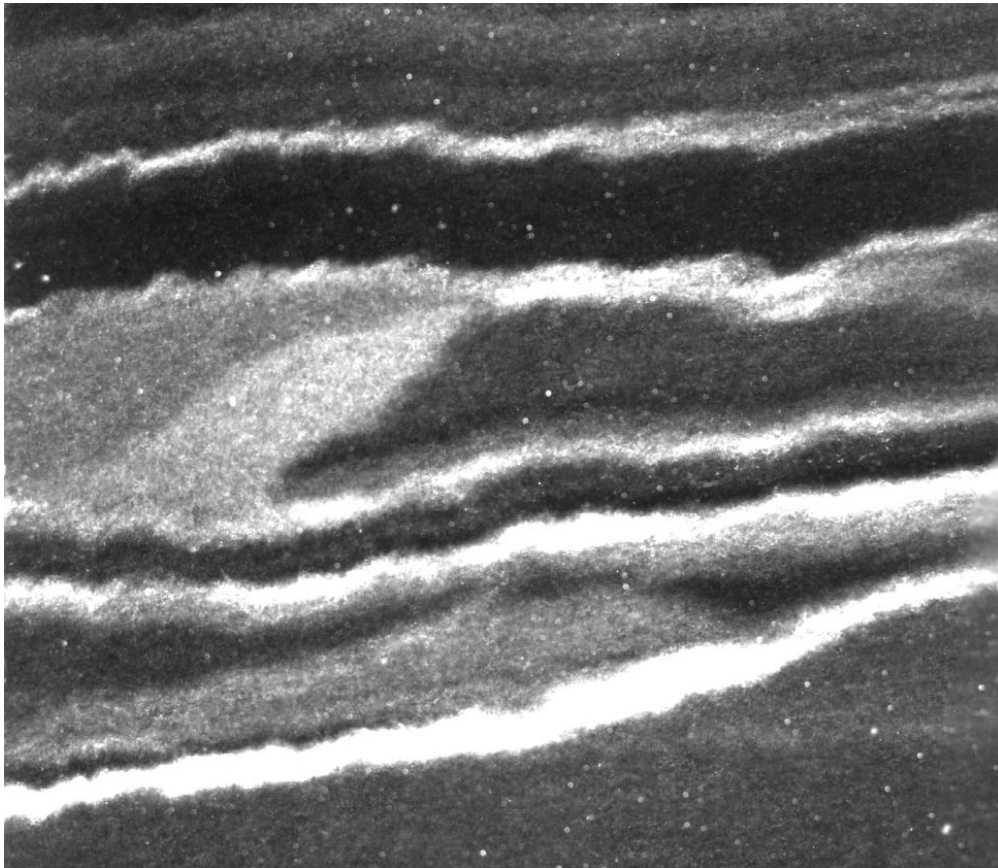
Image: Bag 3004

For questions and remarks contact:
julien.westhoff@nbi.ku.dk

Method and data

Brightness of images:

Bag 2210 to 2344 - integration time: 0.258 ms.

Bag 2345 to 2404 - integration time: 0.406 ms.

Bag 2405 to 3856 - integration time: 0.505 ms.

Aperture constant for all images: f=4.

Focus depth changed from 40 mm to 32 mm from bag 2425 to 2426 respectively.

Top is always left.

Bags 2381, 2382 and 2383 removed as only 1/2 is scanned.

Brightness values for bags 2210 to 2404 have been adjusted to match the bags below. An unaccounted-for brightness bias may occur due to the change of focus depth at bag 2425 to 2426. Values were collected for every row of pixels and averaged over 10,000 values for the figure below.

Values in plot below are measured in a two centimeter wide stripe along the central part of the image. One centimeter corresponds to 186 pixels (px), thus on line analyzed stripe contains $2x186 = 372px$. Average image height is 30,700 px resulting in 30,700 stripes for every 165 cm-long image.

Results
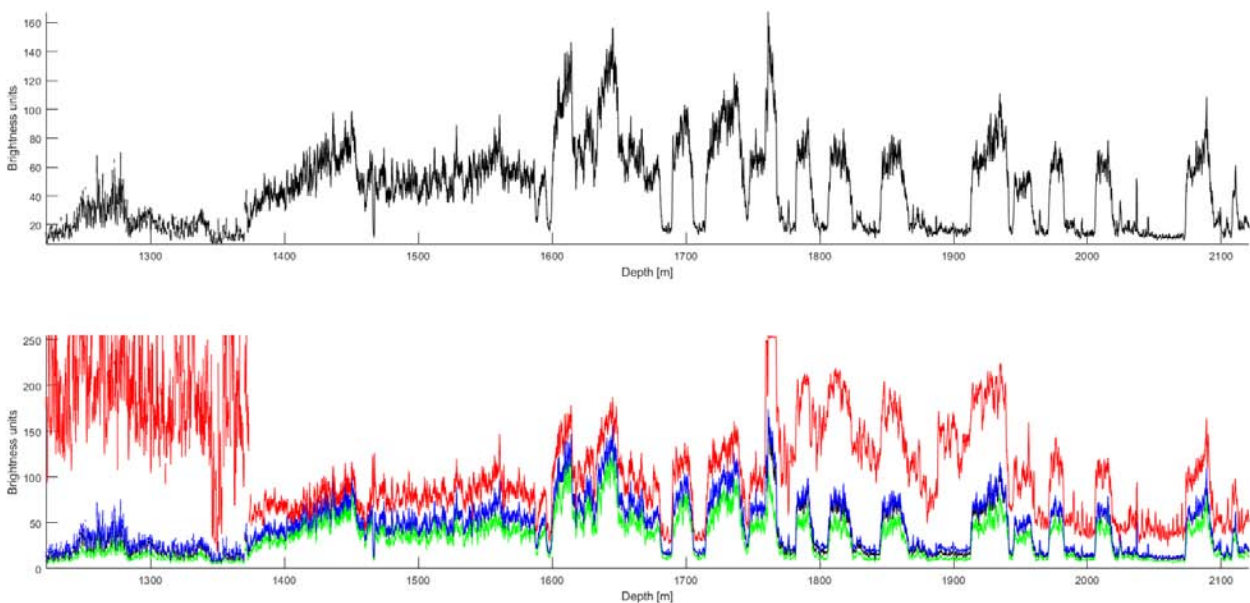
EastGRIP visual stratigraphy image brightness against depth, averaged over 10,000 data points. Black is median value, blue is mean value, green is minimum value, and red is maximum value for every stripe.

1356.85m   2468   2469   2470

1358.50m   2471   2472   2473

1360.15m   2474   2475   2476

1361.80m   2477   2478   2479

1363.45m   2480   2481   2482

1365.10m   2483   2484   2485

1366.75m   2486   2487   2488

1368.40m   2489   2490   2491

1370.50m   2492   2493   2494

1371.70m   2495   2496   2497

1373.35m   2498   2499   2500

1375.00m   2501   2502   2503

1376.65m   2504   2505   2506

1378.30m   2507   2508   2509

1680.25m   3056 | 3057 | 3058

1681.90m   3059 | 3060 | 3061

1683.55m   3062 | 3063 | 3064

1685.20m   3065 | 3066 | 3067

1686.85m   3068 | 3069 | 3070

1688.50m   3071 | 3072 | 3073

1690.15m   3074 | 3075 | 3076

1691.80m   3077 | 3078 | 3079

1693.45m   3080 | 3081 | 3082

1695.10m   3083 | 3084 | 3085

1696.75m   3086 | 3087 | 3088

1698.40m   3089 | 3090 | 3091

1700.05m   3092 | 3093 | 3094

1701.70m   3095 | 3096 | 3097